A Study on Formation Mechanisms of Surface Pressure Distribution around a Laminar Separation Bubble

(層流剥離泡付近の表面圧力分布
形成メカニズムに関する研究)

Department of Aeronautics and Astronautics,
The University of Tokyo

Donghwi Lee
李　東輝

March, 2017

Abstract

In recent years, the interests in development of micro air vehicles (MAV) and unmanned aerial vehicles (UAV) have been growing. Many of these aircrafts are usually small in size and have a low cruising speed, so the Reynolds numbers based on the chord length (Re_c) are between $Re_c = O(10^3) \sim O(10^5)$. Given that the cruise Reynolds numbers of many of commercial airplanes are larger than $Re_c = O(10^7)$, the flight conditions of MAV or UAV correspond to so-called "low Reynolds number region". In this Reynolds number region, a laminar separation bubble (LSB) is often formed through the following process: separation of laminar boundary layer, laminar-turbulent transition, and turbulent reattachment. The LSB consists of two regions, laminar (separation to transition point) and turbulent (transition to reattachment point) regions.

One of the important characteristics of the LSB is a relationship between the LSB and the surface pressure distribution, because the surface pressure distribution directly affects airfoil aerodynamic characteristics. When the LSB is formed, it is often observed that a plateau region appears in the laminar part followed by a rapid pressure recovery region in the turbulent part. The reason of appearing the plateau pressure distribution has been explained that the velocity under the separated shear layer is circulated slowly compared to the freestream, and it can be considered as a practically stationary state. As a result, it leads to the constant pressure distribution. On the other hand, in the rapid pressure recovery region, the three-dimensional turbulent flow enhances mixing and momentum transfer from the freestream to the surface. Consequently, the separated shear layer reattaches to the surface as a turbulent state, which results in the rapid recovery of the surface pressure distribution. In particular, the plateau pressure distribution has been thought as a general feature of LSB, and thus the formation of LSB has been judged by the appearance of the plateau pressure distribution in many previous studies. These explanations are reasonable and can be applied to many of LSB flows. Under some specific flow conditions, however, it has been reported that a gradual pressure recovery occurs within the entire separated region without showing the typical shape of pressure distribution. This result specifically indicates that the plateau pressure distribution is

not a common feature of LSB and some characteristics of the flow lead to the differences in the pressure distribution. In other words, not only a physical reason of appearing different pressure distributions depending on the flow condition but also a mechanism that can comprehensively explain the formation of surface pressure distribution has not been perfectly understood.

From an engineering point of view, it has been well known that the aerodynamic characteristics at low Reynolds numbers are significantly different from those at high ones. Thus, some general knowledge of aerodynamic characteristics of high Reynolds number conditions cannot be directly applied to low Reynolds number ones; and hence, it is necessary to understand the aerodynamic characteristics at low Reynolds numbers and propose newly-designed airfoils for low Reynolds number region. Numerical simulations which can efficiently evaluate the performance of an arbitrary shape of airfoil can become a useful tool for the desing of new airfoils. What is indispensable for evaluating the airfoil aerodynamic characteristics in the low Reynolds number region is an accurate prediction of LSB behavior. The LSB usually involves complicated physical phenomena such as the laminar separation, transition, and turbulent reattachment, so it is necessary to conduct a three-dimensional simulation such as a direct numerical simulation or a large eddy simulation to investigate precise physical properties. These high-accuracy three-dimensional analyses, however, need huge computational resources, so it is desirable to be able to evaluate the airfoil aerodynamic performances by a two-dimensional calculation which has relatively low computational costs. Although it has been known that a two-dimensional unsteady laminar simulation without turbulence models can predict qualitatively characteristics of the LSB, it is still unclear why these complicated flows can be qualitatively predicted by a two-dimensional simulation. Here, it is expected that the reliability of a two-dimensional simulation can be clarified if the formation mechanism of surface pressure distribution around the LSB is elucidated.

Thus, the purpose of this thesis is to clarify the physical mechanisms related to the formation of surface pressure distribution around the LSB by a high-order accurate numerical simulation. This thesis consists of seven chapters. Chapter 1 introduces backgrounds and related previous studies. In Chap. 2, governing equations and numerical methods applied in the present study are described. First, from a physical viewpoint, characteristics of LSBs are discussed in Chap. 3, and then the mechanisms related to the formation of surface pressure distribution around an LSB are explained in Chap. 4. After that, this thesis changes the viewpoint to its engineering application and the reliability of two-dimensional unsteady laminar simulations are discussed in Chap. 5. In Chap. 6, the engineering usefulness of the discussion conducted in this thesis is presented by applying

to flow fields around airfoils. Finally, Chap. 7 summarizes the conclusion of this thesis.

In Chap. 3, three-dimensional large eddy simulations are conducted using a 5% thickness flat palte with a right-angled blunt leading edge at zero angle of attack. The Reynolds numbers based on the plate length are set to $Re_c = 5.0 \times 10^3$, 6.1×10^3, 8.0×10^3, 1.1×10^4, and 2.0×10^4, and targeted flows have a fixed separation point at the leading edge and reattachment of the separated shear layer. From the analysis based on the turbulent kinetic energy (TKE) flow fields within the LSBs, two types of LSBs are classified; the steady laminar separation bubble (LSB_S) at $Re_c \leq 6.1 \times 10^3$ and the steady-fluctuating laminar separation bubble (LSB_SF) at $Re_c \geq 8.0 \times 10^3$. Based on the classification above, the following three phenomena are newly observed; i) there is a possibility that the shape of surface pressure distribution around an LSB may be different depending on the Reynolds numbers; ii) the different shapes of pressure distribution between the LSB_S and LSB_SF in the steady region are affected by other factors rather than the steady flow condition under the separated shear layer; iii) the occurrence of rapid pressure recovery observed in the fluctuating region may not be always substantially affected by the transition and three-dimensional structures.

Chapter 4 discusses the detailed mechanisms with respect to the formation of different pressure distributions around LSBs by means of deriving an averaged streamwise pressure gradient (momentum budget) equation. First of all, in the steady region of the LSB, different pressure gradient between the LSB_S and LSB_SF is caused by the different distribution of the viscous shear stress near the surface. In case of the LSB_S, the continuously distributed viscous shear stress exists near the surface, whereas it becomes negligibly small in the LSB_SF case. Additionally, it is confirmed that the different viscous shear stress near the surface is affected by the different development of the separated shear layer depending on the Reynolds numbers. Next, in the fluctuating region of the LSB, the presence of fluctuating components due to the Reynolds stress (i.e., gradient transport of overall Reynolds stress or called as GTOR in this thesis) induces the strong viscous shear stress near the surface, and hence the rapid pressure recovery is generated. In order to investigate the relevance between the GTOR and flow structures, the GTOR is decomposed into a gradient transport of Reynolds shear stress (GTRS) in the wall-normal direction and that of Reynolds normal stress in the streamwise direction. The results tell us that the momentum transfer in the wall-normal direction induced by the GTRS is an important factor for the rapid pressure recovery. Lastly, the GTRS is additionally decomposed into two- and three-dimensional components. It is revealed that the magnitude of the gradient transport of Reynolds shear stress itself is an important factor rather than the formation of three-dimensional turbulent structures.

In Chap. 5, the two-dimensional unsteady laminar simulation is conducted for a 5% thickness blunt leading edge flat plate in order to verify its reliability in respect to the flow fields around LSBs. The results reveal that following characteristics can be predicted by the two-dimensional laminar simulation: the formation of LSBs, the tendency of varying reattachment points depending on the Reynolds numbers, and reattachment state. Moreover, the two-dimensional laminar simulation can also reproduce the qualitative distribution of averaged surface pressure distribution and skin friction coefficient except for the overshoot phenomenon observed around the transition region. On the other hand, the present results indicate that the accurate prediction of instantaneous flow structures and velocity profiles in the wall-normal direction are difficult in the two-dimensional laminar simulation. Regarding the formation of the surface pressure distribution, the overshoot phenomenon is caused by an overestimation of the Reynolds stress than the three-dimensional simulation. The reason of being able to capture the rapid pressure recovery in the fluctuating region is because the three-dimensional Reynolds shear stress component in the actual flow field is pushed into the two-dimensional one in the two-dimensional simulation. Consequently, the magnitude of overall gradient transport of Reynolds shear stress in two-dimensional simulation becomes similar to that in the three-dimensional one. In conclusion, generation of the positive distribution of overall component away from the surface is a critical point for reproducing the rapid pressure recovery in the flutuating region. Thus, even if the three-dimensional turbulent structure cannot be captured in the fluctuating region, the qualitative distribution of the GTRS which is an important factor for the pressure gradient is similar in both simulations; and hence the rapid pressure recovery also appears in the two-dimensional simulation.

In Chap. 6, not only the formation mechanisms of surface pressure distribution but the reliability of two-dimensional unsteady laminar simulations is investigated for flow fields around airfoils. It is verified that the distribution of near-wall viscous shear stress due to the separated shear layer and the generation of fluctuating component have a major role to the formation of pressure gradient in each region. Therefore, the formation mechanisms of surface pressure distribution proposed in this thesis are also available to practical flow fields. Added to this, it is shown that the distance between the separated shear layer and the surface affects the surface pressure distribution in the steady region. Next, it is confirmed that the two-dimensional laminar simulation which has a relatively low computational cost can be used for evaluating qualitative aerodynamic characteristics of low Reynolds number flows, except for high angles of attack which accompanies massive separation.

Finally, Chap. 7 describes the conclusion of this thesis.

Acknowledgements

I would like to express my special gratitude to Professor Kozo Fujii of Institute of Space and Astronautical Science/Japan Aerospace Exploration Agency (ISAS/JAXA); currently of Tokyo University of Science. His invaluable and appropriate advice coming from his immense knowledge has always led me in the right path during my Master and Ph.D. courses. I also want to express my sincere thanks to Associate Professor Akira Oyama of ISAS/JAXA and the University of Tokyo, who is my current supervisor. His generous supports in all respects of research as well as kindness guidance helped me in all the time of my study and writing of this thesis. Without their continuous support and encouragement, this work would not have been possible.

Besides my advisors, I would like to express my deep appreciation to the rest of my thesis committee: Professor Kenichi Rinoie, Professor Katsuhiro Nishinari, and Associate Professor Taro Imamura of Department of Aeronautics and Astronautics at the University of Tokyo. I am thankful to them for becoming a member of the thesis committee and giving excellent advice.

I would like to thank Associate Professor Soshi Kawai and Associate Professor Taku Nonomura of Tohoku University. I got a lot of inspiration through not only their constructive comments but also their attitude toward research. I would like to thank Assistant Professor Johan Larsson at University of Maryland, who pleasantly accepted me as a visiting student of his laboratory. He showed me the qualities of an excellent researcher and I could learn a lot of things through daily-based discussion and his kind explanations, in spite of his busy schedule.

Special thanks to the present and former members of the laboratory for their friendship and supporting my research. In particular, I am deeply grateful to Assistant Professor Hikaru Aono at Tokyo University of Science, Assistant Professor Masayuki Anyoji at Kyushu University for their constructive comments.

I gratefully acknowledge that this work is partially supported by Doctoral Student Special Incentive Program of the University of Tokyo, the Asahi Glass Scholarship Foundation, the Japan Society of the Promotion of Science, and Graduate Program for Me-

chanical Systems Innovation (GMSI).

Last but not the least, it is my pleasure to express my sincere thanks to my parents and friends for supporting me mentally throughout my ten-year-life in Japan. Without their continuous encouragement, this work could not have been completed.

February 2017

Donghwi Lee

Contents

List of Figures

List of Tables

Nomenclature

Roman Symbols

a	speed of sound
a_c, b_c, c_c	coefficients of compact scheme
A, B, C	flux Jacobian matrix
c	chord length
c_p	specific heat capacity at constant pressure
C_D	drag coefficient
C_f	skin friction coefficient
C_L	lift coefficient
C_p	pressure coefficient
d	wall-normal distance from wall
e	total energy per unit volume
E, F, G	fluxes in Navier-Stokes equations
f, g	arbitrary variable
h	total enthalpy
H	shape factor
i	index of an arbitrary grid point
I	identity matrix
j, k, l	grid index in ξ, η, and ζ directions
J	transformation Jacobian
$\mathcal{L}$	reference length
m	times of subiteration
M	Mach number
n	time step
N_x, N_y, N_z	number of grid points in x, y, and z directions
N_ξ, N_η, N_ζ	number of grid points in ξ, η, and ζ directions
p	static pressure
Pr	Prandtl number

q_i	heat flux vector ($i = 1, 2, 3$)
Q	conservative variables in Navier-Stokes equations
Q_{cr}	Q-criterion
R	gas constant
Re	Reynolds number
s_{ij}	rate of strain tensor ($i, j = 1, 2, 3$)
$\mathcal{S}^{\xi}, \mathcal{S}^{\eta}, \mathcal{S}^{\zeta}$	vectors perpendicular to ξ, η, and ζ directions
t	time in Cartesian coordinate
T	temperature
u, v, w	velocity components in Cartesian coordinate (x, y, z); also u_i ($i = 1, 2, 3$)
u', v', w'	overall velocity fluctuation components; also u_i' ($i = 1, 2, 3$)
$\tilde{u}, \tilde{v}, \tilde{w}$	two-dimensional velocity fluctuation components; also $\tilde{u}_i$ ($i = 1, 2, 3$)
u'', v'', w''	three-dimensional velocity fluctuation components; also u_i'' ($i = 1, 2, 3$)
U, V, W	contravariant velocity components in curvilinear coordinate
$\mathcal{U}$	reference velocity
$\mathcal{V}$	volume of cell
x, y, z	Cartesian coordinate; also x_i ($i = 1, 2, 3$)

Greek Symbols

α	angle of attack
α_c, β_c	coefficient of compact scheme
α_f	coefficient of filter
β	bulk viscosity
γ	specific heat ratio
δ_{ij}	Kronecker's delta ($i, j = 1, 2, 3$)
δ	boundary layer thickness
δ^*	displacement thickness
Δ	discretized step size
θ	momentum thickness
κ	thermal conductivity
$\varkappa$	parameter for adjusting the accuracy of MUSCL
λ	second viscosity coefficient
μ	molecular viscosity
ν	kinematic eddy viscosity
ξ, η, ζ	curvilinear coordinate
ρ	density

$\sigma(A)$	maximum eigenvalue of flux Jacobian matrix A
τ	time in curvilinear coordinate
τ_{ij}	viscous stress tensor $(i, j = 1, 2, 3)$
φ	arbitrary derivative operator
Ω	magnitude of vorticity

Subscripts

∞	freestream condition
$_{\max}$	maximum value
$_{\min}$	minimum value
$_r$	reattachment point
$_t$	thickness of a flat plate

Superscripts

^{L}	left side of the cell interface
^{R}	right side of the cell interface
$'$	first derivative
$''$	second derivative
*	nondimensionalized quantity
$^+$	wall-unit

Symbols

$\hat{Q}$	Q divided by transformation Jacobian
$\acute{Q}$	filtered quantity of Q
$\overline{Q}$	time average of Q
$\langle Q \rangle$	spanwise average of Q

Abbreviations

ADI-SGS	Alternative Direction Implicit Symmetric Gauss-Seidel
AUSM	Advection Upstream Splitting Method
AUSMDV	AUSM with flux Difference splitting and flux Vector splitting
AUSMPW	AUSM by Pressure based Weight functions
CFL	Courant-Friedrichs-Lewy
CUSP	Convective Upstream Split Pressure
DES	Detached Eddy Simulation
DNS	Direct Numerical Simulation

DD-ADI	Diagonally Dominate Alternative Direction Implicit
ENO	Essentially Non-Oscillatory
FDS	Flux Difference Splitting
FF-SGS	Four-Factor Symmetric Gauss-Seidel
FVS	Flux Vector Splitting
GCL	Geometric Conservation Law
GTOR	Gradient Transport of Overall Reynolds stress
GTRN	Gradient Transport of Reynolds Normal stress
GTRS	Gradient Transport of Reynolds Shear stress
ILES	Implicit Large Eddy Simulation
KH	Kelvin-Helmholtz
LES	Large Eddy Simulation
LHS	Left Hand Side
LSB	Laminar Separation Bubble
LU-ADI	Lower-Upper symmetric Alternating Direction Implicit
LU-SGS	Lower-Upper Symmetric Gauss-Seidel
MAV	Micro Air Vehicle
MILES	Monotonically Integrated Large Eddy Simulation
MUSCL	Monotonic Upstream Scheme for Conservation Laws
PSP	Pressure Sensitive Paint
RANS	Reynolds-Averaged Navier-Stokes
RHS	Right Hand Side
SCL	Surface Conservation Law
SGS	SubGrid Scale
SHUS	Simple High-resolution Upwind Scheme
SLAU	Simple Low-dissipation AUSM
TKE	Turbulent Kinetic Energy
TS	Tollmien-Schlichting
UAV	Unmanned Aerial Vehicle
VCL	Volume Conservation Law
WENO	Weighted Essentially Non-Oscillatory
WCNS	Weighted Compact Nonlinear Scheme
2-D Lam	Two-Dimensional unsteady Laminar simulation
2-D RANS(BL)	Two-Dimensional RANS with Baldwin-Lomax turbulence model
2-D RANS(SA)	Two-Dimensional RANS with Spalart-Allmaras turbulence model
3-D LES	Three-Dimensional Large Eddy Simulation

Chapter 1

Introduction

1.1 Micro air vehicles / unmanned aerial vehicles

Commercial airplanes usually have a large size as well as a high cruise speed to transport many passenger as fast as possible. Figure 1.1 (a) is the Boeing 787 Dreamliner which is the latest airplane developed by the Boeing Company. Figure 1.1 (b) is the Airbus A350 XWB which is being developed as a competitive model against the Boeing 787 Dreamliner. Here, let us focus on the Reynolds number (Re) which is one of the important parameters in fluid dynamics. The Reynolds number is defined as follows:

$$Re = \frac{\rho \mathcal{U} \mathcal{L}}{\mu}, \tag{1.1}$$

where ρ is the density; $\mathcal{U}$ is the reference velocity; μ is the molecular viscosity; and $\mathcal{L}$ is the reference length, respectively. Table 1.1 summarizes cruise conditions and flight Reynolds numbers of several commercial airplanes. The cruising altitude is $35,000$[ft]. The speed of sound a, atmospheric density ρ, and molecular viscosity μ of the cruising altitude are assumed as $a = 296.5396$[m/s], $\rho = 0.3796$[kg/m^2], and $\mu = 0.0000143$[Ns/m^2], respectively. As shown in Tab. 1.1, the flight Reynolds numbers of many commercial airplanes based on the chord length (Re_c) are in the range of $Re_c = O(10^7) \sim O(10^8)$, so-called the high Reynolds number region.

In contrast, the interests in development of micro air vehicles (MAV) and unmanned aerial vehicles (UAV) have been growing recent year. Some examples of applications of civilian MAV or UAV include the following cases. From the viewpoint of agricultural usage, they make possible to efficiently spray agricultural pesticide. Taking aerial photography for topography research is also one of a good example of MAV or UAV usage. One of the most useful application is an investigation of areas where people are difficult

(a) Boeing 787 Dreamliner
(http://www.boeing.com/commercial/787/#/gallery)

(b) Airbus 350-1000
(http://www.airbus.com/galleries/photo-gallery)

Figure 1.1: Example of the latest commercial airplanes.

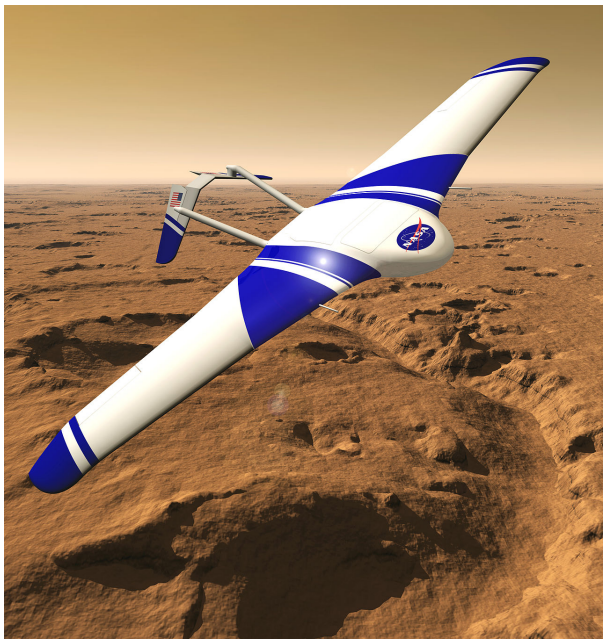

(a) NASA ARES (©NASA)

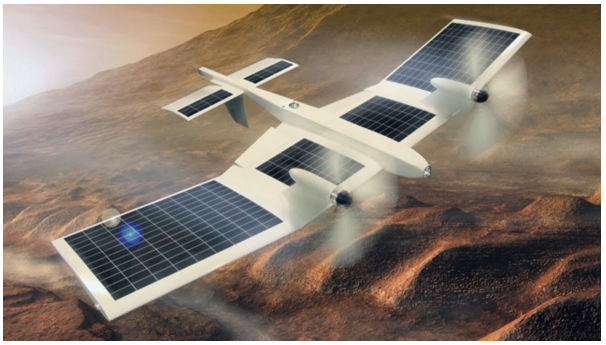

(b) JAXA MELOS (©JAXA)

Figure 1.2: Conceptual diagram of Mars exploration airplanes proposed by (a) NASA and (b) JAXA.

Table 1.1: Cruising conditions and Reynolds numbers of several commercial airplanes.

Aircraft type	Mach number [-]	Speed [km/h]	Mean aerodynamic chord [m]	Re [-]
Airbus 300-600R	0.78	833	6.44	3.9×10^7
Airbus 320-200	0.78	839	4.29	2.6×10^7
Airbus 330-300	0.82	875	7.26	4.7×10^7
Airbus 340-500	0.86	918	8.35	5.6×10^7
Airbus 380-800	0.89	950	12.02	8.4×10^7
Boeing 737-700	0.785	839	3.96	2.4×10^7
Boeing 747-400	0.85	907	8.33	5.6×10^7
Boeing 767-300ER	0.80	854	6.03	3.8×10^7
Boeing 777-200	0.84	896	7.02	4.6×10^7
Boeing 787-8	0.85	907	6.27	4.2×10^7

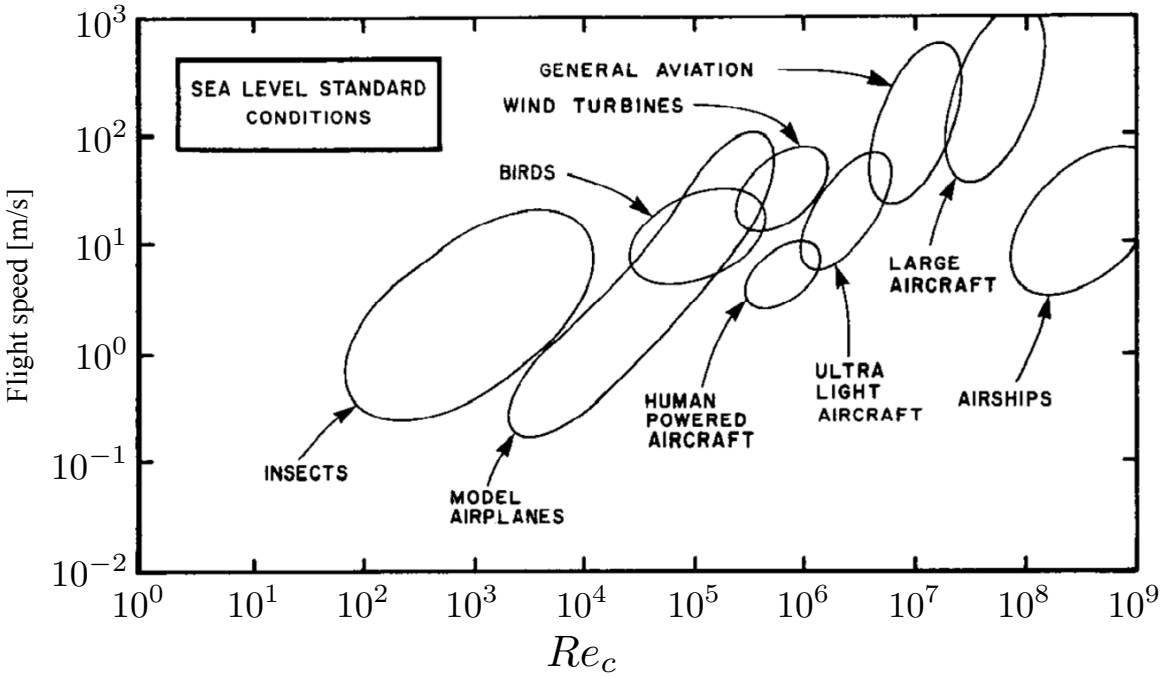

Figure 1.3: Flight Reynolds number spectrum drawn by Lissaman (1983).

to directly enter and survey, such as a disaster area or the polar regions. Besides this, an application of MAV or UAV has been considered as a new device for planetary exploration. For example, the Aerial Regional-scale Environmental Survey (ARES, Fig. 1.2 (a)) by Langley research center in the National Aeronautics and Space Administration (NASA) has proposed the usage of an UAV for the Mars exploration. The concepts of ARES were presented by Murray & Tartabini (2001), Guynn *et al.* (2003), Smith *et al.*

(2003), and Kuhl (2009). Recently, Japan Aerospace Exploration Agency (JAXA) has set up the Mars Exploration with Lander-Orbiter Synergy (MELOS) plan, and a small unmanned-aircraft shown in Fig. 1.2 (b) has been regarded as one of the candidates for Mars exploration devices. These exploration airplanes aim to obtain atmospheric properties such as their composition, dynamic behavior, and terrain mapping, planetary magnetic field patterns as well as searching near-surface water. The flight in the Martian environment, however, is anticipated to be significantly different from that in the Earth. First of all, it has been known that the atmospheric density of Mars is approximately 1/100 for that of the Earth, so called a low-density atmospheric condition. Next, these airplane should be stored in a small volume capsule because there is a restriction of storage capability of a carrying vehicle. Thus, it is desirable to make the airplanes as small as possible. Lastly, a low-speed flight is required due to mission requirements such as taking photographs of terrain. Because of these features, its flight Reynolds number becomes lower than that in the Earth. Specifically, the chord length based Reynolds number of these aircrafts falls into $Re_c = O(10^3) \sim O(10^5)$, which is similar to that of model airplanes or bird in the Earth (see, Fig. 1.3). Several previous studies have classified these region as "ultra-low" (Alam *et al.*, 2010) or "low-to-moderate Reynolds number" (Castiglioni *et al.*, 2014; Cadieux & Domaradzki, 2015; Martinez-Aranda *et al.*, 2016), it will be simply referred to as "low Reynolds number" region in this thesis.

1.2 Aerodynamic characteristics of low Reynolds number flows

It has been known that the airfoil aerodynamic characteristics at the low Reynolds number region are different from those in the high Reynolds number region. One of the specific differences is that it is difficult to gain a high lift-to-drag ratio. Figure 1.4 shows the relationship between maximum lift-to-drag ratio and the Reynolds number (Lissaman, 1983). As the figure indicates, characteristics of smooth surface airfoils remarkably change around $Re_c = O(10^5)$. One reason of appearing this characteristics has been explained as follows. The flow around conventional aircrafts may transit to turbulent rapidly, and the turbulent boundary layer is able to overcome an adverse pressure gradient. Consequently, flows do not separate until high angles of attack. In case of the low Reynolds number flow, however, it is easy to occur the laminar separation even at low angles of attack as well as a mild adverse pressure gradient condition (Jahanmiri, 2011). Moreover, a viscous drag increases in the low Reynolds number region and con-

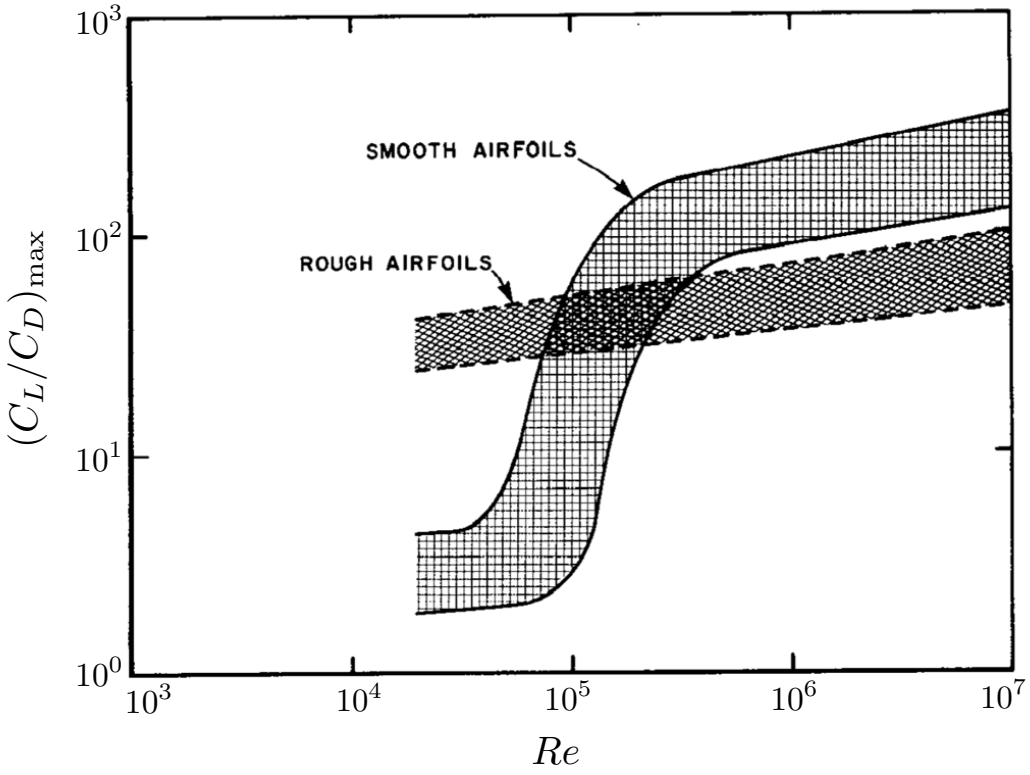

Figure 1.4: Variation of maximum lift-to-drag ratio with the Reynolds number drawn by Lissaman (1983).

sequently, it is difficult to obtain a high lift-to-drag ratio. Especially, many previous studies (Schmitz, 1967; Carmichael, 1982; Lissaman, 1983; Mueller & DeLaurier, 2003) have pointed out that $Re_c \simeq 7.0 \times 10^4$ is one of the critical Reynolds number.

Following factors significantly affect the airfoil aerodynamic performances in the low Reynolds number regime.

Airfoil geometric shape In general, geometric shapes of airfoil are referred to the maximum thickness, camber strength, position of maximum camber and leading edge shape. First, Laitone (1996) performed wind tunnel tests to evaluate the lift and drag of the NACA0012, reversed NACA0012, thin wedge, and 5% camber airfoils at $Re_c = 2.07 \times 10^4$. As shown in Fig. 1.5, the thin wedge and cambered airfoils showed better performance that the NACA0012 airfoil in terms of the lift coefficient. Furthermore, the thin and cambered airfoil produced high lift-to-drag ratios at all angles of attack. These results indicate that better aerodynamic performances can be obtained by using a thin and cambered airfoil rather than a thick and symmetric airfoil in the low Reynolds number region. Laitone (1997) also pointed out that a sharp leading edge produces

higher lift coefficients than a rounded-nose leading edge airfoil. Kunz (2003) made several important statements for effects of airfoil geometric shape. It was shown that a cambered airfoil can obtain higher lift coefficient than a symmetric one. It was also described that the lift coefficient can be improved by adopting a strong camber around the trailing edge, although the drag coefficient increases nonlinearly. In terms of the leading edge shape, a sharp leading edge is more advantageous for the high lift-to-drag ratio than a blunt leading edge. These results are consistent with those reported by Sunada *et al.* (2002). Abdo & Mateescu (2005) conducted numerical analysis of flow past airfoils at $Re_c = 400 \sim 6,000$. Their results tell us that increasing a maximum thickness reduces the lift slope and increases the drag. They concluded that both the lift and drag coefficient increase as the maximum camber increases. Also, the addition of the camber produces higher lift and it leads to higher lift-to-drag ratio, although the drag increases. Summarizing the above, an airfoil which has a sharp leading edge, thin and strong camber near the trailing edge yields good aerodynamic performances in the low Reynolds number region. As depicted in Fig. 1.6, these features are significantly different from the typical shapes of airfoils which are generally used in the high Reynolds number region. Several studies on airfoil design for future Mars exploration airplane also show similar results (Aono *et al.*, 2012; Anyoji *et al.*, 2014; Kondo *et al.*, 2014).

Freestream turbulence intensity Wang *et al.* (2014) investigated the aerodynamic characteristics of the NACA0012 airfoil at $Re_c = 5.3 \times 10^3 \sim 2.0 \times 10^4$ for the variation of the freestream turbulence intensity. It was found that the freestream turbulence intensity has a more pronounced effect at $Re_c < 1.0 \times 10^4$ than $Re_c > 1.0 \times 10^4$. They showed that the separation is postponed and the early transition is induced in the separated shear layer with increase in the intensity. They also noted that the effects of increasing the intensity have similarity to that of increasing the Reynolds numbers. Stevenson *et al.* (2014) measured the effects of the freestream turbulence intensity using high-resolution particle image velocimetry (PIV) data. They mentioned that an increase in the intensity accelerated transition mechanisms in the separated shear layer and it led to shrinking of the time-averaged laminar separation bubble. Hosseinverdi & Fasel (2015) studied a relationship between the physical characteristics of flow and the freestream turbulence intensity by direct numerical simulations. They showed that an inviscid Kelvin-Helmholtz instability is the dominant mechanisms causing the transition in the separation bubble in a low freestream turbulence level, whereas the transition mechanisms is dominated by the Klebanoff modes in a high one. Effects of freestream turbulence intensity on aerodynamic performances were discussed by Huang & Lee (1999).

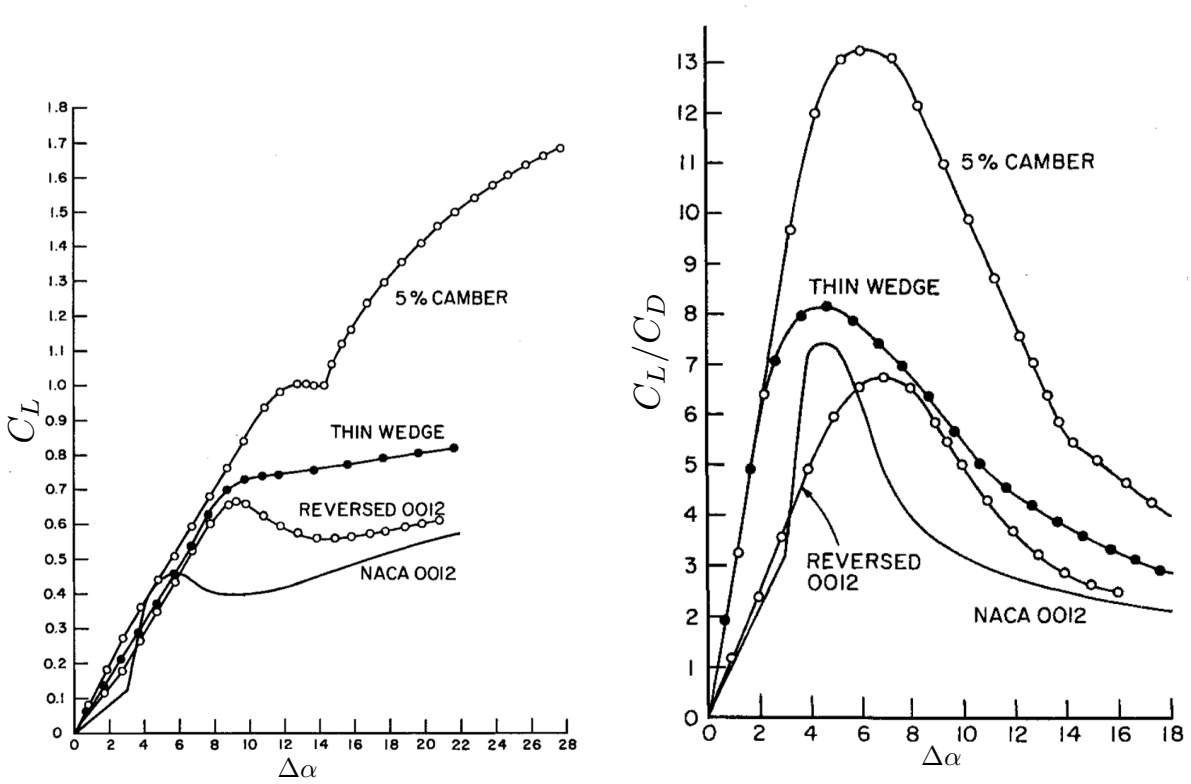

(a) C_L with α from zero lift

(b) C_L/C_D with α from zero lift

Figure 1.5: Variation of (a) lift coefficient and (b) lift-to-drag ratio with angles of attack from zero lift for several airfoils (Laitone, 1996).

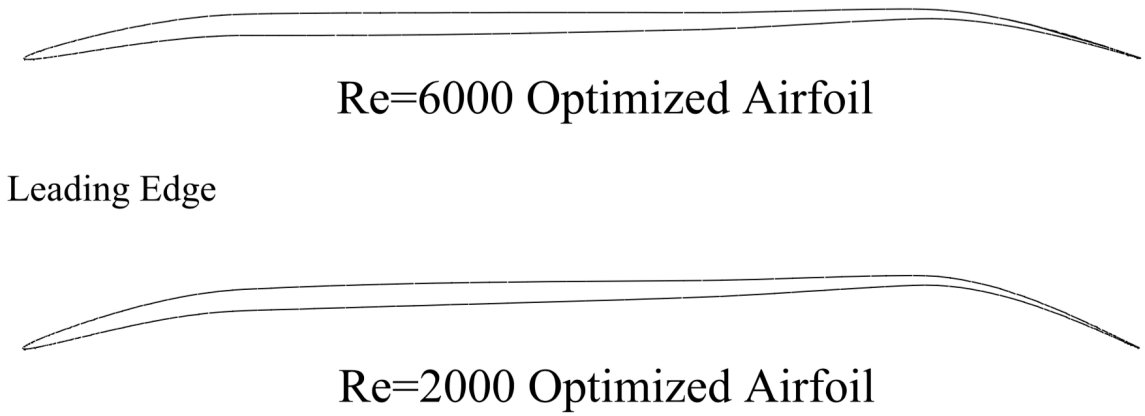

Figure 1.6: Examples of optimized airfoils at $Re_c = 6,000$ (top) and $Re_c = 2,000$ (bottom) (Kunz, 2003).

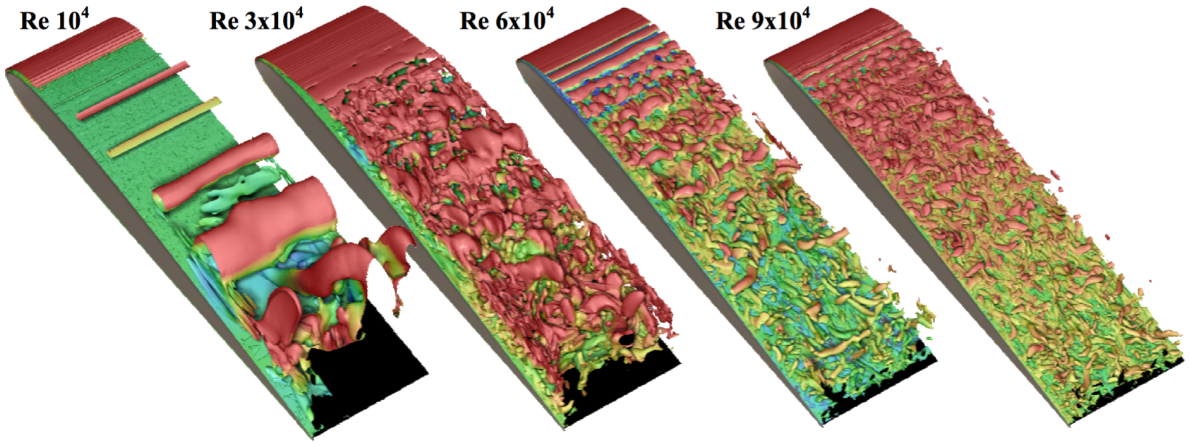

Figure 1.7: Effect of Reynolds numbers to instantaneous flow structures around the SD7003 airfoil at $\alpha = 8.0°$ (Galbraith & Visbal, 2010).

Reynolds number Yarusevych *et al.* (2009) experimentally showed that the flow characteristics varies with increase in the Reynolds numbers; from the boundary layer separation without reattachment to the formation of laminar separation bubble. They also pointed out that the fundamental frequency of the roll-up vortices developed in the separated shear layer scales with the Reynolds numbers, and the shedding frequency of the wake vortex shows a linear dependency on the Reynolds numbers. Numerical investigations conducted by Galbraith & Visbal (2010) showed that the separated shear layer does not reattach on the airfoil surface at $Re_c = 1.0 \times 10^4$ whereas laminar separation bubbles are formed at $Re_c \geq 3.0 \times 10^4$ (see, Fig. 1.7). Increase in the Reynolds numbers makes the separation points move toward the leading edge and reduces the length of the laminar separation bubble. It also affects increase in the lift and decrease in the drag, respectively. Olson *et al.* (2013) mentioned that the reattachment location of the separated shear layer largely changes in the range of $Re_c = 2.0 \times 10^4 \sim 3.0 \times 10^4$. Below this Reynolds number, the reattachment occurs near the trailing edge or is not observed; but a much shorter separation bubble appears at higher Reynolds numbers. These results indicate that little variation of the Reynolds number may largely affect the flow characteristics.

Formation of a laminar separation bubble A laminar separation bubble often affects unfavorably the airfoil aerodynamic characteristics such as decreasing in the lift, nonlinearity of the lift, increase in the pressure drag, generating aerodynamic noise as well as detracting stability (see, Mayle, 1991; Hodson & Howell, 2005; Nakano *et al.*, 2007). Details of a laminar separation bubble will be discussed in Sec. 1.3.

Because of these features, some general knowledge of airfoil aerodynamic characteristics in the high Reynolds number region is not available in the low Reynolds number one. Therefore, it is necessary to newly understand airfoil aerodynamic characteristics.

1.3 Laminar separation bubble

A laminar separation bubble (LSB) is often observed in many practical flows such as MAV airfoils or turbine blades. Several initial investigations about an LSB were conducted by Tani (1964), Gaster (1967), Horton (1968), and Carmichael (1982). A schematic diagram of an LSB is depicted in Fig. 1.8. The LSB is formed through the following processes. When a laminar boundary layer separates due to a strong adverse pressure gradient, the laminar-turbulent transition often occurs in the separated shear layer. In the separated shear layer, two-dimensional spanwise-extended coherent vortex structures are usually observed. These vortex structures are similar to those seen in a free shear layer (Monkewitz & Huerre, 1982; Ho & Huerre, 1984), and their instability mechanism is also analogous to that of a free shear-layer, so-called the Kelvin-Helmholtz (KH) instability (Dovgal *et al.*, 1994). When the vortices described above are formed, they are distorted in the spanwise direction and collapsed to three-dimensional small-scale turbulent structures by the secondary instability. Marxen *et al.* (2013) briefly summarized that at least three different types of instability which may lead to three-dimensional flow exist as follow: the primary global instability, the secondary instability, and the highly localized instability. After that, the turbulent shear layer eventually reattaches to the surface, and a closed-loop of the streamline is formed in the separated region, so-called an LSB.

The LSB is classified into a short bubble and a long bubble (Tani, 1964). One characteristic of a short bubble is that the length of LSB reduces and its location moves towards the leading edge as increase in an angle of attack. In contrast, that of a long bubble is that the reattachment point moves downstream and the length of LSB is extended. Especially, if an angle of attack further increases from that where a short bubble exists, the separated flow suddenly fails to reattach on the surface and a long bubble is started to form. This process is often referred to as the bursting phenomenon of a short bubble (Rinoie *et al.*, 1990). Several essential features which are usually observed in a short bubble are well presented in Marxen & Henningson (2011).

Over the past few decades, a considerable number of studies have been conducted on the characteristics of an LSB. First of all, in terms of the flow structures around an LSB, Sasaki & Kiya (1991) used a water channel and described the three-dimensional

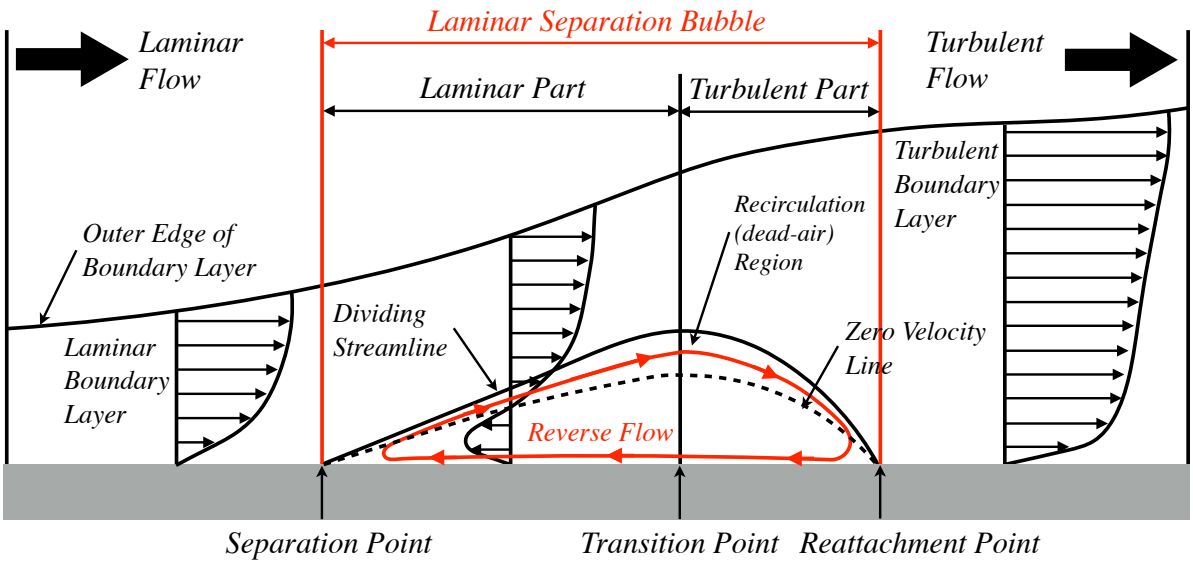

Figure 1.8: Schematic diagram of an LSB (originally drawn by Carmichael (1982) and modified).

vortex structures under various Reynolds number conditions based on the plate thickness ($80 < Re_t < 800$). The corresponding Reynolds numbers based on the plate length are approximately $1.9 \times 10^3 < Re_c < 1.9 \times 10^4$. They investigated that the vortex structures around the LSB are classified into three regimes depending on the Reynolds numbers, and showed that a time-averaged bubble length is given by a function of the Reynolds number. In the first regime ($80 < Re_t < 320$), a laminar structures were observed without the significant spanwise distortion were observed and the separated shear layer reattaches as a laminar state. The time-averaged bubble length increases with Re_t^2. Next, Λ-shape deformation of vortex filaments appeared in the following region ($320 < Re_t < 380$), and the bubble length sharply decreased with increasing Re_t. From this Reynolds number region, the separated shear layer reattaches as a turbulent state. In the third regime ($Re_c > 380$), the flow characteristics had hairpin-like structures and the bubble length remains approximately constant. As described above, complicated vortex structures are formed in flow fields around an LSB depending on the Reynolds numbers.

Many studies have focused on the instability mechanisms around an LSB. Roberts & Yaras (2006) showed that the periodic shedding frequency of the roll-up structures in the separated shear layer which were induced by the KH instability was very close to the dominant Tollmien-Schlichting (TS) waves frequency in the upstream attached boundary layer. It was also reported by Diwan & Ramesh (2009) that the inviscid instability of the separated shear layer should be considered as an extension of the instability of

the upstream attached laminar boundary layer. Hain *et al.* (2009) investigated the dynamics of LSB formed on the surface of SD7003 at $Re_c \simeq 6.6 \times 10^4$ using time-resolved PIV measurements. They experimentally confirmed the generation and amplification of vortices induced by the KH instability in the separated shear layer, weak coherence in the spanwise direction, and vortex breakdown into three-dimensional turbulent flow. Marxen *et al.* (2012) investigated the evolution of two- and three-dimensional small-amplitude disturbances in the laminar part of an LSB, and concluded that both the viscous TS and inviscid KH instability mechanisms contribute to the onset of instability in the upstream of separation, whereas the inviscid mechanism is active inside an LSB. With the improvement of computational capability in recent years, numerical simulations have been performed and revealed various characteristics of an LSB. Pauley *et al.* (1990) conducted two-dimensional numerical simulations under the imposed external adverse pressure gradient at $Re_x \simeq 6.0 \times 10^4$, 1.2×10^5, and 2.4×10^5, where x is a streamwise location. They reported that the strong adverse pressure gradient induces a periodic vortex shedding from the separated shear layer. The shedding Strouhal number based on the local free-stream velocity and the boundary layer momentum thickness at the separation point was found to be constant independent of variation of the Reynolds number as well as the pressure gradient. Muti Lin & Pauley (1996) numerically confirmed the KH instability which causes shear layer unsteadiness, and mentioned that the unsteady large scale structure controls the reattachment of LSB. Direct numerical simulations have been conducted by Alam & Sandham (2000) in order to observe transition phenomena in an LSB, and showed that profiles with more than 15% reverse flow were required for the absolute instability. Brinkerhoff & Yaras (2011) examined the interaction of viscous TS and inviscid KH instability around an LSB, and revealed that vortices developed by a viscous instability in the upstream of separation point affect the separated shear layer and formation of coherent hairpin-like vortices. There are also many references related to an LSB characteristics, such as the transition and heat transfer mechanisms in an LSB (Spalart & Strelets, 2000), the interaction between the separated shear layer and outer potential flow (Diwan & Ramesh, 2012), the primary global instability (Rodríguez & Theofilis, 2010; Rodríguez *et al.*, 2013*a*), the secondary instability (Robinet, 2013), and unsteady behavior of an LSB analyzed by a proper orthogonal decomposition method (Lengani *et al.*, 2014). Several studies have examined behavior of an LSB around some typical airfoils (Shan *et al.*, 2005; Zhang *et al.*, 2008; Jones *et al.*, 2008, 2010; Boutilier & Yarusevych, 2012), that of the bursting phenomena (Rinoie & Hata, 2004; Rinoie & Takemura, 2004; Rinoie *et al.*, 2009; Almutairi *et al.*, 2010), and long bubble characteristics (Choudhry *et al.*, 2015).

1.4 Surface pressure distribution around a separation bubble

As introduced in the previous section, many studies have focused on the physical features of an LSB such as flow field structures or the instability mechanisms. Another important characteristic of LSB is that the formation of LSB sometimes leads to unusual behavior of airfoil aerodynamic characteristics. For example, Fig. 1.9 shows the variations of the flow fields and lift coefficients to angles of attack around the NACA0012-34 airfoil (Anyoji *et al.*, 2011). First of all, at lower angles of attack ($0.0° \leq \alpha \leq 6.0°$), the laminar separation appeared near the trailing edge and the lift slope was obviously lower that the theoretical inviscid lift slope (2π). As the angle of attack increased, the separation point moved toward the leading edge. At the angles of attack where the LSB began to form ($7.0° \leq \alpha \leq 10.0°$), the lift coefficient rapidly increased, and its slope became clearly steeper than the lower angles of attack region. At $\alpha = 14.0°$ where the bursting of the LSB occurred, the decrease in lift coefficient was observed, which is often referred to as a stall phenomenon. Therefore, the formation of LSB is closely linked to the lift coefficient characteristics, and sometimes results in the nonlinearity of lift.

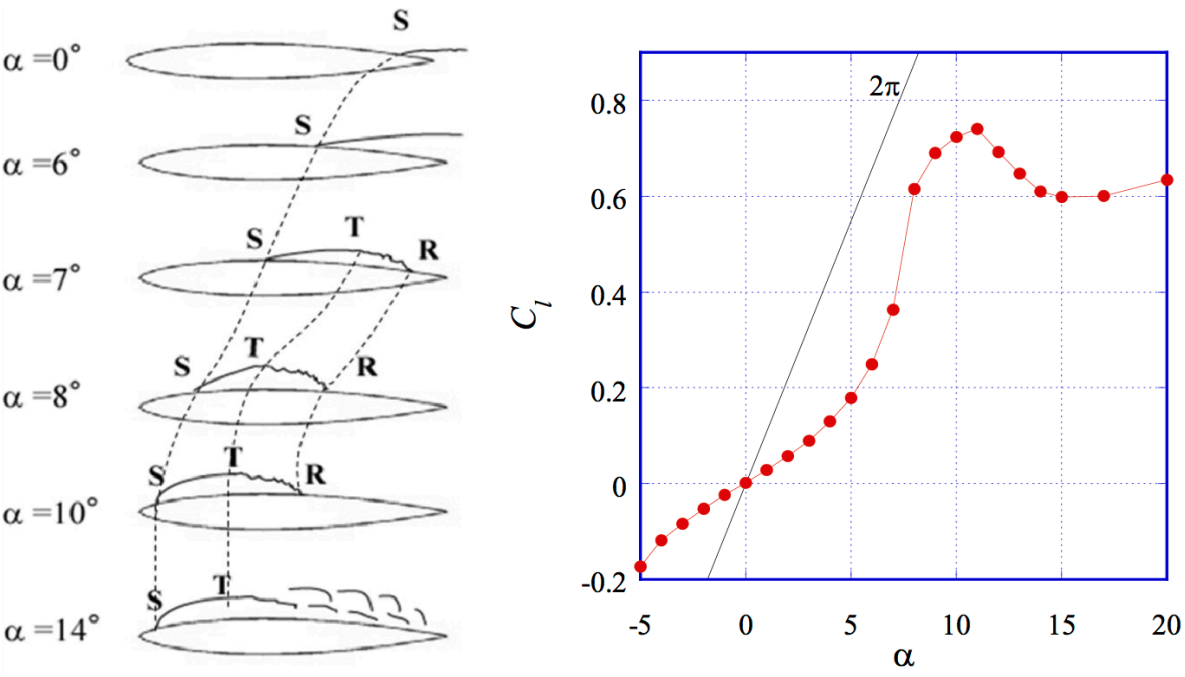

(a) Variation of the flow fields with α

(b) C_L with α

Figure 1.9: (a) Variation of the flow fields (S: separation point; T: transition point; and R: reattachment point) and (b) lift coefficient with angles of attack for the NACA0012-34 airfoil at $Re_c = 1.1 \times 10^4$ (Anyoji *et al.*, 2011).

The lift coefficients are calculated by an integration of the surface pressure distribution; and hence, it is important to understand the formation mechanisms of surface pressure distribution around an LSB. As shown in Fig. 1.10 (a) and (b), inside of an LSB is roughly composed of two parts; laminar region from separation to transition point and turbulent region from transition to reattachment point. As clearly seen in Fig. 1.10 (c), when the LSB is formed, it is often observed that the plateau pressure distribution appears from the separation point to transition point (laminar portion) and the rapid pressure recovery occurs from the transition point to reattachment point (turbulent portion). The physical reasoning of the plateau pressure distribution within the LSB can be found in several previous studies (Roberts, 1980; Watmuff, 1999; Marxen & Henningson, 2011). Within the laminar part of LSB (plateau pressure distribution region), the velocity under the separated shear layer is circulated slowly compared to the freestream, and it can be considered as a practically stationary state. As a result, it leads to the constant pressure distribution. This region is often referred to as the dead-air region. On the other hand, within the turbulent part of LSB (rapid pressure recovery region), the three-dimensional turbulent flow enhances mixing and momentum transfer from the freestream to the near-wall region. As a result, the separated shear layer reattaches to the surface as a turbulent state, which results in the rapid recovery of the surface pressure distribution (Arena & Mueller, 1980; Ripley & Pauley, 1993; Yarusevych *et al.*, 2006). In particular, the plateau pressure distribution has been thought as a general feature of LSB, and it has been mentioned in many previous studies. (Yarusevych *et al.*, 2006; Jones *et al.*, 2008; Hu & Yang, 2008; Karasu *et al.*, 2013; Anyoji *et al.*, 2014). These explanations are reasonable and can be applied to many of LSB flows.

However, the explanations above cannot be adopted under some specific flow conditions. Anyoji *et al.* (2011) experimentally measured surface pressure distributions for a 5% thickness right-angled blunt leading edge flat plate using pressure-sensitive paint (PSP) technique at the plate length based Reynolds numbers of $Re_c = 4.9 \times 10^3$, 6.1×10^3, 1.1×10^4, 2.0×10^4 and 4.1×10^4. From the results, LSBs were observed at all of the Reynolds numbers, but the shapes of surface pressure distribution were different depending on the Reynolds numbers. As shown in Fig. 1.11, they divided the pressure distributions into two types. First, a gradual pressure recovery without the plateau pressure region was obtained at $Re_c \leq 6.1 \times 10^3$, which is not a commonly observed pressure distribution around an LSB. With increasing the Reynolds numbers ($Re_c \geq 1.1 \times 10^4$), the pressure distributions within the LSB region begin to show the common feature of the plateau region followed by the rapid pressure recovery in the downstream region. They also discussed a relationship between the pressure distribution and the reattach-

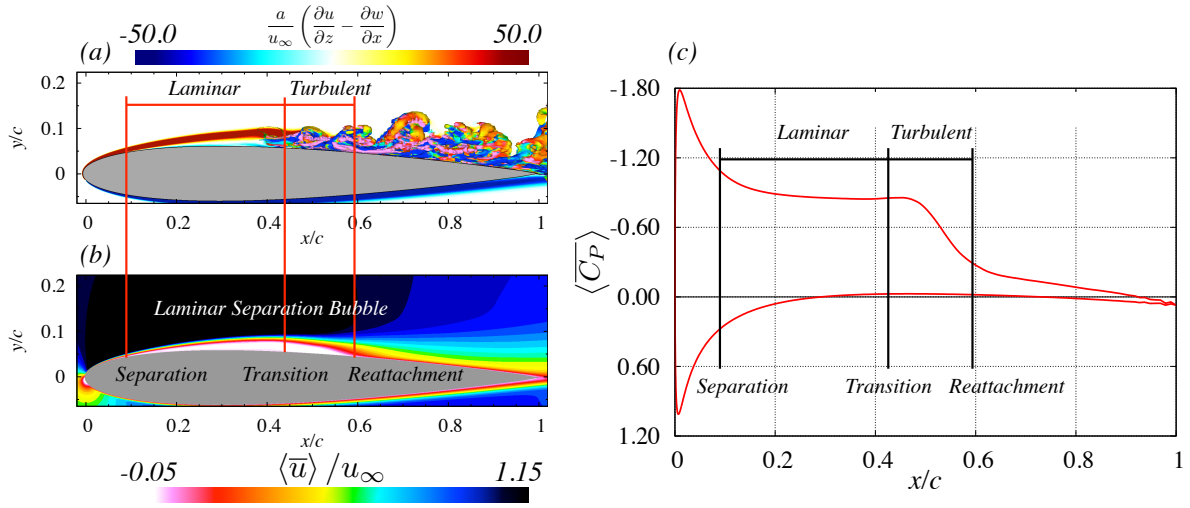

Figure 1.10: The flow fields characteristics around the NACA0012 airfoil at $Re_c = 3.0 \times 10^4$ and $\alpha = 6.0°$ (Lee *et al.*, 2015). (a) Instantaneous flow structures visualized by the second invariant of the velocity gradient tensor and the spanwise vorticity on the side plane, (b) the time- and spanwise-averaged streamwise velocity flow field, and (c) the time- and spanwise-averaged surface pressure distribution.

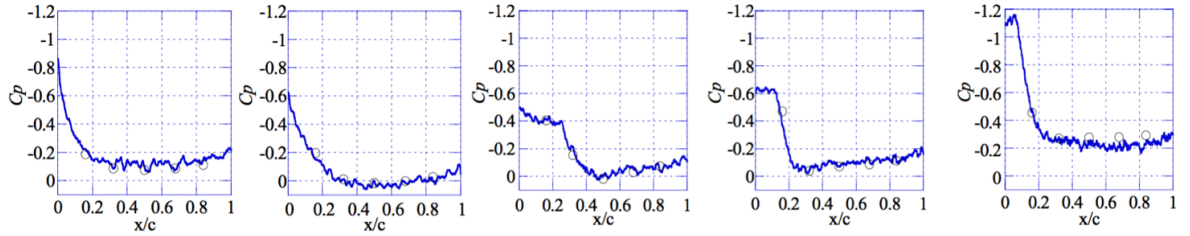

Figure 1.11: Surface pressure distributions around 5% thickness flat plate at each Reynolds number (Anyoji *et al.*, 2011). (From left to right, $Re_c = 4.9 \times 10^3$, 6.1×10^3, 1.1×10^4, 2.0×10^4, and 4.1×10^4).

ment state by referring to Tani *et al.* (1961). It was concluded that the plateau pressure distribution appears in the turbulent reattachment whereas the gradual pressure recovery is observed in the laminar reattachment (see, Fig. 1.12). These results specifically indicate that the plateau pressure distribution is not a common feature for the LSB. In other words, some characteristics of the flows lead to the differences in the pressure distribution. Moreover, discussion about the relationship between the pressure distribution and the reattachment state is still insufficient.

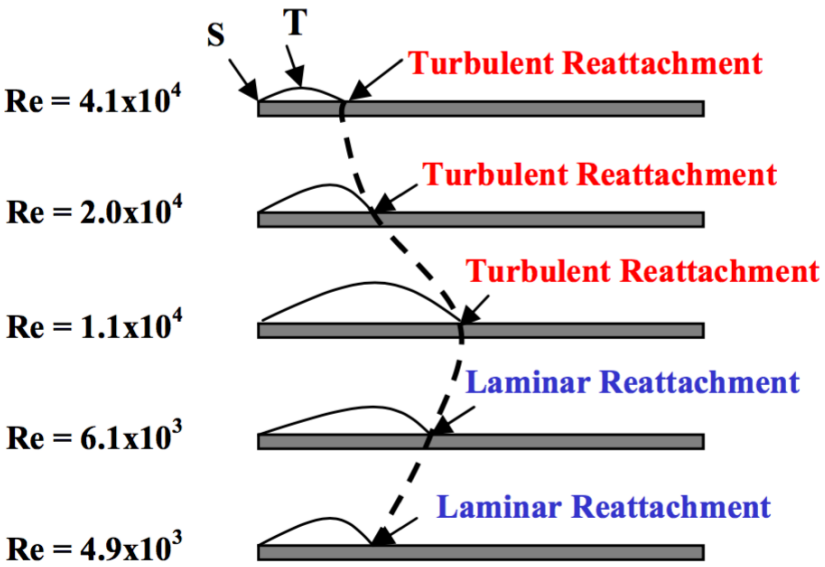

Figure 1.12: Variation of LSBs and reattachment state for a 5% thickness flat plate at various Reynolds numbers (S: separation point; T: transition point (Anyoji *et al.*, 2011)).

1.5 Evaluation of airfoil aerodynamic characteristics

In this section, let us shift our focus from physical to engineering point of view. As mentioned in Sec. 1.2, it is necessary to newly understand aerodynamic characteristics in the low Reynolds number region. Numerous experimental and numerical methods exist to evaluate airfoil aerodynamic characteristics. It is difficult, however, to acquire accurate aerodynamic coefficients by experiments because the flow speed should be set to low to produce the low Reynolds number environment. For instance, when a flow of $Re_c = 3.0 \times 10^4$ is created using an airfoil model whose chord length is c =100[mm], an adequate freestream velocity U_∞ is calculated as follows:

$$U_\infty = \frac{Re_c \times \mu}{\rho c} = \frac{3.0 \times 10^4 \times 1.86 \times 10^{-5}}{1.2 \times 0.1} = 4.65[\mathrm{m/s}], \tag{1.2}$$

where air density $\rho = 1.2[\mathrm{kg/m^3}]$ and molecular viscosity $\mu = 1.86 \times 10^{-5}[\mathrm{Pa{\cdot}s}]$. Because of the low freestream velocity, measured fluid forces also become low. Thus, an accurate measurement of aerodynamic coefficients is difficult. Conversely, a numerical simulation has several advantages. First of all, a numerical simulation is able to set ideal flow conditions and compensates for the uncertainty of experimental conditions. Another advantage is that detailed flow characteristics can be investigated by instantaneous flow data of numerical simulations. Furthermore, general knowledge of airfoil characteristics

in the low Reynolds number region would be relatively easily obtained by conducting parametric studies. Besides, it is also possible to combine numerical simulations and optimization techniques for designing new airfoil shapes (Oyama *et al.*, 2005).

To evaluate airfoil aerodynamic characteristics via numerical simulations in the low Reynolds number region, their reliability and predictability should be verified before adopting them. What is indispensable for evaluating the airfoil aerodynamic characteristics in the low Reynolds number region is an accurate prediction of LSB behavior. As described in Sec. 1.3, the flow field around an LSB involves strong nonstationary three-dimensional structures; and hence, a three-dimensional simulation is needed to understand precise physical phenomena. Several high-accuracy three-dimensional numerical methods have been proposed such as a direct numerical simulation or a large eddy simulation. These simulations, however, still require very large computational resources despite the improvement of computer performances, so a two-dimensional simulation is more desirable than a three-dimensional one from an engineering point of view.

Some approaches with turbulence or transition models have been conducted to calculate flows around an LSB. Howard *et al.* (2000) carried out RANS simulations of an LSB around a flat plate with three methods of transition modeling. It was found that the transition modeling based on the local turbulent Reynolds number predicted a correct transition location but overpredicted the turbulence levels after the transition. Windte *et al.* (2006) employed a RANS simulation coupled with the e^N method to predict the transition location, and the Menter baseline two-layer model showed the best results. Tang (2008) applied a RANS simulation with the Spalart-Allmaras turbulence model around the SD7003 airfoil. Transition points were determined by laminar simulation results and the turbulence model was used after the transition point. It was shown that the technique above was able to capture an LSB. Rumsey & Spalart (2009) investigated the behavior of the Spalart-Allmaras and Menter shear-stress transport turbulence models under low Reynolds number conditions. One of main conclusions was that applying both models to low Reynolds number flows is not appropriate methods because they are intended for fully turbulent and high Reynolds number conditions. Catalano & Tognaccini (2010) conducted the Spalart-Allmaras and $k-\omega$ shear stress transport model with very low values of the freestream turbulence and successfully captured LSBs. They also proposed a modification of $k-\omega$ shear stress transport turbulence model for low Reynolds numbers. Counsil & Goni Boulama (2012) showed the capability of shear stress transport $\gamma - Re_\theta$ model, and Crivellini & D'Alessandro (2014) reported that the Spalart-Allmaras model with setting zero turbulent intensity could capture an LSB behavior at $Re_c \geq 1.5 \times 10^5$. Although there are many analogous studies to calculate low Reynolds

number flows and attempts to development of improved turbulence or transition models, the estimation of laminar separation and transition location by means of turbulence models is still controversial topics. On the other hand, another approaches have been carried out. Kojima *et al.* (2013) and Lee *et al.* (2015) conducted a two-dimensional unsteady laminar simulation without applying any turbulence model, and it was shown that a two-dimensional unsteady laminar simulation could be adopted to estimate qualitative lift and drag coefficients characteristics with a relatively low computational cost. In addition, separation points, reattachment phenomenon and formation of LSBs were captured in a wide range of low Reynolds number conditions ($1.0\times10^4 \leq Re_c \leq 5.0\times10^4$) except for high angles of attack at which massive separation occurs from the leading edge.

1.6 Objectives and outline of this thesis

As discussed above, the surface pressure distribution directly affects airfoil aerodynamic performances. However, not only a physical reason of appearing different pressure distributions depending on the flow condition but also a mechanism that can comprehensively explain the formation of surface pressure distribution are not sufficiently understood. Thus, this thesis will focus on the relationship between the surface pressure distribution around an LSB and related physical phenomena. Added to this, from an engineering point of view, it is unclear why three-dimensional complicated flows around LSB can be qualitatively predicted even by a two-dimensional unsteady laminar simulation. Moreover, it is still unknown the predictability of a two-dimensional laminar simulation for various physical phenomena except for separation and reattachment points. Here, it is expected that the reliability of a two-dimensional simulation can be clarified if the physical mechanism related to the formation of surface pressure distribution around an LSB is elucidated. Additionally, the airfoil aerodynamic characteristics at low Reynolds numbers are very sensitive to the airfoil shape, and hence the dependency of the predictability on the airfoil shape should be investigated.

Based on the questions above, this thesis aims to elucidate the physical mechanisms related to the formation of surface pressure distribution around an LSB by numerical simulations. The contents of this thesis are as follows. First of all, Chap. 2 describes governing equations and numerical methods applied in the present study. From a physical viewpoint, Chap. 3 discusses characteristics of an LSB. Next, formation mechanisms of the surface pressure distribution around an LSB are explained in Chap. 4. In Chaps. 3 and 4, high-order accurate three-dimensional large eddy simulations are conducted for a right-angled blunt leading edge flat plate. After clarifying the mechanisms related to the

formation of surface pressure distribution around an LSB, an engineering application of a two-dimensional simulation will be focused. Thus, two-dimensional unsteady laminar simulations are performed using a blunt leading edge flat plate in Chap. 5. In this chapter, I discuss the predictability of two-dimensional laminar simulations around an LSB flow in terms of instantaneous, averaged quantities and formation mechanisms of surface pressure distribution. In Chap. 6, I apply the contents performed in the previous chapters to flow fields around airfoils, and discuss the engineering usefulness of analysis shown in this thesis in respect to practical flow fields. For this purpose, the three-dimensional large eddy simulation is performed for the NACA0012 airfoil in Sec. 6.1. Next, in Sec. 6.2, the predictability of aerodynamic characteristics of the two-dimensional unsteady laminar simulation is discussed. Three different shape of airfoils such as the NACA0012, NACA0006, and Ishii airfoil are adopted in order to investigate a relationship between the airfoil aerodynamic characteristics predictability and dependency of airfoil geometric shape. Also, two-dimensional Reynolds-averaged Navier-Stokes simulations with the Baldwin-Lomax and Spalart-Allmaras turbulence model are conducted as comparison objects. Finally, the conclusion of this thesis is presented in Chap. 7.

Chapter 2

Numerical methods

In this chapter, numerical methods applied in the present study are described. First, governing equations of fluid dynamics are explained in Sec. 2.1. Then, Sec. 2.2 and Sec. 2.3 show the spatial discretization of three- and two-dimensional simulations, respectively. The time integration method adopted in both simulations is described in Sec. 2.4. In Sec. 2.5, some modeling methodologies to deal with turbulence are introduced, and boundary treatments are described in Sec. 2.6.

2.1 Governing equations of fluid dynamics

2.1.1 Governing equations in the Cartesian coordinate system

The governing equations adopted in this study are three-dimensional compressible Navier-Stokes equations. The conservation forms of mass, momentum, and energy in the Cartesian coordinate system without body forces are written as follows (Tannehill *et al.*, 1997; Hirsch, 2007; Wendt, 2008; Andersson *et al.*, 2012):

$$\frac{\partial \rho}{\partial t} + \frac{\partial (\rho u_i)}{\partial x_i} = 0, \tag{2.1}$$

$$\frac{\partial (\rho u_i)}{\partial t} + \frac{\partial (\rho u_i u_j)}{\partial x_j} = -\frac{\partial p}{\partial x_i} + \frac{\partial \tau_{ij}}{\partial x_j}, \tag{2.2}$$

$$\frac{\partial e}{\partial t} + \frac{\partial ((e+p) u_j)}{\partial x_j} = \frac{\partial (\tau_{ij} u_j - q_j)}{\partial x_j}, \tag{2.3}$$

where ρ is the density; t is the time; e is the total energy per unit volume; and p is the static pressure, respectively. The velocity components are denoted by $u_i (\equiv u, v, w)$ in each direction $x_i (\equiv x, y, z)$ for $i = 1, 2, 3$. The viscous stress tensor τ_{ij}, shown in Fig. 2.1,

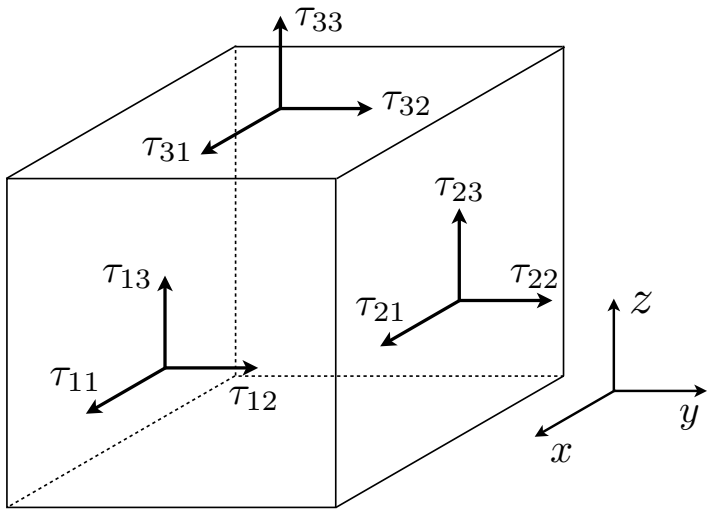

Figure 2.1: Components of the viscous stress tensor

is expressed by

$$\tau_{ij} = 2\mu s_{ij} + \lambda \delta_{ij} s_{kk}, \tag{2.4}$$

where δ_{ij} is the Kronecker delta, which is defined as

$$\delta_{ij} = \begin{cases} 0 & (i \neq j) \\ 1 & (i = j) \end{cases}. \tag{2.5}$$

The molecular viscosity μ which is a function of the temperature T is obtained by Sutherland's law (Sutherland, 1893)

$$\frac{\mu}{\mu_\infty} = \frac{1 + 0.3766}{T/T_\infty + 0.3766} \left(\frac{T}{T_\infty} \right)^{\frac{3}{2}}. \tag{2.6}$$

The subscript ∞ denotes a quantity of the freestream. The second viscosity coefficient λ is usually assumed to be $\lambda = -2\mu/3$ (i.e., bulk viscosity $\beta = \lambda + 2\mu/3 = 0$) according to Stokes' hypothesis (Stokes, 1845). Assuming the Stokes' hypothesis means that the isotropic dilatation of elementary volume of fluid do not produce the viscous stress (Buresti, 2015), and it is a commonly applied method in an analysis of compressible flow. The rate of strain tensor s_{ij} is given by

$$s_{ij} = \frac{1}{2} \left(\frac{\partial u_i}{\partial x_j} + \frac{\partial u_j}{\partial x_i} \right). \tag{2.7}$$

For the ideal gas, the static pressure p is calculated by the perfect gas equation of state,

$$p = \rho RT = (\gamma - 1) \left[e - \frac{1}{2} \rho u_k u_k \right], \tag{2.8}$$

where γ and R denote the specific heat ratio and gas constant, respectively. Fourier's law is applied to the heat flux vector q_j (i.e., q_j is assumed to be a linear function of the gradient of the temperature T); thus, it is written as

$$q_j = -\kappa \frac{\partial T}{\partial x_j}, \tag{2.9}$$

where κ is the thermal conductivity. By defining the Prandtl number Pr expressed as

$$Pr = \frac{\mu c_p}{\kappa}, \tag{2.10}$$

Eq. (2.9) is written by

$$q_j = -\kappa \frac{\partial T}{\partial x_j} = -\frac{\mu}{Pr}\frac{\partial (c_p T)}{\partial x_j} = -\frac{1}{\gamma - 1}\frac{\mu}{Pr}\frac{\partial a^2}{\partial x_j}, \tag{2.11}$$

where c_p and a denote the specific heat capacity at constant pressure and the speed of sound, given by

$$c_p = \frac{\gamma R}{\gamma - 1}\ ,\ a = \sqrt{\gamma R T} = \sqrt{\gamma \frac{p}{\rho}}. \tag{2.12}$$

According to the Einstein summation convention, the conservation of mass (continuity equation, Eq. (2.1)) is expanded as follows:

$$\frac{\partial \rho}{\partial t} + \frac{\partial (\rho u)}{\partial x} + \frac{\partial (\rho v)}{\partial y} + \frac{\partial (\rho w)}{\partial z} = 0. \tag{2.13}$$

The conservation of momentum (Eq. (2.2)) are separated into the scalar equations below:

$$\begin{aligned} &\frac{\partial (\rho u)}{\partial t} + \frac{\partial (\rho u^2 + p)}{\partial x} + \frac{\partial (\rho u v)}{\partial y} + \frac{\partial (\rho u w)}{\partial z} = \\ &\quad \frac{\partial}{\partial x}\left[\frac{2}{3}\mu\left(2\frac{\partial u}{\partial x} - \frac{\partial v}{\partial y} - \frac{\partial w}{\partial z}\right)\right] + \frac{\partial}{\partial y}\left[\mu\left(\frac{\partial v}{\partial x} + \frac{\partial u}{\partial y}\right)\right] + \frac{\partial}{\partial z}\left[\mu\left(\frac{\partial w}{\partial x} + \frac{\partial u}{\partial z}\right)\right], \end{aligned} \tag{2.14}$$

$$\begin{aligned} &\frac{\partial (\rho v)}{\partial t} + \frac{\partial (\rho u v)}{\partial x} + \frac{\partial (\rho v^2 + p)}{\partial y} + \frac{\partial (\rho v w)}{\partial z} = \\ &\quad \frac{\partial}{\partial x}\left[\mu\left(\frac{\partial v}{\partial x} + \frac{\partial u}{\partial y}\right)\right] + \frac{\partial}{\partial y}\left[\frac{2}{3}\mu\left(2\frac{\partial v}{\partial y} - \frac{\partial w}{\partial z} - \frac{\partial u}{\partial x}\right)\right] + \frac{\partial}{\partial z}\left[\mu\left(\frac{\partial w}{\partial y} + \frac{\partial v}{\partial z}\right)\right], \end{aligned} \tag{2.15}$$

$$\frac{\partial(\rho w)}{\partial t}+\frac{\partial(\rho u w)}{\partial x}+\frac{\partial(\rho v w)}{\partial y}+\frac{\partial(\rho w^2+p)}{\partial z}= \frac{\partial}{\partial x}\left[\mu\left(\frac{\partial w}{\partial x}+\frac{\partial u}{\partial z}\right)\right]+\frac{\partial}{\partial y}\left[\mu\left(\frac{\partial w}{\partial y}+\frac{\partial v}{\partial x}\right)\right]+\frac{\partial}{\partial z}\left[\frac{2}{3}\mu\left(2\frac{\partial w}{\partial z}-\frac{\partial u}{\partial x}-\frac{\partial v}{\partial y}\right)\right]. \tag{2.16}$$

The conservation of energy (Eq. (2.3)) is given as

$$\begin{aligned}\frac{\partial e}{\partial t}+\frac{\partial((e+p)u)}{\partial x}+\frac{\partial((e+p)v)}{\partial y}+\frac{\partial((e+p)w)}{\partial z}= &\\ \frac{\partial}{\partial x}\left[\frac{2}{3}\mu\left(2\frac{\partial u}{\partial x}-\frac{\partial v}{\partial y}-\frac{\partial w}{\partial z}\right)u+\mu\left(\frac{\partial u}{\partial y}+\frac{\partial v}{\partial x}\right)v+\mu\left(\frac{\partial u}{\partial z}+\frac{\partial w}{\partial x}\right)w-q_x\right]+ &\\ \frac{\partial}{\partial y}\left[\mu\left(\frac{\partial u}{\partial y}+\frac{\partial v}{\partial x}\right)u+\frac{2}{3}\mu\left(2\frac{\partial v}{\partial y}-\frac{\partial w}{\partial z}-\frac{\partial u}{\partial x}\right)v+\mu\left(\frac{\partial v}{\partial z}+\frac{\partial w}{\partial y}\right)w-q_y\right]+ &\\ \frac{\partial}{\partial z}\left[\mu\left(\frac{\partial u}{\partial z}+\frac{\partial w}{\partial x}\right)u+\mu\left(\frac{\partial v}{\partial z}+\frac{\partial w}{\partial y}\right)v+\frac{2}{3}\mu\left(2\frac{\partial w}{\partial z}-\frac{\partial u}{\partial x}-\frac{\partial v}{\partial y}\right)w-q_z\right].\end{aligned} \tag{2.17}$$

Thus, the governing equations are rewritten in a vector notation as follows:

$$\frac{\partial Q}{\partial t}+\frac{\partial E}{\partial x}+\frac{\partial F}{\partial y}+\frac{\partial G}{\partial z}=\frac{\partial E_\nu}{\partial x}+\frac{\partial Q_\nu}{\partial y}+\frac{\partial G_\nu}{\partial z}, \tag{2.18}$$

$$Q=\begin{bmatrix}\rho\\ \rho u\\ \rho v\\ \rho w\\ e\end{bmatrix},\ E=\begin{bmatrix}\rho u\\ \rho u^2+p\\ \rho uv\\ \rho uw\\ (e+p)u\end{bmatrix},\ F=\begin{bmatrix}\rho v\\ \rho uv\\ \rho v^2+p\\ \rho vw\\ (e+p)v\end{bmatrix},\ G=\begin{bmatrix}\rho w\\ \rho uw\\ \rho vw\\ \rho w^2+p\\ (e+p)w\end{bmatrix},$$

$$E_\nu=\begin{bmatrix}0\\ \tau_{xx}\\ \tau_{yx}\\ \tau_{zx}\\ \beta_x\end{bmatrix},\ F_\nu=\begin{bmatrix}0\\ \tau_{xy}\\ \tau_{yy}\\ \tau_{zy}\\ \beta_y\end{bmatrix},\ G_\nu=\begin{bmatrix}0\\ \tau_{zx}\\ \tau_{zy}\\ \tau_{zz}\\ \beta_z\end{bmatrix},$$

$$\begin{cases}\beta_x=\tau_{xx}u+\tau_{xy}v+\tau_{xz}w-q_x\\ \beta_y=\tau_{yx}u+\tau_{yy}v+\tau_{yz}w-q_y\\ \beta_z=\tau_{zx}u+\tau_{zy}v+\tau_{zz}w-q_z\end{cases},$$

$$\begin{cases}\tau_{xx}=\frac{2}{3}\mu(2u_x-v_y-w_z),\ \tau_{yy}=\frac{2}{3}\mu(2v_y-w_z-u_z),\ \tau_{zz}=\frac{2}{3}\mu(2w_z-u_x-v_y)\\ \tau_{xy}=\tau_{yx}=\mu(u_y+v_x),\ \tau_{yz}=\tau_{zy}=\mu(v_z+w_y),\ \tau_{zx}=\tau_{xz}=\mu(w_x+u_z)\end{cases}.$$

2.1.2 Nondimensional form of governing equations

The governing equations (Eq. (2.18)) are nondimensionalized in this study. The reason of nondimensionalization is that it is easier to compare with another numerical or experimental results using the equation which is standardized by physical representative quantities based on the law of similarity, rather than the equation which is expressed in the real scale. All variables are normalized by the reference length $\mathcal{L}$, density ρ_∞, molecular viscosity μ_∞, and speed of sound a_∞ of the freestream. That is, the following nondimensionalized quantities are introduced:

$$x_i^* = \frac{x_i}{\mathcal{L}} \ , \ t^* = \frac{t}{\mathcal{L}/a_\infty} \ , \ \rho^* = \frac{\rho}{\rho_\infty} \ , \ u^* = \frac{u_i}{a_\infty} \ , \ e^* = \frac{e}{\rho_\infty a_\infty^2} \ ,$$
$$p^* = \frac{p}{\rho_\infty a_\infty^2} \ , \ \tau^* = \frac{\tau_{ij}}{\mu_\infty a_\infty/\mathcal{L}} \ , \ q_i^* = \frac{q}{\mu_\infty a_\infty^2/\mathcal{L}} \ , \tag{2.19}$$

where the variables with an asterisk denote the nondimensional ones. The Nondimensionalized three-dimensional compressible Navier-Stokes equation in the Cartesian coordinate system can be obtained by substituting the relationship above into Eq. (2.18),

$$\frac{\partial Q^*}{\partial t^*} + \frac{\partial E^*}{\partial x^*} + \frac{\partial F^*}{\partial y^*} + \frac{\partial G^*}{\partial z^*} = \frac{1}{Re}\left(\frac{\partial E_\nu^*}{\partial x^*} + \frac{\partial F_\nu^*}{\partial y^*} + \frac{\partial G_\nu^*}{\partial z^*}\right), \tag{2.20}$$

$$Q^* = \begin{bmatrix} \rho^* \\ \rho^* u^* \\ \rho^* v^* \\ \rho^* w^* \\ e^* \end{bmatrix} \ , \ E^* = \begin{bmatrix} \rho^* u^* \\ \rho^* u^{*2} + p^* \\ \rho^* u^* v^* \\ \rho^* u^* w^* \\ (e^* + p^*) u^* \end{bmatrix} \ , \ F^* = \begin{bmatrix} \rho^* v^* \\ \rho^* u^* v^* \\ \rho^* v^{*2} + p^* \\ \rho^* v^* w^* \\ (e^* + p^*) v^* \end{bmatrix} \ , \ G^* = \begin{bmatrix} \rho^* w^* \\ \rho^* u^* w^* \\ \rho^* v^* w^* \\ \rho^* w^{*2} + p^* \\ (e^* + p^*) w^* \end{bmatrix} \ ,$$

$$E_\nu^* = \begin{bmatrix} 0 \\ \tau_{xx}^* \\ \tau_{yx}^* \\ \tau_{zx}^* \\ \beta_x^* \end{bmatrix} \ , \ F_\nu^* = \begin{bmatrix} 0 \\ \tau_{xy}^* \\ \tau_{yy}^* \\ \tau_{zy}^* \\ \beta_y^* \end{bmatrix} \ , \ G_\nu^* = \begin{bmatrix} 0 \\ \tau_{zx}^* \\ \tau_{zy}^* \\ \tau_{zz}^* \\ \beta_z^* \end{bmatrix} \ ,$$

$$\begin{cases} \beta_x^* = \tau_{xx}^* u^* + \tau_{xy}^* v^* + \tau_{xz}^* w^* - q_x^* \\ \beta_y^* = \tau_{yx}^* u^* + \tau_{yy}^* v^* + \tau_{yz}^* w^* - q_y^* \\ \beta_z^* = \tau_{zx}^* u^* + \tau_{zy}^* v^* + \tau_{zz}^* w^* - q_z^* \end{cases} .$$

The Reynolds number Re and Mach number M_∞ are defined as follows:

$$Re = \frac{\rho_\infty a_\infty \mathcal{L}}{\mu_\infty} = \frac{1}{M_\infty}\frac{\rho_\infty U_\infty \mathcal{L}}{\mu_\infty} \quad , \quad M_\infty = \frac{U_\infty}{a_\infty}. \tag{2.21}$$

The asterisk symbol will be omitted from the following discussion for convenience.

2.1.3 Governing equations in the curvilinear coordinate system

The Cartesian coordinate system discussed in the previous section can be used for the calculation when an analysis object has a simple shape (e.g., a channel flow or a backstep-facing flow). For many applications, however, analysis objects usually have more complicated shape, so it is convenient to use the generalized curvilinear coordinate system (i.e., body-fitted coordinate system). Thus, in the present study, the governing equation in the Cartesian coordinate system (x, y, z, t) will be transformed to the curvilinear coordinate system (ξ, η, ζ, τ) as follows (Steger, 1978; Pulliam & Steger, 1980):

$$\begin{cases} x = x(\xi, \eta, \zeta, \tau) \\ y = y(\xi, \eta, \zeta, \tau) \\ z = z(\xi, \eta, \zeta, \tau) \\ t = \tau \end{cases} \Longleftrightarrow \begin{cases} \xi = \xi(x, y, z, t) \\ \eta = \eta(x, y, z, t) \\ \zeta = \zeta(x, y, z, t) \\ \tau = t \end{cases} . \tag{2.22}$$

Figure 2.2 shows a schematic diagram of the coordinate transformation. The space in the Cartesian coordinate system is often referred to as the physical domain whereas that in the curvilinear coordinate system is referred to as the computational domain. There is one-to-one correspondence relationship between the physical and computational domain, and the (ξ, η, ζ) are orthogonal coordinate in the computational domain. Through this transformation, a non-uniform grid in the physical domain is transformed to a uniform grid in the computational domain (Wendt, 2008) and standard unweighted differencing schemes can be applied for arbitrary grid systems and complex geometric shapes (Pulliam, 1986).

The differential form of Eq. (2.22) is given by the chain rule expansions as follows:

$$\begin{cases} dx = x_\xi d\xi + x_\eta d\eta + x_\zeta d\zeta + x_\tau d\tau \\ dy = y_\xi d\xi + y_\eta d\eta + y_\zeta d\zeta + y_\tau d\tau \\ dz = z_\xi d\xi + z_\eta d\eta + z_\zeta d\zeta + z_\tau d\tau \\ dt = t_\xi d\xi + t_\eta d\eta + t_\zeta d\zeta + t_\tau d\tau \end{cases} , \begin{cases} d\xi = \xi_x dx + \xi_y dy + \xi_z dz + \xi_t dt \\ d\eta = \eta_x dx + \eta_y dy + \eta_z dz + \eta_t dt \\ d\zeta = \zeta_x dx + \zeta_y dy + \zeta_z dz + \zeta_t dt \\ d\tau = \tau_x dx + \tau_y dy + \tau_z dz + \tau_t dt \end{cases} . \tag{2.23}$$

Here, $t_\xi = t_\eta = t_\zeta = \tau_x = \tau_y = \tau_z = 0$, and $t_\tau = \tau_t = 1$. Thereby, a matrix form of

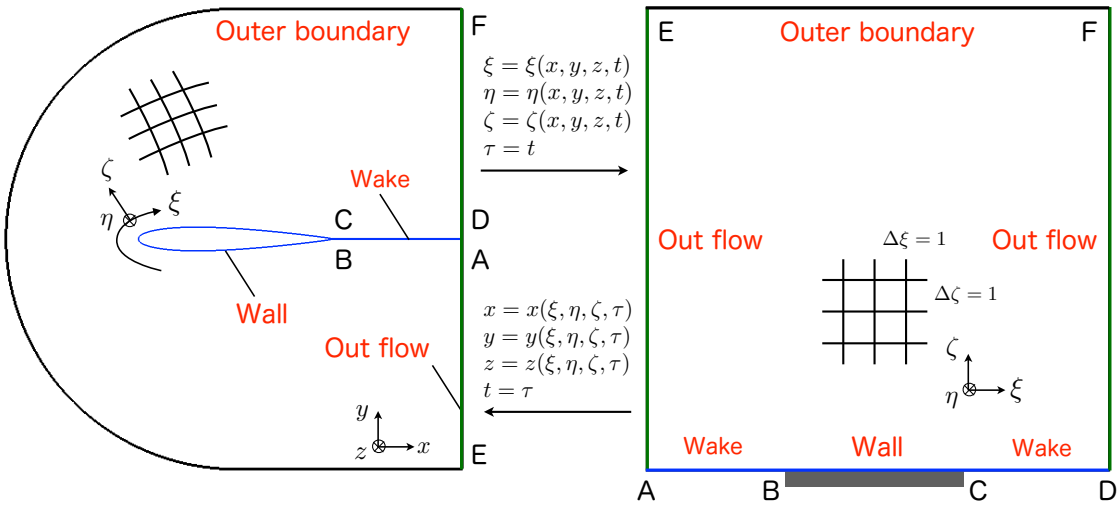

Figure 2.2: Schematic diagram of the coordinate transformation between the Cartesian coordinate (physical domain) and generalized curvilinear coordinate (computation domain) (originally drawn by Pulliam (1986) and modified).

Eq. (2.23) is

$$\begin{bmatrix} dx \\ dy \\ dz \\ dt \end{bmatrix} = \begin{bmatrix} x_\xi & x_\eta & x_\zeta & x_\tau \\ y_\xi & y_\eta & y_\zeta & y_\tau \\ z_\xi & z_\eta & z_\zeta & z_\tau \\ 0 & 0 & 0 & 1 \end{bmatrix} \begin{bmatrix} d\xi \\ d\eta \\ d\zeta \\ d\tau \end{bmatrix}, \quad \begin{bmatrix} d\xi \\ d\eta \\ d\zeta \\ d\tau \end{bmatrix} = \begin{bmatrix} \xi_x & \xi_y & \xi_z & \xi_t \\ \eta_x & \eta_y & \eta_z & \eta_t \\ \zeta_x & \zeta_y & \zeta_z & \zeta_t \\ 0 & 0 & 0 & 1 \end{bmatrix} \begin{bmatrix} dx \\ dy \\ dz \\ dt \end{bmatrix}. \tag{2.24}$$

From the relationship above, metrics (ξ_x, ξ_y, ξ_z, ξ_t, $\cdots$, ζ_t) are computed as follows:

$$\begin{bmatrix} \xi_x & \xi_y & \xi_z & \xi_t \\ \eta_x & \eta_y & \eta_z & \eta_t \\ \zeta_x & \zeta_y & \zeta_z & \zeta_t \\ 0 & 0 & 0 & 1 \end{bmatrix} = \begin{bmatrix} x_\xi & x_\eta & x_\zeta & x_\tau \\ y_\xi & y_\eta & y_\zeta & y_\tau \\ z_\xi & z_\eta & z_\zeta & z_\tau \\ 0 & 0 & 0 & 1 \end{bmatrix}^{-1}$$

$$= J \begin{bmatrix} y_\eta z_\zeta - y_\zeta z_\eta & z_\eta x_\zeta - z_\zeta x_\eta & x_\eta y_\zeta - x_\zeta y_\eta \\ y_\zeta z_\xi - y_\xi z_\zeta & z_\zeta x_\xi - z_\xi x_\zeta & x_\zeta y_\xi - x_\xi y_\zeta \\ y_\xi z_\eta - y_\eta z_\xi & z_\xi x_\eta - z_\eta x_\xi & x_\xi y_\eta - x_\eta y_\xi \\ 0 & 0 & 0 \end{bmatrix}$$

$$\begin{bmatrix} -x_\tau(y_\eta z_\zeta - y_\zeta z_\eta) - y_\tau(z_\eta x_\zeta - z_\zeta x_\eta) - z_\tau(x_\eta y_\zeta - x_\zeta y_\eta) \\ -x_\tau(y_\zeta z_\xi - y_\xi z_\zeta) - y_\tau(z_\zeta x_\xi - z_\xi x_\zeta) - z_\tau(x_\zeta y_\xi - x_\xi y_\zeta) \\ -x_\tau(y_\xi z_\eta - y_\eta z_\xi) - y_\tau(z_\xi x_\eta - z_\eta x_\xi) - z_\tau(x_\xi y_\eta - x_\eta y_\xi) \\ 1 \end{bmatrix}, \tag{2.25}$$

where J is the transformation Jacobian from the Cartesian coordinate system to the generalized curvilinear coordinate system. It is calculated by

$$\begin{aligned} J = \frac{\partial(\xi,\eta,\zeta)}{\partial(x,y,z)} &= \left(\frac{\partial(x,y,z)}{\partial(\xi,\eta,\zeta)}\right)^{-1} = 1/\det\begin{bmatrix} x_\xi & x_\eta & x_\zeta \\ y_\xi & y_\eta & y_\zeta \\ z_\xi & z_\eta & z_\zeta \end{bmatrix} \\ &= \frac{1}{x_\xi(y_\eta z_\zeta - y_\zeta z_\eta) + x_\eta(y_\zeta z_\xi - y_\xi z_\zeta) + x_\zeta(y_\xi z_\eta - y_\eta z_\xi)}. \end{aligned} \tag{2.26}$$

To be summarized, the coordinate transformation metrics are obtained by

$$\begin{aligned} &\xi_x/J = y_\eta z_\zeta - y_\zeta z_\eta \quad , \quad \xi_y/J = z_\eta x_\zeta - z_\zeta x_\eta \quad , \quad \xi_z/J = x_\eta y_\zeta - x_\zeta y_\eta, \\ &\eta_x/J = y_\zeta z_\xi - y_\xi z_\zeta \quad , \quad \eta_y/J = z_\zeta x_\xi - z_\xi x_\zeta \quad , \quad \eta_z/J = x_\zeta y_\xi - x_\xi y_\zeta, \\ &\zeta_x/J = y_\xi z_\eta - y_\eta z_\xi \quad , \quad \zeta_y/J = z_\xi x_\eta - z_\eta x_\xi \quad , \quad \zeta_z/J = x_\xi y_\eta - x_\eta y_\xi. \end{aligned} \tag{2.27}$$

Let us consider the transformation of the nondimensionalized governing equation (Eq. (2.20)). The transformations for x, y, z, and t are given by the chain rule as follows:

$$\begin{cases} \dfrac{\partial}{\partial x} = \xi_x\dfrac{\partial}{\partial\xi} + \eta_x\dfrac{\partial}{\partial\eta} + \zeta_x\dfrac{\partial}{\partial\zeta} + 0, \\ \dfrac{\partial}{\partial y} = \xi_y\dfrac{\partial}{\partial\xi} + \eta_y\dfrac{\partial}{\partial\eta} + \zeta_y\dfrac{\partial}{\partial\zeta} + 0, \\ \dfrac{\partial}{\partial z} = \xi_z\dfrac{\partial}{\partial\xi} + \eta_z\dfrac{\partial}{\partial\eta} + \zeta_z\dfrac{\partial}{\partial\zeta} + 0, \\ \dfrac{\partial}{\partial t} = \xi_t\dfrac{\partial}{\partial\xi} + \eta_t\dfrac{\partial}{\partial\eta} + \zeta_t\dfrac{\partial}{\partial\zeta} + \dfrac{\partial}{\partial\tau}. \end{cases} \tag{2.28}$$

Substituting Eq. (2.28) into Eq. (2.20),

$$\begin{aligned} &\left(\xi_t\frac{\partial Q}{\partial\xi} + \eta_t\frac{\partial Q}{\partial\eta} + \zeta_t\frac{\partial Q}{\partial\zeta} + \frac{\partial Q}{\partial\tau}\right) \\ &\quad + \left(\xi_x\frac{\partial E}{\partial\xi} + \eta_x\frac{\partial E}{\partial\eta} + \zeta_x\frac{\partial E}{\partial\zeta}\right) + \left(\xi_y\frac{\partial F}{\partial\xi} + \eta_y\frac{\partial F}{\partial\eta} + \zeta_y\frac{\partial F}{\partial\zeta}\right) + \left(\xi_z\frac{\partial G}{\partial\xi} + \eta_z\frac{\partial G}{\partial\eta} + \zeta_z\frac{\partial G}{\partial\zeta}\right) \\ &= \frac{1}{Re}\left[\left(\xi_x\frac{\partial E_\nu}{\partial\xi} + \eta_x\frac{\partial E_\nu}{\partial\eta} + \zeta_x\frac{\partial E_\nu}{\partial\zeta}\right) + \left(\xi_y\frac{\partial F_\nu}{\partial\xi} + \eta_y\frac{\partial F_\nu}{\partial\eta} + \zeta_y\frac{\partial F_\nu}{\partial\zeta}\right)\right. \\ &\qquad\qquad \left. + \left(\xi_z\frac{\partial G_\nu}{\partial\xi} + \eta_z\frac{\partial G_\nu}{\partial\eta} + \zeta_z\frac{\partial G_\nu}{\partial\zeta}\right)\right]. \end{aligned} \tag{2.29}$$

If multiplied by $1/J$ in both sides, each term in Eq. (2.29) is written as follows:

$$\begin{aligned}
\text{The } 1^{\text{st}} \text{ term of LHS} &= \frac{\partial}{\partial\xi}\left(\frac{\xi_t}{J}Q\right)+\frac{\partial}{\partial\eta}\left(\frac{\eta_t}{J}Q\right)+\frac{\partial}{\partial\zeta}\left(\frac{\zeta_t}{J}Q\right)+\frac{\partial}{\partial\tau}\left(\frac{1}{J}Q\right) \\
&- Q\left[\frac{\partial}{\partial\xi}\left(\frac{\xi_t}{J}\right)+\frac{\partial}{\partial\eta}\left(\frac{\eta_t}{J}\right)+\frac{\partial}{\partial\zeta}\left(\frac{\zeta_t}{J}\right)+\frac{\partial}{\partial\tau}\left(\frac{1}{J}\right)\right], \qquad (2.30)\\
\text{The } 2^{\text{nd}} \text{ term of LHS} &= \frac{\partial}{\partial\xi}\left(\frac{\xi_x}{J}E\right)+\frac{\partial}{\partial\eta}\left(\frac{\eta_x}{J}E\right)+\frac{\partial}{\partial\zeta}\left(\frac{\zeta_x}{J}E\right) \\
&- E\left[\frac{\partial}{\partial\xi}\left(\frac{\xi_x}{J}\right)+\frac{\partial}{\partial\eta}\left(\frac{\eta_x}{J}\right)+\frac{\partial}{\partial\zeta}\left(\frac{\zeta_x}{J}\right)\right], \qquad (2.31)\\
\text{The } 3^{\text{rd}} \text{ term of LHS} &= \frac{\partial}{\partial\xi}\left(\frac{\xi_y}{J}F\right)+\frac{\partial}{\partial\eta}\left(\frac{\eta_y}{J}F\right)+\frac{\partial}{\partial\zeta}\left(\frac{\zeta_y}{J}F\right) \\
&- F\left[\frac{\partial}{\partial\xi}\left(\frac{\xi_y}{J}\right)+\frac{\partial}{\partial\eta}\left(\frac{\eta_y}{J}\right)+\frac{\partial}{\partial\zeta}\left(\frac{\zeta_y}{J}\right)\right], \qquad (2.32)\\
\text{The } 4^{\text{th}} \text{ term of LHS} &= \frac{\partial}{\partial\xi}\left(\frac{\xi_z}{J}G\right)+\frac{\partial}{\partial\eta}\left(\frac{\eta_z}{J}G\right)+\frac{\partial}{\partial\zeta}\left(\frac{\zeta_z}{J}G\right) \\
&- G\left[\frac{\partial}{\partial\xi}\left(\frac{\xi_z}{J}\right)+\frac{\partial}{\partial\eta}\left(\frac{\eta_z}{J}\right)\frac{\partial}{\partial\zeta}\left(\frac{\zeta_z}{J}\right)\right], \qquad (2.33)\\
\text{The } 1^{\text{st}} \text{ term of RHS} &= \frac{1}{Re}\left[\frac{\partial}{\partial\xi}\left(\frac{\xi_x}{J}E_\nu\right)+\frac{\partial}{\partial\eta}\left(\frac{\eta_x}{J}E_\nu\right)+\frac{\partial}{\partial\zeta}\left(\frac{\zeta_x}{J}E_\nu\right)\right] \\
&- \frac{1}{Re}E_\nu\left[\frac{\partial}{\partial\xi}\left(\frac{\xi_x}{J}\right)+\frac{\partial}{\partial\eta}\left(\frac{\eta_x}{J}\right)+\frac{\partial}{\partial\zeta}\left(\frac{\zeta_x}{J}\right)\right], \qquad (2.34)\\
\text{The } 2^{\text{nd}} \text{ term of RHS} &= \frac{1}{Re}\left[\frac{\partial}{\partial\xi}\left(\frac{\xi_y}{J}F_\nu\right)+\frac{\partial}{\partial\eta}\left(\frac{\eta_y}{J}F_\nu\right)+\frac{\partial}{\partial\zeta}\left(\frac{\zeta_y}{J}F_\nu\right)\right] \\
&- \frac{1}{Re}F_\nu\left[\frac{\partial}{\partial\xi}\left(\frac{\xi_y}{J}\right)+\frac{\partial}{\partial\eta}\left(\frac{\eta_y}{J}\right)+\frac{\partial}{\partial\zeta}\left(\frac{\zeta_y}{J}\right)\right], \qquad (2.35)\\
\text{The } 3^{\text{rd}} \text{ term of RHS} &= \frac{1}{Re}\left[\frac{\partial}{\partial\xi}\left(\frac{\xi_z}{J}G_\nu\right)+\frac{\partial}{\partial\eta}\left(\frac{\eta_z}{J}G_\nu\right)+\frac{\partial}{\partial\zeta}\left(\frac{\zeta_z}{J}G_\nu\right)\right] \\
&- \frac{1}{Re}G_\nu\left[\frac{\partial}{\partial\xi}\left(\frac{\xi_z}{J}\right)+\frac{\partial}{\partial\eta}\left(\frac{\eta_z}{J}\right)\frac{\partial}{\partial\zeta}\left(\frac{\zeta_z}{J}\right)\right]. \qquad (2.36)
\end{aligned}$$

Equations (2.30)-(2.36) include the metric identities so-called the geometric conservation law (GCL) as follows (Vinokur, 1974; Abe *et al.*, 2014):

$$\mathcal{I}_t = \frac{\partial}{\partial\xi}\left(\frac{\xi_t}{J}\right)+\frac{\partial}{\partial\eta}\left(\frac{\eta_t}{J}\right)+\frac{\partial}{\partial\zeta}\left(\frac{\zeta_t}{J}\right)+\frac{\partial}{\partial\tau}\left(\frac{1}{J}\right)=0 \qquad (2.37)$$

$$\mathcal{I}_x = \frac{\partial}{\partial\xi}\left(\frac{\xi_x}{J}\right)+\frac{\partial}{\partial\eta}\left(\frac{\eta_x}{J}\right)+\frac{\partial}{\partial\zeta}\left(\frac{\zeta_x}{J}\right)=0 \qquad (2.38)$$

$$\mathcal{I}_y = \frac{\partial}{\partial\xi}\left(\frac{\xi_y}{J}\right)+\frac{\partial}{\partial\eta}\left(\frac{\eta_y}{J}\right)+\frac{\partial}{\partial\zeta}\left(\frac{\zeta_y}{J}\right)=0 \qquad (2.39)$$

$$\mathcal{I}_z = \frac{\partial}{\partial\xi}\left(\frac{\xi_z}{J}\right)+\frac{\partial}{\partial\eta}\left(\frac{\eta_z}{J}\right)+\frac{\partial}{\partial\zeta}\left(\frac{\zeta_z}{J}\right)=0 \qquad (2.40)$$

The GCL identities consist of the volume conservation law (VCL, Eq. (2.37)) (Zhang *et al.*, 1993; Abe *et al.*, 2013) and the surface conservation law (SCL, Eqs. (2.38)-(2.40)) (Vinokur & Yee, 2002; Deng *et al.*, 2011). These are often introduced as a sufficient condition for a freestream preservation, which indicates that spatially and temporally uniform flow variables can satisfy the governing equations. The GCL identities can also be regarded as a sufficient condition for the commutative property of the governing equation between the Cartesian and curvilinear coordinate system in the strong conservation form. These equations are analytically satisfied, but not numerically guaranteed for the high-order finite difference schemes. These identities should be satisfied numerically to ensure the freestream preservation, so several methods have been proposed to satisfy discretized CGL identities for the metrics and Jacobian discretization. Detailed methods for calculating the metrics and Jacobian will be discussed in Sec. 2.2.3 and Sec. 2.3.3. Substituting Eqs. (2.37)-(2.40) into Eqs. (2.30)-(2.36),

$$\begin{aligned}
&\frac{\partial}{\partial\tau}\left(\frac{1}{J}Q\right)+\frac{\partial}{\partial\xi}\left(\frac{\xi_t}{J}Q+\frac{\xi_x}{J}E+\frac{\xi_y}{J}F+\frac{\xi_z}{J}G\right)\\
&\quad+\frac{\partial}{\partial\eta}\left(\frac{\eta_t}{J}Q+\frac{\eta_x}{J}E+\frac{\eta_y}{J}F+\frac{\eta_z}{J}G\right)+\frac{\partial}{\partial\zeta}\left(\frac{\zeta_t}{J}Q+\frac{\zeta_x}{J}E+\frac{\zeta_y}{J}+\frac{\zeta_z}{J}\right)\\
&=\frac{1}{Re}\left[\frac{\partial}{\partial\xi}\left(\frac{\xi_x}{J}E_\nu+\frac{\xi_y}{J}F_\nu+\frac{\xi_z}{J}G_\nu\right)+\frac{\partial}{\partial\eta}\left(\frac{\eta_x}{J}E_\nu+\frac{\eta_y}{J}F_\nu+\frac{\eta_z}{J}G_\nu\right)\right.\\
&\qquad\left.+\frac{\partial}{\partial\zeta}\left(\frac{\zeta_x}{J}E_\nu+\frac{\zeta_y}{J}F_\nu+\frac{\zeta_z}{J}G_\nu\right)\right].
\end{aligned}\tag{2.41}$$

In case of a stationary grid (i.e., time-invariant coordinate transformation), $\xi_t=\eta_t=\zeta_t=0$; thus, the strong conservation form of the nondimensionalized three-dimensional compressible Navier-Stokes equations in the generalized curvilinear coordinate is obtained as

$$\frac{\partial\hat{Q}}{\partial\tau}+\frac{\partial\hat{E}}{\partial\xi}+\frac{\partial\hat{F}}{\partial\eta}+\frac{\partial\hat{G}}{\partial\zeta}=\frac{1}{Re}\left(\frac{\partial\hat{E}_\nu}{\partial\xi}+\frac{\partial\hat{F}_\nu}{\partial\eta}+\frac{\partial\hat{G}_\nu}{\partial\zeta}\right),\tag{2.42}$$

where

$$\hat{Q}=\frac{1}{J}\begin{bmatrix}\rho\\ \rho u\\ \rho v\\ \rho w\\ e\end{bmatrix},\quad \hat{E}=\frac{1}{J}\begin{bmatrix}\rho U\\ \rho uU+\xi_x p\\ \rho vU+\xi_y p\\ \rho wU+\xi_z p\\ (e+p)U\end{bmatrix},\quad \hat{F}=\frac{1}{J}\begin{bmatrix}\rho V\\ \rho uV+\eta_x p\\ \rho vV+\eta_y p\\ \rho wV+\eta_z p\\ (e+p)V\end{bmatrix},$$

$$\hat{G} = \frac{1}{J}\begin{bmatrix} \rho W \\ \rho u W + \zeta_x p \\ \rho v W + \zeta_y p \\ \rho w W + \zeta_z p \\ (e+p)W \end{bmatrix}, \quad \hat{E}_\nu = \frac{1}{J}\begin{bmatrix} 0 \\ \xi_x\tau_{xx} + \xi_y\tau_{xy} + \xi_z\tau_{xz} \\ \xi_x\tau_{yx} + \xi_y\tau_{yy} + \xi_z\tau_{yz} \\ \xi_x\tau_{zx} + \xi_y\tau_{zy} + \xi_z\tau_{zz} \\ \xi_x\beta_x + \xi_y\beta_y + \xi_z\beta_z \end{bmatrix},$$

$$\hat{F}_\nu = \frac{1}{J}\begin{bmatrix} 0 \\ \eta_x\tau_{xx} + \eta_y\tau_{xy} + \eta_z\tau_{xz} \\ \eta_x\tau_{yx} + \eta_y\tau_{yy} + \eta_z\tau_{yz} \\ \eta_x\tau_{zx} + \eta_y\tau_{zy} + \eta_z\tau_{zz} \\ \eta_x\beta_x + \eta_y\beta_y + \eta_z\beta_z \end{bmatrix}, \quad \hat{G}_\nu = \frac{1}{J}\begin{bmatrix} 0 \\ \zeta_x\tau_{xx} + \zeta_y\tau_{xy} + \zeta_z\tau_{xz} \\ \zeta_x\tau_{yx} + \zeta_y\tau_{yy} + \zeta_z\tau_{yz} \\ \zeta_x\tau_{zx} + \zeta_y\tau_{zy} + \zeta_z\tau_{zz} \\ \zeta_x\beta_x + \zeta_y\beta_y + \zeta_z\beta_z \end{bmatrix},$$

$$\begin{cases} \beta_x = \tau_{xx}u + \tau_{xy}v + \tau_{xz}w - q_x \\ \beta_y = \tau_{yx}u + \tau_{yy}v + \tau_{yz}w - q_y \\ \beta_z = \tau_{zx}u + \tau_{zy}v + \tau_{zz}w - q_z \end{cases},$$

$$\begin{cases} \tau_{xx} = \frac{2}{3}\mu(2u_x - v_y - w_z),\ \tau_{yy} = \frac{2}{3}\mu(2v_y - w_z - u_z),\ \tau_{zz} = \frac{2}{3}\mu(2w_z - u_x - v_y) \\ \tau_{xy} = \tau_{yx} = \mu(u_y + v_x),\ \tau_{yz} = \tau_{zy} = \mu(v_z + w_y),\ \tau_{zx} = \tau_{xz} = \mu(w_x + u_z) \end{cases},$$

or simply,

$$\hat{Q} = \frac{1}{J}Q,$$
$$\hat{E} = \frac{\xi_t}{J}Q + \frac{\xi_x}{J}E + \frac{\xi_y}{J}F + \frac{\xi_z}{J}G\ ,\ \hat{E}_\nu = \frac{\xi_x}{J}E_\nu + \frac{\xi_y}{J}F_\nu + \frac{\xi_z}{J}G_\nu,$$
$$\hat{F} = \frac{\eta_t}{J}Q + \frac{\eta_x}{J}E + \frac{\eta_y}{J}F + \frac{\eta_z}{J}G\ ,\ \hat{F}_\nu = \frac{\eta_x}{J}E_\nu + \frac{\eta_y}{J}F_\nu + \frac{\eta_z}{J}G_\nu,$$
$$\hat{G} = \frac{\zeta_t}{J}Q + \frac{\zeta_x}{J}E + \frac{\zeta_y}{J} + \frac{\zeta_z}{J}G\ ,\ \hat{G}_\nu = \frac{\zeta_x}{J}E_\nu + \frac{\zeta_y}{J}F_\nu + \frac{\zeta_z}{J}G_\nu.$$

Here, U, V, and W are referred to as contravariant velocities in the ξ, η, and ζ directions, respectively.

$$U = \xi_x u + \xi_y v + \xi_z w \quad , \quad V = \eta_x u + \eta_y v + \eta_z w \quad , \quad W = \zeta_x u + \zeta_y v + \zeta_z w \tag{2.43}$$

2.2 Spatial discretization of three-dimensional simulation

2.2.1 Compact finite difference scheme

Lele (1992) proposed a high-order central difference discretization method with a spectral-like resolution, called as the compact finite difference scheme. Gaitonde & Visbal (2000) and Visbal & Rizzetta (2002) applied it to a curvilinear coordinate system. Many previous studies have applied this method to obtain high-accuracy and high-resolution results (e.g., transitional flow (Sayadi & Moin, 2012; Cadieux *et al.*, 2014), flow control problem (Rizzetta *et al.*, 2008; Aono *et al.*, 2015; Sato *et al.*, 2015; Yakeno *et al.*, 2015), shock wave and turbulent boundary layer interaction (Loginov *et al.*, 2006; Morgan *et al.*, 2013), flow around an airfoil (Kawai & Fujii, 2005; Shan *et al.*, 2005; Matsuura & Kato, 2007; Visbal, 2009; Almutairi *et al.*, 2010; Garmann & Visbal, 2015), and analysis of noise sources in turbulent jets (Uzun *et al.*, 2004; Bodony & Lele, 2005; Freund & Colonius, 2009)). Let us consider a scalar quantity (e.g., metric, flux component, or flow variable) and its first derivative denoted by f_i and f'_i, respectively. The compact finite difference scheme defines f'_i as follows:

$$\begin{aligned}\beta_c f'_{i-2} + \alpha_c f'_{i-1} + f'_i + \alpha_c f'_{i+1} + \beta_c f'_{i+2} \\ = c_c \frac{f_{i+3} - f_{i-3}}{6\Delta h} + b_c \frac{f_{i+2} - f_{i-2}}{4\Delta h} + a_c \frac{f_{i+1} - f_{i-1}}{2\Delta h},\end{aligned} \tag{2.44}$$

where Δh indicates a step size of the discretization. The relation between the coefficient α_c, β_c, and a_c, b_c, c_c are obtained by employing the Taylor series expansion as follows:

$$a_c + b_c + c_c = 1 + 2\alpha_c + 2\beta_c \quad (2^{\text{nd}} \text{ order}), \tag{2.45}$$

$$a_c + 2^2 b_c + 3^2 c_c = 2\frac{3!}{2!}(\alpha_c + 2^2\beta_c) \quad (4^{\text{th}} \text{ order}), \tag{2.46}$$

$$a_c + 2^4 b_c + 3^4 c_c = 2\frac{5!}{4!}(\alpha_c + 2^4\beta_c) \quad (6^{\text{th}} \text{ order}), \tag{2.47}$$

$$a_c + 2^6 b_c + 3^6 c_c = 2\frac{7!}{6!}(\alpha_c + 2^6\beta_c) \quad (8^{\text{th}} \text{ order}), \tag{2.48}$$

$$a_c + 2^8 b_c + 3^8 c_c = 2\frac{9!}{8!}(\alpha_c + 2^8\beta_c) \quad (10^{\text{th}} \text{ order}). \tag{2.49}$$

Here, $\beta_c = 0$ gives tri-diagonal schemes whereas $\beta_c \neq 0$ gives penta-diagonal schemes. In addition, if $c_c = 0$ is applied in order to reduce stencils in the RHS of Eq. (2.44), each

coefficient is given by a function of α_c as below:

$$\beta_c = 0 \quad , \quad a_c = \frac{2}{3}(\alpha_c + 2) \quad , \quad b_c = \frac{1}{3}(4\alpha_c - 1) \quad , \quad c_c = 0, \tag{2.50}$$

and Eq. (2.44) is rewritten as

$$\alpha_c(f'_{i+1} + f'_{i-1}) + f'_i = b_c \frac{f_{i+2} - f_{i-2}}{4\Delta h} + a_c \frac{f_{i+1} - f_{i-1}}{2\Delta h}. \tag{2.51}$$

Employing the Taylor series expansion to each term yields

$$\begin{aligned} &2\alpha_c \left(f_i^{(1)} + \frac{1}{2!}(\Delta h)^2 f_i^{(3)} + \frac{1}{4!}(\Delta h)^4 f_i^{(6)} + O\left((\Delta h)^7\right) \right) + f_i^{(1)} \\ &\quad = 2\frac{b_c}{4\Delta h} \left(2\Delta h f_i^{(1)} + \frac{2^3}{3!}(\Delta h)^3 f_i^{(3)} + \frac{2^5}{5!}(\Delta h)^5 f_i^{(5)} + O\left((\Delta h)^6\right) \right) \\ &\qquad + 2\frac{a_c}{2\Delta h} \left(\Delta h f_i^{(1)} + \frac{1}{3!}(\Delta h)^3 f_i^{(3)} + \frac{1}{5!}(\Delta h)^5 f_i^{(5)} + O\left((\Delta h)^6\right) \right). \end{aligned} \tag{2.52}$$

Using Eq. (2.50), the truncation error becomes $\frac{4}{5!}(3\alpha_c - 1)(\Delta h)^4 f_i^{(5)} + O\left((\Delta h)^7\right)$. If $\alpha_c = 1/3$, the fourth order error term vanishes and it leads to the sixth order accuracy. In other words, each coefficient of the sixth order accuracy compact finite difference scheme is acquired by

$$\alpha_c = \frac{1}{3} \quad , \quad \beta_c = 0 \quad , \quad a_c = \frac{14}{9} \quad , \quad b_c = \frac{1}{9} \quad , \quad c_c = 0. \tag{2.53}$$

Table 2.1 summarizes other coefficients of the compact finite difference scheme. Other truncation errors for the first derivative schemes are also provided in Lele (1992). In the actual calculation process, Eq. (2.51) is solved as follows. Let us denote the right hand side of Eq. (2.51) as RHS_i. Then, a matrix form of Eq. (2.51) is

$$\begin{bmatrix} & & & & & \\ \ddots & \ddots & \ddots & & & \\ & \alpha_c & 1 & \alpha_c & & \\ & & \ddots & \ddots & \ddots & \\ & & & & & \end{bmatrix} \begin{bmatrix} \vdots \\ f'_{i-1} \\ f'_i \\ f'_{i+1} \\ \vdots \end{bmatrix} = \begin{bmatrix} \vdots \\ RHS_{i-1} \\ RHS_i \\ RHS_{i+1} \\ \vdots \end{bmatrix}. \tag{2.54}$$

First, the RHS of Eq. (2.54) is computed at every grid point. Then, the tri-diagonal (or penta-diagonal) matrix in the LHS of Eq. (2.54) is inversed using lower-upper decomposition, and the matrix of the first derivatives f'_i is obtained.

One of characteristics of the compact finite difference scheme is that the derivative value f'_i at a certain grid point i is related to the derivative quantities $f'_{i\pm1}$ of adjacent grid points as well as $f_{i\pm1}$ and $f_{i\pm2}$. Thus, physical information of a certain grid point affects all of other differential values. Although the compact finite difference scheme is computationally expensive because it requires calculations of matrix inversion as mentioned above, one of main advantages is a simplicity of boundary condition treatment (Ekaterinaris, 2005). Also, this method can reduce dispersive and dissipative numerical errors associated with the spatial discretization.

Table 2.1: Coefficients of the compact finite difference scheme (Lele, 1992).

Accuracy	α_c	β_c	a_c	b_c	c_c
4^{th} order tri-diagonal	$\frac{1}{4}$	0	$\frac{3}{2}$	0	0
6^{th} order tri-diagonal	$\frac{1}{3}$	0	$\frac{14}{9}$	$\frac{1}{9}$	0
8^{th} order tri-diagonal	$\frac{3}{8}$	0	$\frac{25}{16}$	$\frac{1}{5}$	$-\frac{1}{80}$
8^{th} order penta-diagonal	$\frac{4}{9}$	$\frac{1}{36}$	$\frac{40}{27}$	$\frac{25}{54}$	0
10^{th} order penta-diagonal	$\frac{1}{2}$	$\frac{1}{20}$	$\frac{17}{12}$	$\frac{101}{150}$	$\frac{1}{100}$

Boundary Treatment The basic formulation of the compact finite difference scheme, as described in Eq. (2.44), requires three stencils in the left hand side and five stencils in right hand side to evaluate the first derivative values in the sixth order accuracy case. Thus, this method obviously cannot be applied near the boundary such as $i = 1, 2, i_{\max} - 1, i_{\max}$. In order to solve this problem, explicit and implicit methods have been proposed for treatments of the boundary condition. In case of using the implicit method (Gaitonde & Visbal, 2000), the first derivative values near the boundary are obtained as follows:

$$f'_1 + \alpha_{12} f'_2 = \sum_{i=1}^{N} a_{c,i} f_i \ , \tag{2.55}$$

$$\alpha_{21} f'_1 + f'_2 + \alpha_{23} f'_3 = \sum_{i=1}^{N} b_{c,i} f_i \ , \tag{2.56}$$

where N represents number of grid points. Each coefficient is determined as follows:

$$\alpha_{12} = 3\ ,\ a_{c,1} = -\frac{17}{6}\ ,\ a_{c,2} = \frac{3}{2}\ ,\ a_{c,3} = \frac{3}{2}\ ,\ a_{c,4} = -\frac{1}{6}\ ,$$
$$\alpha_{21} = \frac{1}{6}\ ,\ \alpha_{23} = \frac{1}{2}\ ,\ b_{c,1} = -\frac{5}{9}\ ,\ b_{c,2} = -\frac{1}{2}\ ,\ b_{c,3} = 1\ ,\ b_{c,4} = -\frac{1}{18}\ . \tag{2.57}$$

In case of using the explicit method (e.g., Koutsavdis *et al.*, 1999), the first derivative values near the boundary are obtained as follows:

$$\begin{aligned}
2^{nd}\text{ order}\ :\ & f'_1 = \frac{1}{2}(-3f_1 + 4f_2 - f_3), \\
& f'_2 = \frac{1}{12}(f_3 - f_1), \\
& f'_{\max} = \frac{1}{2}(3f_{\max} - 4f_{\max-1} + f_{\max-2}), \\
& f'_{\max-1} = \frac{1}{12}(-f_{\max-2} + f_{\max}),
\end{aligned} \tag{2.58}$$

$$\begin{aligned}
4^{th}\text{ order}\ :\ & f'_1 = \frac{1}{12}(-25f_1 + 48f_2 - 36f_3 + 16f_4 - 3f_5), \\
& f'_2 = \frac{1}{12}(-3f_1 - 10f_2 + 18f_3 - 6f_4 + f_5), \\
& f'_{\max} = \frac{1}{12}(25f_{\max} - 48f_{\max-1} + 36f_{\max-2} - 16f_{\max-3} + 3f_{\max-4}), \\
& f'_{\max-1} = \frac{1}{12}(3f_{\max} + 10f_{\max-1} - 18f_{\max-2} + 6f_{\max-3} - f_{\max-4}).
\end{aligned} \tag{2.59}$$

2.2.2 Low-pass tri-diagonal filtering

Visbal & Rizzetta (2002) noted that the compact difference discretization is nondissipative and susceptible to numerical instabilities due to the unrestricted growth of a high-frequency mode. Thus, a high-order implicit low-pass spatial filtering scheme (Visbal & Gaitonde, 1999) is usually adopted for practical applications. This filtering approach has an effect of providing dissipation at the high frequency only and suppressing the numerical oscillations. Let us describe an original physical quantity as f and a filtered quantity as $\acute{f}$. Then, $\acute{f}$ is obtained as follows:

$$\alpha_f \acute{f}_{i-1} + \acute{f}_i + \alpha_f \acute{f}_{i+1} = \sum_{n=0}^{N} \frac{a_n}{2}(f_{i+n} + f_{i-n}), \tag{2.60}$$

where N represents number of grid points. Equation (2.60) is based on templates proposed by Alpert (1981) and Lele (1992), and it provides the $2N^{th}$ order formula on $2N+1$

Table 2.2: Coefficients a_n for filter formula at interior points (Gaitonde & Visbal, 2000)

Accuracy	a_0	a_1	a_2	a_3	a_4	a_5
2^{nd} order	$\frac{1+2\alpha_f}{2}$	$\frac{1+2\alpha_f}{2}$	0	0	0	0
4^{th} order	$\frac{5+6\alpha_f}{8}$	$\frac{1+2\alpha_f}{2}$	$\frac{-1+2\alpha_f}{8}$	0	0	0
6^{th} order	$\frac{11+10\alpha_f}{16}$	$\frac{15+34\alpha_f}{32}$	$\frac{-3+6\alpha_f}{16}$	$\frac{1-2\alpha_f}{32}$	0	0
8^{th} order	$\frac{93+70\alpha_f}{128}$	$\frac{7+18\alpha_f}{16}$	$\frac{-7+14\alpha_f}{32}$	$\frac{1-2\alpha_f}{16}$	$\frac{-1+2\alpha_f}{128}$	0
10^{th} order	$\frac{193+126\alpha_f}{256}$	$\frac{105+302\alpha_f}{256}$	$\frac{15(-1+2\alpha_f)}{64}$	$\frac{45(1-2\alpha_f)}{512}$	$\frac{5(-1+2\alpha_f)}{256}$	$\frac{1-2\alpha_f}{512}$

points. For example, the tenth order accuracy is achieved by $N = 5$. The filtering is employed to each ξ, η, and ζ direction, respectively. Table 2.2 shows the coefficients a_n given by a function of α_f. A parameter α_f is called as a filtering coefficient which has a range of $-0.5 < \alpha_f \leq 0.5$. In this range, a higher α_f provides less dissipative effect. The filtering has no effect by setting $\alpha_f = 0.5$ whereas it will no longer be necessary to calculate the inversion of tri-diagonal matrix at $\alpha_f = 0$. The accuracy of filter decides the frequency from which an effect of decay appears and the high-order accuracy filtering delays the beginning of decay frequency.

Boundary Treatment Equation (2.60) cannot be applied to near the boundary because enough number of stencils cannot be secured. Gaitonde & Visbal (2000) suggested a filter formula for near boundary point i. For example, the variables near the boundary are obtained by following equations (in case of the tenth order).

$$\alpha_f \acute{f}_{i-1} + \acute{f}_i + \alpha_f \acute{f}_{i+1} = \sum_{n=1}^{11} a_{n,i} f_n \ , \ i \in \{2, \cdots, 5\}, \tag{2.61}$$

$$\alpha_f \acute{f}_{i-1} + \acute{f}_i + \alpha_f \acute{f}_{i+1} = \sum_{n=0}^{10} a_{\max-n,i} f_{\max-n} \ , \ i \in \{i_{\max}-4, \cdots, i_{\max}-1\}. \tag{2.62}$$

The filtering treatment is not adopted to the first point $i = 1$ and the last point $i = i_{\max}$ at the boundary because the value of those points is given by the boundary condition. The tri-diagonal matrix conformation can be retained near the boundary by using Eq. (2.61). The coefficients $a_{n,i}$ of the sixth and tenth order filtering are listed in Tabs 2.3 and 2.4.

Table 2.3: Coefficients $a_{n,i}$ of the sixth order tri-diagonal filtering (Gaitonde & Visbal, 2000).

i	$a_{1,i}$	$a_{2,i}$	$a_{3,i}$	$a_{4,i}$	$a_{5,i}$	$a_{6,i}$	$a_{7,i}$
2	$\frac{1+62\alpha_f}{64}$	$\frac{29+6\alpha_f}{32}$	$\frac{15+34\alpha_f}{64}$	$\frac{-5+10\alpha_f}{16}$	$\frac{15-30\alpha_f}{64}$	$\frac{-3+6\alpha_f}{32}$	$\frac{1-2\alpha_f}{64}$
3	$\frac{-1+2\alpha_f}{64}$	$\frac{3+26\alpha_f}{32}$	$\frac{49+30\alpha_f}{64}$	$\frac{5+6\alpha_f}{16}$	$\frac{-15+30\alpha_f}{64}$	$\frac{3-6\alpha_f}{32}$	$\frac{-1+2\alpha_f}{64}$

Table 2.4: Coefficients $a_{n,i}$ of the tenth order tri-diagonal filtering (Gaitonde & Visbal, 2000).

i	$a_{1,i}$	$a_{2,i}$	$a_{3,i}$	$a_{4,i}$	$a_{5,i}$	$a_{6,i}$	$a_{7,i}$	$a_{8,i}$	$a_{9,i}$	$a_{10,i}$	$a_{11,i}$
2	$\frac{1+1022\alpha_f}{1024}$	$\frac{507+10\alpha_f}{512}$	$\frac{45+934\alpha_f}{1024}$	$\frac{-15+30\alpha_f}{128}$	$\frac{105-210\alpha_f}{512}$	$\frac{-63+126\alpha_f}{256}$	$\frac{105-210\alpha_f}{512}$	$\frac{-15+30\alpha_f}{128}$	$\frac{45-90\alpha_f}{1024}$	$\frac{-5+10\alpha_f}{512}$	$\frac{1-2\alpha_f}{1024}$
3	$\frac{-1+2\alpha_f}{1024}$	$\frac{5+502\alpha_f}{512}$	$\frac{979+90\alpha_f}{1024}$	$\frac{15+98\alpha_f}{128}$	$\frac{-105+210\alpha_f}{512}$	$\frac{63-126\alpha_f}{256}$	$\frac{-105+210\alpha_f}{512}$	$\frac{15-30\alpha_f}{128}$	$\frac{-45+90\alpha_f}{1024}$	$\frac{5-10\alpha_f}{512}$	$\frac{-1+2\alpha_f}{1024}$
4	$\frac{1-2\alpha_f}{1024}$	$\frac{-5+10\alpha_f}{512}$	$\frac{45+930\alpha_f}{1024}$	$\frac{113-30\alpha_f}{128}$	$\frac{105+302\alpha_f}{512}$	$\frac{-63+126\alpha_f}{256}$	$\frac{105-210\alpha_f}{512}$	$\frac{-15+30\alpha_f}{128}$	$\frac{45-90\alpha_f}{1024}$	$\frac{-5+10\alpha_f}{512}$	$\frac{1-2\alpha_f}{1024}$
5	$\frac{-1+2\alpha_f}{1024}$	$\frac{5-10\alpha_f}{512}$	$\frac{-45+90\alpha_f}{1024}$	$\frac{15+98\alpha_f}{128}$	$\frac{407+210\alpha_f}{512}$	$\frac{63+130\alpha_f}{256}$	$\frac{-105+210\alpha_f}{512}$	$\frac{15-30\alpha_f}{128}$	$\frac{-45+90\alpha_f}{1024}$	$\frac{5-10\alpha_f}{512}$	$\frac{-1+2\alpha_f}{1024}$

2.2.3 Metrics and Jacobian evaluation

Deng *et al.* (2011) discussed a detailed analysis of the geometric conservation law (GCL) for finite difference schemes. From Eq. (2.27), the coordinate transformation metrics are

$$\hat{\xi}_x = \frac{\xi_x}{J} = y_\eta z_\zeta - y_\zeta z_\eta \quad , \quad \hat{\eta}_x = \frac{\eta_x}{J} = y_\zeta z_\xi - y_\xi z_\zeta \quad , \quad \hat{\zeta}_x = \frac{\zeta_x}{J} = y_\xi z_\eta - y_\eta z_\xi \ , \tag{2.63}$$

$$\hat{\xi}_y = \frac{\xi_y}{J} = z_\eta x_\zeta - z_\zeta x_\eta \quad , \quad \hat{\eta}_y = \frac{\eta_y}{J} = z_\zeta x_\xi - z_\xi x_\zeta \quad , \quad \hat{\zeta}_y = \frac{\zeta_y}{J} = z_\xi x_\eta - z_\eta x_\xi \ , \tag{2.64}$$

$$\hat{\xi}_z = \frac{\xi_z}{J} = x_\eta y_\zeta - x_\zeta y_\eta \quad , \quad \hat{\eta}_z = \frac{\eta_z}{J} = x_\zeta y_\xi - x_\xi y_\zeta \quad , \quad \hat{\zeta}_z = \frac{\zeta_z}{J} = x_\xi y_\eta - x_\eta y_\xi \ . \tag{2.65}$$

These equations are conventional forms of the metrics, so-called nonconservative metrics. As already noted in Sec. 2.1.3, the metrics should satisfy the GCL relations as described in Eqs. (2.37)-(2.40). Let us consider a case of solving the equations numerically. By introducing a derivative operator for the spatial derivative as φ_1, Eqs. (2.38)-(2.40) are written as,

$$\mathcal{I}_x^{num} = \varphi_1^\xi\left(\hat{\xi}_x^{num}\right) + \varphi_1^\eta\left(\hat{\eta}_x^{num}\right) + \varphi_1^\zeta\left(\hat{\zeta}_x^{num}\right) = 0 \ , \tag{2.66}$$

$$\mathcal{I}_y^{num} = \varphi_1^\xi\left(\hat{\xi}_y^{num}\right) + \varphi_1^\eta\left(\hat{\eta}_y^{num}\right) + \varphi_1^\zeta\left(\hat{\zeta}_y^{num}\right) = 0 \ , \tag{2.67}$$

$$\mathcal{I}_z^{num} = \varphi_1^\xi\left(\hat{\xi}_z^{num}\right) + \varphi_1^\eta\left(\hat{\eta}_z^{num}\right) + \varphi_1^\zeta\left(\hat{\zeta}_z^{num}\right) = 0 \ , \tag{2.68}$$

where the superscript ^{num} denotes a numerically obtained derivative quantity. If a different derivative operator denoted by φ_2 is applied to the metrics, Eqs. (2.63)-(2.65) are

$$\begin{cases} \hat{\xi}_x^{num} = (\varphi_2^\eta y)(\varphi_2^\zeta z) - (\varphi_2^\zeta y)(\varphi_2^\eta z) \ , \\ \hat{\eta}_x^{num} = (\varphi_2^\zeta y)(\varphi_2^\xi z) - (\varphi_2^\xi y)(\varphi_2^\zeta z) \ , \\ \hat{\zeta}_x^{num} = (\varphi_2^\xi y)(\varphi_2^\eta z) - (\varphi_2^\eta y)(\varphi_2^\xi z) \ , \end{cases} \tag{2.69}$$

$$\begin{cases} \hat{\xi}_y^{num} = (\varphi_2^\eta z)(\varphi_2^\zeta x) - (\varphi_2^\zeta z)(\varphi_2^\eta x) \ , \\ \hat{\eta}_y^{num} = (\varphi_2^\zeta z)(\varphi_2^\xi x) - (\varphi_2^\xi z)(\varphi_2^\zeta x) \ , \\ \hat{\zeta}_y^{num} = (\varphi_2^\xi z)(\varphi_2^\eta x) - (\varphi_2^\eta z)(\varphi_2^\xi x) \ , \end{cases} \tag{2.70}$$

$$\begin{cases} \hat{\xi}_z^{num} = (\varphi_2^\eta x)(\varphi_2^\zeta y) - (\varphi_2^\zeta x)(\varphi_2^\eta y) \ , \\ \hat{\eta}_z^{num} = (\varphi_2^\zeta x)(\varphi_2^\xi y) - (\varphi_2^\xi x)(\varphi_2^\zeta y) \ , \\ \hat{\zeta}_z^{num} = (\varphi_2^\xi x)(\varphi_2^\eta y) - (\varphi_2^\eta x)(\varphi_2^\xi y) \ . \end{cases} \tag{2.71}$$

For example, by substituting Eq. (2.69) into Eq. (2.66), $\mathcal{I}_x^{num} = 0$ cannot be ensured. In other words, the use of different schemes for discretizing the metrics and Jacobian gen-

erally causes the freestream preservation error. In order to solve this problem, Thomas & Lombard (1979) proposed the following conservative metrics.

$$\hat{\xi}_x = (y_\eta z)_\zeta - (y_\zeta z)_\eta \quad , \quad \hat{\eta}_x = (y_\zeta z)_\xi - (y_\xi z)_\zeta \quad , \quad \hat{\zeta}_x = (y_\xi z)_\eta - (y_\eta z)_\xi \ , \tag{2.72}$$

$$\hat{\xi}_y = (z_\eta x)_\zeta - (z_\zeta x)_\eta \quad , \quad \hat{\eta}_y = (z_\zeta x)_\xi - (z_\xi x)_\zeta \quad , \quad \hat{\zeta}_y = (z_\xi x)_\eta - (z_\eta x)_\xi \ , \tag{2.73}$$

$$\hat{\xi}_z = (x_\eta y)_\zeta - (x_\zeta y)_\eta \quad , \quad \hat{\eta}_z = (x_\zeta y)_\xi - (x_\xi y)_\zeta \quad , \quad \hat{\zeta}_z = (x_\xi y)_\eta - (x_\eta y)_\xi \ . \tag{2.74}$$

Then, for example, Eq. (2.66) is transformed as follows:

$$\begin{aligned}
\mathcal{I}_x^{num} &= \varphi_1^\xi \varphi_2^\zeta((\varphi_3^\eta y)z) - \varphi_1^\xi \varphi_2^\eta((\varphi_3^\zeta y)z) \\
&+ \varphi_1^\eta \varphi_2^\xi((\varphi_3^\zeta y)z) - \varphi_1^\eta \varphi_2^\zeta((\varphi_3^\xi y)z) \\
&+ \varphi_1^\zeta \varphi_2^\eta((\varphi_3^\xi y)z) - \varphi_1^\zeta \varphi_2^\xi((\varphi_3^\eta y)z) \\
&= ((\varphi_3^\xi y)z)(\varphi_1^\zeta \varphi_2^\eta - \varphi_1^\eta \varphi_2^\zeta) \\
&+ ((\varphi_3^\eta y)z)(\varphi_1^\xi \varphi_2^\zeta - \varphi_1^\zeta \varphi_2^\xi) \\
&+ ((\varphi_3^\zeta y)z)(\varphi_1^\eta \varphi_2^\xi - \varphi_1^\xi \varphi_2^\eta),
\end{aligned} \tag{2.75}$$

where the derivative operator φ_3 is introduced to calculate the first-level metric derivatives. Here, $\mathcal{I}_x^{num} = 0$ is satisfied when $\varphi_1^\xi \varphi_2^\zeta = \varphi_1^\zeta \varphi_2^\xi$, $\varphi_1^\xi \varphi_2^\eta = \varphi_1^\eta \varphi_2^\xi$, and $\varphi_1^\eta \varphi_2^\zeta = \varphi_1^\zeta \varphi_2^\eta$. For an arbitrary property $f_{j,k.l}$, each derivate operator can be expressed by

$$\varphi_1^\xi f_{j,k.l} = \sum_{p=M_1}^{N_1} a_p (f_{j+p+1,k,l} - f_{j+p,k,l}) \quad , \quad \varphi_1^\zeta f_{j,k.l} = \sum_{q=M_2}^{N_2} b_q (f_{j,k,l+q+1} - f_{j,k,l+q}) \ , \tag{2.76}$$

$$\varphi_2^\xi f_{j,k.l} = \sum_{p=M_3}^{N_3} c_p (f_{j+p+1,k,l} - f_{j+p,k,l}) \quad , \quad \varphi_2^\zeta f_{j,k.l} = \sum_{q=M_4}^{N_4} d_q (f_{j,k,l+q+1} - f_{j,k,l+q}) \ . \tag{2.77}$$

Thus, one of the cross-derivative terms $\varphi_1^\xi \varphi_2^\zeta$ is,

$$\begin{aligned}
\varphi_1^\xi \varphi_2^\zeta f_{j,k,l} &= \sum_{p=M_1}^{N_1} a_p \left[\varphi_2^\zeta f_{j+p+1,k,l} - \varphi_2^\zeta f_{j+p,k,l} \right] \\
&= \sum_{p=M_1}^{N_1} a_p \left[\sum_{q=M_4}^{N_4} d_q (f_{j+p+1,k,l+q+1} - f_{j+p+1,k,l+q}) - \sum_{q=M_4}^{N_4} d_q (f_{j+p,k,l+q+1} - f_{j+p,k,l+q}) \right] \\
&= \sum_{p=M_1}^{N_1} \sum_{q=M_4}^{N_4} \left[a_p d_q (f_{j+p+1,k,l+q+1} - f_{j+p+1,k,l+q} - f_{j+p,k,l+q+1} + f_{j+p,k,l+q}) \right],
\end{aligned} \tag{2.78}$$

and another one $\varphi_1^{\zeta}\varphi_2^{\xi}$ is,

$$\begin{aligned}
\varphi_1^{\zeta}\varphi_2^{\xi} f_{j,k,l} &= \sum_{q=M_2}^{N_2} b_q \left[\varphi_2^{\zeta} f_{j,k,l+q+1} - \varphi_2^{\zeta} f_{j,k,l+q}\right] \\
&= \sum_{q=M_2}^{N_2} b_q \left[\sum_{p=M_3}^{N_3} c_p (f_{j+p+1,k,l+q+1} - f_{j+p+1,k,l+q}) - \sum_{p=M_3}^{N_3} c_p (f_{j+p,k,l+q+1} - f_{j+p,k,l+q})\right] \\
&= \sum_{q=M_2}^{N_2} \sum_{p=M_3}^{N_3} \left[b_q c_p (f_{j+p+1,k,l+q+1} - f_{j+p+1,k,l+q} - f_{j+p,k,l+q+1} + f_{j+p,k,l+q})\right] . \qquad (2.79)
\end{aligned}$$

From the above equations, $\varphi_1^{\xi}\varphi_2^{\zeta} = \varphi_1^{\zeta}\varphi_2^{\xi}$ is satisfied when

$$\begin{aligned}
a_p = c_p \quad , \quad M_1 = M_3 \quad , \quad N_1 = N_3 \ , \\
b_q = d_q \quad , \quad M_2 = M_4 \quad , \quad N_2 = N_4 \ . \qquad (2.80)
\end{aligned}$$

It means that $\varphi_1^{\xi} = \varphi_2^{\xi}$ and $\varphi_1^{\zeta} = \varphi_2^{\zeta}$ must be satisfied. From the analysis above, the SCL identities (i.e., the GCL identities at a stationary grid) can be fulfilled by using the same finite-differential schemes for evaluating the metrics and the spatial derivatives, and by adopting the spatial metric forms based on Eqs. (2.72)-(2.74). Visbal & Gaitonde (2002) and Deng *et al.* (2011) confirmed that the analytical expression for spatial metric form proposed by Thomas & Lombard (1979) satisfies the discretized SCL identities in a linear high-order central-difference scheme. Abe *et al.* (2013) newly suggested the symmetric conservative metrics, which can preserve the freestream in an arbitrary linear high-order finite difference scheme as well as improving the robustness and accuracy of the computational on highly-skewed deforming grids. The metrics are written as follows:

$$\begin{cases}
\hat{\xi}_x = \{(y_\eta z - z_\eta y)_\zeta - (y_\zeta z - z_\zeta y)_\eta\}/2 \ , \\
\hat{\eta}_x = \{(y_\zeta z - z_\zeta y)_\xi - (y_\xi z - z_\xi y)_\zeta\}/2 \ , \\
\hat{\zeta}_x = \{(y_\xi z - z_\xi y)_\eta - (y_\eta z - z_\eta y)_\xi\}/2 \ ,
\end{cases} \qquad (2.81)$$

$$\begin{cases}
\hat{\xi}_y = \{(z_\eta x - x_\eta z)_\zeta - (z_\zeta x - x_\zeta z)_\eta\}/2 \ , \\
\hat{\eta}_y = \{(z_\zeta x - x_\zeta z)_\xi - (z_\xi x - x_\xi z)_\zeta\}/2 \ , \\
\hat{\zeta}_y = \{(z_\xi x - x_\xi z)_\eta - (z_\eta x - x_\eta z)_\xi\}/2 \ ,
\end{cases} \qquad (2.82)$$

$$\begin{cases}
\hat{\xi}_z = \{(x_\eta y - y_\eta x)_\zeta - (x_\zeta y - y_\zeta x)_\eta\}/2 \ , \\
\hat{\eta}_z = \{(x_\zeta y - y_\zeta x)_\xi - (x_\xi y - y_\xi x)_\zeta\}/2 \ , \\
\hat{\zeta}_z = \{(x_\xi y - y_\xi x)_\eta - (x_\eta y - y_\eta x)_\xi\}/2 \ .
\end{cases} \qquad (2.83)$$

2.3 Spatial discretization of two-dimensional simulation

2.3.1 Monotonic upstream-centered scheme for conservation law (MUSCL)

Monotonic upstream-centered scheme for conservation law (MUSCL) was proposed as one of high-order accurate, non-oscillate numerical method for a flow field including discontinuous surface of physical quantities such as shock waves. There are several methods to obtain high order accuracy by the reconstruction of spatial distribution of physical variables or numerical fluxes, such as essentially non-oscillatory (ENO, Harten *et al.*, 1987; Shu & Osher, 1988, 1989), weighted essentially non-oscillatory (WENO, Liu *et al.*, 1994; Jiang & Shu, 1996), or weighted compact nonlinear scheme (WCNS, Deng & Zhang, 2000; Zhang *et al.*, 2008; Nonomura & Fujii, 2009; Nonomura *et al.*, 2010), etc.. In the present thesis, the MUSCL scheme is only explained. The MUSCL sets a virtual cell interface, and physical quantities of the left and right sides (f^L, f^R) at the boundary $i \pm 1/2$ are evaluated by the extrapolation of physical quantities around the cell, such as f_{i-2}, f_{i-1}, f_i, or f_{i+1}. In other words, it approximates the distribution of physical quantities inside a virtual cell, and improves the accuracy by giving the physical quantities close to the actual value at the left and right side of the cell. First of all, by using the Taylor expansion, the distribution of a flow variable (e.g., density, velocity, or, total energy) inside a cell is provided as follows:

$$f(x) = f(x_i) + (x - x_i)f'(x_i) + \frac{1}{2}(x - x_i)^2 f''(x_i) + O\left((\Delta x)^3\right), \tag{2.84}$$

where $x_{i-1/2} \leq x \leq x_{i+1/2}$ and $\Delta x = x_{i+1/2} - x_{i-1/2}$. An averaged flow variable inside the cell f_i is obtained by

$$f_i = \frac{1}{\Delta x}\int_{x_{i-1/2}}^{x_{i+1/2}} f(x)dx = f(x_i) + \frac{(\Delta x)^2}{24}f''(x_i) + O\left((\Delta x)^4\right). \tag{2.85}$$

Similarly, the first and second derivative of f denoted by f' and f'' are given as follows:

$$f'(x) = f'(x_i) + (x - x_i)f'(x_i) + O\left((\Delta x)^2\right), \tag{2.86}$$

$$f''(x) = f''(x_i) + O\left((\Delta x)^2\right). \tag{2.87}$$

Thus, averaged variables of the first and second derivative denoted by f_i' and f_i'' are

$$f_i' = \frac{1}{\Delta x}\int_{x_{i-1/2}}^{x_{i+1/2}} f'(x)dx = f'(x_i) + O\left((\Delta x)^2\right), \tag{2.88}$$

$$f_i'' = \frac{1}{\Delta x}\int_{x_{i-1/2}}^{x_{i+1/2}} f''(x)dx = f''(x_i) + O\left((\Delta x)^2\right). \tag{2.89}$$

Therefore, Eq. (2.84) is rewritten as follows:

$$f(x) = f_i + (x - x_i)f_i' + \frac{1}{2}\left[(x - x_i)^2 - \frac{(\Delta x)^2}{12}\right] f_i'' + O\left((\Delta x)^3\right). \tag{2.90}$$

Here, let us introduce following central differences.

$$f_i' = \frac{f_{i+1} - f_{i-1}}{2\Delta x} + O\left((\Delta x)^2\right), \tag{2.91}$$

$$f_i'' = \frac{f_{i+1} - 2f_i + f_{i-1}}{(\Delta x)^2} + O\left((\Delta x)^2\right). \tag{2.92}$$

Furthermore, by employing a parameter $\varkappa$ which is for adjusting the second order accuracy term in the third term of the RHS of Eq. (2.90), the distribution of an arbitrary variable within the virtual cell is given as follows:

$$f(x) = f_i + (x - x_i)\frac{f_{i+1} - f_{i-1}}{2\Delta x} + \frac{\varkappa}{2}\left[(x - x_i)^2 - \frac{(\Delta x)^2}{12}\right]\frac{f_{i+1} - 2f_i + f_{i-1}}{(\Delta x)^2} + O\left((\Delta x)^3\right). \tag{2.93}$$

Then, the physical quantity on the left side of the cell interface is the value of the right boundary of the distribution above at a grid point i.

$$\begin{aligned} f_{i+1/2}^L &= f_i + \left(\frac{1}{2}\Delta x\right)\frac{f_{i+1} - f_{i-1}}{2\Delta x} + \frac{\varkappa}{2}\left(\frac{2}{12}(\Delta x)^2\right)\frac{f_{i+1} - 2f_i + f_{i-1}}{(\Delta x)^2} \\ &= f_i + \frac{1 - \varkappa}{4}(f_i - f_{i-1}) + \frac{1 + \varkappa}{4}(f_{i+1} - f_i). \end{aligned} \tag{2.94}$$

Similarly, the physical quantity on the right side of the cell interface is the value of the left boundary of the distribution above at a grid point $i + 1$.

$$\begin{aligned} f_{i+1/2}^R &= f_{i+1} + \left(-\frac{1}{2}\Delta x\right)\frac{f_{i+2} - f_i}{2\Delta x} + \frac{\varkappa}{2}\left(\frac{2}{12}(\Delta x)^2\right)\frac{f_{i+2} - 2f_{i+1} + f_i}{(\Delta x)^2} \\ &= f_{i+1} - \frac{1 - \varkappa}{4}(f_{i+2} - f_{i+1}) - \frac{1 + \varkappa}{4}(f_{i+1} - f_i). \end{aligned} \tag{2.95}$$

When $\varkappa = 1/3$, physical quantities of the left side of the virtual boundary cell is

$$f^L_{i+1/2} = f_i + \frac{f_{i+1} - f_i}{3} + \frac{f_i - f_{i-1}}{6}, \tag{2.96}$$

and the accuracy of spatial difference on the grid point i is

$$\begin{aligned}
\left(\frac{\partial f}{\partial x}\right)_i &\simeq \frac{f^L_{i+1/2} - f^L_{i-1/2}}{\Delta x} \\
&= \frac{1}{\Delta x}\left[(f_i - f_{i-1}) + \frac{(f_{i+1} - f_i) - (f_i - f_{i-1})}{3} + \frac{(f_i - f_{i-1}) - (f_{i-1} - f_{i-2})}{6}\right] \\
&= \frac{1}{\Delta x}\frac{2(f_{i+1} - f_i) + 5(f_i - f_{i-1}) - (f_{i-1} - f_{i-2})}{6} \\
&= \frac{1}{\Delta x}\frac{2}{6}\left[f_i + \left(\frac{\partial f}{\partial x}\right)_i \Delta x + \frac{1}{2}\left(\frac{\partial^2 f}{\partial x^2}\right)_i (\Delta x)^2 + O((\Delta x)^3) - f_i\right] \\
&+ \frac{1}{\Delta x}\frac{5}{6}\left[f_i - f_i + \left(\frac{\partial f}{\partial x}\right)_i \Delta x - \frac{1}{2}\left(\frac{\partial^2 f}{\partial x^2}\right)_i (\Delta x)^2 + O((\Delta x)^3)\right] \\
&- \frac{1}{\Delta x}\frac{1}{6}\left[f_i - \left(\frac{\partial f}{\partial x}\right)_i \Delta x + \frac{1}{2}\left(\frac{\partial^2 f}{\partial x^2}\right)_i (\Delta x)^2 + O((\Delta x)^3)\right] \\
&+ \frac{1}{\Delta x}\frac{1}{6}\left[f_i - 2\left(\frac{\partial f}{\partial x}\right)_i \Delta x + \frac{4}{2}\left(\frac{\partial^2 f}{\partial x^2}\right)_i (\Delta x)^2 + O((\Delta x)^3)\right] \\
&= \left(\frac{\partial f}{\partial x}\right)_i + O((\Delta x)^3).
\end{aligned} \tag{2.97}$$

It means that the value of i is obtained by those of $i-2, i-1, i$, and $i+1$ and the third order accuracy is acquired. This case is not a complete upwind scheme, but the quantities from the upwind side are mainly taken; thus, this scheme is called the third order upwind biased scheme. The variation of the numerical accuracy depending on $\varkappa$ is summarized in Tab. 2.5. As a methodology in order to avoid the numerical instability and satisfy the total variation diminishing (TVD) condition, Van Albada *et al.* (1982) proposed a limiter function which suppresses numerical oscillation by switching the first order accuracy at a discontinuous surface whereas maintains higher order accuracy in a continuous flow. The Van Albada's limiter s is written as follows:

$$s = \frac{2\Delta_+\Delta_- + \epsilon}{\Delta_+^2 + \Delta_-^2 + \epsilon}, \tag{2.98}$$

where, ϵ is taken to be sufficiently small value in order to prevent division by zero. In that case, Eqs. (2.94) and (2.95) are given by

$$f^L_{i+1/2} = f_i + \frac{s}{4}[(1-\varkappa s)\Delta_- + (1+\varkappa s)\Delta_+]_i, \tag{2.99}$$

$$f^R_{i+1/2} = f_{i+1} - \frac{s}{4}[(1-\varkappa s)\Delta_+ + (1+\varkappa s)\Delta_-]_{i+1}, \tag{2.100}$$

where $\Delta_- = f_i - f_{i-1}$, and $\Delta_+ = f_{i+1} - f_i$.

Table 2.5: Variation of the numerical accuracy depending on $\varkappa$ of the MUSCL.

$\varkappa$	Accuracy
0	2^{nd} order upwind-biased
1/3	3^{rd} order upwind-biased
1/2	1^{st} order upwind
1	2^{nd} order fully upwind

2.3.2 Simple high-resolution upwind scheme (SHUS)

After calculating the physical properties at both side of the cell interface (e.g., $Q^L_{i+1/2}$ and $Q^R_{i+1/2}$) by MUSCL, it is necessary to evaluate the numerical flux of the convection term. For example, a derivative form of convection term in ξ direction is expressed by following numerical flux:

$$\left(\frac{\partial E}{\partial \xi}\right)_i = \frac{E_{i+1/2} - E_{i-1/2}}{\Delta\xi} \tag{2.101}$$

As a representation method of the numerical flux $E_{i+1/2}$, flux difference splitting (FDS, Roe, 1981; Osher & Solomon, 1982) and flux vector splitting (FVS, Steger & Warming, 1981; Van Leer, 1982) have been widely used in the simulation of aerodynamic fields. According to Morinishi & Koga (2014), the numerical flux with FDS is given by

$$E^{\mathrm{FDS}}_{i+1/2} \simeq \frac{E^R_{i+1/2} + E^L_{i+1/2}}{2} - |A|_{i+1/2}\frac{Q^R_{i+1/2} - Q^L_{i+1/2}}{2}, \tag{2.102}$$

where $A = \partial E/\partial Q$ is Jacobian matrix of the flux. On the other hand, that with FVS is

$$E^{\mathrm{FVS}}_{i+1/2} \simeq \frac{A^R_{i+1/2} - |A|^R_{i+1/2}}{2}Q^R_{i+1/2} + \frac{A^L_{i+1/2} - |A|^L_{i+1/2}}{2}Q^L_{i+1/2}. \tag{2.103}$$

The different point between both of the methods is that the FDS solves local Riemann problem and try to get an exact numerical flux at a cell interface whereas the FVS splits the flux according to the sign of its eigenvalues. Note that the FVS is a more efficient method than the FDS in terms of the computational cost because a scalar calculation is performed in the FVS whereas a matrix calculation is conducted in the FDS (Kim *et al.*, 1998). There is another effort to provide less dissipate upwind schemes by simplifying the FVS. Liou & Steffen (1993) proposed the advection upstream splitting method (AUSM). There are several AUSM family schemes, such as CUSP (convective upstream split pressure, Jameson, 1995*a*,*b*), AUSM$^+$ (Liou, 1996), AUSMDV (AUSM with flux difference splitting and flux vector splitting, Wada & Liou, 1997), AUSMPW (AUSM by pressure based weight functions, Kim *et al.*, 1998), AUSMPW$^+$ (Kim *et al.*, 2001), AUSM$^+$-up (Liou, 2006), SHUS (simple high-resolution upwind scheme, Shima & Jounouchi, 1997), SLAU (simple low-dissipation AUSM, Shima & Kitamura, 2011), SLAU2 (Kitamura & Shima, 2013), and HR-SLAU, HR-SLAU2, HR-AUSM$^+$-up (Kitamura & Hashimoto, 2016). The AUSM family schemes are first developed for typical compressible aerodynamic flows, but they have been employed to solve flows from low-Mach number to hypersonic aerodynamics. These schemes are based on the idea that the inviscid fluxes are divided into two components: the convective flux (flow speed, linear field) and the pressure flux (acoustic speed, nonlinear field). More concretely, the numerical flux of AUSM-familiy is described as below:

$$E_{i+1/2}^{\mathrm{AUSM}} = \frac{\mathcal{M} + |\mathcal{M}|}{2}\Phi^L + \frac{\mathcal{M} - |\mathcal{M}|}{2}\Phi^R + \mathcal{P}D_\xi, \tag{2.104}$$

where $\Phi = [1, u, v, w, h]^T$; $D_\xi = [0, \xi_x/J, \xi_y/J, \xi_z/J, 0]^T$; and h is the total enthalpy ($h = (e + p)/\rho$). In addition, $\mathcal{M}$ and $\mathcal{P}$ correspond to the mass flux and the pressure flux, respectively. Many of the AUSM-family schemes apply the following pressure flux:

$$\mathcal{P} = \Upsilon^L p^L + \Upsilon^R p^R, \tag{2.105}$$

where Υ is a parameter determined as follows:

$$\Upsilon^L = \begin{cases} \dfrac{1}{4}\left(2 - M^L\right)\left(M^L + 1\right)^2 & , \text{ if } |M^L| \le 1 \\ \dfrac{1}{2}\dfrac{M^L + |M^L|}{|M^L|} & , \text{ otherwise} \end{cases}, \tag{2.106}$$

$$\Upsilon^R = \begin{cases} \dfrac{1}{4}\left(2 + M^R\right)\left(M^R - 1\right)^2 & , \text{ if } |M^R| \le 1 \\ \dfrac{1}{2}\dfrac{M^R - |M^R|}{|M^R|} & \text{ohterwise} \end{cases}, \tag{2.107}$$

where M is the mach number. The differences among the AUSM type schemes comes from the expression of the mass flux. Many AUSM-type schemes calculate the mass flux based on the concept of FVS, but the SHUS assesses it using the concept of FDS. The mass flux of SHUS in ξ direction is given as follows:

$$\begin{aligned}\mathcal{M} &= \frac{1}{2}\left\{(\rho U)^L + (\rho U)^R\right\} - \frac{1}{2}|\overline{U}|\Delta\rho \\ &- \frac{|\overline{M}+1| - |\overline{M}-1|}{4}\overline{\rho}\Delta U - \frac{|\overline{M}+1| + |\overline{M}-1| - 2|\overline{M}|}{4}\frac{\Delta p}{\overline{a}},\end{aligned} \tag{2.108}$$

where,

$$\Delta f = f^R - f^L \quad , \quad \overline{f} = \frac{f^L + f^R}{2} \quad , \quad \overline{a} = \sqrt{\gamma\frac{\overline{p}}{\overline{\rho}}} \quad , \quad \overline{M} = \frac{\overline{U}}{\overline{a}}. \tag{2.109}$$

Each term in RHS of Eq. (2.108) represent the average of the left and right states, density difference, velocity difference, and pressure difference term (Shima & Kitamura, 2011). The numerical fluxes in other two direction can also be obtained by a similar manner. By defining the mass flux such as this, the pressure difference generates the mass flux and it can be avoided an over shot phenomenon on a discontinuous surface.

2.3.3 Metrics and Jacobian evaluation

In general, a cell consists of a hexahedron with the unit length in the computational domain whereas it is distorted in the physical domain. Here, a vector perpendicular to the ξ plane $\mathcal{S}^\xi$ is written as $\mathcal{S}^\xi = \mathbf{r}_\eta \times \mathbf{r}_\zeta$, where $\mathbf{r}$ is a vector which is composed by (x, y, z) components. In a similar fashion, vectors perpendicular to the η and ζ plane are given by $\mathcal{S}^\eta = \mathbf{r}_\zeta \times \mathbf{r}_\xi$ and $\mathcal{S}^\zeta = \mathbf{r}_\xi \times \mathbf{r}_\eta$, respectively. Then, $\mathcal{S}^\xi$, $\mathcal{S}^\eta$, and $\mathcal{S}^\zeta$ are given by

$$\begin{aligned}\mathcal{S}^\xi &= (x_\eta, y_\eta, z_\eta) \times (x_\zeta, y_\zeta, z_\zeta) = (y_\eta z_\zeta - y_\zeta z_\eta \ , \ z_\eta x_\zeta - z_\zeta x_\eta \ , \ x_\eta y_\zeta - x_\zeta y_\eta), \\ \mathcal{S}^\eta &= (x_\zeta, y_\zeta, z_\zeta) \times (x_\xi, y_\xi, z_\xi) = (y_\zeta z_\xi - y_\xi z_\zeta \ , \ z_\zeta x_\xi - z_\xi x_\zeta \ , \ x_\zeta y_\xi - x_\xi y_\zeta), \\ \mathcal{S}^\zeta &= (x_\xi, y_\xi, z_\xi) \times (x_\eta, y_\eta, z_\eta) = (y_\xi z_\eta - y_\eta z_\xi \ , \ z_\xi x_\eta - z_\eta x_\xi \ , \ x_\xi y_\eta - x_\eta y_\xi).\end{aligned} \tag{2.110}$$

The equation above can be rewritten by using Eqs. (2.63)-(2.65),

$$\mathcal{S}^\xi = \frac{1}{J}(\xi_x \ , \ \xi_y \ , \ \xi_z) \ , \ \mathcal{S}^\eta = \frac{1}{J}(\eta_x \ , \ \eta_y \ , \ \eta_z) \ , \ \mathcal{S}^\zeta = \frac{1}{J}(\zeta_x \ , \ \zeta_y \ , \ \zeta_z). \tag{2.111}$$

Thus, transformation metrics are equal to components of the surface vector, and each component of the surface vector can be interpreted as the projected area of a cell surface

to each direction. Here, the concept of calculating the metrics is shown in Fig. 2.3. The metrics at an arbitrary grid point are calculated by taking the cross product of the diagonal elements of the cells surrounding the grid point and averaging it. As expressed mathematically,

$$\begin{aligned}(\xi_x\ ,\ \xi_y\ ,\ \xi_z) = J \cdot \mathcal{S}^{\xi}_{j,k,l} \ &= \ \frac{1}{4}\Bigg[\frac{1}{2}\left(\mathbf{r}_{j,k+1,l+1} - \mathbf{r}_{j,k,l}\right) \times \left(\mathbf{r}_{j,k+1,l} - \mathbf{r}_{j,k,l+1}\right) \\ &\quad + \frac{1}{2}\left(\mathbf{r}_{j,k,l+1} - \mathbf{r}_{j,k-1,l}\right) \times \left(\mathbf{r}_{j,k,l} - \mathbf{r}_{j,k-1,l+1}\right) \\ &\quad + \frac{1}{2}\left(\mathbf{r}_{j,k+1,l} - \mathbf{r}_{j,k,l-1}\right) \times \left(\mathbf{r}_{j,k+1,l-1} - \mathbf{r}_{j,k,l}\right) \\ &\quad + \frac{1}{2}\left(\mathbf{r}_{j,k,l} - \mathbf{r}_{j,k-1,l-1}\right) \times \left(\mathbf{r}_{j,k,l-1} - \mathbf{r}_{j,k-1,l}\right)\Bigg] \end{aligned} \tag{2.112}$$

The volume of a cell is calculated by

$$\begin{aligned}\mathcal{V} \ &= \ \mathbf{r}_\xi \cdot (\mathbf{r}_\eta \times \mathbf{r}_\zeta) \\ &= \ x_\xi(y_\eta z_\zeta - y_\zeta z_\eta) + y_\xi(x_\zeta z_\eta - z_\zeta x_\eta) + z_\xi(x_\eta y_\zeta - y_\eta z_\zeta) \\ &= \ x_\xi(y_\eta z_\zeta - y_\zeta z_\eta) + x_\eta(y_\zeta z_\xi - y_\xi z_\zeta) + x_\zeta(y_\xi z_\eta - y_\eta z_\xi) = \frac{1}{J}. \end{aligned} \tag{2.113}$$

From the results, the volume of a cell represents the reciprocal of transformation Jacobian. The transformation Jacobian has an another important meaning. Let us consider a small cell in the physical and computational domain. Three vectors denoted by $\mathcal{A}$, $\mathcal{B}$, and $\mathcal{C}$ which compose a small cell in the physical domain are written as follows:

$$\mathcal{A} = \begin{bmatrix} x(\xi + d\xi, \eta, \zeta) - x(\xi, \eta, \zeta) \\ y(\xi + d\xi, \eta, \zeta) - y(\xi, \eta, \zeta) \\ z(\xi + d\xi, \eta, \zeta) - z(\xi, \eta, \zeta) \end{bmatrix} = \begin{bmatrix} \frac{\partial x}{\partial \xi} d\xi \\ \frac{\partial y}{\partial \xi} d\xi \\ \frac{\partial z}{\partial \xi} d\xi \end{bmatrix} = \begin{bmatrix} x_\xi \\ y_\xi \\ z_\xi \end{bmatrix} d\xi, \tag{2.114}$$

$$\mathcal{B} = \begin{bmatrix} x(\xi, \eta + d\eta, \zeta) - x(\xi, \eta, \zeta) \\ y(\xi, \eta + d\eta, \zeta) - y(\xi, \eta, \zeta) \\ z(\xi, \eta + d\eta, \zeta) - z(\xi, \eta, \zeta) \end{bmatrix} = \begin{bmatrix} \frac{\partial x}{\partial \eta} d\eta \\ \frac{\partial y}{\partial \eta} d\eta \\ \frac{\partial z}{\partial \eta} d\eta \end{bmatrix} = \begin{bmatrix} x_\eta \\ y_\eta \\ z_\eta \end{bmatrix} d\eta, \tag{2.115}$$

$$\mathcal{C} = \begin{bmatrix} x(\xi, \eta, \zeta + d\zeta) - x(\xi, \eta, \zeta) \\ y(\xi, \eta, \zeta + d\zeta) - y(\xi, \eta, \zeta) \\ z(\xi, \eta, \zeta + d\zeta) - z(\xi, \eta, \zeta) \end{bmatrix} = \begin{bmatrix} \frac{\partial x}{\partial \zeta} d\zeta \\ \frac{\partial y}{\partial \zeta} d\zeta \\ \frac{\partial z}{\partial \zeta} d\zeta \end{bmatrix} = \begin{bmatrix} x_\zeta \\ y_\zeta \\ z_\zeta \end{bmatrix} d\zeta. \tag{2.116}$$

Then, the volume of a cell made by three vectors is

$$\begin{aligned}\mathcal{V}_{phy} &= \mathcal{A}\cdot(\mathcal{B}\times\mathcal{C}) = \begin{vmatrix} x_\xi & x_\eta & x_\zeta \\ y_\xi & y_\eta & y_\zeta \\ z_\xi & z_\eta & z_\zeta \end{vmatrix} d\xi d\eta d\zeta \\ &= (x_\xi(y_\eta z_\zeta - y_\zeta z_\eta) + x_\eta(y_\zeta z_\xi - y_\xi z_\zeta) + x_\zeta(y_\xi z_\eta - y_\eta z_\xi))d\xi d\eta d\zeta \\ &= \frac{\mathcal{V}_{com}}{J}, \end{aligned} \tag{2.117}$$

where $\mathcal{V}_{com} = d\xi d\eta d\zeta$, and Eq. (2.26) is used. Thus,

$$J = \frac{\text{(The volume of cell in the COMPUTATIONAL domain)}}{\text{(The volume of cell in the PHYSICAL domain)}}. \tag{2.118}$$

This means that the transformation Jacobian represents the ratio of the area/volume of a cell between the computational domain and physical domain in the two-/three-dimension space. Therefore, the transformation Jacobian is determined by a reciprocal of the cell volume, and the volume of a cell at a certain grid point is calculated by averaging the volume of the eight cells surrounding the grid point. As expressed mathematically,

$$\mathcal{V} = \frac{1}{J} = \frac{1}{8}\left(\mathcal{V}_{j,k,l} + \mathcal{V}_{j-1,k,l} + \mathcal{V}_{j-1,k-1,l} + \mathcal{V}_{j,k-1,l} + \mathcal{V}_{j,k,l-1} + \mathcal{V}_{j-1,k,l-1} + \mathcal{V}_{j-1,k-1,l-1} + \mathcal{V}_{j,k-1,l-1}\right) \tag{2.119}$$

$$\mathcal{V}_{j,k,l} = \frac{1}{3}\left(\mathcal{S}^{\xi}_{j,k,l} + \mathcal{S}^{\eta}_{j,k,l} + \mathcal{S}^{\zeta}_{j,k,l}\right)\cdot(\mathbf{r}_{j+1,k+1,l+1} - \mathbf{r}_{j,k,l})\,. \tag{2.120}$$

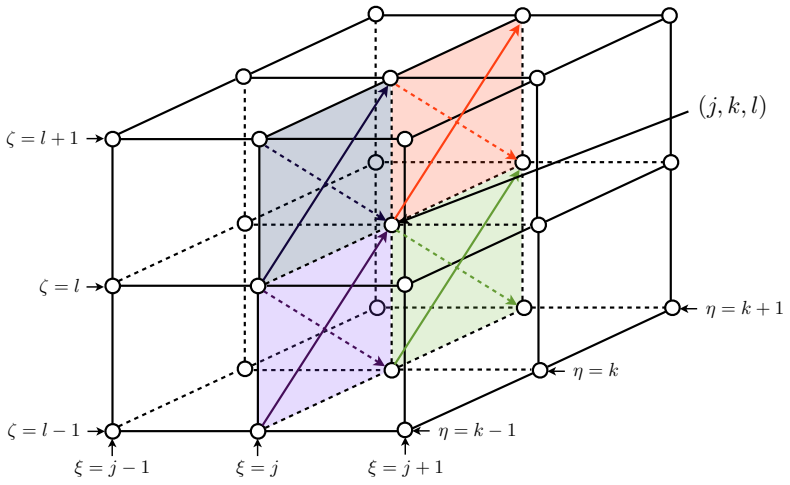

Figure 2.3: Evaluation of the metrics in ξ-direction at a grid point (j,k,l)

2.4 Time integration

2.4.1 ADI-SGS Implicit Method

If the viscous terms ($\partial\hat{E}_\nu, \partial\hat{F}_\nu$, and $\partial\hat{G}_\nu$ in Eq. (2.42)) are treated explicitly (Yee, 1987), then the governing equation is simply written as

$$\frac{\partial\hat{Q}}{\partial\tau} + \frac{\partial\hat{E}}{\partial\xi} + \frac{\partial\hat{F}}{\partial\eta} + \frac{\partial\hat{G}}{\partial\zeta} = 0. \tag{2.121}$$

The discretized form of the first order temporal accuracy is

$$\frac{\hat{Q}^{n+1}_{j,k,l} - \hat{Q}^{n}_{j,k,l}}{\Delta\tau} + \left[\vartheta\left(\frac{\partial\hat{E}}{\partial\xi}\right)^{n+1}_{j,k,l} + (1-\vartheta)\left(\frac{\partial\hat{E}}{\partial\xi}\right)^{n}_{j,k,l} + \vartheta\left(\frac{\partial\hat{F}}{\partial\eta}\right)^{n+1}_{j,k,l} + (1-\vartheta)\left(\frac{\partial\hat{F}}{\partial\eta}\right)^{n}_{j,k,l} + \vartheta\left(\frac{\partial\hat{G}}{\partial\zeta}\right)^{n+1}_{j,k,l} + (1-\vartheta)\left(\frac{\partial\hat{G}}{\partial\zeta}\right)^{n}_{j,k,l}\right] = 0, \tag{2.122}$$

where n is a current time step. The time integration method is determined by the way of setting ϑ.

$$\begin{cases} \vartheta = 0 & \text{First order Euler explicit scheme} \\ \vartheta = 1/2 & \text{Crank-Nicolson second order implicit scheme} \\ \vartheta = 1 & \text{First order Euler implicit scheme} \end{cases}$$

One of the typical explicit method for time integration is the Runge-Kutta method (Fyfe, 1966). According to the CFL condition reported by Courant-Friedrich-Lewy (Courant *et al.*, 1967), however, there is a restriction for the time step size $\Delta\tau$ when applying the explicit scheme. Especially, in respect to the the flow field for which viscous effects have to be considered, the restriction of the grid distribution near the boundary layer or wake becomes strict. In contrast, the implicit method has loose requirements for the time step and it is considered as a more feasible way than the explicit methods for simulations within a limited time. One of the implicit time integration method is the alternative direction implicit symmetric Gauss-Seidel (ADI-SGS, Fujii, 1998; Iizuka, 2006; Nishida & Nonomura, 2009) scheme. The ADI-SGS implicit time integration method, which is the same type of idea as four-factor symmetric Gauss-Seidel (FF-SGS, Fujii, 1999) scheme, uses both lower-upper symmetric alternating direction implicit (LU-ADI, Fujii & Obayashi, 1986; Obayashi *et al.*, 1986; Fujii & Obayashi, 1987) and lower-upper sym-

metric Gauss-Seidel (LU-SGS, Yoon & Jameson, 1988) schemes. This method is highly suitable for vector/paralled hybrid architectures because along a direction in being swept, other two directions which can be vectorlized/parallelized are free (for three-dimensional case). It also eliminates the need for inversion of block diagonal matrices which is seen in the LU-ADI scheme, and can achieve further reduction of calculation process compared to the LU-ADI scheme. In case of the first order Euler implicit scheme, Eq. (2.122) is written as

$$\frac{\hat{Q}^{n+1}_{j,k,l} - \hat{Q}^{n}_{j,k,l}}{\Delta\tau} + \left[\left(\frac{\partial \hat{E}}{\partial \xi} \right)^{n+1}_{j,k,l} + \left(\frac{\partial \hat{F}}{\partial \eta} \right)^{n+1}_{j,k,l} + \left(\frac{\partial \hat{G}}{\partial \zeta} \right)^{n+1}_{j,k,l} \right] = 0. \tag{2.123}$$

Beam & Warming (1978) proposed a linearization approach in time direction as below:

$$\hat{E}^{n+1}_{j,k,l} = \hat{E}^{n}_{j,k,l} + \left(\frac{\partial \hat{E}}{\partial \hat{Q}} \right)^{n}_{j,k,l} \left(\hat{Q}^{n+1}_{j,k,l} - \hat{Q}^{n}_{j,k,l} \right) + O((\Delta\tau)^2) \ , \tag{2.124}$$

$$\hat{F}^{n+1}_{j,k,l} = \hat{F}^{n}_{j,k,l} + \left(\frac{\partial \hat{F}}{\partial \hat{Q}} \right)^{n}_{j,k,l} \left(\hat{Q}^{n+1}_{j,k,l} - \hat{Q}^{n}_{j,k,l} \right) + O((\Delta\tau)^2) \ , \tag{2.125}$$

$$\hat{G}^{n+1}_{j,k,l} = \hat{G}^{n}_{j,k,l} + \left(\frac{\partial \hat{G}}{\partial \hat{Q}} \right)^{n}_{j,k,l} \left(\hat{Q}^{n+1}_{j,k,l} - \hat{Q}^{n}_{j,k,l} \right) + O((\Delta\tau)^2) \ . \tag{2.126}$$

Substituting Eqs. (2.124)-(2.126) into Eq. (2.123) yields

$$\Delta\hat{Q}^{n}_{j,k,l} = -\Delta\tau \left[\frac{\partial}{\partial \xi} \left(\hat{E} + \hat{A}\Delta\hat{Q} \right)^{n}_{j,k,l} + \frac{\partial}{\partial \eta} \left(\hat{F} + \hat{B}\Delta\hat{Q} \right)^{n}_{j,k,l} + \frac{\partial}{\partial \zeta} \left(\hat{G} + \hat{C}\Delta\hat{Q} \right)^{n}_{j,k,l} \right], \tag{2.127}$$

where $\Delta\hat{Q}^{n}_{j,k,l} = \hat{Q}^{n+1}_{j,k,l} - \hat{Q}^{n}_{j,k,l}$, and $\hat{A}$, $\hat{B}$, and $\hat{C}$ represent the flux Jacobian matrices expressed as follows:

$$\hat{A} = \frac{\partial \hat{E}}{\partial \hat{Q}} \ , \quad \hat{B} = \frac{\partial \hat{F}}{\partial \hat{Q}} \ , \quad \hat{C} = \frac{\partial \hat{G}}{\partial \hat{Q}} \ , \tag{2.128}$$

$$
\hat{A} \text{ or } \hat{B} \text{ or } \hat{C}
$$

$$
= \begin{bmatrix}
\psi_t & \psi_x & \psi_y & \psi_z & 0 \\
-u\varpi + \psi_x\phi^2 & \psi_t + \varpi - (\gamma-2)\psi_x u & \psi_y u - \psi_x(\gamma-1) & \psi_z u - \psi_x(\gamma-1) & \psi_x(\gamma-1) \\
-v\varpi + \psi_y\phi^2 & \psi_x v - \psi_y(\gamma-1) & \psi_t + \varpi - (\gamma-2)\psi_y v & \psi_z v - \psi_y(\gamma-1) & \psi_y(\gamma-1) \\
-w\varpi + \psi_z\phi^2 & \psi_x w - \psi_z(\gamma-1) & \psi_y w - \psi_z(\gamma-1) & \psi_t + \varpi - (\gamma-2)\psi_z w & \psi_z(\gamma-1) \\
-\varpi\left(\dfrac{\gamma e}{\rho} - 2\phi^2\right) & \psi_x\left(\dfrac{\gamma e}{\rho} - \phi^2\right) - (\gamma-1)u\varpi & \psi_y\left(\dfrac{\gamma e}{\rho} - \phi^2\right) - (\gamma-1)v\varpi & \psi_z\left(\dfrac{\gamma e}{\rho} - \phi^2\right) - (\gamma-1)w\varpi & \psi_t + \gamma\varpi
\end{bmatrix} ,
$$

$$
\varpi = \psi_x u + \psi_y v + \psi_z w \quad , \quad \phi^2 = \frac{(\gamma-1)}{2}(u^2+v^2+w^2) \ ,
$$

with $\psi = \xi$, η, and ζ for $\hat{A}$, $\hat{B}$, and $\hat{C}$, respectively. By transposing $\Delta\hat{Q}^n_{j,k,l}$ to the left side of Eq. (2.127), we obtain

$$
\begin{aligned}
\left(I + \Delta\tau\frac{\partial}{\partial\xi}\hat{A} + \Delta\tau\frac{\partial}{\partial\eta}\hat{B} + \Delta\tau\frac{\partial}{\partial\zeta}\hat{C}\right)^n_{j,k,l} \Delta\hat{Q}^n_{j,k,l} &= -\Delta\tau\left(\frac{\partial\hat{E}}{\partial\xi} + \frac{\partial\hat{F}}{\partial\eta} + \frac{\partial\hat{G}}{\partial\zeta}\right)^n_{j,k,l} \\
&\equiv (RHS)^n_{j,k,l} \ , \qquad (2.129)
\end{aligned}
$$

where I is the identity matrix. Here, the approximate ADI factorization (Beam & Warming, 1978) is adopted to the operator in the LHS of Eq. (2.129).

$$
I + \Delta\tau\frac{\partial}{\partial\xi}\hat{A} + \Delta\tau\frac{\partial}{\partial\eta}\hat{B} + \Delta\tau\frac{\partial}{\partial\zeta}\hat{C} \doteq \left[I + \Delta\tau\frac{\partial}{\partial\xi}\hat{A}\right]\left[I + \Delta\tau\frac{\partial}{\partial\eta}\hat{B}\right]\left[I + \Delta\tau\frac{\partial}{\partial\zeta}\hat{C}\right] \ . \qquad (2.130)
$$

Additionally, the approximate lower-diagonal-upper (LDU) factorization (Fujii & Obayashi, 1986) is applied to each term in the RHS of Eq. (2.130). The basic idea of the LDU factorization so-called diagonally dominate ADI (DD-ADI) schemes was proposed by Lombard *et al.* (1983), that is more stable than the simple lower-upper (LU) factorization (Jameson *et al.*, 1981). For instance, the first term in the RHS of Eq. (2.130) is written as below:

$$
\left[I + \Delta\tau\frac{\partial}{\partial\xi}\hat{A}\right] = L + D + U \approx [L+D]D^{-1}[D+U] \ , \qquad (2.131)
$$

where

$$L + D = I - \frac{\Delta\tau}{\Delta\xi}\hat{A}^{n-}_{j,k,l} + \Delta\tau\varphi^b_\xi \hat{A}^{n+}_{j,k,l} \ , \tag{2.132}$$

$$D = I + \frac{\Delta\tau}{\Delta\xi}\left(\hat{A}^{n+}_{j,k,l} - \hat{A}^{n-}_{j,k,l}\right) \ , \tag{2.133}$$

$$D + U = I + \frac{\Delta\tau}{\Delta\xi}\hat{A}^{n+}_{j,k,l} + \Delta\tau\varphi^f_\xi \hat{A}^{n-}_{j,k,l} \ . \tag{2.134}$$

The matrices denoted by L, D, and U are the left-lower triangle, diagonal, and right-upper triangle matrices, respectively. Furthermore, φ^b and φ^f indicate the first order backward and forward difference operators, respectively. For example, if the first order upwind difference is applied as the finite difference method, the operators are written by

$$\varphi^b_\xi \hat{A}^{n+}_{j,k,l} = \frac{\hat{A}^{n+}_{j,k,l} - \hat{A}^{n+}_{j-1,k,l}}{\Delta\xi} \ , \quad \varphi^f_\xi \hat{A}^{n-}_{j,k,l} = \frac{\hat{A}^{n-}_{j+1,k,l} - \hat{A}^{n-}_{j,k,l}}{\Delta\xi} \ , \tag{2.135}$$

$$\varphi^b_\eta \hat{B}^{n+}_{j,k,l} = \frac{\hat{B}^{n+}_{j,k,l} - \hat{B}^{n+}_{j,k-1,l}}{\Delta\eta} \ , \quad \varphi^f_\eta \hat{B}^{n-}_{j,k,l} = \frac{\hat{B}^{n-}_{j,k+1,l} - \hat{B}^{n-}_{j,k,l}}{\Delta\eta} \ , \tag{2.136}$$

$$\varphi^b_\zeta \hat{C}^{n+}_{j,k,l} = \frac{\hat{C}^{n+}_{j,k,l} - \hat{C}^{n+}_{j,k,l-1}}{\Delta\zeta} \ , \quad \varphi^f_\zeta \hat{C}^{n-}_{j,k,l} = \frac{\hat{C}^{n-}_{j,k,l+1} - \hat{C}^{n-}_{j,k,l}}{\Delta\zeta} \ . \tag{2.137}$$

As a consequence, Eq. (2.129) is rewritten as

$$\begin{aligned}
&\left[I - \frac{\Delta\tau}{\Delta\xi}\hat{A}^{n-}_{j,k,l} + \Delta\tau\varphi^b_\xi \hat{A}^{n+}_{j,k,l}\right]\left[I + \frac{\Delta\tau}{\Delta\xi}\left(\hat{A}^{n+}_{j,k,l} - \hat{A}^{n-}_{j,k,l}\right)\right]^{-1}\left[I + \frac{\Delta\tau}{\Delta\xi}\hat{A}^{n+}_{j,k,l} + \Delta\tau\varphi^f_\xi \hat{A}^{n-}_{j,k,l}\right] \\
&\left[I - \frac{\Delta\tau}{\Delta\eta}\hat{B}^{n-}_{j,k,l} + \Delta\tau\varphi^b_\eta \hat{B}^{n+}_{j,k,l}\right]\left[I + \frac{\Delta\tau}{\Delta\eta}\left(\hat{B}^{n+}_{j,k,l} - \hat{B}^{n-}_{j,k,l}\right)\right]^{-1}\left[I + \frac{\Delta\tau}{\Delta\eta}\hat{B}^{n+}_{j,k,l} + \Delta\tau\varphi^f_\eta \hat{B}^{n-}_{j,k,l}\right] \\
&\left[I - \frac{\Delta\tau}{\Delta\zeta}\hat{C}^{n-}_{j,k,l} + \Delta\tau\varphi^b_\zeta \hat{C}^{n+}_{j,k,l}\right]\left[I + \frac{\Delta\tau}{\Delta\zeta}\left(\hat{C}^{n+}_{j,k,l} - \hat{C}^{n-}_{j,k,l}\right)\right]^{-1}\left[I + \frac{\Delta\tau}{\Delta\zeta}\hat{C}^{n+}_{j,k,l} + \Delta\tau\varphi^f_\zeta \hat{C}^{n-}_{j,k,l}\right]\Delta\hat{Q}^n_{j,k,l} \\
&\quad = (RHS)^n_{j,k,l}
\end{aligned} \tag{2.138}$$

Although there are several methods to evaluate $A^\pm$,$B^\pm$, and $C^\pm$ (e.g., Steger-Warming FVS (Steger & Warming, 1981) or diagonal form (Pulliam & Chaussee, 1981) of LU-ADI), the idea of LU-SGS (Yoon & Jameson, 1988) written as follows is considered as a more suitable way for reducing the computational cost.

$$\hat{A}^\pm = \frac{1}{2}(\hat{A} \pm \sigma(\hat{A})I) \ , \quad \hat{B}^\pm = \frac{1}{2}(\hat{B} \pm \sigma(\hat{B})I) \ , \quad \hat{C}^\pm = \frac{1}{2}(\hat{C} \pm \sigma(\hat{C})I) \ , \tag{2.139}$$

where, $\sigma(\hat{A})$, $\sigma(\hat{B})$, and $\sigma(\hat{C})$) are maximum eigenvalues of the flux Jacobian matrices $\hat{A}$, $\hat{B}$, and $\hat{C}$, respectively, which is often referred to as the spectral radius. Each spectral

radius is obtained as follows:

$$\sigma(\hat{A}) = |U| + a\sqrt{\xi_x^2 + \xi_y^2 + \xi_z^2}\ , \tag{2.140}$$

$$\sigma(\hat{B}) = |V| + a\sqrt{\eta_x^2 + \eta_y^2 + \eta_z^2}\ , \tag{2.141}$$

$$\sigma(\hat{C}) = |W| + a\sqrt{\zeta_x^2 + \zeta_y^2 + \zeta_z^2}\ . \tag{2.142}$$

Because of the approximation of the split Jacobian matrices with those spectral radius, it is thought that the ADI-SGS scheme is more stable than the LU-ADI scheme. As a result, the solution of Eq. (2.138) is obtained by following procedures ($\Delta\xi = \Delta\eta = \Delta\zeta = 1$).

1. ξ-direction

   (a) Forward sweep $(j_{\min}+1 \longrightarrow j_{\max})$

$$(1 + \Delta\tau\sigma^n_{\xi j,k,l})\Delta\tilde{\tilde{Q}}^{n*}_{j,k,l} = (RHS)^n_{j,k,l} + \Delta\tau\left(\hat{A}^+\Delta\tilde{\tilde{Q}}^*\right)^n_{j-1,k,l},$$

$$\text{where}\quad \Delta\tilde{\tilde{Q}}^{n*}_{j,k,l} = (1 + \Delta\tau\sigma^n_{\xi j,k,l})^{-1}(1 + \Delta\tau\sigma^n_{\xi j,k,l} + \Delta\tau\hat{A}^{n-}_{j+1,k,l})\Delta\tilde{\tilde{Q}}^n_{j,k,l}.$$

   (b) Backward sweep $(j_{\max}-1 \longrightarrow j_{\min})$

$$(1 + \Delta\tau\sigma^n_{\xi j,k,l})\Delta\tilde{\tilde{Q}}^n_{j,k,l} = (1 + \Delta\tau\sigma^n_{\xi j,k,l})\Delta\tilde{\tilde{Q}}^{n*}_{j,k,l} - \Delta\tau\left(\hat{A}^-\Delta\tilde{\tilde{Q}}\right)^n_{j+1,k,l}$$

$$\rightarrow\quad \Delta\tilde{\tilde{Q}}^n_{j,k,l} = \frac{1}{1 + \Delta\tau\sigma^n_{\xi j,k,l}}\left((1 + \Delta\tau\sigma^n_{\xi j,k,l})\Delta\tilde{\tilde{Q}}^{n*}_{j,k,l} - \Delta\tau\left(\hat{A}^-\Delta\tilde{\tilde{Q}}\right)^n_{j+1,k,l}\right),$$

$$\text{where}\quad \Delta\tilde{\tilde{Q}}^n_{j,k,l} = \left[I + \Delta\tau\frac{\partial}{\partial\xi}\hat{B}\right]\Delta\tilde{Q}^n_{j,k,l}.$$

2. η-direction

   (a) Forward sweep $(k_{\min}+1 \longrightarrow k_{\max})$

$$(1 + \Delta\tau\sigma^n_{\eta j,k,l})\Delta\tilde{Q}^{n*}_{j,k,l} = \Delta\tilde{\tilde{Q}}^n_{j,k,l} + \Delta\tau\left(\hat{B}^+\Delta\tilde{\tilde{Q}}^*\right)^n_{j,k-1,l},$$

$$\text{where}\quad \Delta\tilde{Q}^{n*}_{j,k,l} = (1 + \Delta\tau\sigma^n_{\eta j,k,l})^{-1}(1 + \Delta\tau\sigma^n_{\eta j,k,l} + \Delta\tau\hat{B}^{n-}_{j,k+1,l})\Delta\tilde{Q}^n_{j,k,l}.$$

(b) Backward sweep $(k_{\max}-1 \longrightarrow k_{\min})$

$$(1+\Delta\tau\sigma^n_{\eta j,k,l})\Delta\tilde{Q}^n_{j,k,l} = (1+\Delta\tau\sigma^n_{\eta j,k,l})\Delta\tilde{Q}^{n*}_{j,k,l} - \Delta\tau\left(\hat{B}^-\Delta\tilde{Q}\right)^n_{j,k+1,l}$$
$$\rightarrow \quad \Delta\tilde{Q}^n_{j,k,l} = \frac{1}{1+\Delta\tau\sigma^n_{\eta j,k,l}}\left((1+\Delta\tau\sigma^n_{\eta j,k,l})\Delta\tilde{Q}^{n*}_{j,k,l} - \Delta\tau\left(\hat{B}^-\Delta\tilde{Q}\right)^n_{j,k+1,l}\right),$$
$$\text{where} \quad \Delta\tilde{Q}^n_{j,k,l} = \left[I+\Delta\tau\frac{\partial}{\partial\xi}\hat{C}\right]\Delta\hat{Q}^n_{j,k,l}.$$

3. ζ-direction

(a) Forward sweep $(l_{\min}+1 \longrightarrow l_{\max})$

$$(1+\Delta\tau\sigma^n_{\zeta j,k,l})\Delta\hat{Q}^{n*}_{j,k,l} = \Delta\tilde{Q}^n_{j,k,l} + \Delta\tau\left(\hat{C}^+\Delta\tilde{Q}^*\right)^n_{j,k,l-1},$$
$$\text{where} \quad \Delta\hat{Q}^{n*}_{j,k,l} = (1+\Delta\tau\sigma^n_{\zeta j,k,l})^{-1}(1+\Delta\tau\sigma^n_{\zeta j,k,l}+\Delta\tau\hat{C}^{n-}_{j,k,l+1})\Delta\hat{Q}^n_{j,k,l}.$$

(b) Backward sweep $(l_{\max}-1 \longrightarrow l_{\min})$

$$(1+\Delta\tau\sigma^n_{\zeta j,k,l})\Delta\hat{Q}^n_{j,k,l} = (1+\Delta\tau\sigma^n_{\zeta j,k,l})\Delta\hat{Q}^{n*}_{j,k,l} - \Delta\tau\left(\hat{C}^-\Delta\hat{Q}\right)^n_{j,k,l+1}$$
$$\rightarrow \quad \Delta\hat{Q}^n_{j,k,l} = \frac{1}{1+\Delta\tau\sigma^n_{\zeta j,k,l}}\left((1+\Delta\tau\sigma^n_{\zeta j,k,l})\Delta\hat{Q}^{n*}_{j,k,l} - \Delta\tau\left(\hat{C}^-\Delta\hat{Q}\right)^n_{j,k,l+1}\right).$$

Next, although we assumed here that the viscous terms (∂E_ν, ∂F_ν, and ∂G_ν in Eq. (2.42)) can be treated explicitly, it is also possible to add them to the LHS of Eq. (2.42) as implicit operators (Steger, 1978; Pulliam & Steger, 1980). Strictly speaking, the flux Jacobian matrices of the viscous terms should be added to the implicit operator to the LHS of the equations as the convective numerical fluxes do (Steger, 1978). Nevertheless, various approximations have been already adopted to the operator on the LHS, so an accurate formulation is not particularly required. Thereby, it is known that the viscous terms can be put only in the right hand side and dealt with explicitly for practical usage (Yee, 1987). For simplicity and efficiency of the calculation, the approximation of viscous fluxes is added to the maximum eigenvalues (Obayashi & Kuwahara, 1986), which is similar to the implicit MacCormack scheme (Maccormack, 1982). As expressed

mathematically, Eqs. (2.140)-(2.142) are modified as follows:

$$\sigma(\hat{A}) = |U| + a\sqrt{\xi_x^2 + \xi_y^2 + \xi_z^2} + 2\nu_\xi \quad , \quad \nu_\xi = \frac{\mu(\xi_x^2 + \xi_y^2 + \xi_z^2)}{Re\rho\Delta\xi} \, , \tag{2.143}$$

$$\sigma(\hat{B}) = |V| + a\sqrt{\eta_x^2 + \eta_y^2 + \eta_z^2} + 2\nu_\eta \quad , \quad \nu_\eta = \frac{\mu(\eta_x^2 + \eta_y^2 + \eta_z^2)}{Re\rho\Delta\eta} \, , \tag{2.144}$$

$$\sigma(\hat{C}) = |W| + a\sqrt{\zeta_x^2 + \zeta_y^2 + \zeta_z^2} + 2\nu_\zeta \quad , \quad \nu_\zeta = \frac{\mu(\zeta_x^2 + \zeta_y^2 + \zeta_z^2)}{Re\rho\Delta\zeta} \, . \tag{2.145}$$

2.4.2 Newton-Raphson Iteration

In general, the approximate factorization does not guarantee the time discretization accuracy because several approximations are already introduced. Therefore, the multiple subiterations are usually employed for the time step between n and $n+1$ step (Chakravarthy, 1984). Let us employ m-times subiterations to the LHS of Eq. (2.123),

$$\begin{aligned} \hat{Q}^{(m)} - \hat{Q}^n &= \Delta\hat{Q}^{(m)} + \hat{Q}^{(m-1)} - \hat{Q}^n \\ &= -\Delta\tau \left[\frac{\partial \hat{E}}{\partial \xi} + \frac{\partial \hat{F}}{\partial \eta} + \frac{\partial \hat{G}}{\partial \zeta} \right]_{j,k,l}^{(m)} , \end{aligned} \tag{2.146}$$

where $\Delta\hat{Q}^{(m)} = \hat{Q}^{(m)} - \hat{Q}^{(m-1)}$; and thus, $\lim_{m\to\infty} \Delta\hat{Q}^{(m)} = 0$. Furthermore,

$$\hat{Q}^{(0)} = \hat{Q}^n \quad , \quad \lim_{m\to\infty} \hat{Q}^{(m)} = \hat{Q}^{n+1}. \tag{2.147}$$

A Newton-Raphson method can be constructed for $\hat{Q}^{(m)}$ by the following linearization:

$$\begin{aligned} &\left[I + \Delta\tau \left(\frac{\partial \hat{A}}{\partial \xi} + \frac{\partial \hat{B}}{\partial \eta} + \frac{\partial \hat{C}}{\partial \zeta} \right)^{(m)} \right] \Delta\hat{Q}^{(m)} \\ &\qquad = -\left(\hat{Q}^{(m)} - \hat{Q}^n \right) - \Delta\tau \left[\frac{\partial \hat{E}}{\partial \xi} + \frac{\partial \hat{F}}{\partial \eta} + \frac{\partial \hat{G}}{\partial \zeta} \right]_{j,k,l}^{(m)} . \end{aligned} \tag{2.148}$$

If $\Delta\hat{Q}^{(m)} \to 0$, then Eq. (2.148) is written as

$$\begin{aligned} &-\left(\hat{Q}^{(m)} - \hat{Q}^n \right) - \Delta\tau \left[\frac{\partial \hat{E}}{\partial \xi} + \frac{\partial \hat{F}}{\partial \eta} + \frac{\partial \hat{G}}{\partial \zeta} \right]_{j,k,l}^{(m)} \\ &\qquad \approx -\left(\frac{\partial \hat{Q}}{\partial \tau} + \frac{\partial \hat{E}}{\partial \xi} + \frac{\partial \hat{F}}{\partial \eta} + \frac{\partial \hat{G}}{\partial \zeta} \right) \to 0 \, . \end{aligned} \tag{2.149}$$

The equation above satisfies unsteady Navier-Stokes equations which provide the flow variables fluctuating in time and space. Hence, no matter what approximation is applied to the LHS of Eq. (2.123), exact temporal accuracy is realized if the subiterations converge. In case of the second order temporal accuracy,

$$\begin{aligned}\frac{3\hat{Q}^{(m)}-4\hat{Q}^{n}+\hat{Q}^{n-1}}{2} &= \frac{3\Delta\hat{Q}^{(m)}+3\hat{Q}^{(m-1)}-4\hat{Q}^{n}+\hat{Q}^{n-1}}{2} \\ &= -\Delta\tau\left[\left(\frac{\partial\hat{E}}{\partial\xi}\right)+\left(\frac{\partial\hat{F}}{\partial\eta}\right)+\left(\frac{\partial\hat{G}}{\partial\zeta}\right)\right]^{(m)}_{j,k,l}. \end{aligned} \tag{2.150}$$

Applying a linearization to the equation above, we obtain,

$$\begin{aligned}&\left[I+\frac{2}{3}\Delta\tau\left(\frac{\partial\hat{A}}{\partial\xi}+\frac{\partial\hat{B}}{\partial\eta}+\frac{\partial\hat{C}}{\partial\zeta}\right)\right]^{(m)}\Delta\hat{Q}^{(m)} \\ &\quad=-\frac{2}{3}\Delta\tau\left\{\frac{3\hat{Q}^{(m)}-4\hat{Q}^{n}+\hat{Q}^{n-1}}{2\Delta\tau}+\left[\frac{\partial\hat{E}}{\partial\xi}+\frac{\partial\hat{F}}{\partial\eta}+\frac{\partial\hat{G}}{\partial\zeta}\right]^{(m)}_{j,k,l}\right\}. \end{aligned} \tag{2.151}$$

The second order accurate in time can be maintained when $\Delta\hat{Q}^{(m)}\to 0$. As a consequence, the discretized form of governing equation (Eq. (2.42)) which has the second order accuracy in time with m-times subiterations can be expressed as follows:

$$\begin{aligned}&\left[I+\frac{2}{3}\Delta\tau\left(\frac{\partial\hat{A}}{\partial\xi}+\frac{\partial\hat{B}}{\partial\eta}+\frac{\partial\hat{C}}{\partial\zeta}\right)-\frac{2}{3}\Delta\tau\frac{1}{Re}\left(\frac{\partial\hat{A}_\nu}{\partial\xi}+\frac{\partial\hat{B}_\nu}{\partial\eta}+\frac{\partial\hat{C}_\nu}{\partial\zeta}\right)\right]^{(m)}\Delta\hat{Q}^{(m)} \\ &\quad=-\frac{3\hat{Q}^{(m)}-4\hat{Q}^{n}+\hat{Q}^{n-1}}{3}-\frac{2}{3}\Delta\tau\left[\left(\frac{\partial\hat{E}}{\partial\xi}+\frac{\partial\hat{F}}{\partial\eta}+\frac{\partial\hat{G}}{\partial\zeta}\right)-\frac{1}{Re}\left(\frac{\partial\hat{E}_\nu}{\partial\xi}+\frac{\partial\hat{F}_\nu}{\partial\eta}+\frac{\partial\hat{G}_\nu}{\partial\zeta}\right)\right]^{(m)}_{j,k,l}, \end{aligned} \tag{2.152}$$

where

$$\hat{A}=\frac{\partial\hat{E}}{\partial\hat{Q}}\ ,\ \hat{B}=\frac{\partial\hat{F}}{\partial\hat{Q}}\ ,\ \hat{C}=\frac{\partial\hat{G}}{\partial\hat{Q}}\ ,\ \hat{A}_\nu=\frac{\partial\hat{E}_\nu}{\partial\hat{Q}}\ ,\ \hat{B}_\nu=\frac{\partial\hat{F}_\nu}{\partial\hat{Q}}\ ,\ \hat{C}_\nu=\frac{\partial\hat{G}_\nu}{\partial\hat{Q}}\ . \tag{2.153}$$

2.5 Treatment of turbulence

2.5.1 Numerical methods for turbulent flow

Turbulent flows accompany three-dimensional unsteady and highly irregular motions in time and space. As shown in Fig. 2.4 which illustrates an energy spectrum of a turbulent flow, various and continuous spectrum from largest to smallest scales coexist in a turbulent flow; and thus, a wide range of length- and time-scale should be simultaneously considered to precisely resolve turbulent characteristics. There are two important effects in turbulent motions so-called the viscous effect and the convective effect. The viscous effect transports momentum from high-momentum region to low-momentum one through a random molecular motion, and it usually homogenizes the velocity distribution. It also dissipates kinetic energy of the flow to heat. The viscous effects contribute to the birth and death of turbulence in the large scale and dissipation region, respectively. The convective effect transports physical quantities associated with flow in a flow direction, and it is much more effective way to the momentum transport than the viscous effect. Because of the convective effect, the nonlinearity of turbulent is created and smaller vortices are generated. Thus, it can be considered that the origin of turbulence comes from the convective effect. The convective motion usually takes place in the inertial subrange where the energy spectrum are decayed by the -5/3 power of the wave number (see, Fig. 2.4). It is often referred to as the Kolmogorov's -5/3 law. When the flow becomes turbulent, large scale eddies pass their kinetic energy to smaller ones, and this process is referred to as the energy cascade. During the energy cascade procedure, the viscous effects play no essential role and can be neglected in general. When the eddies become under a certain size, the kinetic energy is ultimately dissipated to heat by the molecular viscosity. The smallest scales of turbulent flows are often referred to as dissipation scales or Kolmogorov scales.

Numerous methods have been proposed to obtain a solution of turbulent flow numerically. Direct numerical simulation (DNS) is the most accurate approach to simulate turbulent flows. As illustrated in Fig. 2.4, since the DNS resolves whole range of turbulent motions with a sufficiently fine grid to capture the smallest scales (Kolmogorov scale) without any modeling. Thus, it yields a complete three-dimensional time-dependent solution of the Navier-Stokes equations. A drawback of DNS, however, is that it requires very huge computational resources. In terms of computational grids, the number of grid points in each direction is proportional to the ratio between the largest and smallest eddy. In other words, it is roughly proportional to $Re_{\mathcal{L}}^{9/4}$ for three-dimensional simula-

tion, where $Re_{\mathcal{L}}$ is the Reynolds number based on the integral scale of the flow (Piomelli & Balaras, 2002). Another estimation was reported that the cost of DNS is proportional to $Re_{\mathcal{L}_x}^{37/14}$, where $Re_{\mathcal{L}_x}$ is the Reynolds number based on the flat-plate length in the streamwise direction (Choi & Moin, 2012). Thus, the DNS is still not a feasible method for many engineering problems of high Reynolds number flows, although it has been widely applied in academic research to understand fundamental characteristics of turbulent flows (e.g., channel flow: Kim *et al.* (1987); Del Alamo *et al.* (2004); Hoyas & Jimenez (2006), zero-pressure-gradient turbulent boundary layer: Schlatter & Orlu (2010); Sayadi *et al.* (2013); Sillero *et al.* (2013)). Some reviews of DNS can be found in Moin & Mahesh (1998) or Ishihara *et al.* (2009).

On the other hand, Reynolds averaged Navier-Stokes (RANS) simulation has been widely used in many engineering applications. Briefly speaking, the RANS is only interested in the averaged quantities and effects of instantaneous turbulent fluctuating motions are modeled by so-called turbulence models. In other words, the entire process of the energy cascade and energy dissipation are modeled in the RANS (see, Fig. 2.4). What needs to be emphasized is that there is no universal model which can be applied to any turbulent flow, and the reliability of RANS simulation significantly depends on turbulence models. Some extensive reviews of turbulence models have been made by Bredberg (2001), Wilcox (2001), Wilcox (2006), and Argyropoulos & Markatos (2015). The derivation of the RANS equation and turbulence models employed in this thesis will be introduced in Sec. 2.5.3.

There is a method so-called large eddy simulation (LES) at the intermediate area between the DNS and the RANS. Recently, it has become a popular and promising approach for simulating turbulent flows. The LES was first proposed by Smagorinsky (1963) and applied to engineering flow field by Deardorff (1970). According to the Kolmogorov's universality assumption (similarity hypothesis), large eddies in the flow are dependent on the geometry whereas small eddies are statistically isotropic and universal (Pope, 2000; McDonough, 2004). The large scale eddies usually contain most of the turbulent energy and take a role of most of the momentum transfer and turbulent mixing. Thus, in the LES, the important large scale motions are directly resolved whereas smaller scale ones (part of the inertial subrange and dissipation scales) are modeled (see, Fig. 2.4). The smallest scales considered in the LES are related to the grid size, so the modeling are referred to as subgrid scale (SGS) models (see, Sec. 2.5.2). Because of directly solving large scale eddies, the LES is more accurate method than the RANS. Moreover, according to the grid-point requirements by Chapman (1979) and Choi & Moin (2012), the required number of grid points in the LES is only proportional to $Re_{\mathcal{L}_x}^{9/5}$ and $Re_{\mathcal{L}_x}^{13/7}$,

respectively; thus, the LES demands less computational costs than DNS. Some reviews of LES can be found in Piomelli (1999), Larsson & Wang (2014), Gourdain *et al.* (2014), and Yang (2015).

It is still difficult, however, to apply the LES to many practical high Reynolds number flows which include a wall boundary. Especially, the required number of grid points to resolve near-wall area inside the boundary layer ($\lesssim 0.2\delta$ where δ is boundary layer thickness) enormously increases as the Reynolds number increases. In order to solve this problem which is often referred to as the near-wall problem of LES, several wall-modeled LES techniques have been proposed such as hybrid LES/RANS (Frohlich & von Terzi, 2008) detached eddy simulation (DES, Spalart, 2009), and wall-stress-models (e.g., Kawai & Larsson, 2012, 2013). According to the recommendation of Chapman (1979) and Choi & Moin (2012), the number of grid points required for the wall-modeled LES is proportional to $Re_{\mathcal{L}_x}^{2/5}$ and $Re_{\mathcal{L}_x}$, respectively; and this is obviously cheaper than that of the LES mentioned above (so-called wall-resolved LES). Some reviews of these numerical methods have been given in Piomelli & Balaras (2002), Leschziner *et al.* (2009), Tucker (2011), Deck *et al.* (2014), or Larsson *et al.* (2015).

2.5.2 Subgrid scale modeling in LES

There are many ways of representing sub-grid scale (SGS) effects such as Smagorinsky model (Smagorinsky, 1963), dynamic Smagorinsky model (Germano *et al.*, 1991; Moin *et al.*, 1991), dynamic localization model (Ghosal *et al.*, 1995), Lagrangian dynamic SGS model (Meneveau *et al.*, 1996), or coherent structure model (Kobayashi, 2005; Kobayashi *et al.*, 2008). As depicted in Fig. 2.4, a part of the inertial subrange and dissipation range are modeled by SGS models and the reliability of modeling significantly depends on the grid size. Some alternatives to the SGS-based LES have been proposed. For example, the monotonically integrated LES (MILES, Boris *et al.*, 1992) uses unfiltered forms of the governing equations with a monotone-preserving numerical method, and successfully adopted to various flow fields (Grinstein & Fureby, 2002). It relies upon the inherent dissipation coming from the numerical schemes, whose effect is similar to that provided by traditional SGS models. Another technique, which is similar to the MILES, is the high-fidelity implicit LES (ILES, Visbal & Gaitonde, 1999) in which no explicit SGS model is adopted. Unlike the MILES, the dissipation at high wave numbers is not implicitly provided by the inherent dissipation of the discretization scheme, but explicitly brought by the high-order Pade-type low-pass spatial filter. This explicit filter provides adequate dissipation to the turbulent kinetic energy at scales that cannot be accurately

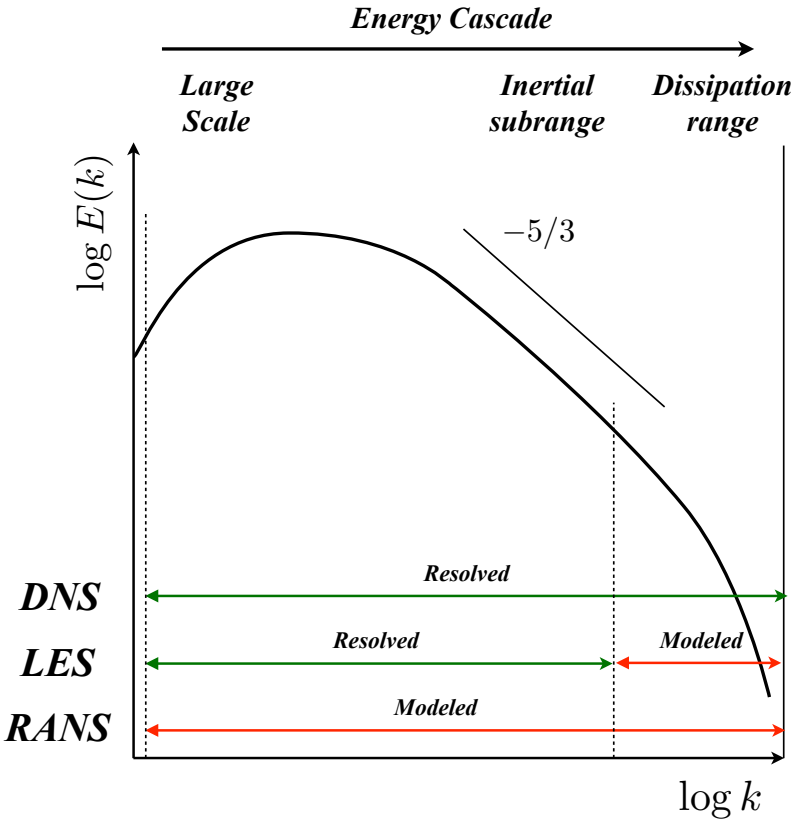

Figure 2.4: Schematic diagram of the energy spectrum variation for turbulent flows for a wave number k, and modeling region of DNS, LES, and RANS

resolved on a given grid, in a similar way to SGS models. The ILES methodology permits a seamless transition from LES to DNS as increasing in the resolution. Also, the computational cost for evaluating SGS models can be avoided, and hence the ILES is a numerically stable and efficient method compared to the SGS-based LES. Many previous studies have demonstrated the attractiveness of the ILES as an alternative to the traditional SGS-based LES. Visbal & Rizzetta (2002) presented that the ILES showed better agreement with the DNS than the standard LES technique with either the Smagorinsky and dynamic Smagorinsky models in the isotropic turbulence flow. Bogey & Bailly (2006) and Marsden *et al.* (2008) also pointed out that the lack or addition of an explicit SGS model did not have a significant effect on the solution. Kawai *et al.* (2010) mentioned that the high-order numeric schemes with a sufficiently high grid resolution without SGS models showed better resolution for turbulence, whereas an explicitly added SGS model resulted in additional damping of the resolved turbulence. Garmann *et al.* (2013) performed the comparative study of ILES and SGS-based LES for low Reynolds number transitional flows around an airfoil, and concluded that the addition of the SGS

model does not significantly affect the time-mean flow or statistical quantities. Therefore, the ILES approach is used in this thesis.

2.5.3 Turbulence modeling in RANS

Reynolds Averaged Navier-Stokes Equation Reynolds averaged Navier-Stokes (RANS) simulation is a statistical method in which all unsteady turbulent motions are replaced by a turbulence model. Reynolds (1895) proposed a statistical approach so-called Reynolds decomposition: an instantaneous variable f (e.g., pressure or velocity components) is decomposed into average and fluctuation contributions,

$$f = \overline{f} + f'. \tag{2.154}$$

There are many possible methods for statistical analysis of turbulence, but the following Reynolds averaging which include time, spatial, and ensemble averaging is often adopted. The time averaging is defined as

$$\overline{f}(x,y,z) = \lim_{T\to\infty} \frac{1}{T} \int_t^{t+T} f(x,y,z,t)dt \ . \tag{2.155}$$

The spatial averaging is given by

$$\overline{f}(t) = \lim_{\mathcal{V}\to\infty} \frac{1}{\mathcal{V}} \iiint_{\mathcal{V}} f(x,y,z,t)d\mathcal{V} \ . \tag{2.156}$$

The ensemble averaging is provided by

$$\overline{f}(x,y,z,t) = \lim_{N\to\infty} \frac{1}{N} \sum_{n=1}^{N} f(x,y,z,t) \ , \tag{2.157}$$

where N is the number of members of the ensemble which must be large enough to eliminate the effect of fluctuations. The followings are satisfied in the Reynolds decomposition (White, 2006),

$$\overline{\overline{f}} = \overline{f} \quad , \quad \overline{f'} = 0 \quad , \quad \overline{\overline{f}g'} = 0 \quad , \quad \overline{\overline{f}g} = \overline{f}\,\overline{g} \quad , \quad \overline{f+g} = \overline{f} + \overline{g}. \tag{2.158}$$

There is an another method so-called the Farve averaging or mass-weighted averaging for the compressible Navier-Stokes equations (Farve, 1983), but this thesis will only focus on the Reynolds averaging. Let us introduce the relationship above into the three-dimensional incompressible Navier-Stokes equations. First, the continuity equation is

written by

$$\overline{\frac{\partial(\overline{u}_i + u_i')}{\partial x_i}} = \frac{\partial \overline{\overline{u}_i}}{\partial x_i} + \frac{\partial \overline{u_i'}}{\partial x_i} = \frac{\partial \overline{u}_i}{\partial x_i} = 0. \tag{2.159}$$

Second, the momentum equation is written by

$$\overline{\rho \frac{\partial(\overline{u}_i + u_i')}{\partial t}} + \overline{\rho(\overline{u}_j + u_j')} \overline{\frac{\partial(\overline{u}_i + u_i')}{\partial x_j}} = \overline{\frac{\partial(\overline{p} + p')}{\partial x_i}} + \overline{\frac{\partial}{\partial x_j}\left[\mu\left(\frac{\partial(\overline{u}_i + u_i')}{\partial x_j} + \frac{\partial(\overline{u}_j + u_j')}{\partial x_i}\right)\right]}. \tag{2.160}$$

Here, the second term in the LHS of equation above is rewritten as follows:

$$\begin{aligned} \overline{\rho(\overline{u}_j + u_j')} \overline{\frac{\partial(\overline{u}_i + u_i')}{\partial x_j}} &= \overline{\rho \frac{\partial(\overline{u}_i + u_i')(\overline{u}_j + u_j')}{\partial x_j}} - \overline{\rho(\overline{u}_i + u_i')} \overline{\frac{\partial(\overline{u}_j + u_j')}{\partial x_j}} \\ &= \overline{\rho \frac{\partial(\overline{u}_i + u_i')(\overline{u}_j + u_j')}{\partial x_j}}, \end{aligned} \tag{2.161}$$

where Eq. (2.159) is used. Consequently, each term of Eq. (2.160) is

$$\text{The } 1^{\text{st}} \text{ LHS} = \overline{\rho \frac{\partial(\overline{u}_i + u_i')}{\partial t}} = \rho \frac{\partial \overline{\overline{u}_i}}{\partial t} + \rho \frac{\partial \overline{u}_i'}{\partial t} = \rho \frac{\partial \overline{u}_i}{\partial t}, \tag{2.162}$$

$$\text{The } 2^{\text{nd}} \text{ LHS} = \overline{\rho \frac{\partial(\overline{u}_i \overline{u}_j + \overline{u}_i u_j' + u_i' \overline{u}_j + u_i' u_j')}{\partial x_j}} = \rho \frac{\partial}{\partial x_j}(\overline{u}_i \overline{u}_j + \overline{u_i' u_j'}), \tag{2.163}$$

$$\text{The } 1^{\text{st}} \text{ RHS} = \overline{\frac{\partial(\overline{p} + p')}{\partial x_i}} = \frac{\partial \overline{\overline{p}}}{\partial x_i} + \frac{\partial \overline{p'}}{\partial x_i} = \frac{\partial \overline{p}}{\partial x_i}, \tag{2.164}$$

$$\text{The } 2^{\text{nd}} \text{ RHS} = \frac{\partial}{\partial x_j}\left[\mu\left(\frac{\partial \overline{u}_i}{\partial x_j} + \frac{\partial \overline{u}_j}{\partial x_i}\right)\right] = 2\mu \overline{s}_{ij}. \tag{2.165}$$

Therefore, the RANS equation is obtained as follows:

$$\rho \frac{\partial \overline{u}_i}{\partial t} + \rho \frac{\partial(\overline{u}_i \overline{u}_j)}{\partial x_j} = -\frac{\partial \overline{p}}{\partial x_i} + \frac{\partial}{\partial x_j}\left(-\rho \overline{u_i' u_j'} + 2\mu \overline{s}_{ij}\right), \tag{2.166}$$

where $\tau_{ij}^{\text{RANS}} = -\rho \overline{u_i' u_j'}$ is referred to as the Reynolds stress. The matrix representation of the Reynolds stress is written as

$$\tau_{ij}^{\text{RANS}} = -\rho \begin{bmatrix} \overline{u'^2} & \overline{u'v'} & \overline{u'w'} \\ \overline{u'v'} & \overline{v'^2} & \overline{v'w'} \\ \overline{u'w'} & \overline{v'w'} & \overline{w'^2} \end{bmatrix}. \tag{2.167}$$

This is a symmetric tensor, and hence the Reynolds stress consists of six independent components. The diagonal components are the normal stress while the off-diagonal ones are the shear stress. It can be interpreted that the Reynolds stress is responsible for an interaction between the average and turbulent motion. Davidson (2015) pointed out that the Reynolds stress is not really a stress in the conventional sense of the word but represents the mean momentum fluxes induced by the turbulence.

Turbulence modeling The statistical averaging procedure in the RANS equations yields the Reynolds stress (Eq. (2.167)) which has six unknown variables. If the higher order transport equations are derived to obtain this unknown Reynolds stress, they includes higher order unknown correlations such as $-\rho\overline{u_i' u_j' u_k'}$, $-\rho\overline{u_i' u_j' u_k' u_l'}$; thus, the equation system is unclosed. In order to avoid this problem, the Reynolds stress should be represented by some variables which are already known. The simplest way of modeling the Reynolds stress is the use of Boussinesq approximation which uses the turbulent eddy viscosity μ_{tur}. Chang (1970) mentioned that the turbulent eddy viscosity usually has a larger effect than the molecular viscosity μ. This approximation assumes that the Reynolds stress tensor is proportional to the averaged rate of strain tensor written as follows:

$$\tau_{ij}^{\text{RANS}} = \mu_{\text{tur}} \left(\frac{\partial u_i}{\partial x_j} + \frac{\partial u_j}{\partial x_i} \right) - \frac{2}{3}\rho k \delta_{ij} \quad , \quad k = \frac{1}{2}\overline{u_i' u_i'} \, . \tag{2.168}$$

From a dimensional analysis, it is known that μ_{tur} should be proportional to a representative velocity $\mathcal{U}_{\text{tur}}$ and a length scale $\mathcal{L}_{\text{tur}}$ of the turbulent motion. The linear eddy viscosity model applies this concept and it is roughly categorized by four parts: zero-equation (algebraic), half equation, one-equation, and two-equation models. The differences among the turbulence model lies in the way of choosing the physical scale which will be calculated. For instance, both the representative velocity and length scale are described by algebraic expressions in the zero equation model. On the other hand, the one-equation model solves a transport equation for one representative scale and another scale is algebraically modeled. The two-equation model solves two transport equations for both of the scales. In particular, one of them is usually the transport equation for the turbulent kinetic energy. Various physical quantities have been proposed for the other transport equation; the dissipation rate of turbulent kinetic energy ε, specific dissipation rate ω, time scale τ, etc.. Furthermore, many models have been proposed such as non-linear eddy viscosity models or Reynolds stress transportation models. Some representative turbulence models of each category are summarized as below.

- Linear eddy viscosity model
  - 0-equation (algebraic model) :
    - Baldwin-Lomax model (Baldwin & Lomax, 1978) etc.
  - 1/2-equation :
    - Johnson-King model (Johnson & King, 1985)
  - 1-equation :
    - Baldwin-Barth model (Baldwin & Barth, 1991)
    - Spalart-Allmaras model (Spalart & Allmaras, 1992) etc.
  - 2-equation :
    - $k-\varepsilon$ model
      - Jones-Launder model (Jones & Launder, 1972)
      - standard model (Launder & Sharma, 1974)
      - RNG model (Yakhot *et al.*, 1992) etc.
      - realisable model (Shih *et al.*, 1995) etc.
    - $k-\omega$ model
      - Wilcox model (Wilcox, 1988)
      - SST model (Menter, 1994) etc.
    - $k-\tau$ model
      - Speziale-Abid-Anderson model (Speziale *et al.*, 1992) etc.
- Non-linear eddy viscosity model
  - Quadratic model
    - Nisizima-Yoshizawa model (Nisizima & Yoshizawa, 1987)
    - Rubinstein-Barton model (Rubinstein & Barton, 1990) etc.
  - Cubic model
    - Craft-Launder-Suga model (Craft *et al.*, 1996)
    - Ehrhard-Moussiopoulos model (Ehrhard & Moussiopoulos, 2000) etc.
- Reynolds stress transportation model
  - Lunder-Reece-Rodi model (Launder *et al.*, 1975)
  - Speziale-Sarkar-Gatski model (Speziale *et al.*, 1991) etc.

Baldwin-Lomax Turbulence Model The Baldwin-Lomax algebraic turbulence model (Baldwin & Lomax, 1978) evaluates the turbulent eddy viscosity from the velocity profile in the wall-normal direction. This model decomposes the boundary layer into the inner and outer region, and the kinematic eddy viscosity $\nu_{\mathrm{tur}}(=\mu_{\mathrm{tur}}/\rho)$ in each region is

defined by different algebraic equations as follows:

$$\nu_{\text{tur}} = \begin{cases} (\nu_{\text{tur}})_{\text{inner}} & (d \leq d_{\text{cross}}) \\ (\nu_{\text{tur}})_{\text{outer}} & (d > d_{\text{cross}}) \end{cases}, \tag{2.169}$$

where d is the normal distance from the wall and d_{cross} is decided as the smallest value of d where $(\nu_{\text{tur}})_{\text{inner}} = (\nu_{\text{tur}})_{\text{outer}}$. The Prandtl-Van Driest formulation is applied to the kinematic eddy viscosity of the inner region. It is given by

$$(\nu_{\text{tur}})_{\text{inner}} = \mathcal{L}_{\text{tur}}^2 |\Omega|, \tag{2.170}$$

where $|\Omega|$ is the magnitude of the vorticity described by

$$|\Omega| = \sqrt{\left(\frac{\partial u}{\partial y} - \frac{\partial v}{\partial x}\right)^2 + \left(\frac{\partial v}{\partial z} - \frac{\partial w}{\partial y}\right)^2 + \left(\frac{\partial w}{\partial x} - \frac{\partial u}{\partial z}\right)^2}. \tag{2.171}$$

The mixing length $\mathcal{L}_{\text{tur}}$ is given by (Van Driest, 1956)

$$\mathcal{L}_{\text{tur}} = \kappa d[1 - \exp(-d^+/A^+)], \tag{2.172}$$

where κ is the Karman constant. The dimensionless wall distance d^+ is defined by

$$d^+ = \frac{u_\tau}{\nu_w} d = \frac{\sqrt{\rho_w \tau_w}}{\mu_w} d, \tag{2.173}$$

where $u_\tau = \sqrt{\tau_w/\rho_w}$ is the friction velocity and τ_w is the wall shear stress. The kinematic eddy viscosity of the outer region is given by,

$$(\nu_{\text{tur}})_{\text{outer}} = 1.6 K F_{wake} F_{kleb}(d), \tag{2.174}$$

where K is the Clauser constant. F_{wake} and $F_{kleb}(d)$ are represented by

$$F_{wake} = \min(d_{max} F_{max} \ , \ 0.25 d_{\max} u_{dif}^2 / F_{\max}), \tag{2.175}$$

$$F_{kleb}(d) = \left[1 + 5.5 \left(\frac{0.3d}{d_{\max}}\right)^6\right]^{-1}. \tag{2.176}$$

The quantities F_{max} and d_{max} are determined by following function:

$$F(y) = d|\Omega|[1 - \exp(-d^+/A^+)]. \tag{2.177}$$

Here, F_{max} is the maximum value of $F(d)$ along the wall-normal direction, and d_{max} is the distance where maximum $F(d)$ appears. Furthermore, u_{dif} is the difference between maximum and minimum velocity in the velocity profile defined by

$$u_{dif} = \left(\sqrt{u^2+v^2+w^2}\right)_{\max} - \left(\sqrt{u^2+v^2+w^2}\right)_{\min}. \tag{2.178}$$

Some related constants are given as follows:

$$\kappa = 0.4\ ,\ A^+ = 26\ ,\ K = 0.0168. \tag{2.179}$$

Spalart-Allmaras Turbulence Model The kinematic eddy viscosity of the Spalart-Allmaras turbulence model (Spalart & Allmaras, 1992) is obtained by

$$\nu_{\rm tur} = \tilde{\nu}_{\rm tur} f_{v1} \quad , \quad f_{v1} = \frac{\chi^3}{\chi^3 + C_{v1}^3} \quad , \quad \chi = \frac{\tilde{\nu}_{\rm tur}}{\nu_{\rm lam}}\ , \tag{2.180}$$

where $\nu_{\rm lam}$ is the kinematic molecular viscosity. The variable $\tilde{\nu}_{\rm tur}$ is calculated by the following partial differential equation:

$$\frac{\partial \tilde{\nu}_{\rm tur}}{\partial t} + \frac{\partial (u_j \tilde{\nu}_{\rm tur})}{\partial x_j} = P(\tilde{\nu}_{\rm tur}) + V(\tilde{\nu}_{\rm tur}) + D(\tilde{\nu}_{\rm tur}), \tag{2.181}$$

where $P(\tilde{\nu}_{\rm tur})$, $V(\tilde{\nu}_{\rm tur})$, and $D(\tilde{\nu}_{\rm tur})$ represent production, diffusion and destruction terms, respectively. The detailed expression of each term is given by

$$P(\tilde{\nu}_{\rm tur}) = C_{b1}(1-f_{t2})\tilde{S}\tilde{\nu}_t\ , \tag{2.182}$$

$$V(\tilde{\nu}_{\rm tur}) = \frac{1}{\sigma}[\nabla\cdot(\nu_l+\tilde{\nu}_t)\nabla\tilde{\nu}_t + C_{b2}(\nabla\tilde{\nu}_t)^2]\ , \tag{2.183}$$

$$D(\tilde{\nu}_{\rm tur}) = -\left[C_{w1}f_w - \frac{C_{b1}}{\kappa^2}f_{t2}\right]\left(\frac{\tilde{\nu}_t}{d}\right)^2, \tag{2.184}$$

where d is the wall-normal distance from the wall. First of all, $\tilde{S}$ in the production term is calculated by the following equation:

$$\tilde{S} = f_{v3}|\Omega| + \frac{\tilde{\nu}_t}{\kappa^2 d^2} f_{v2}\ , \tag{2.185}$$

where $|\Omega|$ is the magnitude of the vorticity (see, Eq. (2.171)). Rumsey *et al.* (2001) described two versions of the Spalart-Allmaras model which are referred to as the standard

and modified version in this thesis. f_{v2} and f_{v3} in the standard version are obtained by

$$f_{v2} = 1 - \frac{\chi}{1 + \chi f_{v1}} \quad , \quad f_{v3} = 1 \ , \tag{2.186}$$

while those in the modified version are given by

$$f_{v2} = \frac{1}{(1 + \chi/5)^3} \quad , \quad f_{v3} = \left(\frac{1}{\chi} + f_{v1}\right)(1 - f_{v2}) \ . \tag{2.187}$$

χ is replaced by $\chi = \max(\chi, 0.001)$ in order to avoid division by zero in f_{v3}, and $\tilde{S}$ is replaced by $\tilde{S} = \max(\tilde{S}, 0.3|\Omega|)$. f_{t2} in the diffusion and destruction terms is

$$f_{t2} = C_{t3} exp(-C_{t4}\chi^2). \tag{2.188}$$

The function f_w in the destruction term is

$$f_w = g\left[\frac{1 + C_{w3}^6}{g^6 + C_{w3}^6}\right]^{1/6} \quad , \quad g = r + C_{w2}(r^6 - r) \quad , \quad r = \min\left[\frac{\tilde{\nu}_t}{\tilde{S}\kappa^2 d^2}, 10\right] \ . \tag{2.189}$$

Some related constants are given as follows:

$$\begin{aligned} &\sigma = \frac{2}{3} \quad , \quad C_{b1} = 0.1355 \quad , \quad C_{b2} = 0.622 \quad , \quad \kappa = 0.41 \ , \\ &C_{w1} = \frac{C_{b1}}{\kappa^2} + \frac{1 + C_{b2}}{\sigma} \quad , \quad C_{w2} = 0.3 \quad , \quad C_{w3} = 2.0 \ , \\ &C_{v1} = 7.1 \quad , \quad C_{v2} = 5.0 \quad , \quad C_{t3} = 1.2 \quad , \quad C_{t4} = 0.5 \ . \end{aligned} \tag{2.190}$$

2.6 Boundary condition

2.6.1 Solid wall boundary condition

The boundary condition of surface is treated as a non-slip wall and adiabatic surface. Under the non-slip wall condition, the velocity components at the wall are given by

$$u = \xi_\tau \quad , \quad v = \eta_\tau \quad , \quad w = \zeta_\tau \ , \tag{2.191}$$

and each term becomes zero in a stationary grid. There is no heat flux through the surface in the adiabatic wall condition (Hirsch, 2007). If we consider the index of wall as $l = 1$, the density of the surface denoted by $\rho_{j,k,1}$ is simply extrapolated from the

adjacent node as follows:

$$\rho_{j,k,1} = \rho_{j,k,2}. \tag{2.192}$$

The total energy per unit volume at the wall $e_{j,k,1}$ is calculated by using Eq. (2.8),

$$e_{j,k,1} = \frac{p_{j,k,2}}{\gamma - 1} + \frac{1}{2}\rho_{j,k,1}(u_{j,k,1}^2 + v_{j,k,1}^2 + w_{j,k,1}^2). \tag{2.193}$$

2.6.2 External boundary condition

The inflow and outflow condition on external boundaries is decided by a sign of the contravariant velocity. If we consider the index of outer boundary as $l = l_{\max}$, the external boundary condition is determined by a sign of the flow velocity toward the outer layer, i.e., a direction of the contravariant velocity at $l = l_{\max} - 1$.

1. Outflow condition ($W > 0$)

$$Q_{j,k,l_{\max}} = \left[\begin{array}{c} \rho \\ \rho u \\ \rho v \\ \rho w \\ \dfrac{p_\infty}{\gamma - 1} + \dfrac{1}{2}\rho\left(u^2 + v^2 + w^2\right) \end{array} \right]_{j,k,l_{\max}-1} \tag{2.194}$$

2. Inflow condition ($W < 0$)

$$Q_{j,k,l_{\max}} = Q_\infty \tag{2.195}$$

2.6.3 Periodic boundary condition

When applying the periodic boundary to k-index using ten points, flow variables around both boundary exchanged as follows:

$$Q_{j,k,l} \quad \leftarrow \quad Q_{j,k_{\max}-10+k,l} \quad , \quad (k = 1, \cdots, 5) \tag{2.196}$$

$$Q_{j,k,l} \quad \rightarrow \quad Q_{j,k_{\max}-10+k,l} \quad , \quad (k = 6, \cdots, 10) \tag{2.197}$$

Chapter 3

Classification of the separation bubble characteristics

In this chapter, three-dimensional large eddy simulations with the high-order compact finite difference scheme are carried out in order to examine the characteristics of LSB depending on the Reynolds numbers. First of all, the analysis object, flow conditions, numerical schemes, and accuracy assessments are presented in Sec. 3.1. Section 3.2 discusses instantaneous flow structures corresponding to various Reynolds numbers. Then, the time- and spanwise-averaged flow quantities are described in Sec. 3.3. Characteristics of LSBs are classified by the turbulent kinetic energy distribution within LSBs, and the relationship between the LSB characteristics and surface pressure distribution is discussed. Finally, the reattachment state of the separated shear layer is shown.

3.1 Computational setup

3.1.1 Analysis object

The analysis object in this chapter is a 5% thickness flat plate with a right-angled blunt leading edge. This is chosen to set similar conditions to those of Anyoji *et al.* (2011). The LSB has been investigated by many previous studies. Diwan & Ramesh (2012) mentioned that there are two different configurations of LSB. The first one is called as a pressure gradient induced LSB which often occurs on flow fields over an airfoil. Some research which focuses on the pressure gradient induced LSB has been carried out numerically (Jones *et al.*, 2008; Castiglioni *et al.*, 2014) and experimentally (Burgmann & Schröder, 2008; Hain *et al.*, 2009; Yarusevych *et al.*, 2009). It can be considered that this type is the most natural formation of LSB. When using an airfoil, however, the analysis becomes

difficult due to variations of the separation and reattachment point as well as those of the length of LSB depending on the angle of attack, Reynolds number, and airfoil shape. Hence, many studies have adopted a method of creating LSB using a flat plate. Since the pressure gradient of the flat plate is zero, however, flows over it do not naturally separate unless a special treatment is applied. There are generally two methods for inducing the adverse pressure gradient on the flat plate: a suction method and a contoured wall method. First, the section method is an approach of forcibly separating boundary layer by adding the velocity in the vertical direction to the wall at the upper boundary surface (e.g., see Pauley *et al.*, 1990; Alam & Sandham, 2000; Cadieux & Domaradzki, 2015). On the other hand, in the contoured wall approach (Marxen *et al.*, 2004, 2009; Simoni *et al.*, 2012), a displacement body is set at the boundary surface to induce a favorable pressure gradient followed by an adverse pressure gradient. An LSB is developed in the region where the adverse pressure gradient exists. Another configuration is referred to as a geometry induced LSB which is observed in the flow over a backward-facing step or the flow turning around a corner such as a blunt leading edge flat plate. In particular, a blunt leading edge flat plate has several advantages. For example, the separation point can be fixed to the leading edge regardless of the Reynolds number or angles of attack, and hence the analysis can be simplified. Thus, it has been applied in many previous studies (Cherry *et al.*, 1984; Kiya & Sasaki, 1985; Yanaoka *et al.*, 2003; Marty *et al.*, 2008; Debesse *et al.*, 2016). Since the separation is forcibly caused by an extremely high adverse pressure gradient at the blunt leading edge, however, detailed instability mechanisms of the separated shear layer and reattachment characteristics may change compared with the case of airfoil or that of pressure gradient induced LSB over a flat plate. Ota *et al.* (1981) investigated effects of the leading edge shape and reported that the length of LSB becomes shorter as the apex angle of leading edge increases. Furthermore, it is considered that a physical characteristic such as the instability interaction between the separated shear layer and attached boundary layer before the separation may differ depending on the geometric shapes. Dandois *et al.* (2007), however, summarized that the shedding (convective instability) and flapping (absolute instability) frequency of the separated shear layer are approximately similar regardless of the geometric shape which induces the separated flow (backward-facing step, blunt leading edge flat-plate, circular cylinder aligned coaxially with the freestream, and fence). Besides, it should be noted that the typical shape of pressure distribution (the plateau region followed by the rapid pressure recovery, Sec. 1.3) is observed irrespective of the method of inducing LSB. Thus, a blunt leading edge flat plate is adopted as the analysis object because this thesis focuses on the pressure distribution around LSBs and elucidate its formation mechanisms.

3.1.2 Computational grid and flow conditions

Figure 3.1 shows a computational grid around a 5% thickness blunt leading edge flat plate. The outer boundary is extended to 25 times of the chord length to avoid reflection of the pressure wave. The minimum grid spacing in the wall-normal direction is $\Delta y_{\min} = 2.0\times10^{-4}$. Non-slip and adiabatic conditions are adopted on the surface (Sec. 2.6.1). The spanwise domain size is employed 20% of the chord length with the periodic boundary condition (Sec. 2.6.3). In terms of the spanwise domain size, Rodríguez *et al.* (2013*b*) conducted a DNS for the NACA0012 airfoil at $Re_c = 5.0 \times 10^4$. They reported that the spanwise two-point correlations vanished by applying the spanwise length as $0.1c$, even at a stall angle of attack. Zhang & Samtaney (2016) investigated the spanwise domain size effects on the transitional flow over the NACA0012 airfoil at $Re_c = 5.0 \times 10^4$. They concluded that its effect can be neglected in terms of the time-averaged aerodynamic quantities. Also the spanwise size of $0.2c$ with periodic boundary conditions have been adopted in many previous numerical studies (Schmidt & Thiele, 2003; Wissink & Rodi, 2006; You *et al.*, 2008; Visbal, 2009; Almutairi *et al.*, 2010; Gross & Fasel, 2010; Zaki *et al.*, 2010). Next, three levels of grid resolution are employed for evaluating the grid convergence. The number of grid points in each grid type in the chordwise (N_x), wall-normal (N_y), and spanwise (N_z) direction as well as total number of grid points are listed in Tab. 3.1. The results of grid convergence will be discussed in Sec. 3.1.4. The free-stream Mach number (M_∞) with zero freestream turbulence, the specific heat ratio (γ), and the Prandtl number (Pr) are set to 0.2, 1.4, and 0.72, respectively. The Reynolds numbers based on the freestream velocity and plate length (Re_c) are set to $Re_c = 5.0 \times 10^3$, 6.1×10^3, 8.0×10^3, 1.1×10^4, and 2.0×10^4 that are similar conditions to those of the experimental studies by Anyoji *et al.* (2011). An angle of attack (α) is set to $\alpha = 0.0°$.

Table 3.1: The number of grid points for three levels of systematic mesh refinement.

Grid	N_x	N_y	N_z	Total points
Grid A	571	433	125	30,905,375
Grid B	471	359	101	17,077,989
Grid C	373	285	81	8,610,705

3.1.3 Numerical schemes

The spatial derivatives of the convective and viscous terms are evaluated by the sixth order compact difference scheme (Sec. 2.2.1) with the tenth order low-pass filtering

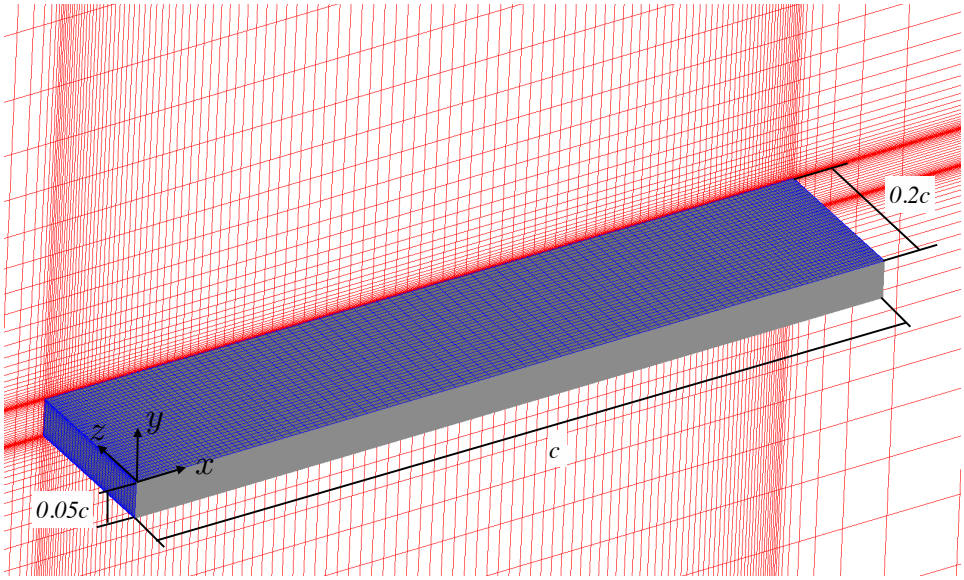

Figure 3.1: Computational grid (Grid B) for the 5 % thickness blunt leading edge flat plate. Every third grid point in each direction is shown.

(Sec. 2.2.2). The filtering coefficient α_f is set to be 0.495. The metrics and Jacobian are also calculated by the sixth order compact difference scheme (Sec. 2.2.3). The second order backward differencing which is converged by the ADI-SGS method (Sec. 2.4.1) and five subiterations (Sec. 2.4.2) are adopted for the time integration. The computational time step Δt is 2.0×10^{-4}[s], and the maximum local CFL number is approximately 1.1. Although there are many ways of representing subgrid-scale (SGS) effects, an implicit approach is applied because of the reasons mentioned in Sec. 2.5.2.

3.1.4 Accuracy assessments

The three levels of systematic mesh refinement are conducted at the highest Reynolds number case ($Re_c = 2.0 \times 10^4$) in order to evaluate the grid convergence of the results. Table 3.2 summarizes the maximum grid spacing based on the wall unit, where Δx^+ is the streamwise; Δy^+ is the wall-normal; and Δz^+ is the spanwise grid spacing. As shown by Kawai & Fujii (2008), the grid resolution of $\Delta x^+ \simeq 36$, $\Delta y^+ \simeq 1$, and $\Delta z^+ \simeq 15$ is required to resolve coherent structures in the transitional region. Georgiadis *et al.* (2010) mentioned criteria of wall-resolved LES as $50 \leq \Delta x^+ \leq 150$, $\Delta y^+ < 1$, and $15 \leq \Delta z^+ \leq 40$ and those of DNS as $10 \leq \Delta x^+ \leq 20$, $\Delta y^+ < 1$, and $5 \leq \Delta z^+ \leq 10$. All three grid resolution in the present study sufficiently satisfy the criteria above. Choi & Moin (1994) reported for the time-step size that $\Delta t^+ < 0.4$ is required for proper temporal resolution in a turbulent channel flow using an implicit time integration method. The

maximum time-step size based on the wall units of this study is $\Delta t^+ < 0.015$.

The time- and spanwise-averaged pressure distribution ($\langle \overline{C}_p \rangle$) and skin friction coefficient ($\langle \overline{C}_f \rangle$) for the three grids are shown in Fig. 3.2. From the results, there is no significant difference among the three grids; and hence, Grid B is chosen.

Qualitative comparison between the computational and experimental results of the surface pressure distribution is shown in Fig. 3.3. The pressure distributions in the experiments are firstly measured by multi-channel pressure scanners. After that, the data measured by the PSP (Anyoji *et al.*, 2011) are calibrated based on the results of the pressure scanners. The error bars for the the pressure values detected by the pressure scanner indicate two standard deviations (2σ) obtained by an experimental uncertainty analysis. As shown in the figure, quantitative discrepancies are observed at $Re_c = 2.0 \times 10^4$. One possibility which causes this discrepancies is the effects of freestream turbulent intensity which may exist in the experiment. Except for this Reynolds numbers, however, the present results at other Reynolds numbers are quantitatively consistent with the experimental results. Beside this, they are qualitatively in a good agreement with the experimental data at all the Reynolds numbers.

Figure 3.4 shows the comparison of the averaged skin friction distribution to the numerical results of Tafti & Vanka (1991*b*) at $Re_c = 2.0 \times 10^4$ (i.e., $Re_t = 1,000$, where Re_t is the plate thickness based Reynolds number). The streamwise location is normalized by the averaged reattachment point (i.e., length of the LSB). From the figure, it is confirmed that the qualitative shape of distribution is in good agreement. Next, the averaged streamwise velocity profiles and fluctuation components in the wall-normal direction at several locations within the LSB are shown in Fig. 3.5. The location from the wall (vertical axis in each figure) is normalized by the averaged reattachment point. In Fig. 3.5 (a), the results of this study show quantitatively good predictability in the strength of reverse flow and distribution of the separated shear layer. In terms of the fluctuation components (Figs. 3.5 (b)-(e)), characteristics near the reattachment point and attached boundary layer are well estimated whereas there are underpredicted regions in the front side of the LSB.

Table 3.2: The maximum grid spacing values of three levels of systematic mesh refinement.

Grid	Δx^+	Δy^+	Δz^+	Δt^+
Grid A	6.45	0.455	3.67	0.0105
Grid B	8.49	0.466	4.65	0.0110
Grid C	10.3	0.503	6.29	0.0129

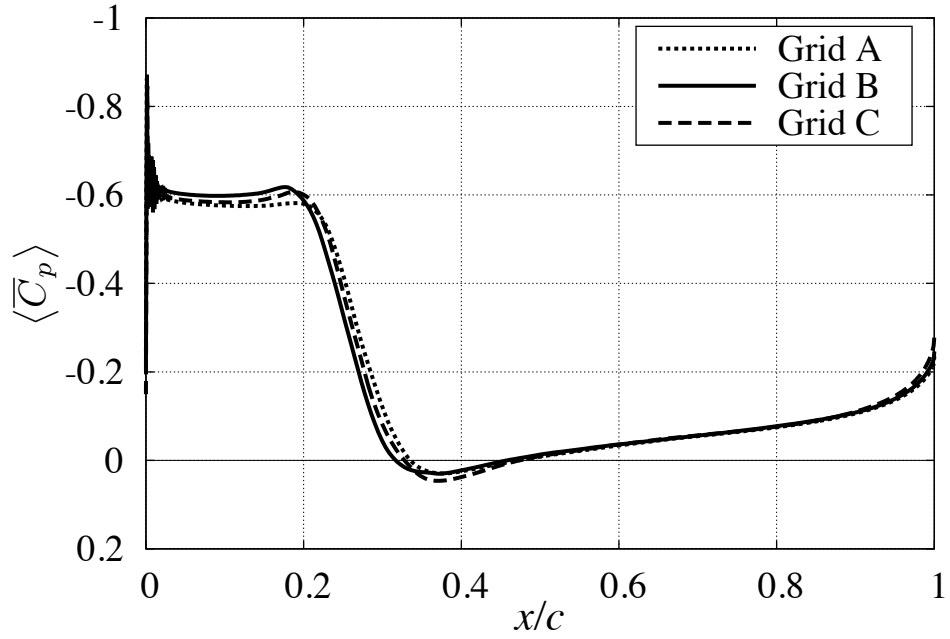

(a) Surface pressure distribution

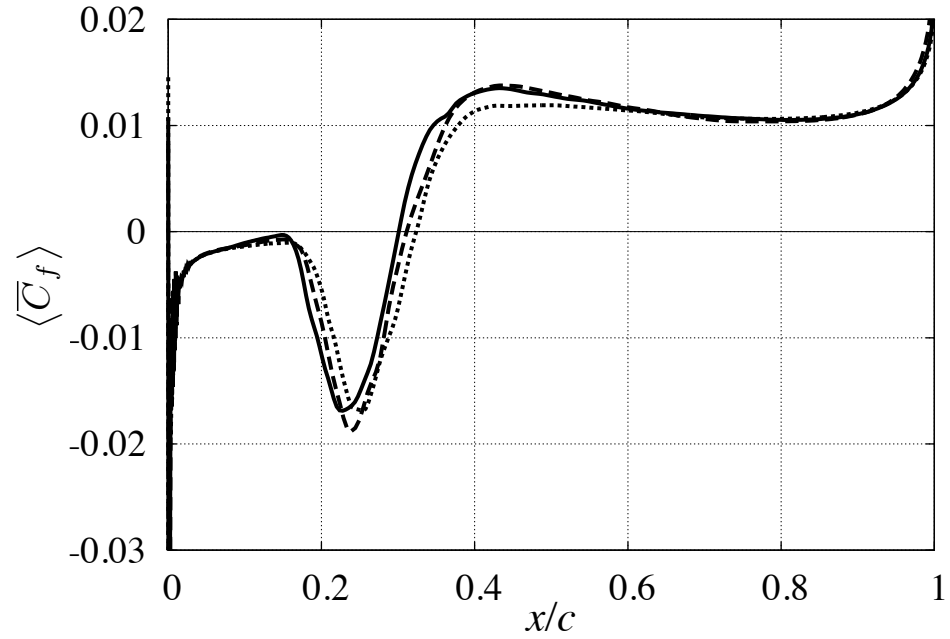

(b) Skin friction coefficient

Figure 3.2: The time- and spanwise-averaged (a) surface pressure distributions and (b) skin friction coefficient obtained by Grid A (dotted-line), Grid B (solid-line), and Grid C (dashed-line).

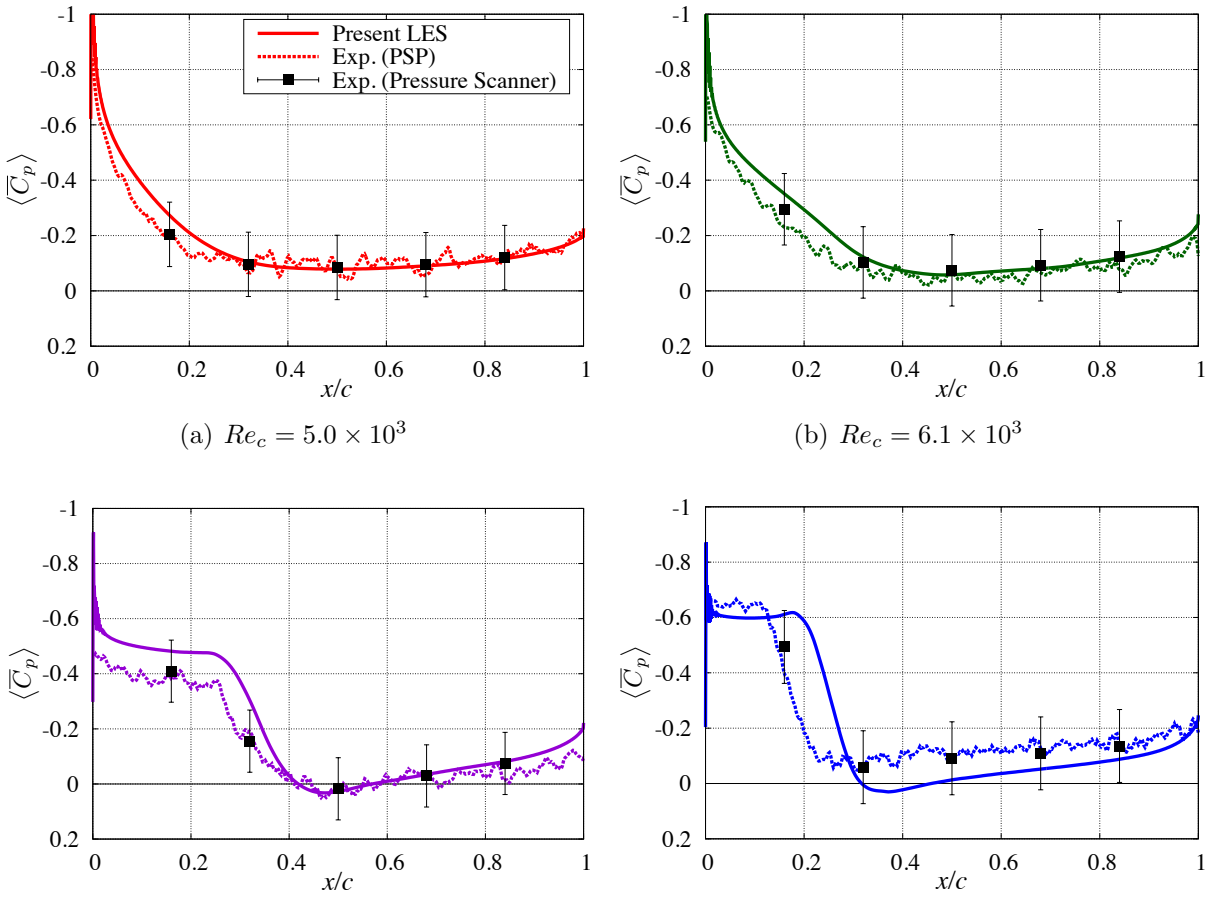

(a) $Re_c = 5.0 \times 10^3$ (b) $Re_c = 6.1 \times 10^3$

(c) $Re_c = 1.1 \times 10^4$ (d) $Re_c = 2.0 \times 10^4$

Figure 3.3: Surface pressure distributions of the present simulation results (solid-line) at (a) $Re_c = 5.0 \times 10^3$, (b) 6.1×10^3, (c) 1.1×10^4, and (d) 2.0×10^4 compared with calibrated PSP data (dashed-line) and pressure scanner data (squares with error bars) (Anyoji *et al.*, 2011).

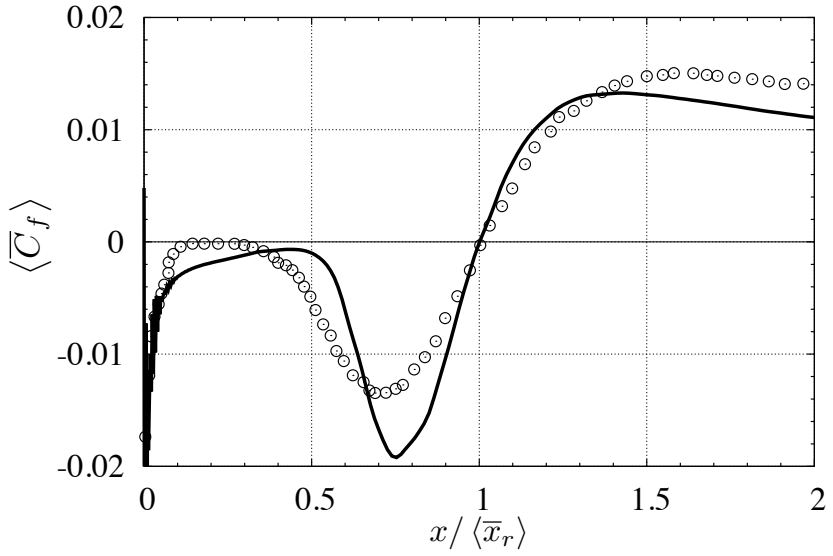

Figure 3.4: Variation of the averaged skin friction with the streamwise location normalized by the averaged reattachment point at $Re_c = 2.0 \times 10^4$. (solid-lines: present results; open-circles: numerical results by Tafti & Vanka (1991*b*).)

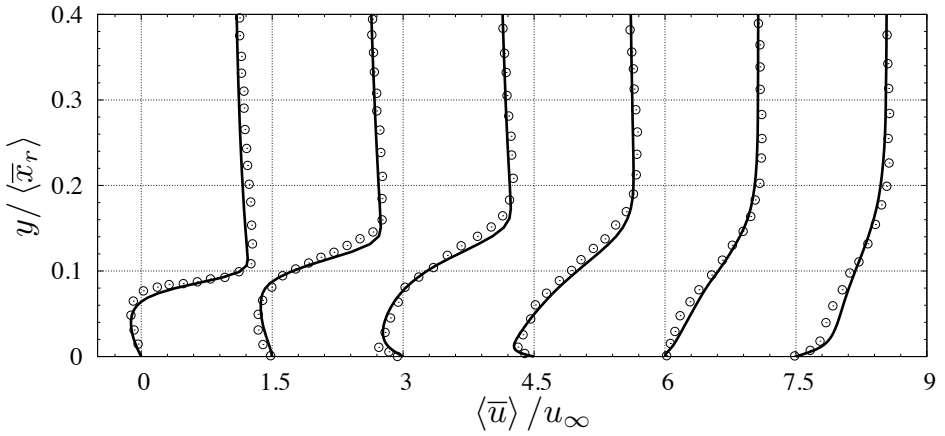

(a) Streamwise velocity

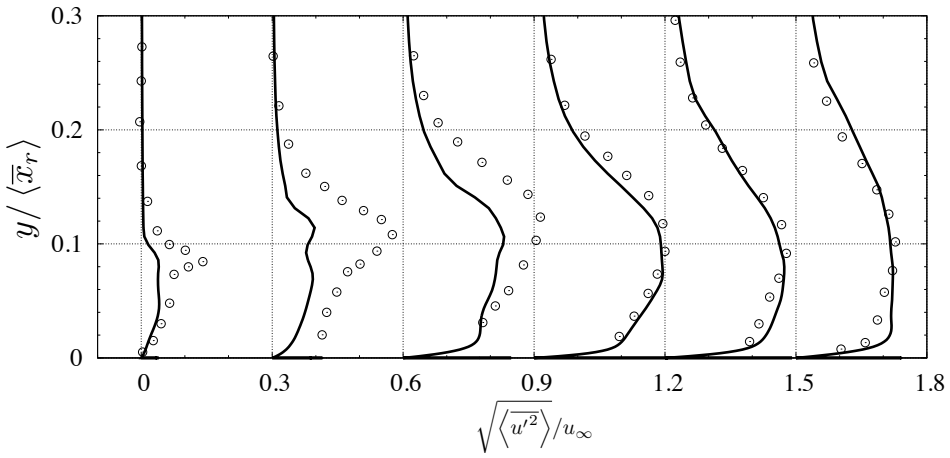

(b) Streamwise Reynolds normal stress

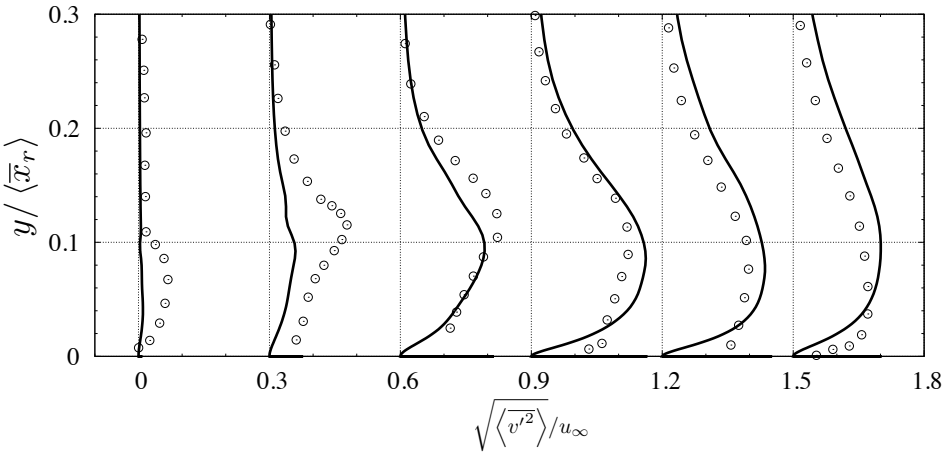

(c) Wall-normal Reynolds normal stress

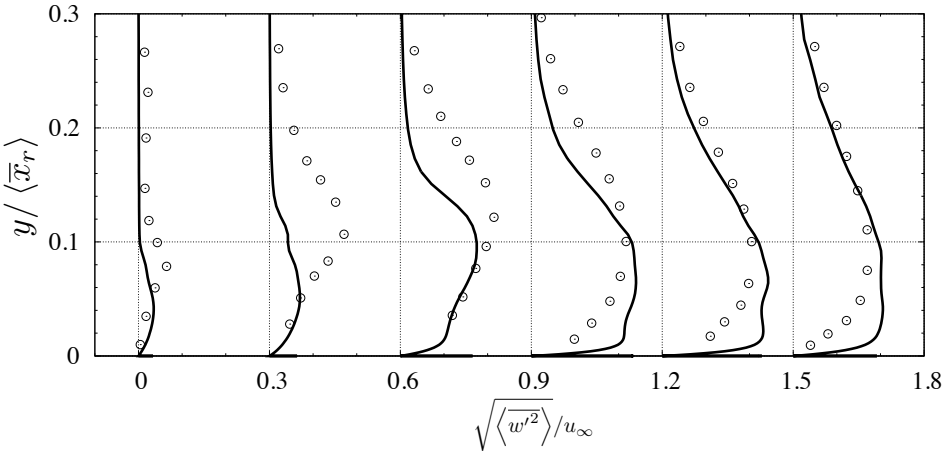

(d) Spanwise Reynolds normal stress

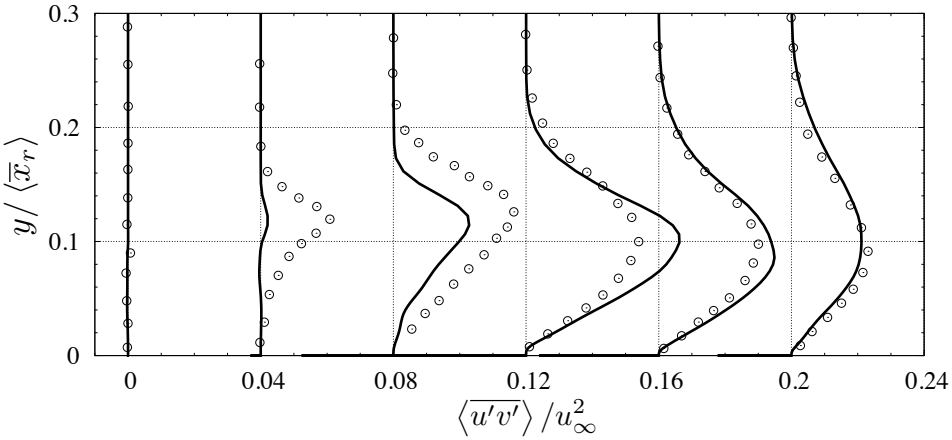

(e) Reynolds shear stress

Figure 3.5: (a) Streamwise velocity, (b) streamwise Reynolds normal stress, (c) wall-normal Reynolds normal stress, (d) spanwise Reynolds normal stress, and (e) Reynolds shear stress as a function of wall-normal distance at $x/\langle\overline{x}_r\rangle = 0.2$, 0.4, 0.6, 0.8, 1.0, and 1.2 and at $Re_c = 2.0 \times 10^4$. Each plot is separated by a horizontal offset of 1.5 in (a); 0.3 in (b), (c), and (d); and 0.04 in (e). (solid-lines: present results; open-circles: numerical results by Tafti & Vanka (1991*b*).)

3.2 Flow structures of instantaneous flow fields

Instantaneous flow fields around the flat plate for each Reynolds number are presented in this section. Figure 3.6 shows the instantaneous flow structures at $tu_\infty/c = 24$. The isosurfaces of the second invariant of the velocity gradient tensor (Q-criterion, Hunt *et al.*, 1988) are used to visualize vortex structures, where

$$Q_{cr} = \frac{1}{2}\frac{c^2}{u_\infty^2}\left(s_{ij}s_{ij} - (s_{kk})^2\right). \tag{3.1}$$

The value of $Q_{cr} = 1$ is selected for the visualization because the differences of the flow structures at the different Reynolds numbers are clearly visualized by this value. From the figure, different flow structures are clearly observed depending on the Reynolds number. First of all, the flows are separated from the leading edge at all of the Reynolds number cases. At $Re_c = 5.0 \times 10^3$, the separated shear layer reattaches on the surface without shedding of vortices. On the other hand, at $Re_c = 6.1 \times 10^3$ and 8.0×10^3, two-dimensional vortices which have an axis in the spanwise direction are generated from the separated shear layer. These consecutive vortex structures are created by the KH instability, and convected to downstream as maintaining two-dimensional structures in the entire flow fields. As further increasing the Reynolds number ($Re_c = 1.1 \times 10^4$ and 2.0×10^4), it is clearly seen that two-dimensional spanwise-extended vortices collapse to three-dimensional turbulent structures, and those structures reattach to the surface. In particular, the spanwise vorticity weakens in the downstream where the three-dimensional structures are generated. Figure 3.7 shows time histories of velocity profile at a certain point in the attached boundary layer for each Reynolds number. As can be seen from the figure, it is observed large fluctuation of the velocity and irregular oscillation due to turbulent structures at $Re_c = 1.1\times10^4$ and 2.0×10^4. At $Re_c = 6.1\times10^3$ and 8.0×10^3, it is seen the oscillation of velocity synchronized with the advection of the two-dimensional vortex. Although the instantaneous flow field of $Re_c = 5.0 \times 10^3$ seems that the separated shear layer steadily reattaches to the surface, it is also confirmed that the flow is not a completely steady state.

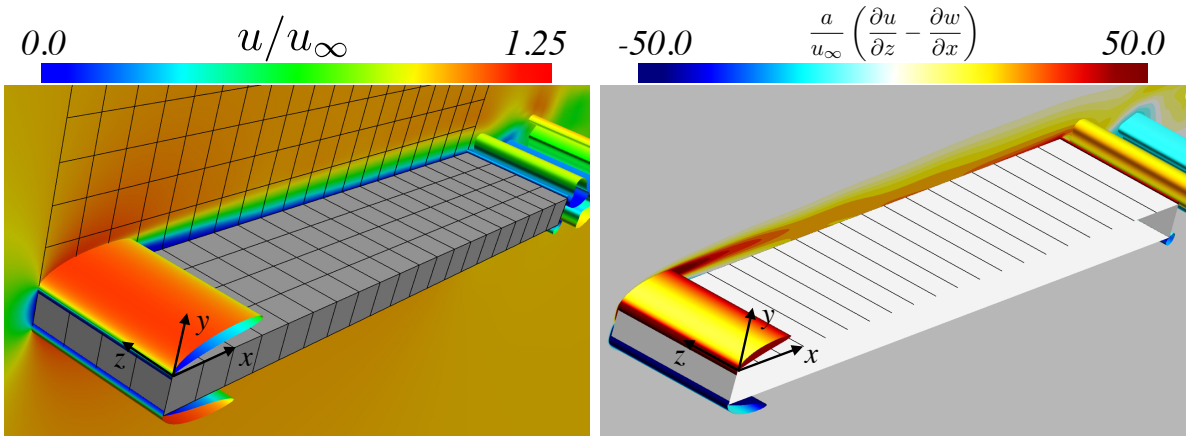

(a) $Re_c = 5.0 \times 10^3$

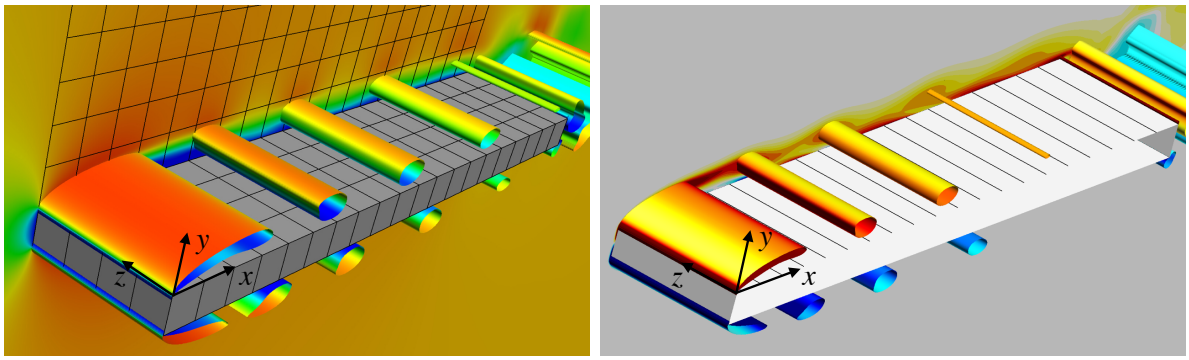

(b) $Re_c = 6.1 \times 10^3$

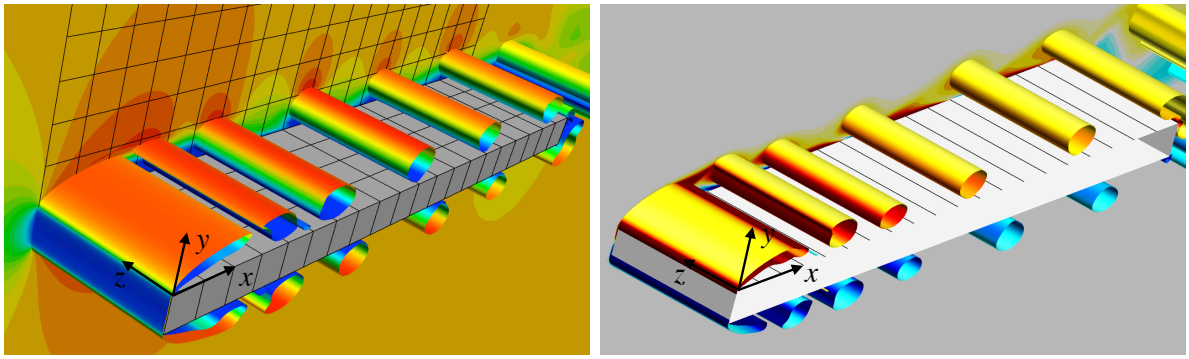

(c) $Re_c = 8.0 \times 10^3$

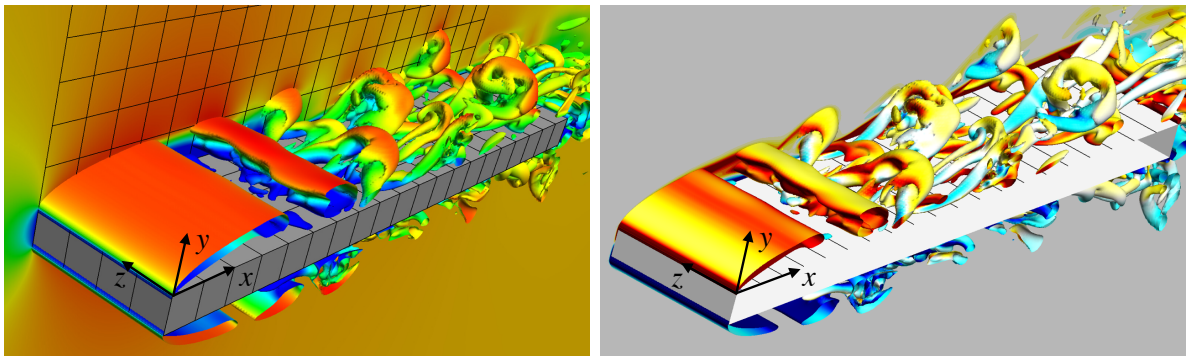

(d) $Re_c = 1.1 \times 10^4$

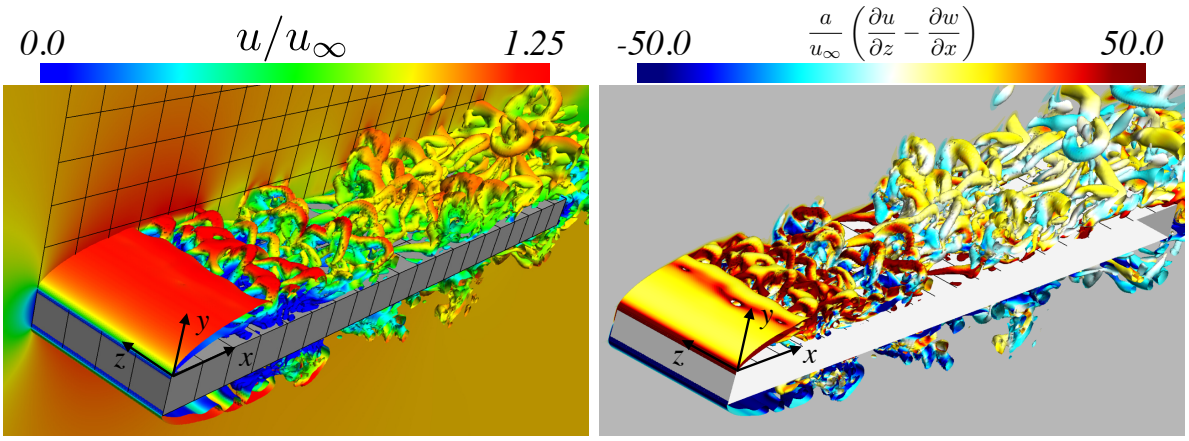

(e) $Re_c = 2.0 \times 10^4$

Figure 3.6: Instantaneous flow structures at $tu_\infty/c = 24$ at (a) $Re_c = 5.0 \times 10^3$, (b) $Re_c = 6.1 \times 10^3$, (c) $Re_c = 8.0 \times 10^3$, (d) $Re_c = 1.1 \times 10^4$, and (e) $Re_c = 2.0 \times 10^4$. The isosurfaces of the second invariant of the velocity gradient tensor ($Q_{cr} = 1.0$) are visualized in both column. The isosurfaces are colored by streamwise velocity (left column) and spanwise vorticity (right column). Every $0.05x/c$, $0.05y/c$, and $0.05z/c$ (left column) and $0.05x/c$ (right column) position is denoted by black lines.

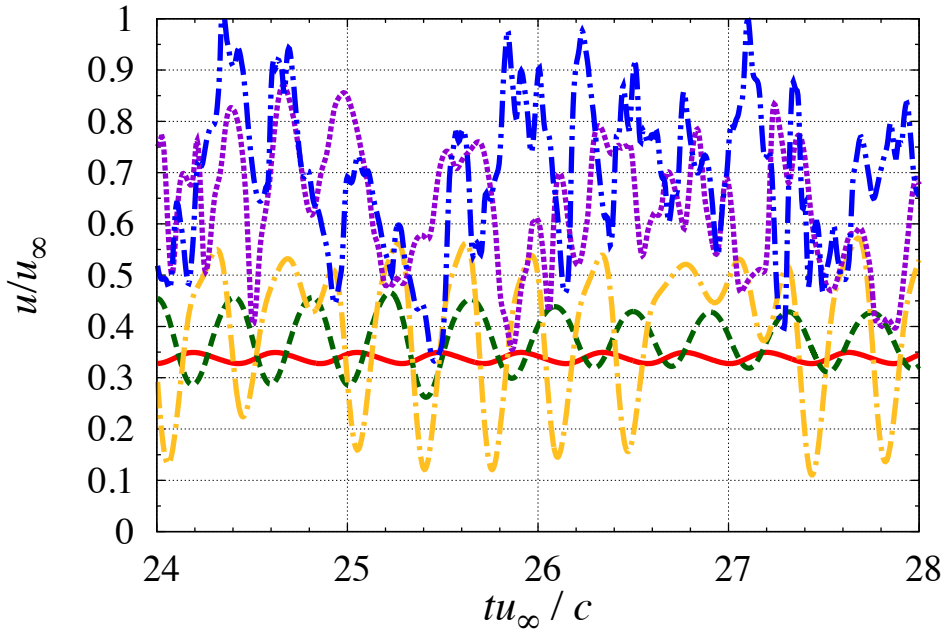

Figure 3.7: Time histories of the streamwise velocity ($x/c = 0.8$, $y/c = 0.015$, and $z/c = 0.1$) at $Re_c = 5.0 \times 10^3$ (solid-line, red), 6.1×10^3 (dashed-line, green), 8.0×10^3 (dashed-dotted-line, yellow), 1.1×10^4 (dotted-line, violet), and 2.0×10^4 (dashed-dobule-dotted-line, blue).

3.3 Classification of the separation bubble in averaged flow fields

3.3.1 Velocity and turbulent kinetic energy fields

Figure 3.8 shows the time- and spanwise-averaged streamwise velocity fields. Considering that white regions correspond to the reverse flows, the results indicate that the flow separates from the leading edge and reattaches on the surface; as a consequence, LSBs are formed at all the Reynolds numbers. The averaged reattachment points ($\langle \overline{x}_r \rangle / c$) are given in Tab. 3.3. They are determined as locations where $\langle \overline{C}_f \rangle$ becomes zero with a positive slope (i.e., the skin friction coefficient turns from negative to positive). The reattachment point first moves to the downstream as the Reynolds number increases, and then the reattachment point moves upstream by increasing the Reynolds number. The maximum length of the LSB is observed at $Re_c = 1.1 \times 10^4$ in this study.

Table 3.3: Reattachment points ($\langle \overline{x}_r \rangle / c$) of each Reynolds number

Re_c	5.0×10^3	6.1×10^3	8.0×10^3	1.1×10^4	2.0×10^4
$\langle \overline{x}_r \rangle / c$	0.242	0.345	0.345	0.388	0.277

Although formation of LSBs are observed at all Reynolds numbers, interesting characteristics appear in the turbulent kinetic energy (TKE) flow fields inside of LSBs. Figure 3.9 shows TKE fields near LSBs, where the TKE is defined by following equations,

$$\mathrm{TKE} = \frac{1}{2} \frac{\left\langle \overline{u'^2} \right\rangle + \left\langle \overline{v'^2} \right\rangle + \left\langle \overline{w'^2} \right\rangle}{u_\infty^2}. \tag{3.2}$$

First of all, the TKE is negligibly small at the lower Reynolds numbers ($Re_c = 5.0 \times 10^3$ and 6.1×10^3) through the entire LSB, although the instantaneous flow fields are not completely steady states because of the weak two-dimensional vortices. At these Reynolds numbers, it is confirmed by Fig. 3.10 that the maximum TKE is less than $0.003 u_\infty^2$. Hereafter, this type of LSB is called as a steady laminar separation bubble, or simply *"LSB_S"*, in this thesis. At the higher Reynolds numbers ($Re_c = 8.0 \times 10^3$, 1.1×10^4 and 2.0×10^4), however, the characteristics of the LSB show two region. The first region is that the TKE is approximately zero ($0.0 \leq x/c \lesssim 0.21$ at $Re_c = 8.0 \times 10^3$, $0.0 \leq x/c \lesssim 0.19$ at $Re_c = 1.1 \times 10^4$, and $0.0 \leq x/c \lesssim 0.14$ at $Re_c = 2.0 \times 10^4$), as similar to the LSB_S cases. Following the steady region, a high TKE region appears

in the downstream due to the fluctuation ($0.21 \lesssim x/c \leq 0.345$ at $Re_c = 8.0 \times 10^3$, $0.19 \lesssim x/c \leq 0.388$ at $Re_c = 1.1 \times 10^4$, and $0.14 \lesssim x/c \leq 0.277$ at $Re_c = 2.0 \times 10^4$). In other words, the steady (laminar) and fluctuating (turbulent) parts coexist within the LSB. Hereafter, this type of LSB is called as a steady-fluctuating laminar separation bubble, or simply *"LSB_SF"*. The characteristics of LSB is clearly seen by the maximum TKE distributions at the location normalized by the averaged reattachment point (see, Fig. 3.10). The maximum TKE is negligible at the lower Reynolds number whereas that abruptly increases from 40% of the bubble length at higher Reynolds numbers. After that, the maximum TKE shows the maximum value at approximately 80% of the LSB length and then decreases toward the reattachment point irrespective of the Reynolds numbers. Here, the criterion for dividing of the steady and fluctuating region in this thesis is considered as the location where the maximum TKE becomes larger than 2% of u_∞^2. It should be noted that the critical Reynolds number which allows the classification of LSB_S and LSB_SF may change depending on the criterion value. Also, the length of each region is affected by setting of the criterion. However, the identification of critical Reynolds number is not an objective of this study, and an important point is that the internal state of LSBs varies with the Reynolds number even similar LSBs are observed in appearance. As a result, the criterion adopted in the present study appears around 50% to 60% of the LSB length. In other words, with respect to 50% of the LSB length, the front side corresponds to the steady region and the rear side does the fluctuating region, respectively.

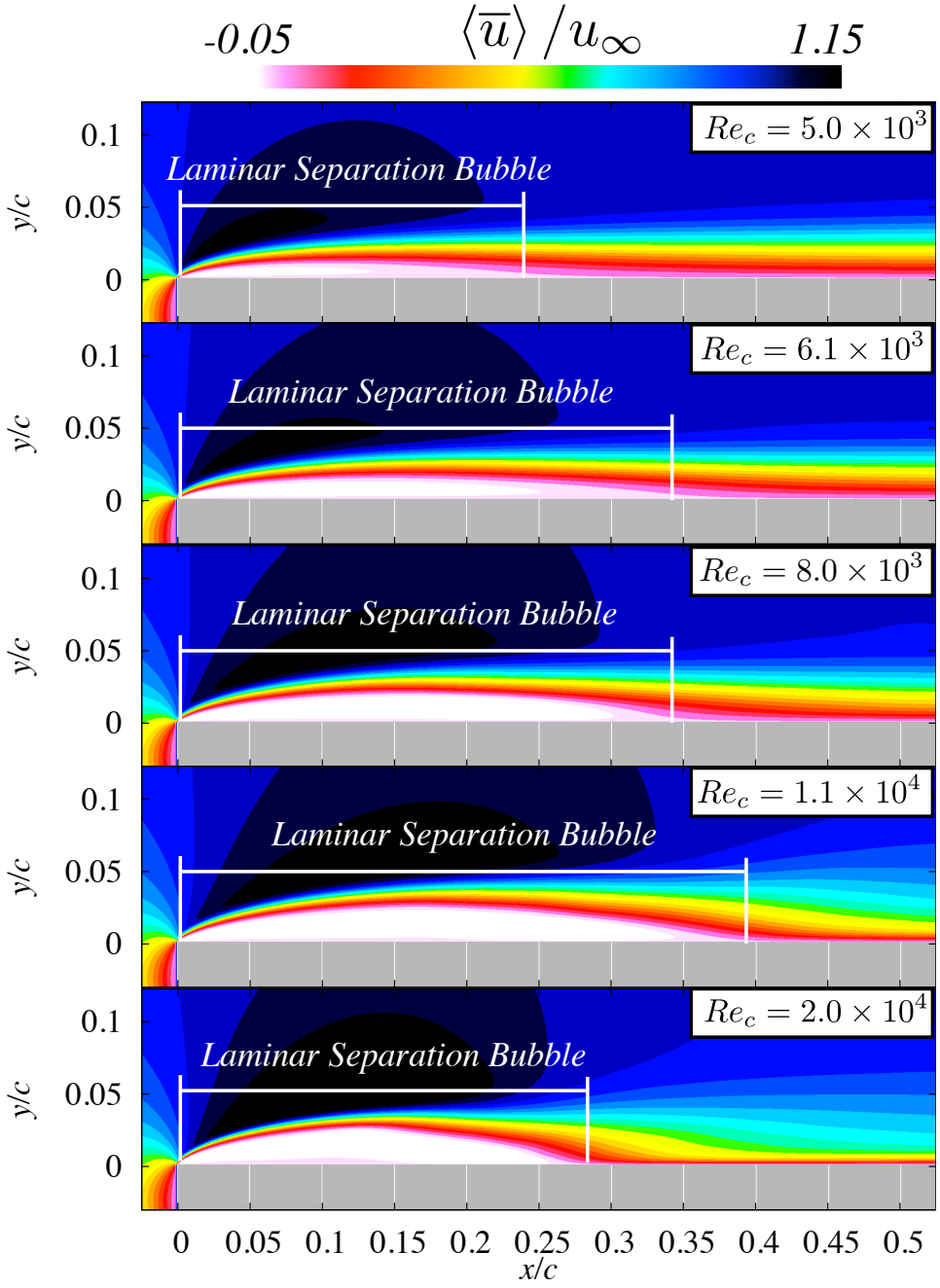

Figure 3.8: Time- and spanwise-averaged streamwise velocity fields around LSBs at $Re_c = 5.0 \times 10^3$, 6.1×10^3, 8.0×10^3, 1.1×10^4, and 2.0×10^4.

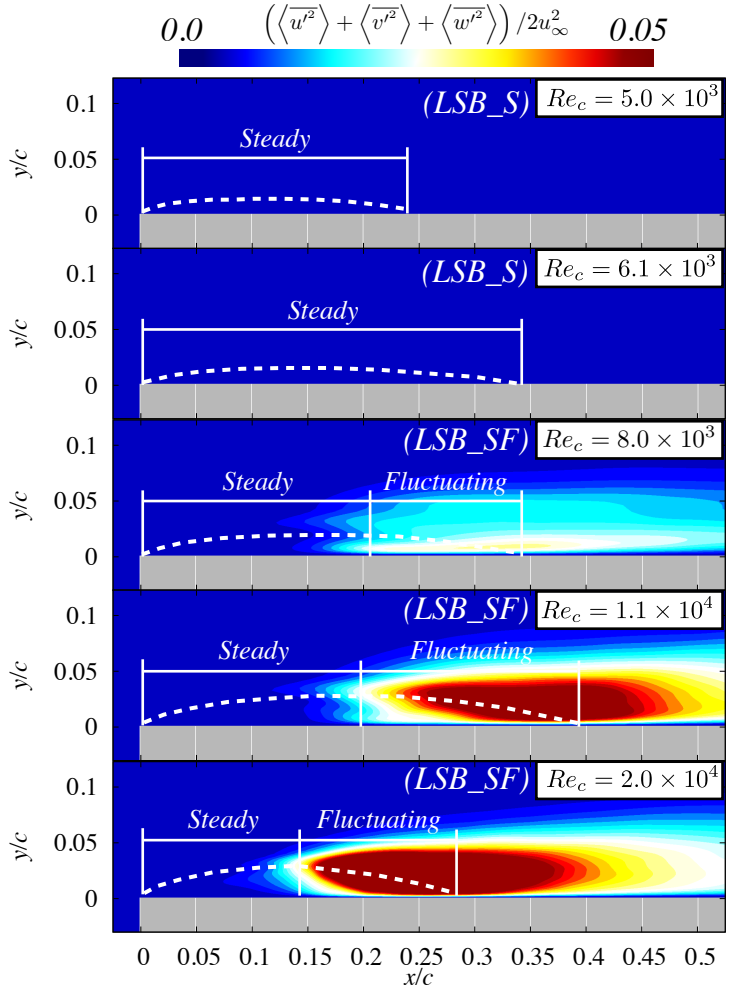

Figure 3.9: Turbulent kinetic energy flow fields at $Re_c = 5.0 \times 10^3$, 6.1×10^3, 8.0×10^3, 1.1×10^4, and 2.0×10^4. White dashed-lines indicate the outer layer of LSBs.

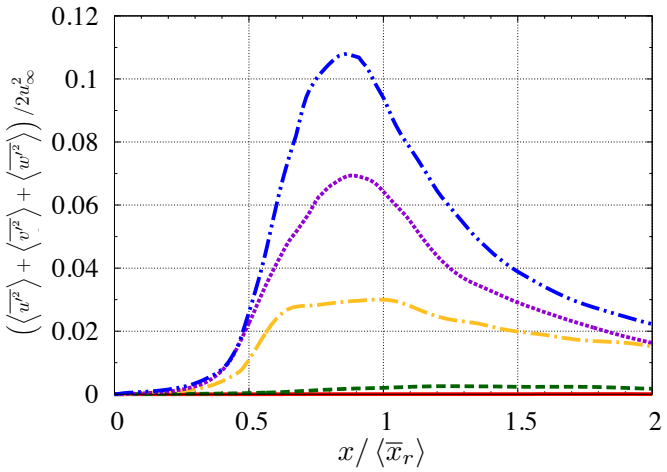

Figure 3.10: Maximum turbulent kinetic energy distributions at $Re_c = 5.0 \times 10^3$ (solid-line, red), 6.1×10^3 (dashed-line, green), 8.0×10^3 (dashed-dotted-line, yellow), 1.1×10^4 (dotted-line, violet), and 2.0×10^4 (dashed-dobule-dotted-line, blue).

3.3.2 Surface pressure distribution and skin friction coefficient

The averaged pressure coefficient ($\langle \overline{C}_p \rangle$) on the surface and skin friction coefficient ($\langle \overline{C}_f \rangle$) around LSBs are shown in Fig. 3.11. Note that the streamwise location is normalized by the plate length in Fig. 3.11 (a) while by the averaged reattachment point in Fig. 3.11 (b), respectively. Thus, $0 \leq x/\langle \overline{x}_r \rangle \leq 1$ corresponds to the separated area while $x/\langle \overline{x}_r \rangle \geq 1$ does the attached boundary layer. First of all, in the LSB_S cases ($Re_c \leq 6.1 \times 10^3$), the continuous gradual pressure recovery is observed within the entire separated region without showing the plateau distribution. The skin friction coefficient also gradually and monotonically increases toward the reattachment point. On the other hand, as the Reynolds number increases ($Re_c \geq 8.0 \times 10^3$, LSB_SF), the pressure distributions begin to show the typical plateau region followed by the rapid pressure recovery in the downstream. It is clearly seen in Fig. 3.11 (b) that the plateau and rapid pressure recovery region are approximately divided by 50% of the bubble length. Considering the fact discussed in the previous section, the plateau pressure distribution is observed in the steady region whereas the rapid pressure recovery appears in the fluctuating region. At these Reynolds numbers, the skin friction coefficient monotonically increases in the steady region whereas a negative peak appears within the fluctuating region. An interesting point is that the shape of pressure distributions are different between the LSB_S and LSB_SF cases even in the same steady flow. In other words, the gradual pressure recovery region appears within the steady region of the LSB_S cases, whereas the constant pressure distribution is observed inside the steady region of the LSB_SF cases. This fact suggests that the different shapes of pressure distribution are affected by other factors rather than the steady flow condition under the separated shear layer.

Let us focus on the flow state under the separated shear layer. Figures 3.12 and 3.13 show the streamwise velocity flow fields in the reverse flow region and minimum streamwise velocity distributions inside the LSB. In the LSB_S cases, once the maximum reverse flow region is formed near the leading edge, its strength gradually decreases toward the reattachment point. In the LSB_SF cases, however, the reverse flow is further strongly formed from the vicinity of the center of LSB, and it becomes drastically weak from 75% of bubble length to the reattachment point. Here, let us consider the previous explanations about formation mechanisms of surface pressure distribution around an LSB (see, Sec. 1.3). The region of appearing the plateau pressure distribution has been thought that the velocity of the flow under the separated shear layer is circulated slowly, and it results in the constant pressure distributions. From Fig. 3.13, however, the strength of reverse flow in the steady region is similar (approximately 10% to the freestream)

regardless of the Reynolds numbers. Strictly speaking, the strength of reverse flow of the LSB_S is slightly lower than that of the LSB_SF. Assuming, however, that this is not a meaningful difference, it is seen that the shapes of surface pressure distribution are different even in the similar reverse flow state under the separated shear layer. Moreover, another interesting point is that the flow structures of $Re_c = 8.0 \times 10^3$ remain two-dimensional in the entire flow fields even though the rapid pressure recovery region is observed. As already noted, it has been thought that the momentum transfer by three-dimensional turbulent motions is a key factor for the rapid pressure recovery. These results, however, indicate that the pressure gradient can be suddenly varied even if there is no transition. In other words, the occurrence of rapid pressure recovery may not be always substantially affected by the transition and three-dimensional structures.

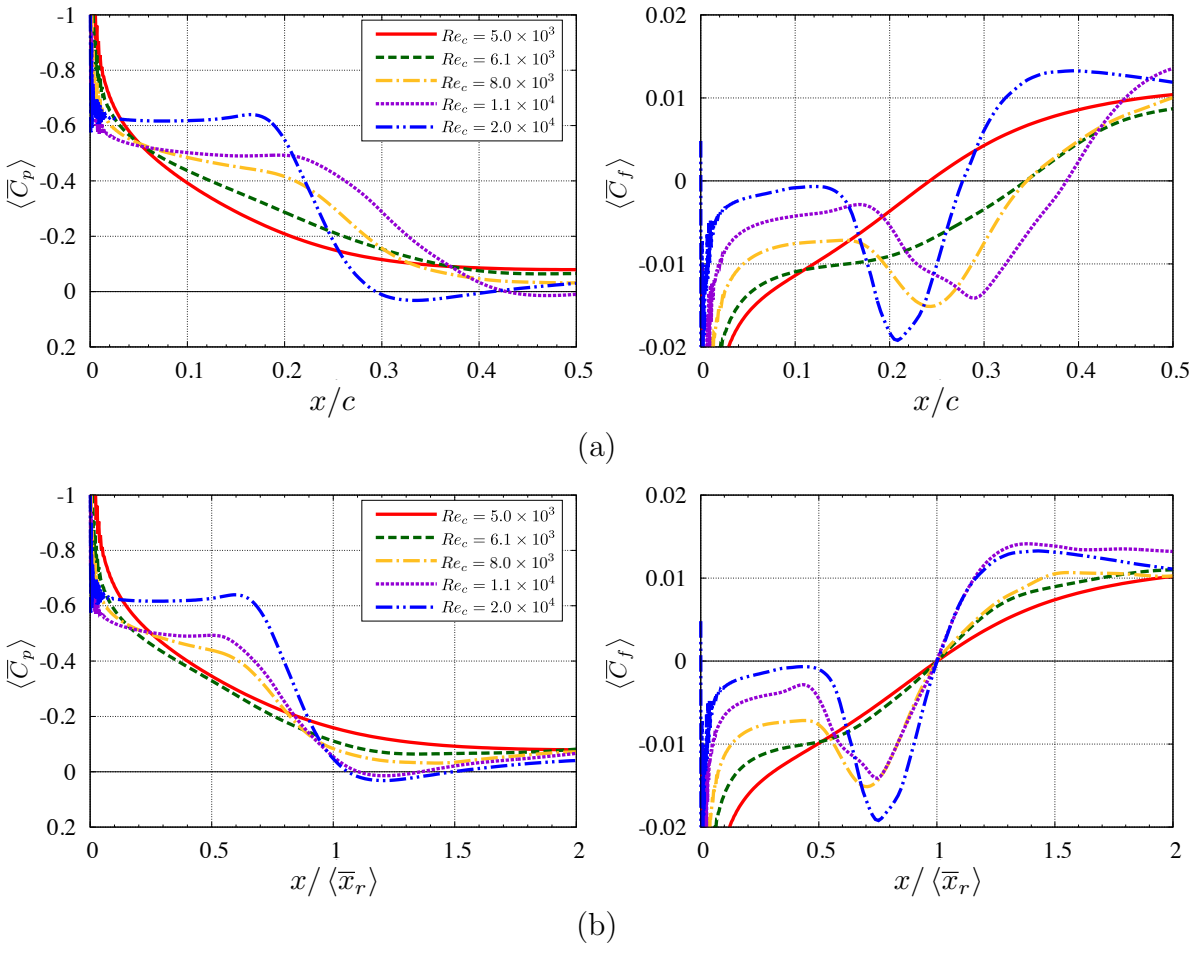

Figure 3.11: Time- and Spanwise averaged surface pressure distributions (left) and skin friction coefficients (right) at $Re_c = 5.0 \times 10^3$ (solid-line, red), 6.1×10^3 (dashed-line, green), 8.0×10^3 (dashed-dotted-line, yellow), 1.1×10^4 (dotted-line, violet), and 2.0×10^4 (dashed-dobule-dotted-line, blue). The location from the leading edge is normalized by the (a) plate length and (b) length of the LSB, respectively.

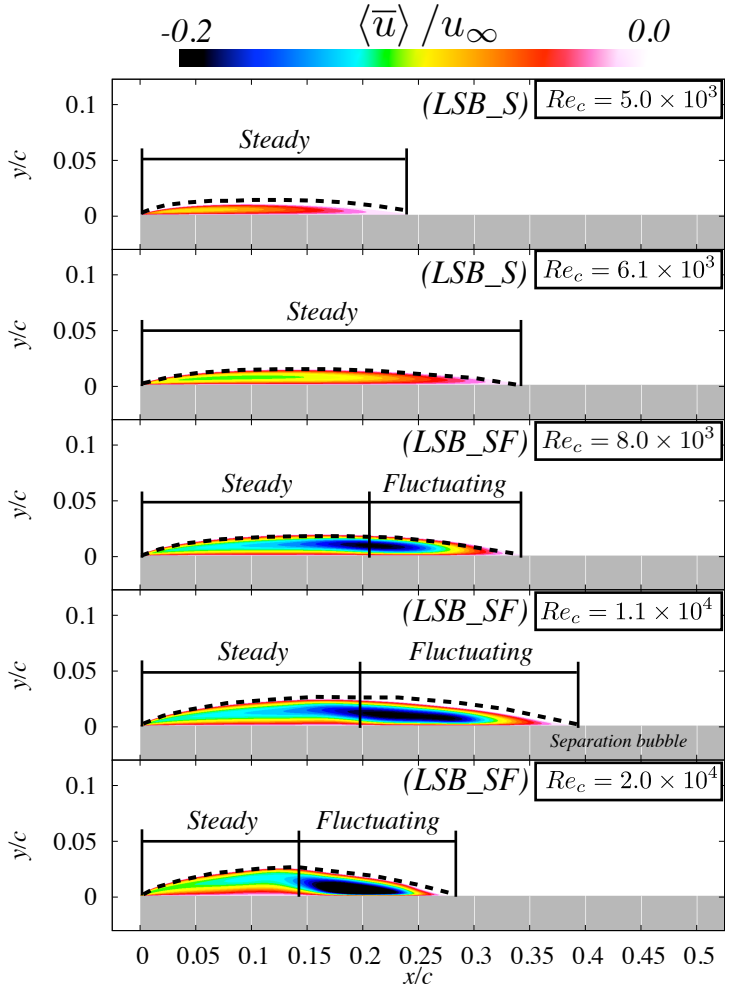

Figure 3.12: Reverse flow region inside the LSBs at $Re_c = 5.0 \times 10^3$, 6.1×10^3, 8.0×10^3, 1.1×10^4, and 2.0×10^4. Black dashed-lines indicate the outer layer of LSBs.

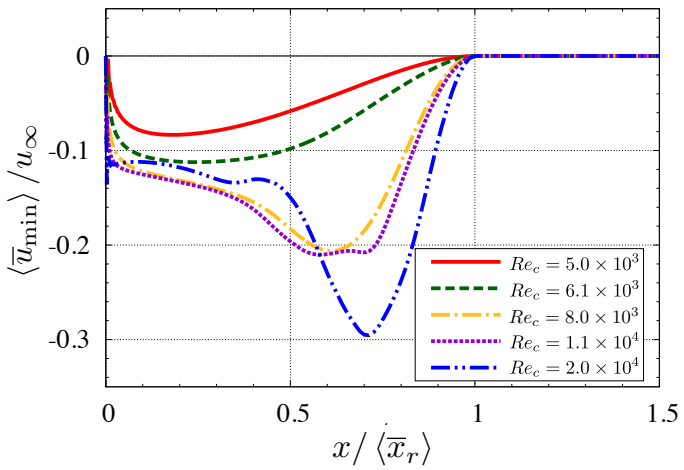

Figure 3.13: Minimum streamwise velocity distribution inside the LSBs at $Re_c = 5.0 \times 10^3$ (red, line), 6.1×10^3 (green, dashed-line), 8.0×10^3 (yellow, dashed-dotted-line), 1.1×10^4 (purple, dotted-line), and 2.0×10^4 (blue, dashed-double-dotted-line).

3.3.3 Shape factor and reattachment state

In this section, the reattachment state of the separated shear layer depending on the Reynolds number is discussed. The instantaneous flow structures suggest that the flow reattaches as the laminar state at $Re_c \leq 8.0 \times 10^3$ while as the turbulent state at $Re_c \geq 1.1 \times 10^4$. For more precise determination of the reattachment state, the time- and spanwise-averaged velocity profiles at $0.7x/c$ from the leading edge are investigated (see, Fig. 3.14). First of all, it is confirmed that the profiles of $Re_c \leq 8.0 \times 10^3$ follow closely to $\langle\overline{u}\rangle^+ = y^+$. Thus, it indicates that the attached boundary layer has a laminar characteristic at these Reynolds numbers. In addition, this result suggests that the reattachment state can be judged as the laminar state even in the unsteady flow in which the two-dimensional spanwise vortices convect. On the other hand, the buffer layer ($5 < y^+ < 30$) and log-law region ($y^+ > 30$) are seen at $Re_c \geq 1.1 \times 10^4$, which indicates a turbulent boundary layer profile. Therefore, it is judged that the laminar reattachment occurs at $Re_c \leq 8.0 \times 10^3$ whereas the turbulent reattachment appears at $Re_c \geq 1.1 \times 10^4$ in this thesis. These results agree with the experimental results of Anyoji *et al.* (2011), as shown in Fig. 1.12.

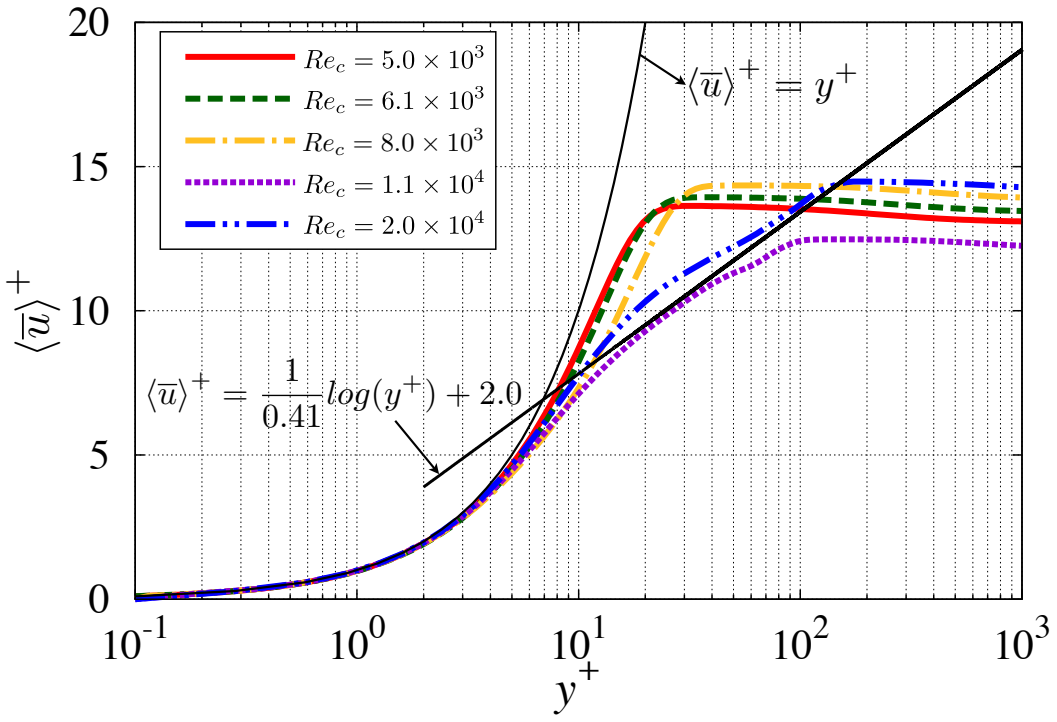

Figure 3.14: Time- and spanwise-averaged velocity profiles at $0.7x/c$ at $Re_c = 5.0 \times 10^3$ (solid-line, red), 6.1×10^3 (dashed-line, green), 8.0×10^3 (dashed-dotted-line, yellow), 1.1×10^4 (dotted-line, violet), and 2.0×10^4 (dashed-dobule-dotted-line, blue).

Another evidence for the reattachment state is found in the time- and spanwise-averaged shape factor $\langle \overline{H} \rangle$ at the reattachment points ($\langle \overline{H}_r \rangle$) and $0.7x/c$ ($\langle \overline{H}_{0.7x/c} \rangle$), as shown in Fig. 3.15. The shape factor is given by the following equation:

$$\langle \overline{H} \rangle = \frac{\langle \overline{\delta^*} \rangle}{\langle \overline{\theta} \rangle}, \tag{3.3}$$

and the displacement thickness $\langle \overline{\delta^*} \rangle$ and momentum thickness $\langle \overline{\theta} \rangle$ for the averaged streamwise velocity profiles are defined by

$$\langle \overline{\delta^*} \rangle = \int_0^{0.99u_\infty} \left(1 - \frac{\langle \overline{u}(y) \rangle}{u_\infty} \right) dy, \tag{3.4}$$

$$\langle \overline{\theta} \rangle = \int_0^{0.99u_\infty} \frac{\langle \overline{u}(y) \rangle}{u_\infty} \left(1 - \frac{\langle \overline{u}(y) \rangle}{u_\infty} \right) dy. \tag{3.5}$$

The results also indicate that the laminar reattachment appears at $Re_c \leq 8.0 \times 10^3$ and turbulent reattachment occurs at $Re_c \geq 1.1 \times 10^4$. First, $\langle \overline{H}_r \rangle$ is approximately 2.8 in the turbulent reattachment case. Dengel & Fernholz (1990) and Alving & Fernholz (1995) reported that the shape factor of turbulent reattachment point is $2.75 \sim 2.85$, and the present results are in good agreement with them. In the laminar reattachment cases, on the other hand, $\langle \overline{H}_r \rangle > 3.8$ which is obviously higher than that of the turbulent reattachment cases. The value of $\langle \overline{H}_{0.7x/c} \rangle$ can also identify the boundary layer state in the downstream of the reattachment. The conventional values of the shape factor for the laminar and turbulent boundary layers over a zero pressure gradient flat plate are referred to as $\langle \overline{H} \rangle = 2.6$ and $\langle \overline{H} \rangle = 1.4$, respectively (Schlichting & Gersten, 1979; Suluksan & Juntasaro, 2008). It is confirmed that the values of $Re_c \leq 8.0 \times 10^3$ are close to those of the laminar boundary layer whereas those of $Re_c \geq 1.1 \times 10^4$ are slightly higher but close to those of the turbulent boundary layer. One more characteristic point is that the shape factor clearly decreases when the flow state changes from laminar to turbulent state, and it is independent the location where the shape factor is taken. In order to examine the reason of appearing these differences, the displacement thickness and momentum thickness at each Reynolds numbers are investigated as shown in Fig. 3.16. Pope (2000) interpreted the physical meaning of shape factor as the quantification of the flatness of velocity profiles. Schubauer & Spangengerg (1960) mentioned that the mixing effect inside the attached boundary layer can be quantitatively represented by the shape factor, and the reason of decreasing shape factor from the laminar to turbulent boundary layer is caused by the decreasing of the displacement thickness. From the figure, it is also shown that the displacement thickness of the turbulent boundary layer is lower than

that of the laminar boundary layer in the attached region ($x/\langle\overline{x}_r\rangle = 2.0$). In addition, the momentum thickness increases as the flow changes from the laminar to turbulent boundary layer, and hence it results in the decreasing of the shape factor in the turbulent boundary layer. In terms of the reattachment point, it is observed that the momentum thickness abruptly increases when the flow is reattached by three-dimensional structures. Thus, it can be considered that an increase in the momentum thickness contributes to a decrease in the shape factor. One more important point for the relationship between surface pressure distribution and reattachment state is that the laminar reattachment may occurs when the LSB_SF is formed. As discussed in the previous section, it has been thought that the rapid pressure recovery is caused by the presence of three-dimensional turbulent structures, but the result of $Re_c = 8.0 \times 10^3$ indicates that the rapid pressure recovery may occur even without the transition phenomena.

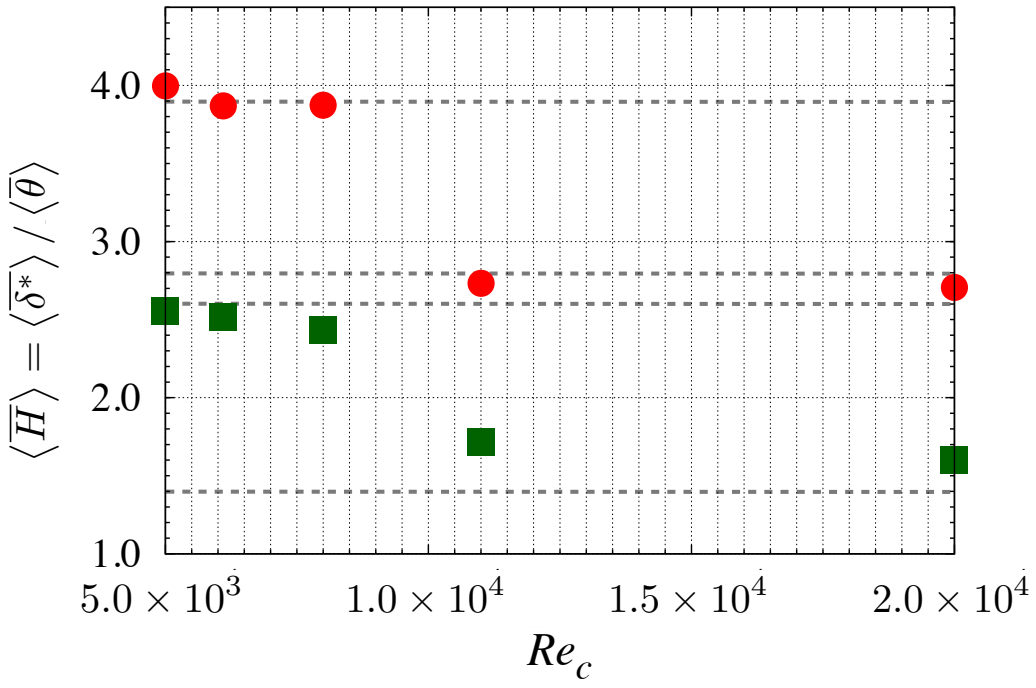

Figure 3.15: Variation of the shape factors at $0.7x/c$ (filled-circles, red) and reattachment point (filled-squares, green). Four different dashed-lines colored by grey indicate the reference values in case of laminar reattachment at reattachment point ($\langle\overline{H}\rangle = 3.9$), turbulent reattachment at reattachment point ($\langle\overline{H}\rangle = 2.8$), laminar boundary layer ($\langle\overline{H}\rangle = 2.6$), and turbulent boundary layer ($\langle\overline{H}\rangle = 1.4$).

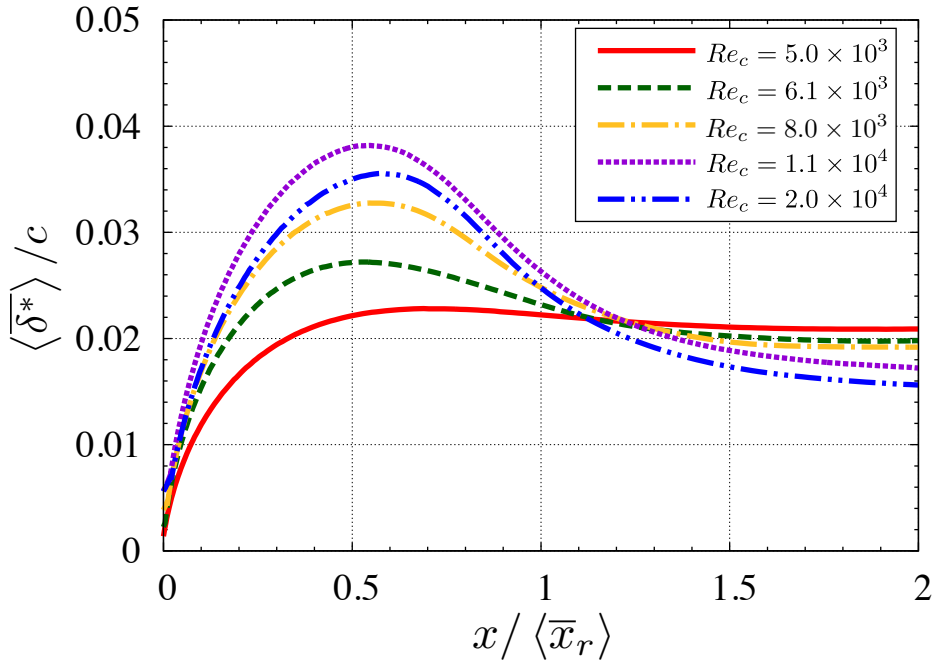

(a) Displacement thickness

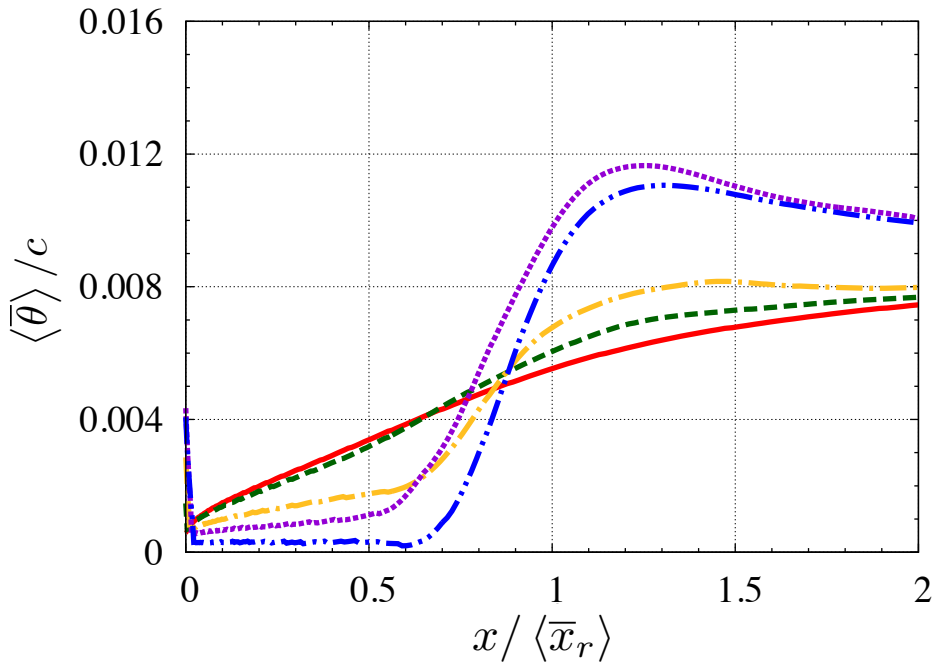

(b) Momentum thickness

Figure 3.16: (a) Displacement thickness and (b) momentum thickness distributions at $Re_c = 5.0 \times 10^3$ (solid-line, red), 6.1×10^3 (dashed-line, green), 8.0×10^3 (dashed-dotted-line, yellow), 1.1×10^4 (dotted-line, violet), and 2.0×10^4 (dashed-dobule-dotted-line, blue).

3.4 Summary

In this chapter, the classification of LSB characteristics is discussed. First of all, two types of LSBs are shown by the analysis based on the TKE flow fields. At $Re_c = 5.0 \times 10^3$ and 6.1×10^3, the flow can be considered as the laminar (steady) state within the entire LSB because of the negligibly small TKE, and this type of LSB is called as the steady laminar separation bubble (LSB_S). At $Re_c = 8.0 \times 10^3$, 1.1×10^4, and 2.0×10^4, on the other hand, the laminar (steady) and turbulent (fluctuating) portions coexist within the LSB, and hence this type of LSB is called as the steady-fluctuating laminar separation bubble (LSB_SF) in the present study. Note that the criterion of dividing of the steady and fluctuating region is considered as the location where the maximum TKE becomes larger than 2% of u_∞^2. Next, the instantaneous flow fields of $Re_c = 5.0 \times 10^3$, 6.1×10^3, and 8.0×10^3 remain two-dimensional structures in the entire fields whereas those of $Re_c = 1.1 \times 10^4$ and 2.0×10^4 have transition and three-dimensional turbulent structures. Corresponding to the instantaneous flow fields, the laminar reattachment occurs at $Re_c = 5.0 \times 10^3$, 6.1×10^3, and 8.0×10^3 whereas the turbulent reattachment is observed at $Re_c = 1.1 \times 10^4$ and 2.0×10^4. The reattachment characteristics is confirmed by the wall-unit based velocity profiles at attached boundary layer as well as the shape factors of the reattachment point and those of the attached boundary layer. Through the analysis of the present chapter, following three phenomena are newly observed.

- Depending on the LSB characteristics classified above, different shape of pressure distribution is observed. First of all, in the LSB_S cases ($Re_c \leq 6.1 \times 10^3$), the continuous gradual pressure recovery is observed without showing the plateau region. On the other hand, in the LSB_SF cases ($Re_c \geq 8.0 \times 10^3$), the pressure distributions begin to show the typical plateau region in the steady region and the rapid pressure recovery appears in the fluctuating region. The shape of pressure distribution such as the constant pressure region followed by the rapid pressure recovery has been observed in many cases of an LSB. From the results of LSB_S, it is newly found that the formation of LSB is not always accompanying the typical shape of pressure distribution mentioned above.

- The pressure distributions are different depending on the Reynolds numbers, despite of the fact that a two-dimensional similar steady state appeared under the separated shear layer. Different pressure distribution is obtained even the flow is two-dimensional and its state under the separated shear layer is similarly steady. The pressure is recovered gradually in the LSB_S cases whereas the constant pres-

sure distribution appears in the LSB_SF cases. The reason of appearing the plateau pressure distribution region has been thought that because the velocity of the flow under the separated shear layer is slowly circulated. It can be considered as a practically steady state, so the streamwise pressure gradient is nearly zero and the plateau pressure distribution appears. The results of LSB_S, however, suggest that the different shapes of pressure distribution are affected by other factors rather than the steady flow condition under the separated shear layer.

- The laminar reattachment may occur even an LSB is formed with appearing the typical shape of pressure distribution. The flow structures of $Re_c = 8.0 \times 10^3$ remain two-dimensional in the entire flow fields even though the rapid pressure recovery region is observed in the surface pressure distributions. It has been thought that the rapid pressure recovery is caused by the momentum transfer due to the three-dimensional turbulent structures. These results, however, clearly indicate that the pressure gradient can be suddenly varied even if there is no transition. In other words, the occurrence of rapid pressure recovery may not be always substantially affected by the transition and three-dimensional structures.

Chapter 4

Formation mechanisms of surface pressure distribution

In this chapter, I discuss the mechanisms behind the different shapes of pressure distribution in each steady and fluctuating region of LSBs. First of all, a derivation of the averaged pressure gradient equation from the streamwise momentum equation is described in Sec. 4.1. Section 4.2 presents spatial distributions of each term which composes the averaged pressure gradient equation. It is qualitatively discussed the physical phenomena which affect the formation of pressure gradient, and then the physical mechanisms related to the formation of surface pressure gradient in the steady and fluctuating region are discussed in Sec. 4.3 and Sec. 4.4, respectively.

4.1 Derivation of the averaged pressure gradient equation

As a methodology for clarifying the physical mechanisms of the different shapes of pressure distribution, an averaged pressure gradient equation is derived from the streamwise momentum equation. From Eq. (2.2), the momentum equation in x direction is

$$\frac{\partial}{\partial t}(\rho u) + \frac{\partial}{\partial x_j}(\rho u u_j) = -\frac{\partial p}{\partial x} + \frac{1}{Re_c}\frac{\partial}{\partial x_j}\tau_{1j} \ , \qquad (j = 1, 2, 3). \tag{4.1}$$

Substituting the viscous stress tensor (Eq. (2.4)) into the equation,

$$\frac{\partial}{\partial t}(\rho u) + \frac{\partial}{\partial x_j}(\rho u u_j) = -\frac{\partial p}{\partial x} + \frac{1}{Re_c}\frac{\partial}{\partial x_j}\left(2\mu s_{1j} - \frac{2}{3}\mu\delta_{1j}s_{kk}\right) \ , \ (j = 1, 2, 3). \tag{4.2}$$

The second term in the RHS of Eq. (4.2) can be rewritten by substituting the rate of strain tensor (Eq. (2.7)),

$$\begin{aligned}
\frac{1}{Re_c}\frac{\partial}{\partial x_j}\left(2\mu s_{1j}-\frac{2}{3}\mu\delta_{1j}s_{kk}\right) &= \frac{1}{Re_c}\frac{\partial}{\partial x_j}\left(\mu\left(\frac{\partial u}{\partial x_j}+\frac{\partial u_j}{\partial x}\right)-\frac{2}{3}\mu\left(\frac{\partial u_j}{\partial x_j}\right)\right)\\
&= \frac{1}{Re_c}\frac{\partial}{\partial x_j}\left(\mu\frac{\partial u}{\partial x_j}\right)+\frac{1}{Re_c}\frac{\partial}{\partial x_j}\left(\mu\frac{\partial u_j}{\partial x}\right)-\frac{2}{3}\frac{1}{Re_c}\frac{\partial}{\partial x}\left(\mu\frac{\partial u_j}{\partial x_j}\right)\\
&= \frac{1}{Re_c}\frac{\partial}{\partial x_j}\left(\mu\frac{\partial u}{\partial x_j}\right)+\frac{1}{Re_c}\frac{\partial}{\partial x}\left(\mu\frac{\partial u_j}{\partial x_j}\right)-\frac{2}{3}\frac{1}{Re_c}\frac{\partial}{\partial x}\left(\mu\frac{\partial u_j}{\partial x_j}\right)\\
&= \frac{1}{Re_c}\frac{\partial}{\partial x_j}\left(\mu\frac{\partial u}{\partial x_j}\right)+\frac{1}{3}\frac{1}{Re_c}\frac{\partial}{\partial x}\left(\mu\frac{\partial u_j}{\partial x_j}\right). \qquad (4.3)
\end{aligned}$$

Therefore,

$$\frac{\partial}{\partial t}(\rho u)+\frac{\partial}{\partial x_j}(\rho u u_j)=-\frac{\partial p}{\partial x}+\frac{1}{Re_c}\frac{\partial}{\partial x_j}\left(\mu\frac{\partial u}{\partial x_j}\right)+\frac{1}{3}\frac{1}{Re_c}\frac{\partial}{\partial x}\left(\mu\frac{\partial u_j}{\partial x_j}\right),\ (j=1,2,3). \quad (4.4)$$

Here, any flow variable f is decomposed into an average component $\overline{f}$ and a fluctuating component f', i.e. $f=\overline{f}+f'$. If the time- and spanwise-averaged solution is considered, the first term of LHS in Eq. (4.4) (i.e., time derivative term) can be ignored. Moreover, some terms related to the spanwise direction ($j=3$) can be also neglected. As a result, the second term of LHS in Eq. (4.4) is

$$\begin{aligned}
\left\langle\overline{\frac{\partial}{\partial x_j}(\rho u u_j)}\right\rangle &= \frac{\partial}{\partial x_j}\left\langle\overline{(\overline{\rho}+\rho')\,(\overline{u}+u')\,(\overline{u}_j+u'_j)}\right\rangle\\
&= \frac{\partial}{\partial x_j}\left\langle\overline{\overline{\rho}\;\overline{u}\;\overline{u}_j}+\overline{\overline{\rho}\;\overline{u}\;u'_j}+\overline{\overline{\rho}\;u'\;\overline{u}_j}+\overline{\overline{\rho}\;u'u'_j}+\overline{\rho'\;\overline{u}\;\overline{u}_j}+\overline{\rho'\;\overline{u}\;u'_j}+\overline{\rho'u'\;\overline{u}_j}+\overline{\rho'u'u'_j}\right\rangle\\
&= \frac{\partial}{\partial x_j}\left\langle\overline{\rho}\;\overline{u}\;\overline{u}_j\right\rangle+\frac{\partial}{\partial x_j}\left\langle\overline{\rho}\overline{u'u'_j}\right\rangle+\frac{\partial}{\partial x_j}\left\langle\overline{u}\overline{\rho'u'_j}+\overline{u}_j\overline{\rho'u'}+\overline{\rho'u'u'_j}\right\rangle,\quad (j=1,2), \quad (4.5)
\end{aligned}$$

and each term in the RHS of Eq. (4.4) becomes

$$-\left\langle\overline{\frac{\partial p}{\partial x}}\right\rangle = -\frac{\partial}{\partial x}\left\langle\overline{\overline{p}+p'}\right\rangle=-\frac{\partial\left\langle\overline{p}\right\rangle}{\partial x}, \quad (4.6)$$

$$\frac{1}{Re_c}\left\langle\overline{\frac{\partial}{\partial x_j}\left(\mu\frac{\partial u}{\partial x_j}\right)}\right\rangle = \frac{1}{Re_c}\frac{\partial}{\partial x_j}\left(\mu\frac{\partial}{\partial x_j}\left\langle\overline{\overline{u}+u'}\right\rangle\right)=\frac{1}{Re_c}\frac{\partial}{\partial x_j}\left(\mu\frac{\partial\left\langle\overline{u}\right\rangle}{\partial x_j}\right), \quad (4.7)$$

$$\frac{1}{3}\frac{1}{Re_c}\left\langle\overline{\frac{\partial}{\partial x}\left(\mu\frac{\partial u_j}{\partial x_j}\right)}\right\rangle = \frac{1}{3}\frac{1}{Re_c}\frac{\partial}{\partial x}\left(\mu\frac{\partial}{\partial x_j}\left\langle\overline{\overline{u}_j+u'_j}\right\rangle\right)=\frac{1}{3}\frac{1}{Re_c}\frac{\partial}{\partial x}\left(\mu\frac{\partial\left\langle\overline{u}_j\right\rangle}{\partial x_j}\right) \quad (4.8)$$

where $j = 1, 2$. Thus, the Reynolds averaged pressure gradient equation in the streamwise direction is obtained as follows:

$$\begin{aligned}\frac{\partial \langle \overline{p} \rangle}{\partial x} = &- \frac{\partial}{\partial x_j} \langle \overline{\rho}\ \overline{u}\ \overline{u}_j \rangle + \frac{1}{Re_c} \frac{\partial}{\partial x_j} \left(\mu \frac{\partial \langle \overline{u} \rangle}{\partial x_j} \right) + \frac{1}{3} \frac{1}{Re_c} \frac{\partial}{\partial x} \left(\mu \frac{\partial \langle \overline{u}_j \rangle}{\partial x_j} \right) \\ &+ \frac{\partial}{\partial x_j} \langle -\overline{\rho} \overline{u' u'_j} \rangle - \frac{\partial}{\partial x_j} \left(\langle \overline{u} \overline{\rho' u'_j} \rangle + \langle \overline{u}_j \overline{\rho' u'} \rangle + \langle \overline{\rho' u' u'_j} \rangle \right) \ , \ (j = 1, 2).\end{aligned} \tag{4.9}$$

The flow fields considered in this study can be assumed as incompressible because of the low freestream Mach number ($M_\infty = 0.2$). It is numerically confirmed that $\rho_{\max} < 1.02\rho_\infty$. Therefore, the density component can be considered as a constant, but the equation that includes the density contribution is adopted in this study. It is also confirmed that the density fluctuation ρ' can be ignored ($\rho'_{\max} < 0.007\rho_\infty$), and hence the last term in Eq. (4.9) vanishes. Furthermore, the second term in Eq. (4.9) can be decomposed into two terms.

$$\frac{1}{Re_c} \frac{\partial}{\partial x_j} \left(\mu \frac{\partial \langle \overline{u} \rangle}{\partial x_j} \right) = \frac{1}{Re_c} \frac{\partial}{\partial x} \left(\mu \frac{\partial \langle \overline{u} \rangle}{\partial x} \right) + \frac{1}{Re_c} \frac{\partial}{\partial y} \left(\mu \frac{\partial \langle \overline{u} \rangle}{\partial y} \right). \tag{4.10}$$

Figure 4.1 shows the distributions of two terms in the RHS of equation above near the surface at $Re_c = 6.1 \times 10^3$ (LSB_S) and 2.0×10^4 (LSB_SF). As clearly seen, it mainly consists of the second term in the RHS of Eq. (4.10) which stands for the diffusion of viscous shear stress in the wall-normal direction. As a result, Eq. (4.9) is given as follows:

$$\begin{aligned}\underbrace{\frac{\partial \langle \overline{p} \rangle}{\partial x}}_{\text{Pressure gradient}} = &\underbrace{-\frac{\partial}{\partial x_j} \langle \overline{\rho}\ \overline{u}\ \overline{u}_j \rangle}_{\text{Convective}} + \underbrace{\frac{1}{Re_c} \frac{\partial}{\partial y} \left(\mu \frac{\partial \langle \overline{u} \rangle}{\partial y} \right)}_{\text{The 1st viscous diffusion}} \\ &+ \underbrace{\frac{1}{3} \frac{1}{Re_c} \frac{\partial}{\partial x} \left(\mu \frac{\partial \langle \overline{u}_j \rangle}{\partial x_j} \right)}_{\text{The 2nd viscous diffusion}} + \underbrace{\frac{\partial}{\partial x_j} \langle -\overline{\rho} \overline{u' u'_j} \rangle}_{\text{Gradient transport of Reynolds stress}} \ , \ (j = 1, 2).\end{aligned} \tag{4.11}$$

This equation means that the streamwise pressure gradient equals to sum of the convective, viscous diffusion, and gradient transport of Reynolds stress terms. Here, note that the pressure gradient also affects the distribution of four terms in the RHS of Eq. (4.11) in the actual physical phenomena. In other words, it should be considered that each term in the RHS of Eq. (4.11) does not unilaterally determine the pressure gradient, but the pressure gradient is formed by the balance after the interaction of five terms. In this study, however, the pressure gradient is assumed as a sort of dependent variable. Thus, by examining the spatial distribution of each term in the RHS of Eq. (4.11), it can be investigated what physical phenomenon affects the formation of the pressure gradient.

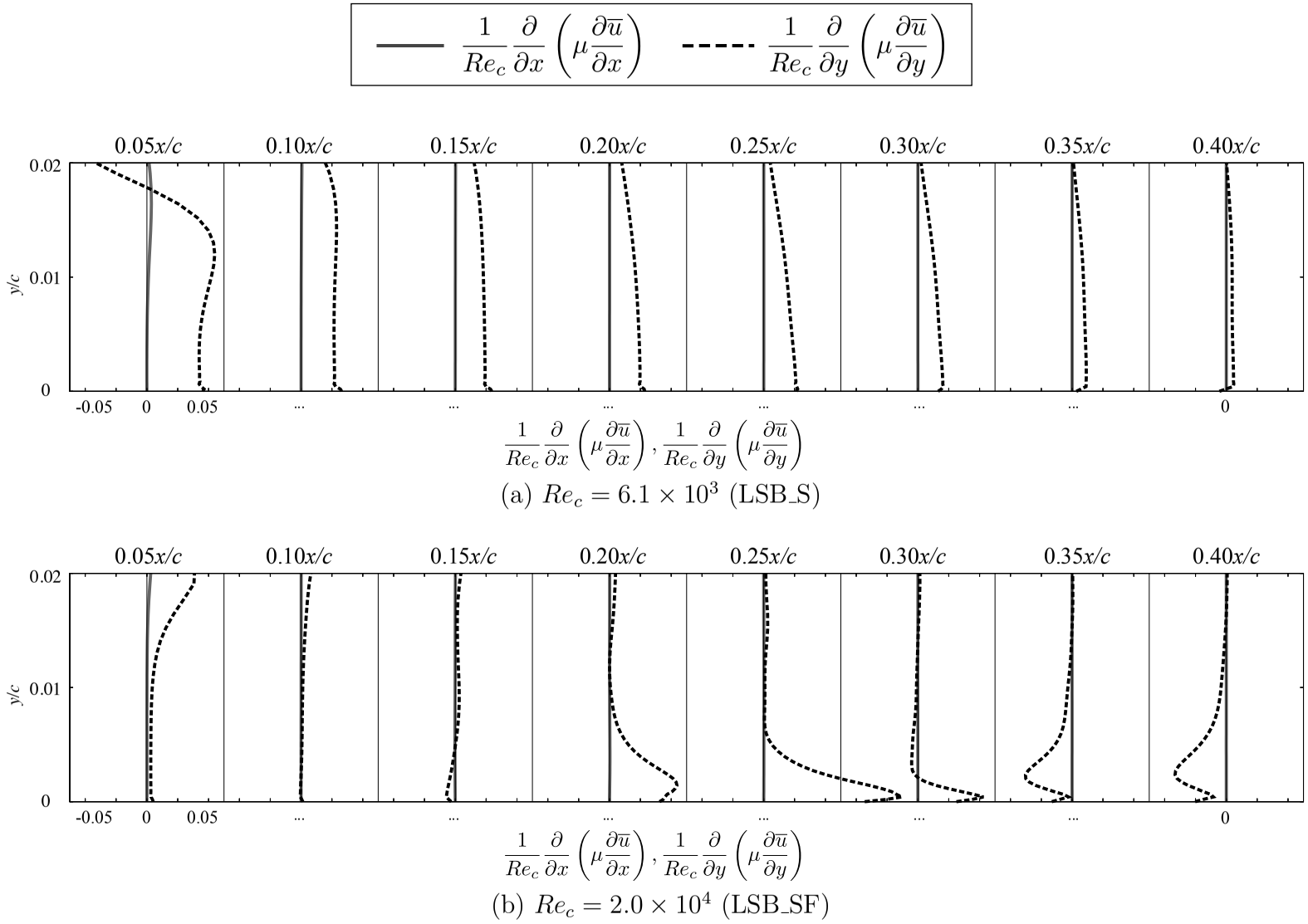

(a) $Re_c = 6.1 \times 10^3$ (LSB_S)

(b) $Re_c = 2.0 \times 10^4$ (LSB_SF)

Figure 4.1: The distributions of the first (solid-lines) and second (dashed-lines) term in the RHS of Eq. (4.10) at (a) $Re_c = 6.1 \times 10^3$ (LSB_S) and (b) $Re_c = 2.0 \times 10^4$ (LSB_SF).

4.2 Spatial distribution of each term in pressure gradient equation

Figure 4.2 shows the flow fields of each term close to the wall in the RHS of Eq. (4.11). First, in the steady region of the convective flow fields (Fig. 4.2 (a)), a positive distribution is observed on the outside of LSB irrespective of the LSB characteristics. As the Reynolds number increases, the negative distribution becomes stronger at the outer edge of LSB. On the other hand, the effect of convective term is negligible inside LSBs regardless of the LSB characteristics. In the fluctuating region, the influence of convective term becomes strong on the outside of LSB in the LSB_SF cases. These distributions are obviously different from the LSB_S cases in which the convective term decreases as going downstream. This feature is induced by nonlinear phenomena due to the laminar-turbulent transition. Next, Fig. 4.2 (b) shows the flow fields of the first viscous diffusion term. First of all, positive and negative distributions are observed from the outer edge of LSB regardless of the LSB types. This distribution is created by the difference of the streamwise velocity existing in the separated shear layer. Discrepancies between the LSB_S and LSB_SF are clearly observed near the surface of the steady region. The first viscous diffusion effects are seen near the surface of the steady region of the LSB_S, whereas it becomes negligibly small as increasing the Reynolds number in the steady region of the LSB_SF. In the fluctuating region of LSB_SF, the strong viscous diffusion effects are created near the surface. In terms of the second viscous diffusion (Fig. 4.2 (c)), its effect can be ignored throughout the flow fields. Here, the second viscous diffusion term is constituted by the divergence of velocity ($\mathrm{Div} \cdot \langle \vec{\overline{u}} \rangle = \dfrac{\partial \langle \overline{u}_j \rangle}{\partial x_j}$) which represents the compression and expansion of a fluid element. Considering that the flow field considered in the present study has low freestream Mach number ($M_\infty = 0.2$), this result comes from the fact that the compressible effect can be neglected. Finally, as shown in Fig. 4.2(d), the gradient transport of Reynolds stress is approximately zero in the steady region irrespective of the type of LSB. On the other hand, in the fluctuating region, it has a negative distribution on the outside of LSB whereas it has a positive distribution from the outer edge of LSB to the inside of LSB. In summary, it is qualitatively confirmed that the first viscous diffusion near the surface is a factor which contributes the different pressure gradient in the steady region of LSB_S and LSB_SF. Additionally, its distribution near the surface also affects the pressure gradient in the fluctuating region of the LSB_SF.

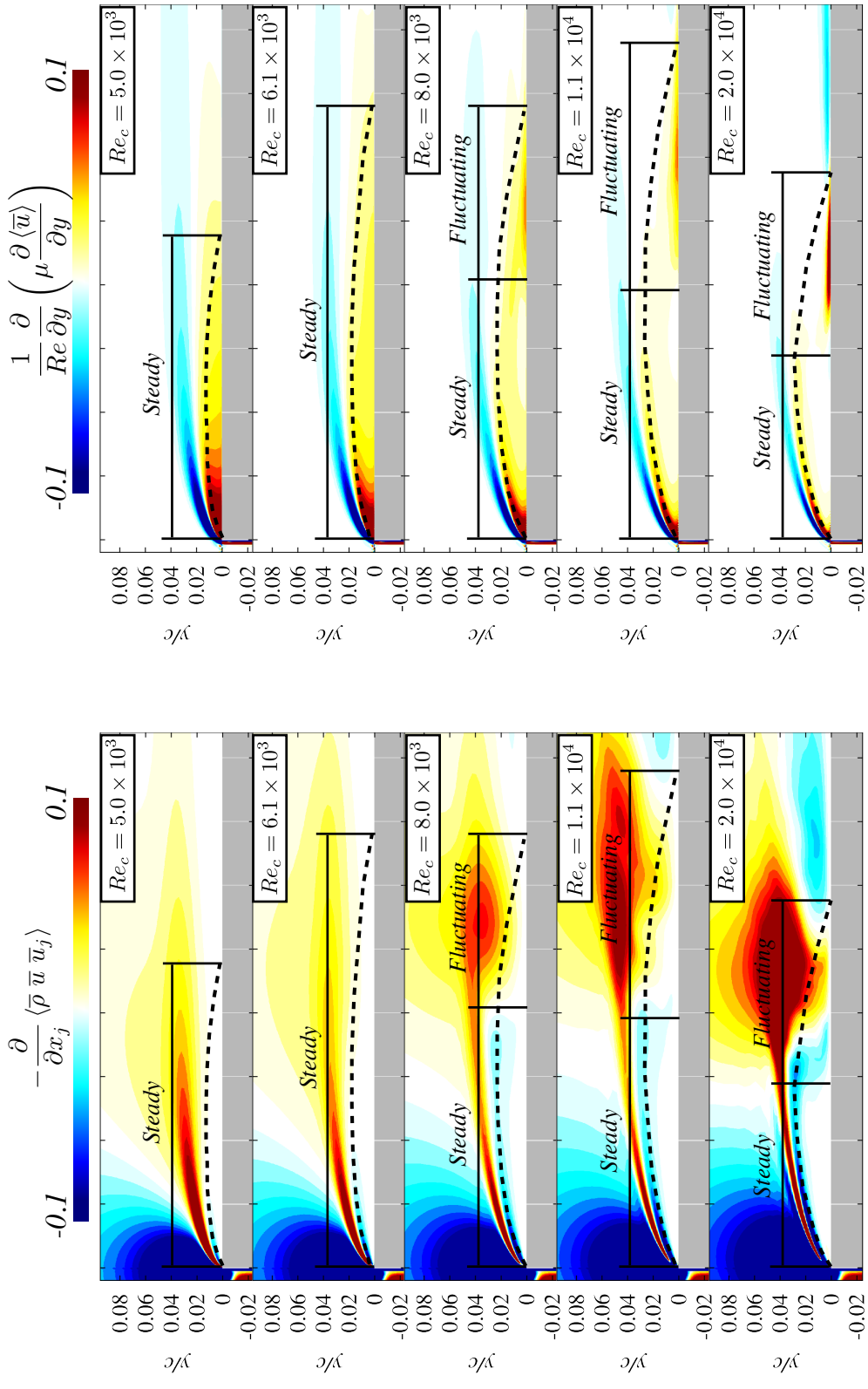

(a) Convective

(b) 1st viscous diffusion

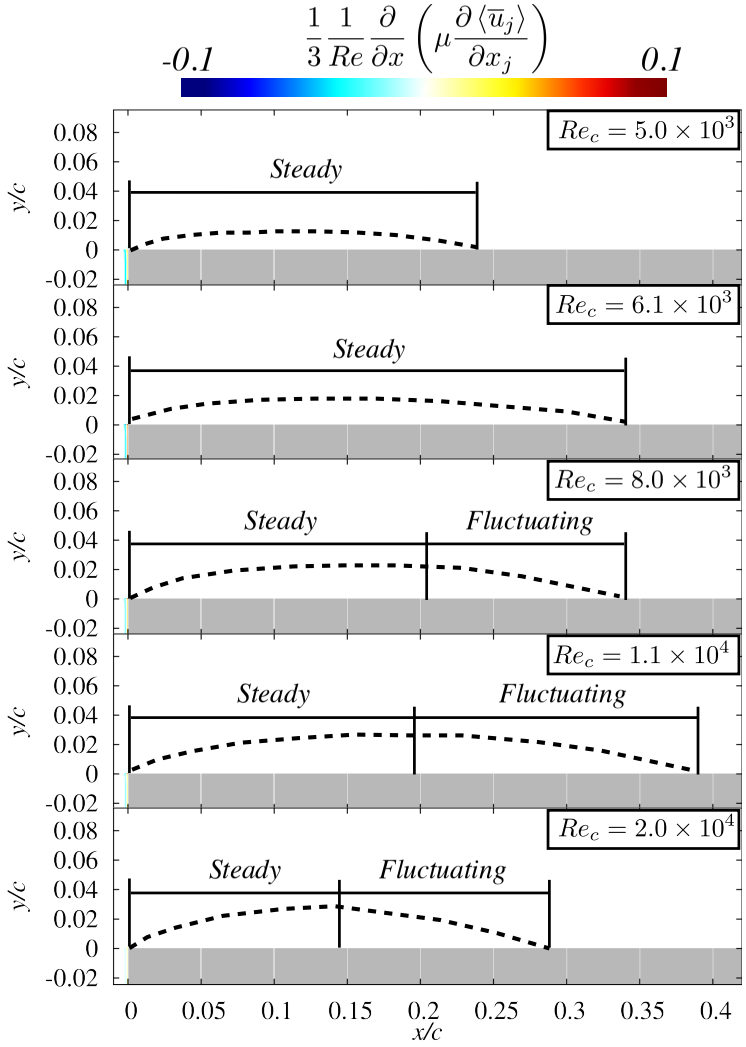

(c) 2nd viscous diffusion

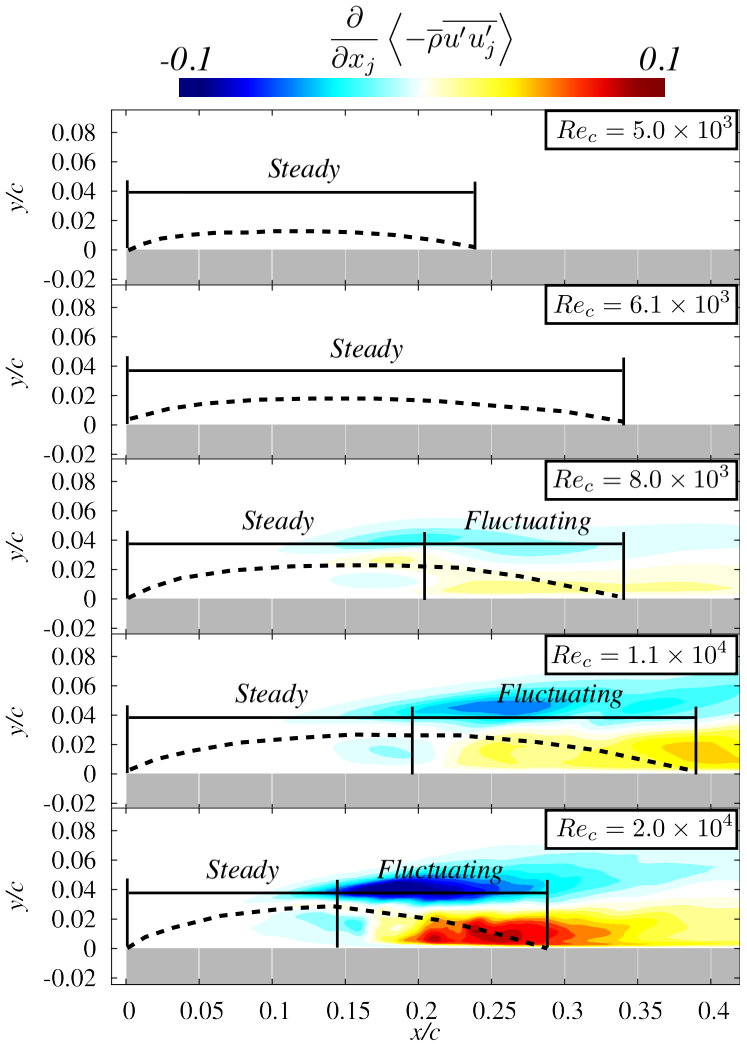

(d) Gradient transport of Reynolds stress

Figure 4.2: Spatial distributions of (a) convective, (b) the first viscous diffusion, (c) the second viscous diffusion, and (d) gradient transport of Reynolds stress terms in Eq. (4.11) at $Re_c = 5.0 \times 10^3$, 6.1×10^3, 8.0×10^3, 1.1×10^4, and 2.0×10^4.

4.3 Steady region of the separation bubble

4.3.1 Momentum budget in the wall-normal direction

In this section, a quantitative analysis within the steady region of LSB is discussed. Figure 4.3 shows the momentum budget in the wall-normal direction at several locations in the steady region of the LSB_S and LSB_SF. From the figure, it can be confirmed that the reason of appearing different pressure gradient even in the same steady region is explained by the different distribution of the first viscous diffusion term. As qualitatively discussed in Sec. 4.2, the convective, second viscous diffusion and gradient transport of Reynolds stress terms are negligible near the surface ($y/c < 0.01$) irrespective of the Reynolds number and the type of LSB. In contrast, the distribution of the first viscous diffusion varies depending on the Reynolds numbers. For example, at $Re_c = 5.0 \times 10^3$ as shown in Fig. 4.3 (a), the first viscous diffusion has a positive value and constantly distributed in the wall-normal direction. In other words, among four terms in the RHS of Eq. (4.11), only the first viscous diffusion distribution contributes to the formation of pressure gradient and the its positive value make a favorable pressure gradient ($\partial\overline{p}/\partial x > 0$). Therefore, the pressure is gradually recovered within the entire separated region without showing the plateau distribution. Note that the contributions of the Reynolds stress is negligibly small within the entire LSB and hence the separated shear layer reattaches on the surface due to the viscous stress in the LSB_S cases. As increasing the Reynolds numbers, the value of first viscous diffusion gradually decreases. In case of the highest Reynolds number in this study ($Re_c = 2.0 \times 10^4$, Fig. 4.3 (e)), the first viscous diffusion effects near the surface becomes negligibly small as similar to other three terms. In other words, all terms of RHS in Eq. (4.11) are approximately zero and it leads to the plateau pressure distributions. In the next section, the physical phenomena which make the first viscous diffusion will be discussed in more detail.

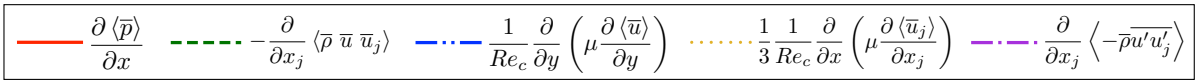

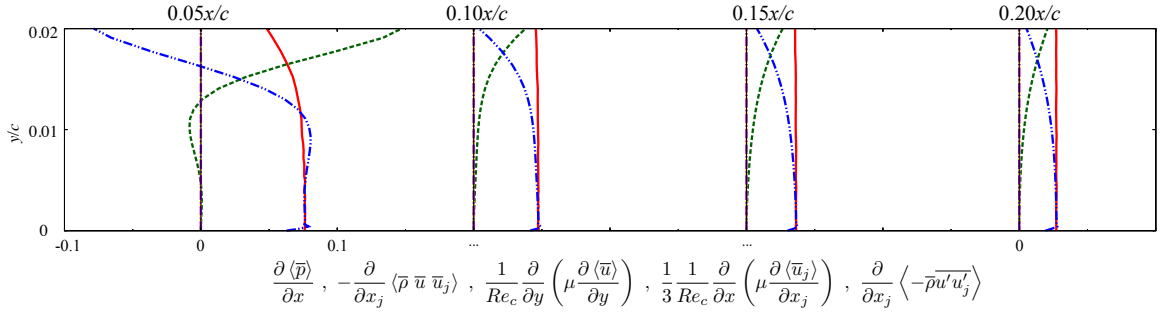

(a) $Re_c = 5.0 \times 10^3$ (LSB_S)

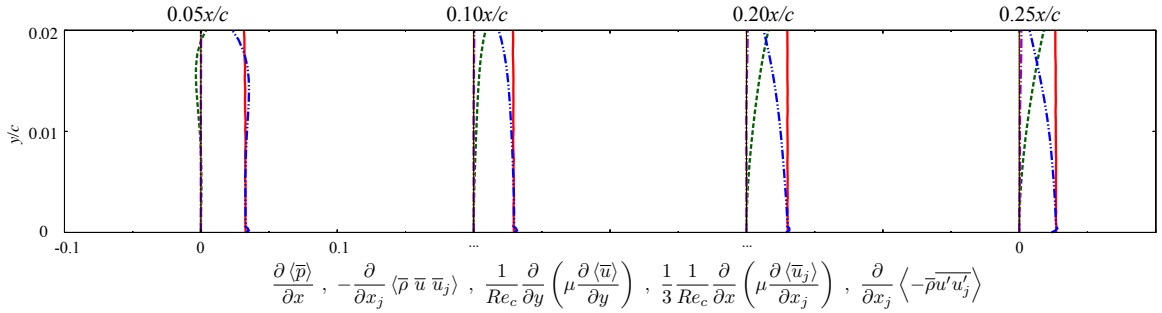

(b) $Re_c = 6.1 \times 10^3$ (LSB_S)

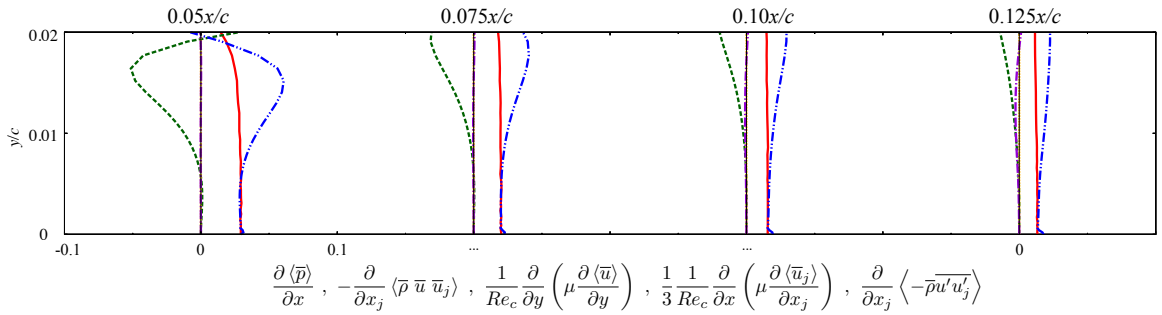

(c) $Re_c = 8.0 \times 10^3$ (LSB_SF)

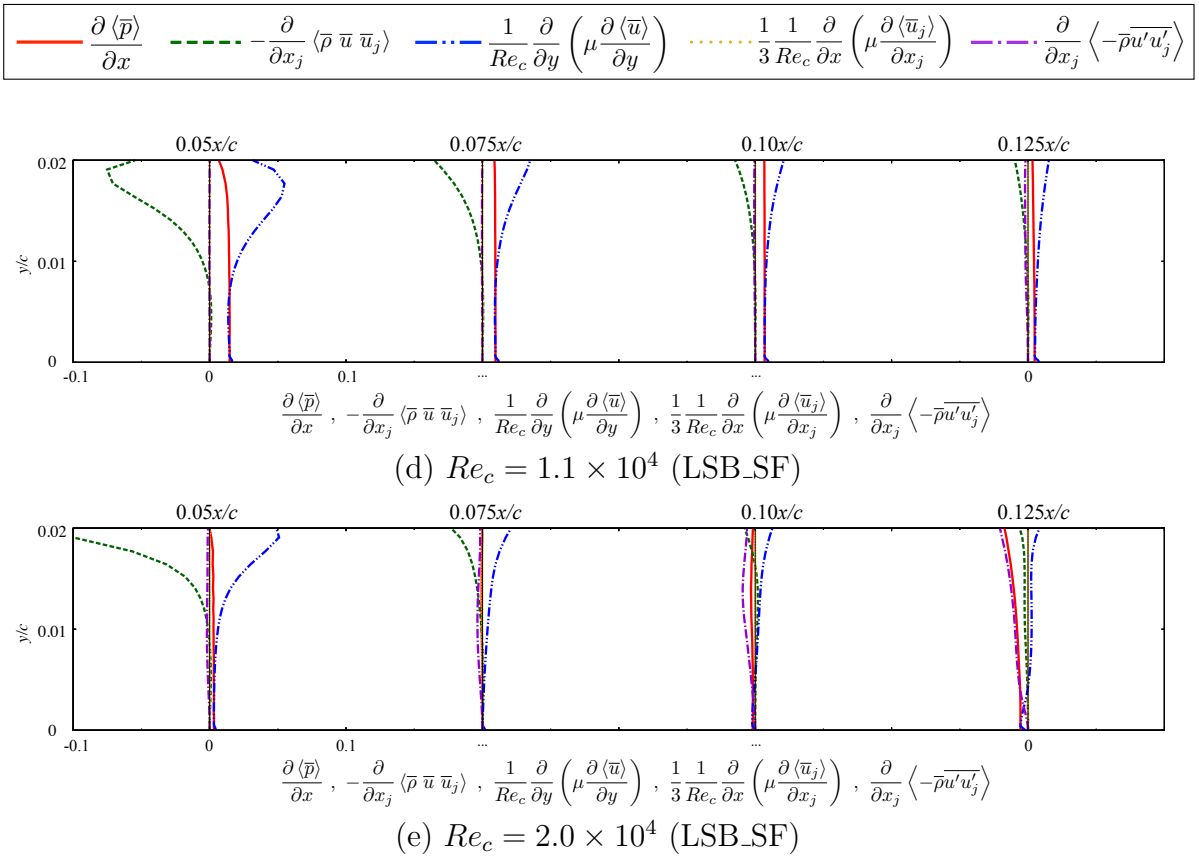

(d) $Re_c = 1.1 \times 10^4$ (LSB_SF)

(e) $Re_c = 2.0 \times 10^4$ (LSB_SF)

Figure 4.3: Momentum budget in Eq. (4.11) in the wall-normal direction at several positions within the steady region at (a) $Re_c = 5.0 \times 10^3$ (LSB_S), (b) $Re_c = 6.1 \times 10^3$ (LSB_S), (c) $Re_c = 8.0 \times 10^3$ (LSB_SF), (d) $Re_c = 1.1 \times 10^4$ (LSB_SF), and (e) $Re_c = 2.0 \times 10^4$ (LSB_SF); Pressure gradient (solid-lines, red), convective (dashed-lines, green), the first viscous diffusion (dashed-double-dotted-lines, blue), the second viscous diffusion (dotted-lines, yellow), and gradient transport of Reynolds stress (dashed-dotted-lines, violet) terms.

4.3.2 Streamwise velocity and viscous shear stress distribution

Since the first viscous diffusion term contains the viscous shear stress $\mu\frac{\partial \langle\overline{u}\rangle}{\partial y}$, and the viscous shear stress consists of the streamwise velocity $\langle\overline{u}\rangle$ distributions, the differences in the first viscous diffusion at the different Reynolds numbers can be explained by distributions of those two components. Figure 4.4 shows the streamwise velocity, viscous shear stress, and the first viscous diffusion distributions in the wall-normal direction at several locations in the steady region of the LSB_S and LSB_SF. From the figure, it is confirmed that the different viscous shear stress near the surface is affected by the different development of the separated shear layer depending on the Reynolds numbers. In case of the LSB_S, the minimum value of the velocity distribution exists near the surface. Here, if I consider the upper side from the minimum velocity as the beginning of the separated shear layer, a thickly developed shear layer is formed by the low Reynolds numbers effects. Consequently the effects of the separated shear layer continuously exists near the surface. It leads to the non-negligible viscous shear stress near the surface, and contributes to the formation of positive viscous diffusion. As the Reynolds number increases, the separated shear layer becomes relatively thinner and the influence of the shear stress near the surface is reduced. At the highest Reynolds number ($Re_c = 2.0\times10^4$, LSB_SF), the viscous shear stress near the surface becomes considerably smaller than the lower Reynolds number cases because of the thin shear layer. As a consequence, the first viscous diffusion effects near the surface becomes negligibly small. The thickness of the shear layer can be examined indirectly by the momentum thickness. As already shown in Fig. 3.16 (b), it is seen that the momentum thickness is thicker as the Reynolds number is lower, and the momentum thickness in the LSB_S cases gradually increases as moving to downstream. On the other hand, in the LSB_SF cases, it remains approximately constant and low in the steady region and then abruptly increases in the fluctuating region. Therefore, this result quantitatively suggests that the thickness of the separated shear layer is different depending on the Reynolds numbers, and this different growth of the separated shear layer results in the different viscous shear stress near the surface. As a result, the shapes of the pressure distribution become different between the LSB_S and LSB_SF depending on the Reynolds numbers even in the similar steady region.

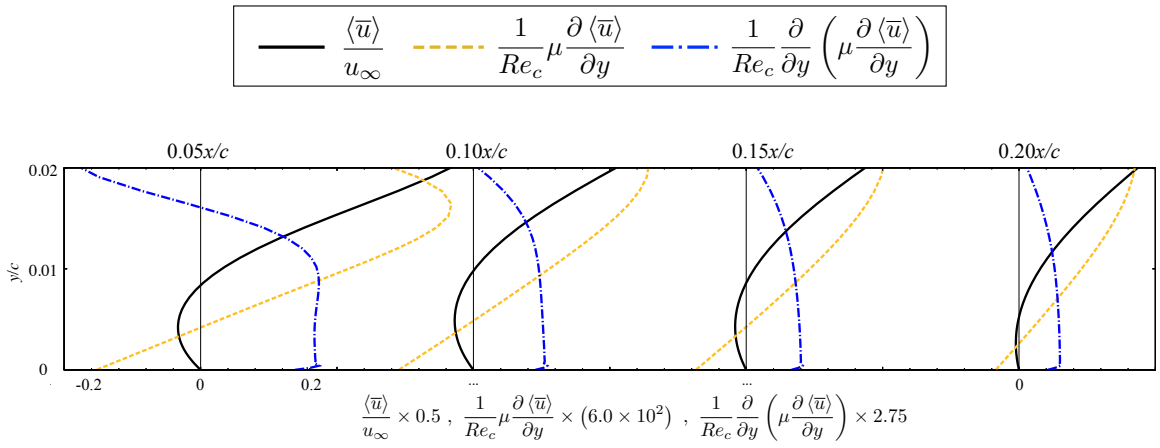

(a) $Re_c = 5.0 \times 10^3$ (LSB_S)

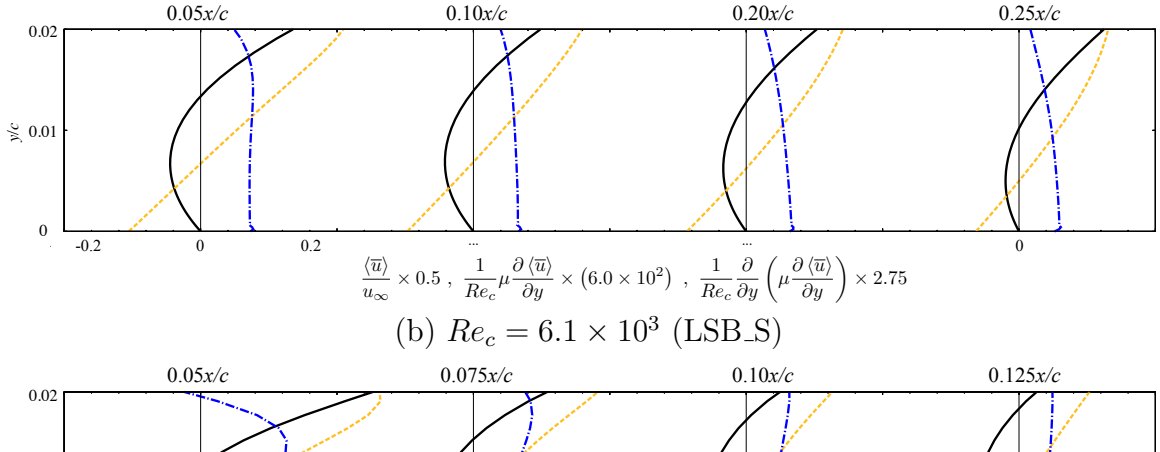

(b) $Re_c = 6.1 \times 10^3$ (LSB_S)

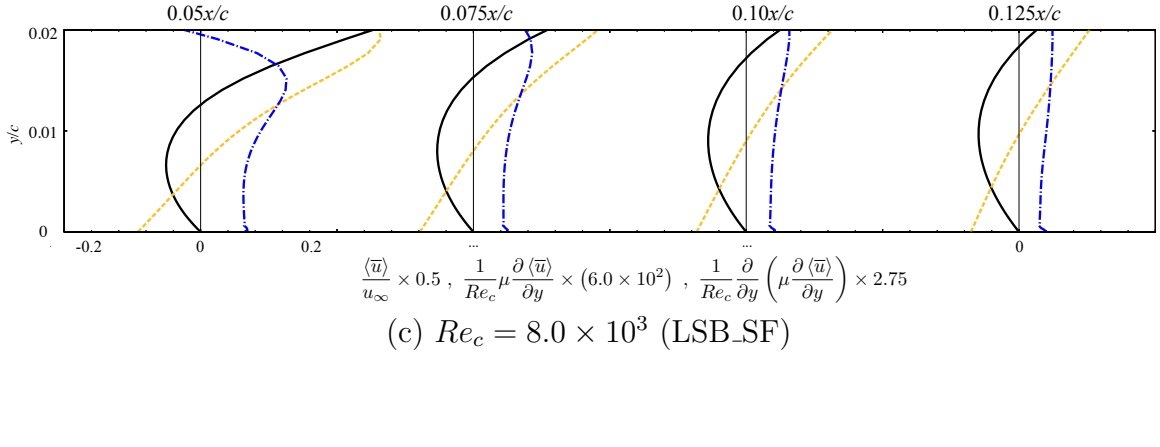

(c) $Re_c = 8.0 \times 10^3$ (LSB_SF)

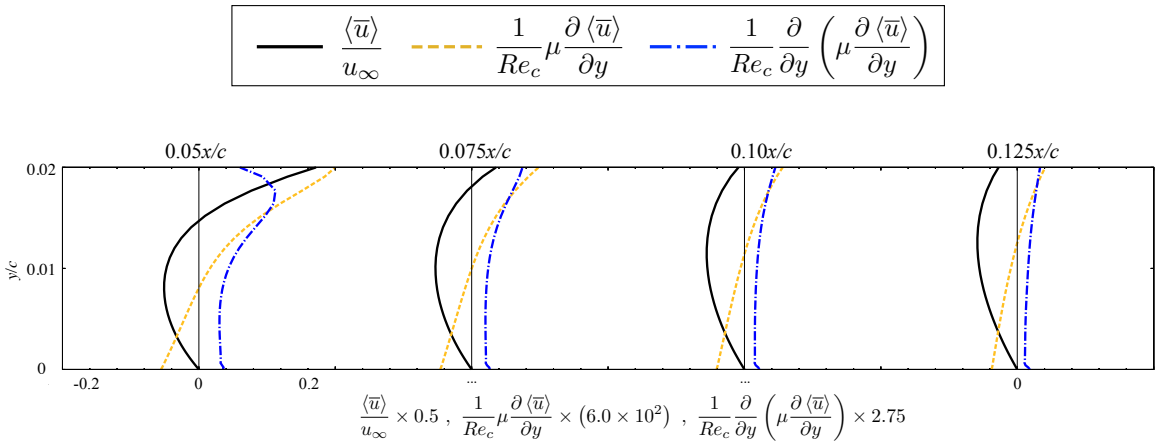

(d) $Re_c = 1.1 \times 10^4$ (LSB_SF)

(e) $Re_c = 2.0 \times 10^4$ (LSB_SF)

Figure 4.4: Time- and spanwise-averaged streamwise velocity (dashed-lines, black), viscous shear stress (solid-lines, yellow), and first viscous diffusion (dashed-dotted-lines, blue) at several positions within the steady region at (a) $Re_c = 5.0 \times 10^3$ (LSB_S), (b) $Re_c = 6.1 \times 10^3$ (LSB_S), (c) $Re_c = 8.0 \times 10^3$ (LSB_SF), (d) $Re_c = 1.1 \times 10^4$ (LSB_SF), and (e) $Re_c = 2.0 \times 10^4$ (LSB_SF).

4.4 Fluctuating region of the separation bubble

4.4.1 Momentum budget in the wall-normal direction

In this section, a quantitative analysis within the fluctuating region of LSB is discussed. The flow states of the LSB_S are steady through the entire separated region and the fluctuating region only appears in the LSB_SF. Thus, the results of $Re_c \geq 8.0 \times 10^3$ will be treated from the following discussion. Figure 4.5 shows the momentum budget in the wall-normal direction at several locations in the fluctuating region of the LSB_SF. From the figure, it can be considered that the presence of fluctuating component (i.e., Reynolds stress) and its gradient $\left(\dfrac{\partial}{\partial x_j} \left\langle -\overline{\rho} \overline{u' u'_j} \right\rangle \right)$, referred to as the gradient transport of Reynolds stress in this study, are important factors for the rapid pressure recovery phenomenon. First of all, as qualitatively discussed in Sec. 4.2, the second viscous diffusion is negligible irrespective of the Reynolds numbers. Considering that the Reynolds stress is derived by the statistical processing of the convective term, the influence of the convective term is observed together with the formation of the gradient transport of Reynolds stress. From the figure, however, it can be confirmed that effect of the gradient transport of Reynolds stress is stronger that that of the convective term. It induces the strong first viscous diffusion near the surface and the first viscous diffusion makes the RHS of Eq. (4.11) larger than zero. Therefore, a high pressure gradient is created ($\partial \overline{p} / \partial x \gg 0$), which stands for the rapid pressure recovery. On the other hand, the convective and Reynolds stress terms contribute to the high pressure gradient away from the surface. One of the interesting result is that the characteristics of distribution mentioned above do not depend on the instantaneous flow structure. In other words, the convective and gradient transport of Reynolds stress distributions away from the surface as well as the first viscous stress distributions near the surface are qualitatively similar regardless of the instantaneous flow structures (two-dimensional at $Re_c = 8.0 \times 10^3$ or three-dimensional at $Re_c \geq 1.1 \times 10^4$, see Sec. 3.2). Thus, the relevance between the distributions of gradient transport of Reynolds stress and the flow structures should be examined in detail. From now on, the gradient transport of Reynolds stress will be referred to as gradient transport of overall Reynolds stress, or simply *"GTOR"*.

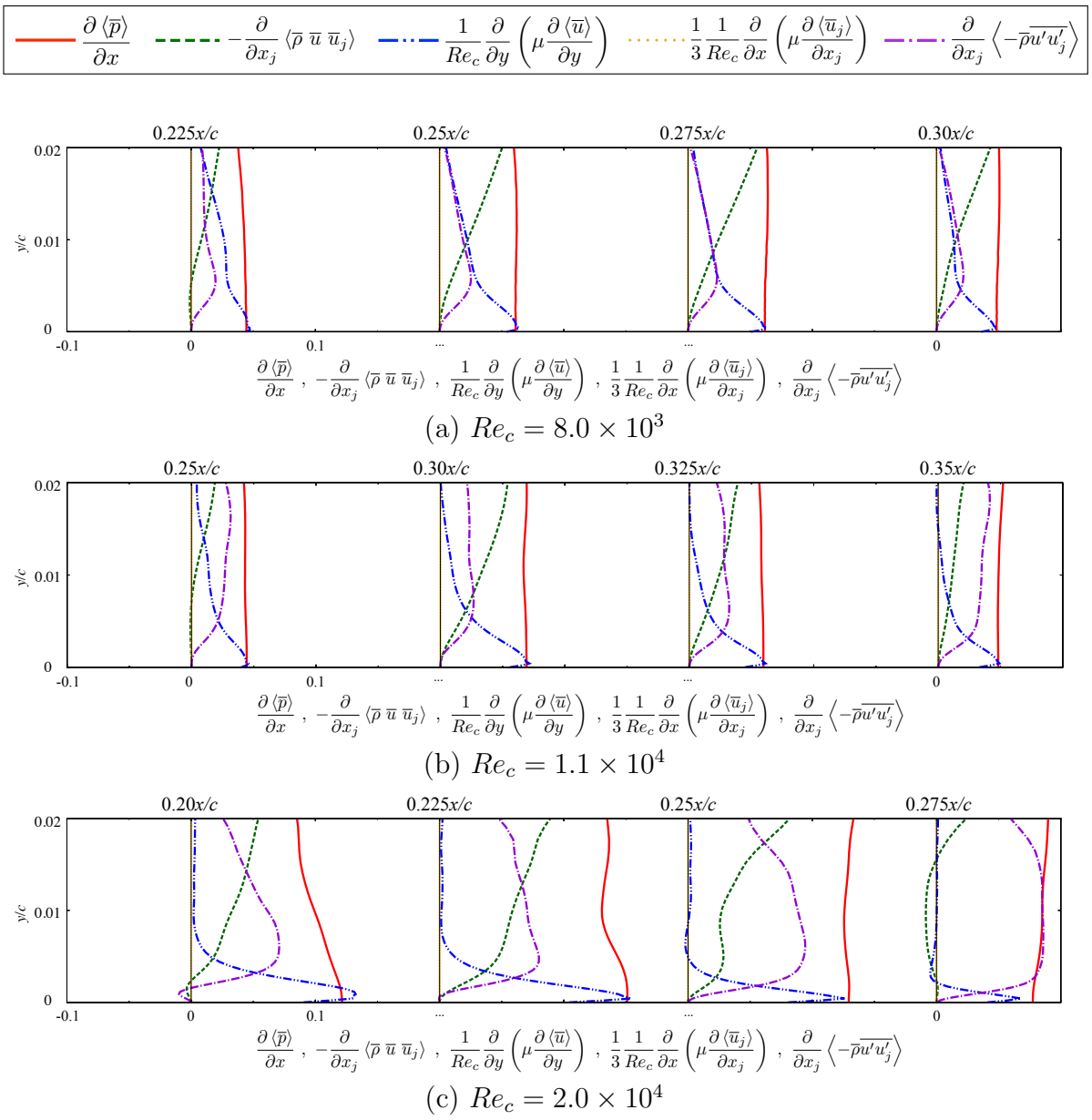

(a) $Re_c = 8.0 \times 10^3$

(b) $Re_c = 1.1 \times 10^4$

(c) $Re_c = 2.0 \times 10^4$

Figure 4.5: Momentum budget in Eq. (4.11) in the wall-normal direction at several positions within the fluctuating region at (a) $Re_c = 8.0 \times 10^3$, (b) $Re_c = 1.1 \times 10^4$, and (c) $Re_c = 2.0 \times 10^4$; Pressure gradient (solid-lines, red), convective (dashed-lines, green), the first viscous diffusion (dashed-double-dotted-lines, blue), the second viscous diffusion (dotted-lines, yellow), and gradient transport of Reynolds stress (dashed-dotted-lines, violet) terms.

4.4.2 Decomposition of the gradient transport of Reynolds stress

As previously discussed, the occurrence of GTOR is an important factor for formation of the rapid pressure recovery. In this section, the GTOR can be additionally decomposed into a gradient transport of Reynolds normal stress (*"GTRN"*) in the streamwise direction and a gradient transport of Reynolds shear stress (*"GTRS"*) in the wall-normal direction, which is expressed as

$$\underbrace{\frac{\partial}{\partial x_j}\left\langle -\overline{\rho u' u_j'}\right\rangle}_{\substack{\text{Gradient transport of}\\ \text{overall Reynolds stress (GTOR)}}} = \underbrace{\frac{\partial}{\partial x}\left\langle -\overline{\rho u' u'}\right\rangle}_{\substack{\text{Gradient transport of}\\ \text{Reynolds normal stress (GTRN)}}} + \underbrace{\frac{\partial}{\partial y}\left\langle -\overline{\rho u' v'}\right\rangle}_{\substack{\text{Gradient transport of}\\ \text{Reynolds shear stress (GTRS)}}}. \tag{4.12}$$

It can be interpreted that the GTOR is affected by the momentum transfer in the streamwise direction induced by the Reynolds normal stress and that in the wall-normal direction induced by the Reynolds shear stress. Figure 4.6 shows the distributions of each term in Eq. (4.12) near the surface. From the figure, the GTRS in the wall-normal direction is a main contributor to the formation of GTOR regardless of the Reynolds numbers as well as the flow structures. Tennekes & Lumley (1972) mentioned that the Reynolds normal stress contributes little to the momentum transfer, whereas the Reynolds shear stress plays a dominant role to it in many flow fields. As reported by many previous studies introduced in Sec. 1.3, the present results also suggest that the momentum transfer in the wall-normal direction is an important factor for inducing the rapid pressure recovery. The momentum transfer in the wall-normal direction, however, can be generated not only by the three-dimensional turbulent motions shown at $Re_c \geq 1.1 \times 10^4$ but also by the two-dimensional spanwise vortex motions shown in the $Re_c = 8.0 \times 10^3$ case. Hence, it is necessary to analyze a relationship between the GTRS and flow structures in more detail.

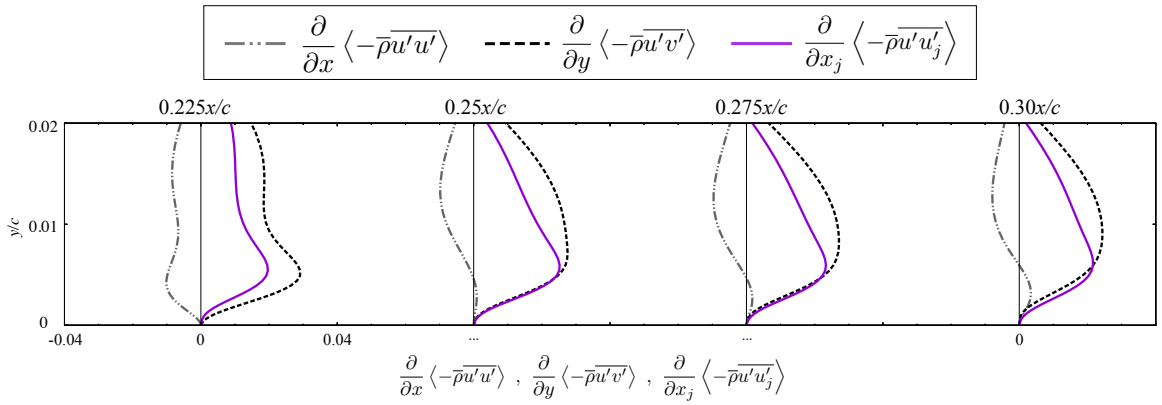

(a) $Re_c = 8.0 \times 10^3$

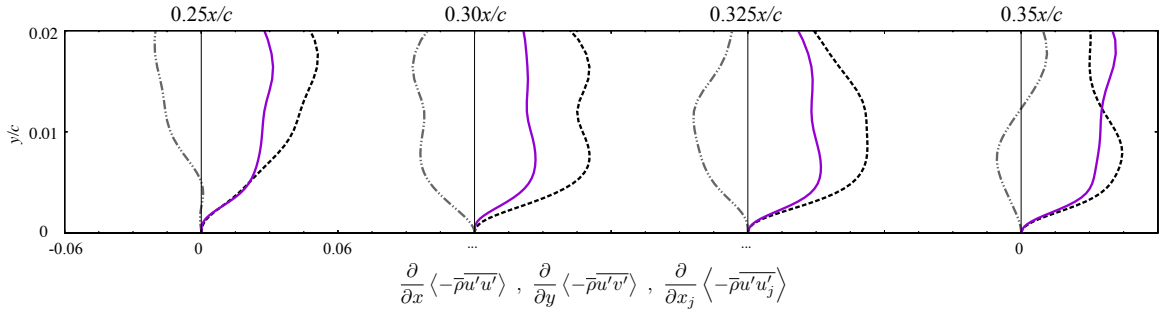

(b) $Re_c = 1.1 \times 10^4$

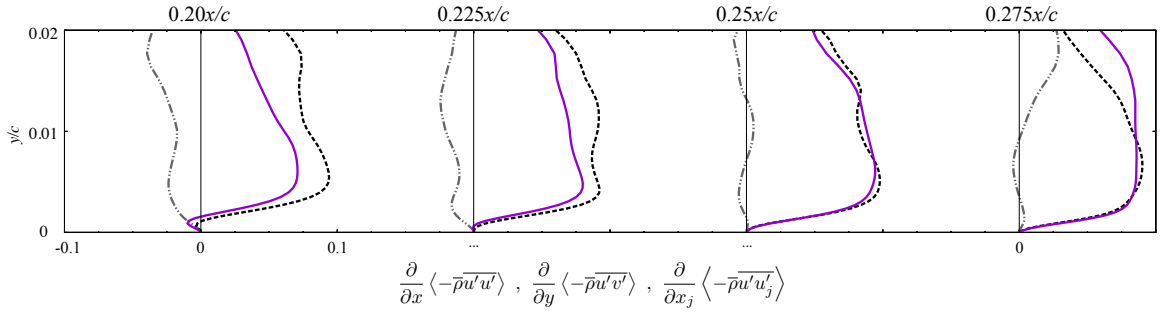

(c) $Re_c = 2.0 \times 10^4$

Figure 4.6: Budget of gradient transport of Reynolds stress in the wall-normal direction at several positions within the fluctuating region at (a) $Re_c = 8.0 \times 10^3$, (b) $Re_c = 1.1 \times 10^4$, and (c) $Re_c = 2.0 \times 10^4$; Gradient transport of overall Reynolds stress (GTOR; solid-lines, violet), gradient transport of Reynolds normal stress in the streamwise direction (GTRN; dashed-double-dotted-lines, gray), and gradient transport of Reynolds shear stress in the wall-normal direction (GTRS; dashed-lines, black).

4.4.3 Decomposition of fluctuation into two- and three-dimensional components

An additional decomposition is applied to elucidate the physical phenomena that causes the fluctuation in the wall-normal direction. This additional analysis is designed to decompose the overall fluctuation f' into two- and three-dimensional ones as follows:

$$f = \underbrace{\langle \overline{f} \rangle}_{\text{average}} + \underbrace{f'}_{\substack{\text{Overall} \\ \text{fluctuation}}} = \underbrace{\langle \overline{f} \rangle}_{\text{average}} + \underbrace{\tilde{f}}_{\substack{\text{Two-dimensional} \\ \text{fluctuation}}} + \underbrace{f''}_{\substack{\text{Three-dimensional} \\ \text{fluctuation}}} , \tag{4.13}$$

where $\tilde{f}$ and f'' represent the two- and three-dimensional fluctuating components, respectively. This triple decomposition approach is similar to the phase averaging analysis proposed by Hussain & Reynolds (1970) and Reynolds & Hussain (1972). It was also introduced to extract coherent structures in turbulent flow (Sengupta & Lekoudis, 1985; Lekoudis & Sengupta, 1986). Here, it can be considered that the unsteadiness induced by both two- and three-dimensional structures remains in an instantaneous variable f, i.e., $f = f(x, y, z, t)$. On the other hand, the unsteadiness induced by three-dimensional turbulent motion is only removed in the spanwise-averaged quantity $\langle f \rangle$ although it is still a time dependent variable ($\langle f \rangle = \langle f \rangle (x, y, t)$). The time-averaged quantity $\overline{f}$ is a function of the spatial coordinate only ($\overline{f} = \overline{f}(x, y, z)$). Each fluctuating component is obtained by

$$f' = f - \langle \overline{f} \rangle , \tag{4.14}$$

$$\tilde{f} = \langle f \rangle - \overline{f} , \tag{4.15}$$

$$f'' = f - \langle f \rangle . \tag{4.16}$$

To calculate the each fluctuating component, the spanwise-averaged quantities $\langle f \rangle$ is calculated at each time step. When the entire calculation is completed, the time-averaged quantities $\overline{f}$ can be obtained. After that, the two-dimensional fluctuation $\tilde{f}$ is obtained by subtracting the time-averaged from the spanwise-averaged quantities (Eq. (4.15)). In a similar manner, the three-dimensional fluctuation f'' is computed by the difference between the instantaneous and the spanwise-averaged quantities (Eq. (4.16)). The physical meaning of each fluctuating component can be interpreted as follows: the two-dimensional fluctuation represents the fluctuation induced by two-dimensional large vortex motions, whereas the three-dimensional fluctuation corresponds to the fluctuation created by three-dimensional turbulent motions. Furthermore, it is assumed that

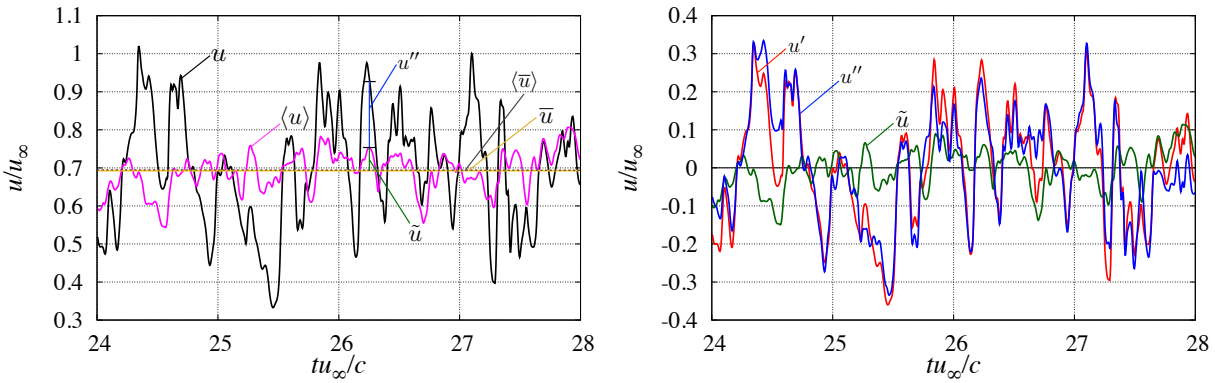

(a) (b)

Figure 4.7: Time histories of the streamwise velocity at $Re_c = 2.0 \times 10^4$, $x/c = 0.8$, $y/c = 0.015$, and $z/c = 0.1$. (a) Instantaneous (u; black), spanwise-averaged ($\langle u\rangle$; magenta), time-averaged ($\overline{u}$; yellow), and time- and spanwise averaged ($\langle\overline{u}\rangle$; dashed-line, gray) streamwise velocity; (b) overall fluctuation (u'; red), two-dimensional fluctuation ($\tilde{u}$; green), and three-dimensional fluctuation (u''; blue).

$\langle\overline{f}\rangle = \overline{f}$ is satisfied in this study. The time histories for averaged and fluctuating component of the streamwise velocity are shown in Fig. 4.7. As shown in the figure, $\langle\overline{u}\rangle$ and $\overline{u}$ are independent on the time, and time-averaged and time- and spanwise-averaged values are approximately same, so the assumption above is satisfied.

So far I have discussed the decomposition for a single physical quantity; from now on, the decomposition for the correlation between two physical variables such as Reynolds stress will be led. An instantaneous velocity quantity is decomposed into two- and three-dimensional components as follow:

$$u_i' = \tilde{u}_i + u_i''. \tag{4.17}$$

Correlated quantities of u_i and u_j are written as

$$u_i'u_j' = \tilde{u}_i\tilde{u}_j + u_i''u_j'' + \tilde{u}_iu_j'' + u_i''\tilde{u}_j. \tag{4.18}$$

By taking time- and spanwise-averaging into the equation above,

$$\langle\overline{u_i'u_j'}\rangle = \langle\overline{\tilde{u}_i\tilde{u}_j}\rangle + \langle\overline{u_i''u_j''}\rangle + T_{2D3D}\ ,\ T_{2D3D} = \langle\overline{\tilde{u}_iu_j''}\rangle + \langle\overline{u_i''\tilde{u}_j}\rangle\,. \tag{4.19}$$

In the phase averaging method, an instantaneous variable f is decomposed into an overall time average $\overline{f}$, a periodic perturbation $\tilde{f}$, and a turbulent fluctuation f''. The

correlation of the periodic perturbation and the turbulent fluctuation is assumed to be zero (i.e., $\left\langle \overline{\tilde{f}f''} \right\rangle = 0$), where $\overline{f}$ and $\langle f \rangle$ represent the time and phase averaging operators, respectively. In a similar manner, it is expected that the correlation between two- and three-dimensional fluctuating components (T_{2D3D}) vanishes but it should be confirmed. Here, a typical description of the overall Reynolds stress $\left\langle \overline{u_i' u_j'} \right\rangle$ is given by

$$\left\langle \overline{u_i' u_j'} \right\rangle = \left\langle \overline{u_i u_j} \right\rangle - \left\langle \overline{u}_i \overline{u}_j \right\rangle - T_{overall} \ , \ T_{overall} = \left\langle \overline{\overline{u}_i u_j'} \right\rangle + \left\langle \overline{u_i' \overline{u}_j} \right\rangle , \tag{4.20}$$

Similarly, the two- and three-dimensional Reynolds stress components are obtained by

$$\left\langle \overline{\tilde{u}_i \tilde{u}_j} \right\rangle = \left\langle \overline{\langle u_i \rangle \langle u_j \rangle} \right\rangle - \left\langle \overline{u}_i \overline{u}_j \right\rangle - T_{2D} \quad , \quad T_{2D} = \left\langle \overline{\overline{u}_i \tilde{u}_j} \right\rangle + \left\langle \overline{\tilde{u}_i \overline{u}_j} \right\rangle , \tag{4.21}$$

$$\left\langle \overline{u_i'' u_j''} \right\rangle = \left\langle \overline{u_i u_j} \right\rangle - \left\langle \overline{\langle u_i \rangle \langle u_j \rangle} \right\rangle - T_{3D} \quad , \quad T_{3D} = \left\langle \overline{\langle u_i \rangle u_j''} \right\rangle + \left\langle \overline{u_i'' \langle u_j \rangle} \right\rangle . \tag{4.22}$$

Therefore,

$$\begin{aligned} \left\langle \overline{u_i' u_j'} \right\rangle + T_{overall} &= \left\langle \overline{\tilde{u}_i \tilde{u}_j} \right\rangle + \left\langle \overline{u_i'' u_j''} \right\rangle + T_{overall} + T_{2D3D} \\ &= \left\langle \overline{\tilde{u}_i \tilde{u}_j} \right\rangle + \left\langle \overline{u_i'' u_j''} \right\rangle + T_{2D} + T_{3D}. \end{aligned} \tag{4.23}$$

Thus,

$$T_{2D3D} = T_{2D} + T_{3D} - T_{overall}. \tag{4.24}$$

Here, it is known that the product of an averaged quantity and fluctuating quantity is zero: $T_{overall} = 0$ (Wilcox, 2006). In the same manner, $T_{2D} = T_{3D} = 0$ because each of the correlations has averaged quantities. As a consequence, $T_{2D3D} = 0$ and the overall Reynolds stress is equal to the sum of the two- and three-dimensional components as follows:

$$\underbrace{\left\langle \overline{u_i' u_j'} \right\rangle}_{\substack{\text{Overall} \\ \text{Reynolds stress}}} = \underbrace{\left\langle \overline{\tilde{u}_i \tilde{u}_j} \right\rangle}_{\substack{\text{Two-dimensional} \\ \text{Reynolds stress}}} + \underbrace{\left\langle \overline{u_i'' u_j''} \right\rangle}_{\substack{\text{Three-dimensional} \\ \text{Reynolds stress}}} \quad , \ (i, j = 1, 2). \tag{4.25}$$

Figure 4.8 show the instantaneous and averaged flow fields of the correlated quantities between u and v (i.e., Reynolds shear stress). In particular, at $Re_c = 2.0 \times 10^4$ where the three-dimensional structures appear, the product of two- and three-dimensional fluctuating components cannot be ignored in the instantaneous flow (see, the left figure in Fig 4.8 (d)). However, for the time- and spanwise-averaged flow fields shown in the right figure in Fig 4.8 (d), the averaged correlation clearly vanishes in the entire flow fields; it means that $T_{2D3D} = 0$ is satisfied. Therefore, I can adopt the relationship in Eq. (4.25) for Reynolds stress analysis. In the actual calculation process, the overall Reynolds stress

is computed by

$$\left\langle \overline{u_i' u_j'} \right\rangle = \left\langle \overline{u_i u_j} \right\rangle - \left\langle \overline{u}_i \overline{u}_j \right\rangle \ , \ (i,j=1,2), \tag{4.26}$$

and the two- and three-dimensional components are obtained by

$$\left\langle \overline{\tilde{u}_i \tilde{u}_j} \right\rangle = \left\langle \overline{\langle u_i \rangle \langle u_j \rangle} \right\rangle - \left\langle \overline{u_i u_j} \right\rangle \ , \ (i,j=1,2), \tag{4.27}$$

$$\left\langle \overline{u_i'' u_j''} \right\rangle = -\left\langle \overline{\langle u_i \rangle \langle u_j \rangle} \right\rangle + \left\langle \overline{u_i u_j} \right\rangle \ , \ (i,j=1,2). \tag{4.28}$$

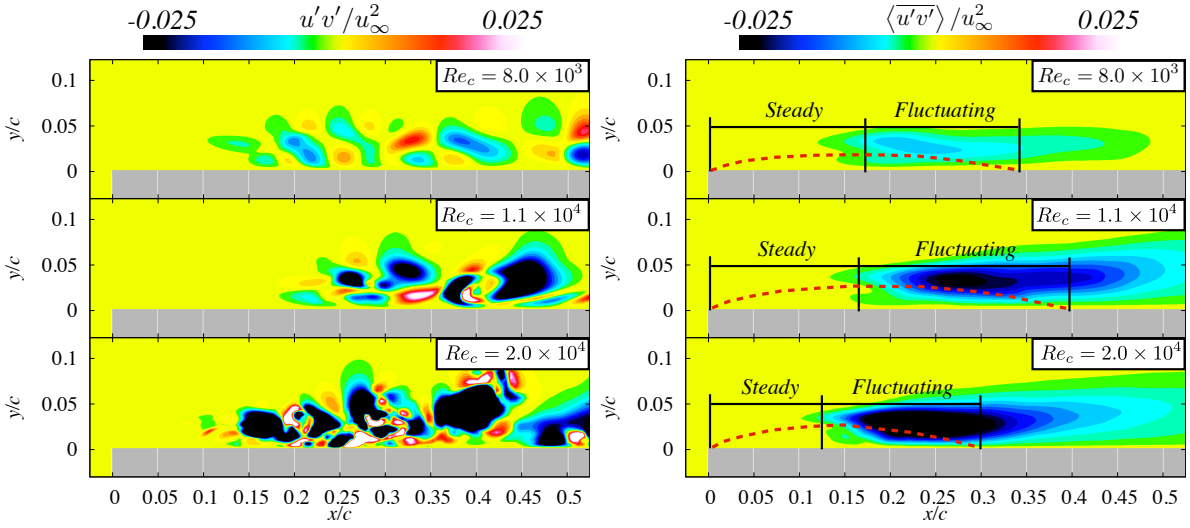

(a) Overall component

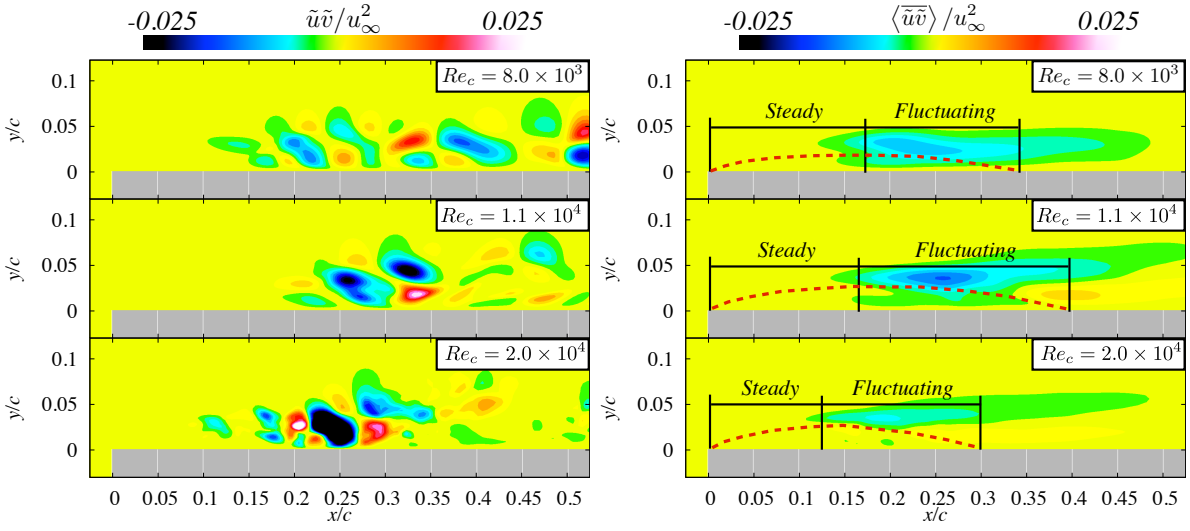

(b) Two-dimensional component

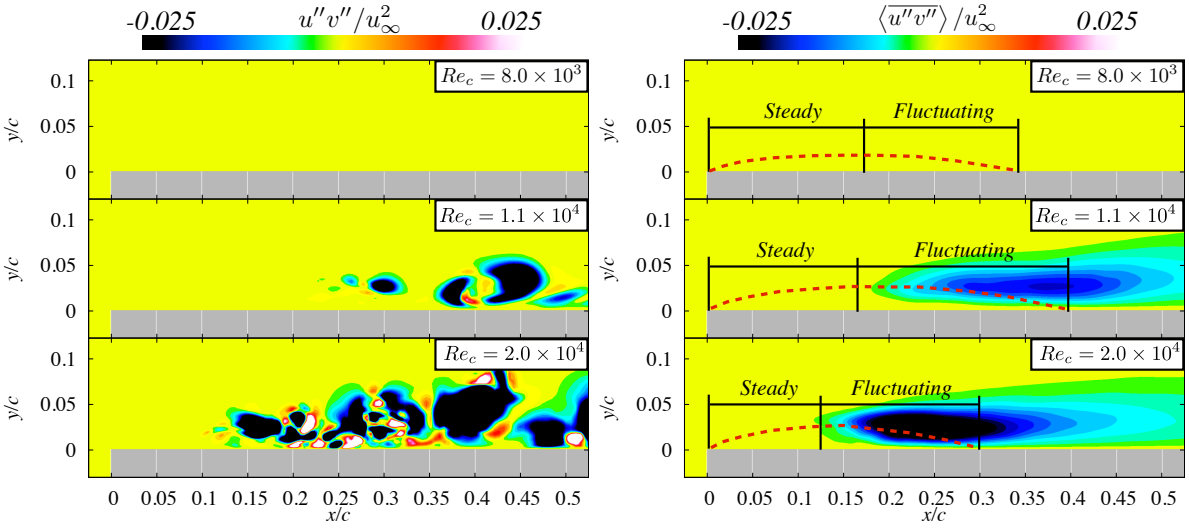

(c) Three-dimensional component

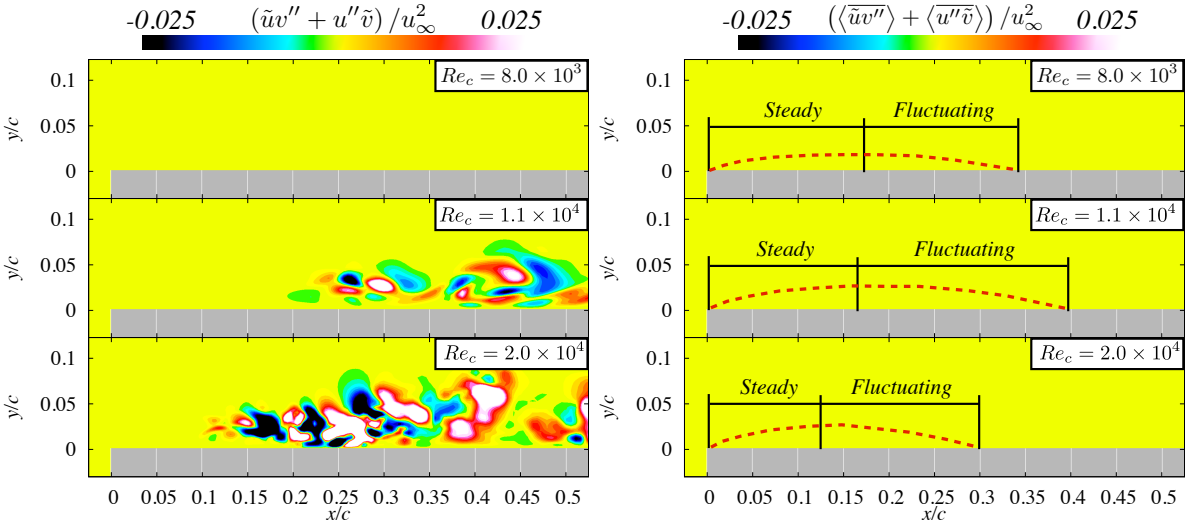

(d) Residual component

Figure 4.8: Instantaneous (left column) and averaged (right column) flow fields of each term in Eq. (4.18) of (a) Overall fluctuation $u'v'$, (b) two-dimensional fluctuation $\tilde{u}\tilde{v}$, (c) three-dimensional fluctuation $u''v''$, and (d) residual component $\tilde{u}v'' + u''\tilde{v}$ at $Re_c = 8.0 \times 10^3$, 1.1×10^4, and 2.0×10^4 ($i = 1$ and $j = 2$). In the averaged flows, the outer layer of LSB is denoted by red-dashed lines.

For simplicity, the term of *Reynolds stress* from the following discussion indicates the Reynolds shear stress component. Figure 4.9 shows the flow fields of overall, two-dimensional, and three-dimensional Reynolds stress components. From the figure, it can be confirmed the following physical characteristics. First of all, as the Reynolds number increases, the overall Reynolds stress increases whereas the two-dimensional component slightly decreases. The second point is that the overall Reynolds stress is affected by the two-dimensional component at $Re_c = 8.0 \times 10^3$, whereas it is mainly contributed by the three-dimensional component at $Re_c \geq 1.1 \times 10^4$. These characteristics are quantitatively confirmed by the distribution of each component near the surface in the wall-normal direction (see, Fig. 4.10). First, the three-dimensional Reynolds stress component is negligible in the entire flow fields at $Re_c = 8.0 \times 10^3$. Thus, the overall Reynolds stress distribution is exactly the same as the two-dimensional component. This result arises from the fact that the entire flow field remains two-dimensional structures (see, Sec. 3.2). In contrast, when three-dimensional turbulent structures appear ($Re_c \geq 1.1 \times 10^4$), distributions of the two-dimensional components are very small and the overall Reynolds stress mainly consists of the three-dimensional component. In other words, the main component of the overall Reynolds stress $\langle \overline{u'v'} \rangle$ at $Re_c = 8.0 \times 10^3$ is the two-dimensional Reynolds stress $\langle \overline{\tilde{u}\tilde{v}} \rangle$, which is induced by the two-dimensional vortex motion. By contrast, the main component of the overall Reynolds stress at $Re_c \geq 1.1 \times 10^4$ is the three-dimensional Reynolds stress $\langle \overline{u''v''} \rangle$, which is induced by the three-dimensional turbulent structures. Considering that the Reynolds stress is responsible for the momentum transfer in the wall-normal direction, the momentum transfer in the wall-normal direction is created by the two-dimensional vortex motion at $Re_c = 8.0 \times 10^3$, whereas it is generated by three-dimensional turbulent structures at $Re_c \geq 1.1 \times 10^4$.

It should be noted, however, that the gradient transport of each component in the wall-normal direction is the important factor for the formation of rapid pressure recovery phenomenon. That is, distributions of two- and three dimensional components of GTRS as well as the overall GTRS should be investigated. As expressed mathematically,

$$\underbrace{\frac{\partial}{\partial y}\left\langle -\overline{\rho u'v'} \right\rangle}_{\text{overall GTRS}} = \underbrace{\frac{\partial}{\partial y}\left\langle -\overline{\rho}\overline{\tilde{u}\tilde{v}} \right\rangle}_{\substack{\text{Two-dimensional} \\ \text{component of GTRS}}} + \underbrace{\frac{\partial}{\partial y}\left\langle -\overline{\rho u''v''} \right\rangle}_{\substack{\text{Three-dimensional} \\ \text{component of GTRS}}} . \tag{4.29}$$

Figure 4.11 shows the each component of GTRS in the wall-normal direction. At $Re_c = 8.0 \times 10^3$, the overall GTRS is exactly consistent with the two-dimensional GTRS component. Therefore, it can be considered that the rapid pressure recovery is generated

by the two-dimensional component of GTRS which is induced by the two-dimensional vortex motion. By contrast, the rapid pressure recovery is mainly generated by the three-dimensional component of GTRS, which is induced by the three-dimensional turbulent structures at $Re_c > 1.1 \times 10^4$. In summary, the momentum transfer from the freestream to the surface is the important factor for rapid pressure recovery, but the physical phenomenon responsible for the rapid pressure recovery might differ depending on the Reynolds numbers. That is, the presence of fluctuation is important but the three-dimensional turbulent structures are not always required for the rapid pressure recovery. Moreover, the magnitude of gradient transport of Reynolds shear stress is important and the formation of three-dimensional turbulent structures is not a necessary condition for the rapid pressure recovery.

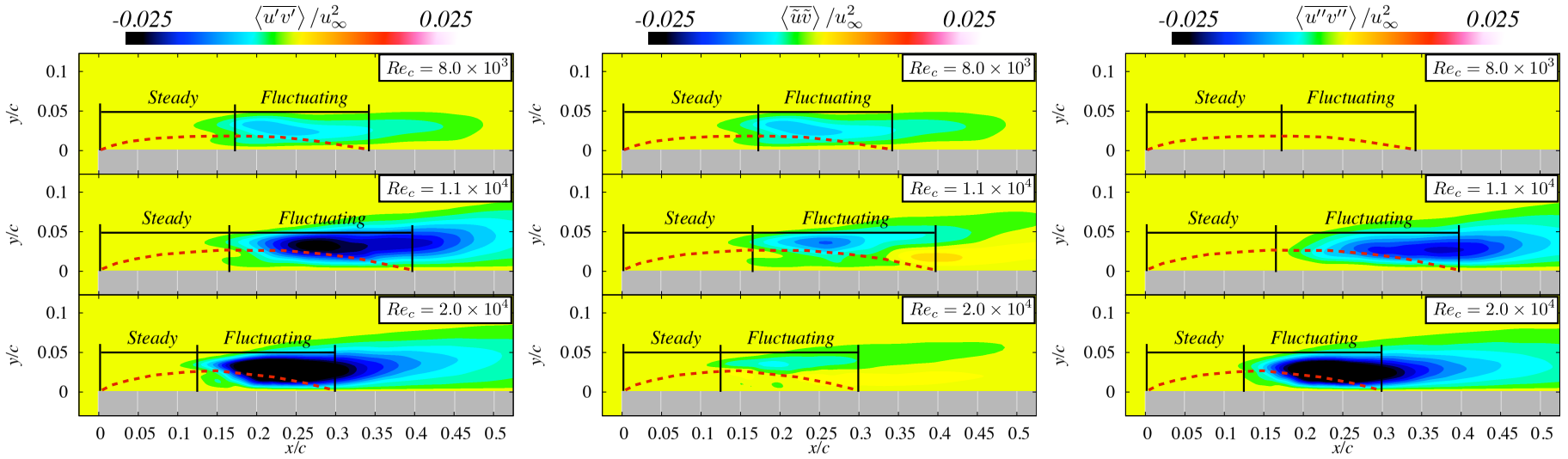

(a) Overall component

(b) Two-dimensional component

(c) Three-dimensional component

Figure 4.9: Reynolds shear stress flow fields of (a) overall $\langle \overline{u'v'} \rangle$, (b) two-dimensional $\langle \overline{\tilde{u}\tilde{v}} \rangle$, and (c) three-dimensional $\langle \overline{u''v''} \rangle$ components at $Re_c = 8.0 \times 10^3$, 1.1×10^4, and 2.0×10^4. In the averaged flows, the outer layer of LSB is denoted by red-dashed lines.

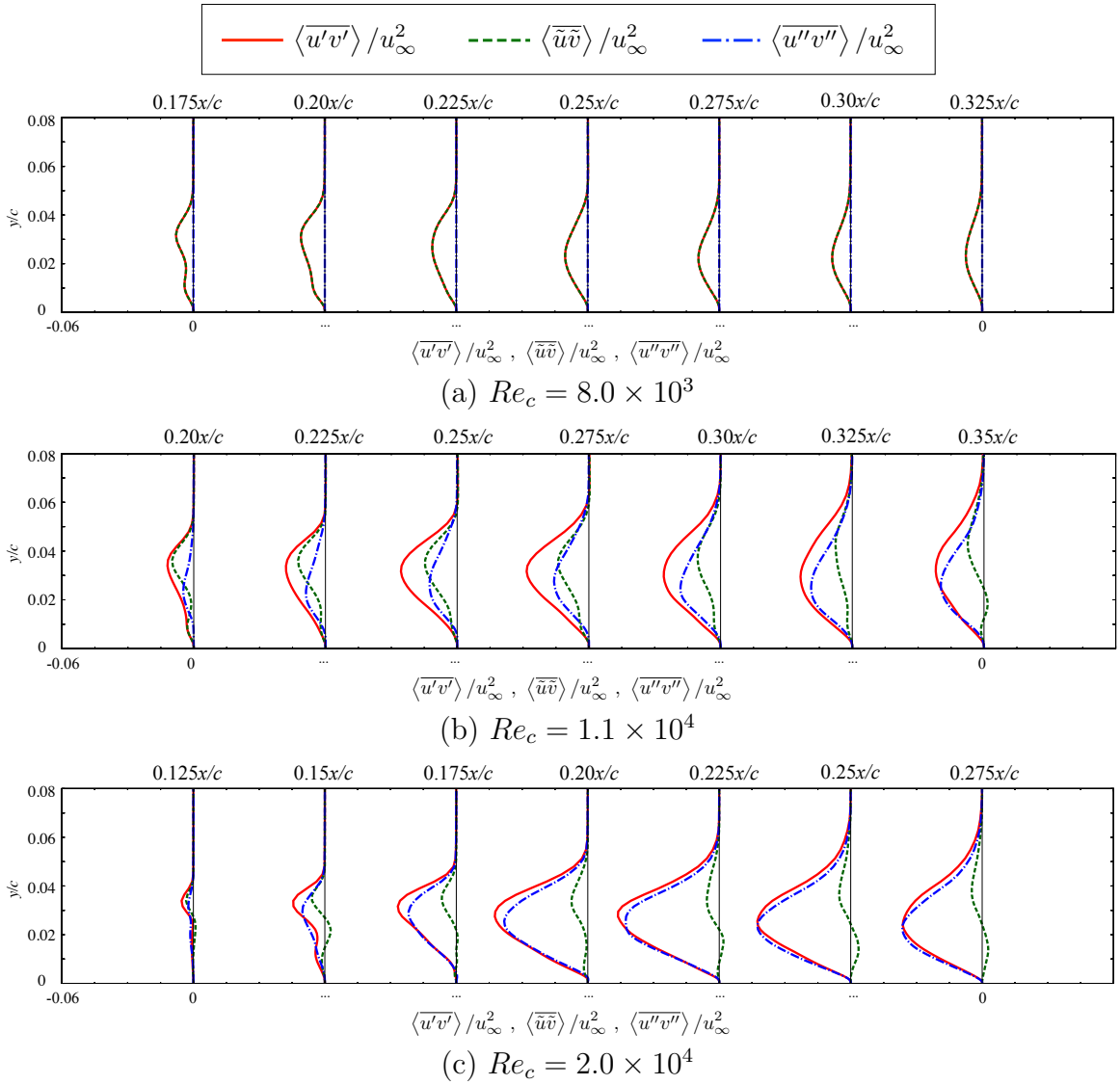

(a) $Re_c = 8.0 \times 10^3$

(b) $Re_c = 1.1 \times 10^4$

(c) $Re_c = 2.0 \times 10^4$

Figure 4.10: Budget of Reynolds shear stress in the wall normal direction at several positions within the fluctuating region at (a) $Re_c = 8.0 \times 10^3$, (b) $Re_c = 1.1 \times 10^4$, and (c) $Re_c = 2.0 \times 10^4$; The overall Reynolds stress (solid-lines, red), two-dimensional (dashed-lines, green), and three-dimensional (dashed-dotted-lines, blue) components.

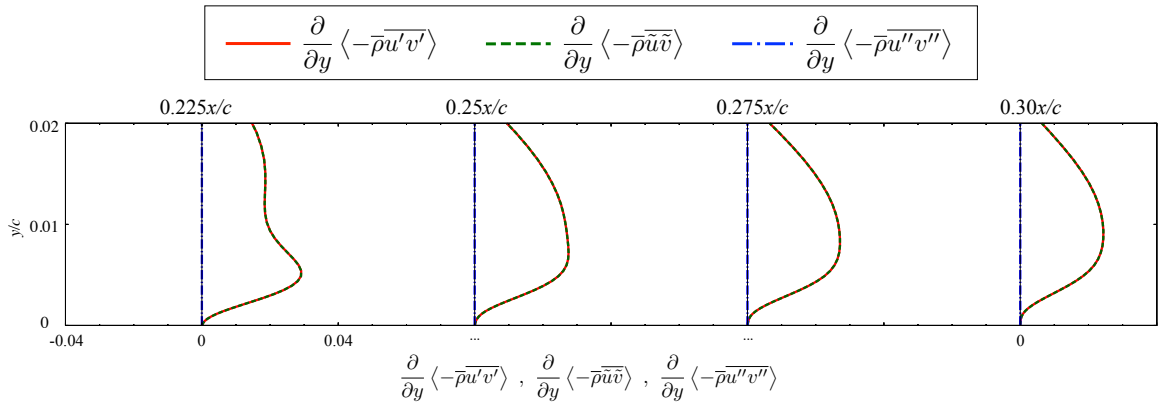

(a) $Re_c = 8.0 \times 10^3$

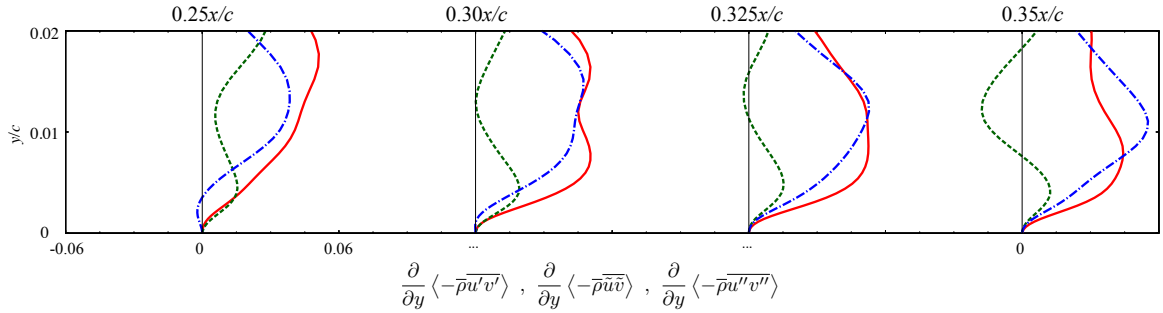

(b) $Re_c = 1.1 \times 10^4$

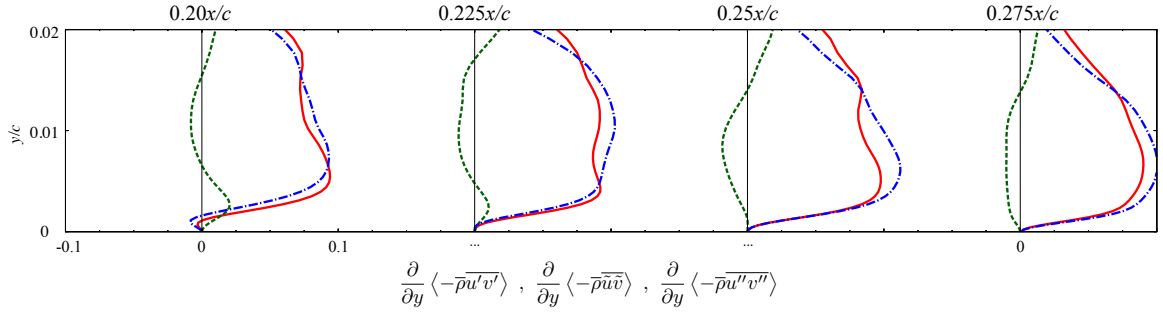

(c) $Re_c = 2.0 \times 10^4$

Figure 4.11: Budget of gradient transport of Reynolds shear stress in the wall-normal direction at several positions within the fluctuating region at (a) $Re_c = 8.0 \times 10^3$, (b) $Re_c = 1.1 \times 10^4$, and (c) $Re_c = 2.0 \times 10^4$; The overall Reynolds stress (solid-lines, red), two-dimensional (dashed-lines, green), and three-dimensional (dashed-dotted-lines, blue) components.

4.5 Summary

In this chapter, the mechanisms behind the different shapes of pressure distribution within the LSB is discussed from a new point of view. By deriving the averaged streamwise pressure gradient (momentum budget) equation (Eq. (4.11)), it is investigated the detailed mechanisms related to the formation of surface pressure distribution around an LSB. Through the analysis of the present chapter, following mechanisms are newly found in the steady (laminar part) and fluctuating (turbulent part) region of an LSB, respectively.

Steady region The convective, second viscous diffusion and gradient transport of Reynolds stress terms in the averaged streamwise pressure gradient equation are negligible near the surface irrespective of the Reynolds number and the type of the LSB. On the other hand, the different pressure gradient in the same steady region of LSB_S and LSB_SF is caused by the different distribution of the first viscous diffusion term. In the LSB_S, the distribution of the first viscous diffusion term only affects the formation of pressure gradient unlike three terms mentioned above, and its positive value make the gradual pressure recovery. As the Reynolds number increases, the value of first viscous diffusion gradually decreases, and the first viscous diffusion effects near the surface becomes negligibly small as similar to other three terms. Consequently, this leads to the zero pressure gradient which corresponds to the plateau pressure distributions. The differences in the first viscous diffusion at the different Reynolds numbers are explained by the streamwise velocity and viscous shear stress distributions. From the results, it is confirmed that the different viscous shear stress near the surface is affected by the different development of the separated shear layer depending on the Reynolds numbers. In the LSB_S, a thickly developed shear layer is formed by the low Reynolds numbers effects, and consequently the effect of the separated shear layer continuously exists near the surface. It leads to the non-negligible viscous shear stress near the surface, and contributes the formation of the positive first viscous diffusion. In the LSB_SF, the viscous shear stress near the surface becomes considerably smaller than the lower Reynolds number cases because of the relatively thin shear layer, and hence the first viscous diffusion effects near the surface become negligibly small.

Fluctuating region First of all, it is shown that the presence of fluctuating component and the gradient transport of Reynolds stress, called as GTOR (gradient transport of overall Reynolds stress) in this chapter, are important factors for the rapid pressure

recovery phenomenon. The presence of fluctuating components due to the Reynolds stress induces the strong viscous shear stress near the surface, and the rapid pressure recovery is generated. One of the interesting result is that these characteristics do not depend on the instantaneous flow structures. In order to investigate the relevance between the distributions of GTOR and the flow structures, the GTOR is decomposed into a gradient transport of Reynolds normal stress in the streamwise direction and a gradient transport of Reynolds shear stress (GTRS) in the wall-normal direction. The decomposition results tell us that the momentum transfer in the wall-normal direction induced by the GTRS component is an important factor for the rapid pressure recovery. Next, the overall GTRS is additionally decomposed into two- and three-dimensional components. The results indicate that the two-dimensional spanwise vortex contributes to the GTRS at $Re_c = 8.0 \times 10^3$, whereas the three-dimensional turbulent structures is the main contributor to the GTRS at $Re_c \geq 1.1 \times 10^4$. In conclusion, the presence of fluctuation and its gradient play an important role in the rapid pressure recovery, but the physical phenomenon that creates the Reynolds shear stress is not a critical factor. Moreover, the magnitude of gradient transport of Reynolds shear stress is important and the formation of three-dimensional turbulent structures is not a necessary condition for the rapid pressure recovery.

Chapter 5

Reliability of the two-dimensional laminar simulation

In the previous chapters, I discussed the physical mechanisms related to the formation of surface pressure distribution around LSBs. It was revealed that the flow structures are basically two-dimensional, and capturing the behavior of separated shear layer accurately is important in the steady region. In the fluctuating region, the magnitude of gradient of the Reynolds shear stress itself is more important rather than the physical phenomenon which creates it. Considering these mechanisms, it is expected that some characteristics of an LSB which includes complicated nonstationary three-dimensional flows can be predicted even by a two-dimensional simulation. As reported by Kojima *et al.* (2013) and Lee *et al.* (2015), it was shown that a two-dimensional unsteady laminar simulation could be adopted to estimate qualitative lift and drag coefficients characteristics with a relatively low computational cost. These results support the usefullness of two-dimensional simulations, but it is still unknown the predictability of a two-dimensional laminar simulation for various physical phenomena except for separation and reattachment points. To verify the hypothesis mentioned above, two-dimensional unsteady laminar simulations are conducted for a 5% thickness blunt leading edge flat plate in this chapter. First, the analysis object, flow conditions, numerical schemes, and accuracy assessments are presented in Sec. 5.1. Section 5.2 discusses the predictability in terms of instantaneous flow fields and some averaged physical properties. Then, in Sec. 5.3, the predictability of surface pressure distribution of the two-dimensional laminar simulation as well as physical mechanisms related to its formation are presented.

5.1 Computational setup

5.1.1 Analysis object

Since the purpose of this chapter is to verify the reliability of the two-dimensional simulations, it is necessary to compare it with the high-fidelity three-dimensional simulation results. Therefore, a 5% thickness flat plate with a blunt leading edge is adopted as the analysis object which is same in Chap. 3.

5.1.2 Computational grid and flow conditions

Figure 5.1 shows a two-dimensional computational grid around a 5% thickness blunt leading edge flat plate. One of the spanwise cross sections of the three-dimensional grid is used for two-dimensional simulations. Other conditions, such as the extension length of outer boundary and the minimum grid spacing in the wall-normal direction, are as exactly same as the grid of three-dimensional simulations. Non-slip and adiabatic conditions are adopted on the surface (Sec. 2.6.1). Three levels of grid resolution are employed for evaluating grid convergence, as similar to those of the three-dimensional simulations. The accuracy assessment including the grid convergence as well as several factors which may lead to numerical errors will be discussed in Sec. 5.1.4. The freestream Mach number (M_∞) with zero freestream turbulence, the specific heat ratio (γ), and the Prandtl number (Pr) are set to 0.2, 1.4, and 0.72, respectively. The Reynolds number based on the plate length (Re_c) are set to $1, 2, 5, 1.0 \times 10^1, 2.0 \times 10^1, 5.0 \times 10^1, 1.0 \times 10^2, 2.0 \times 10^2, 5.0 \times 10^2, 1.0 \times 10^5$, and intervals of every $1,000$ in the range of $1.0 \times 10^3 \sim 4.0 \times 10^4$ (total 50 cases).

5.1.3 Numerical schemes

The third order MUSCL (Section 2.3.1) without any limiter and the SHUS (Section 2.3.2) are employed for evaluating the convective terms. The viscous terms are computed by the second order central differencing without any turbulence model. The second order backward differencing converged by the ADI-SGS method (Section 2.4.1) is adopted for time integration. The effects of time step size will be discussed in Sec. 5.1.4. The flow fields are assumed to be laminar in the entire region and no turbulence models are employed.

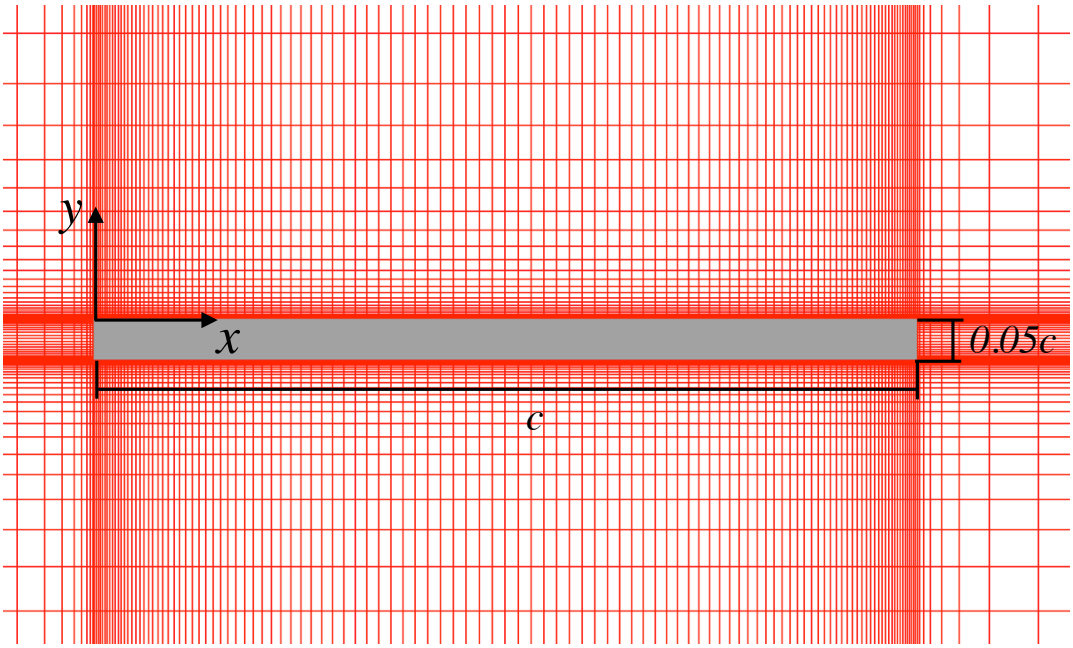

Figure 5.1: Computational grid (Grid B) for the 5 % thickness blunt leading edge flat plate. Every third grid point in each direction is shown.

5.1.4 Accuracy assessments

In performing numerical experiments, it must be examined some factors which may produce numerical errors (e.g., the number of grid points, time step size Δt, and minimum grid spacing $\Delta x_{\min}$, $\Delta y_{\min}$) in order to reduce numerical errors and prevent misleading of the discussion. The accuracy assessment studies are conducted at $Re_c = 2.0 \times 10^4$.

The first one is the grid convergence. The number of each grid point in the chordwise (x), wall-normal (y), and spanwize (z) directions denoted by N_x, N_y, and N_z, respectively, are listed in Tab. 5.1. In this convergence study, the time step size and minimum grid spacing in each direction are fixed to $\Delta t = 0.0002$, $\Delta x_{\min} = 3.5\Delta y_{\min}$, and $\Delta y_{\min} = 0.0002$, respectively. Figure 5.2 shows the results of convergence study for the number of grid points. The results indicate that Grid B are sufficient for further analysis.

The next one is an investigation of the time step size effect. The cases of time step size are listed in Tab. 5.2. In this convergence study, Grid B is adopted and the minimum grid spacing in each direction are set to $\Delta x_{\min} = 3.5\Delta y_{\min}$, and $\Delta y_{\min} = 0.0002$, respectively. Figure 5.3 shows the results of convergence study for the time step size. For the quantitative evaluation of the time step effect, the maximum CFL number

is examined in the present study. The CFL number is defined as follow:

$$\mathrm{CFL} = \Delta t \frac{\max(\sigma_x, \sigma_y, \sigma_z)}{\min(\Delta x, \Delta y, \Delta z)}, \tag{5.1}$$

where σ_x, σ_y, and σ_z correspond to the maximum eigenvalue of flux Jacobian (spectral radius of flux Jacobian) as described in Eq. (2.140)-(2.142). It is found that the maximum CFL number should be lower than 1.2 and time B is sufficient for analysis.

One more important factor is the minimum grid spacing in the streamwise direction near the leading edge $\Delta x_{\min}$. In case of the flat plate, a very thin laminar boundary layer flowing in y direction is formed at the leading edge. If the resolution for this boundary layer is insufficient, it may affect the characteristics of separated shear layer formed by turning around the corner of the leading edge. Therefore, $\Delta x_{\min}$ is important for the resolution of the boundary layer at the leading edge. As already mentioned in Sec. 5.1.2, the minimum grid spacing in the wall-normal direction on the upper and lower surface is $\Delta y_{\min} = 0.0002$. Fujii (1994) suggested that the minimum grid spacing should be $\Delta y_{\min} < 0.1/\sqrt{Re_c}$; and the current $\Delta y_{\min}$ satisfies the criteria at $Re_c = 2.0 \times 10^4$. Note that this width also satisfies the criteria of $\Delta y^+ < 1$ in the three-dimensional LES. Based on $\Delta y_{\min}$, the cases of $\Delta x_{\min}$ are listed in Tab. 5.3. In this convergence study, Grid B is adopted and the time step size is set to $\Delta t = 0.0002$. Figure 5.4 shows the results of convergence study for minimum grid spacing in the streamwise direction. The results show that $\Delta x_{\min} = 3.5\Delta y_{\min}$ is sufficient. As a results, the conditions of Grid B, Time A and Min A are applied in this study. Additionally, the effects of cross-sectional aspact ratio of flat plate on flow characteristics are discussed in App. A.

Table 5.1: Cases of the number of grid points.

Grid	N_x	N_y	N_z	Total points
Grid A	373	285	1	106,305
Grid B	471	359	1	169,090
Grid C	571	433	1	247,243

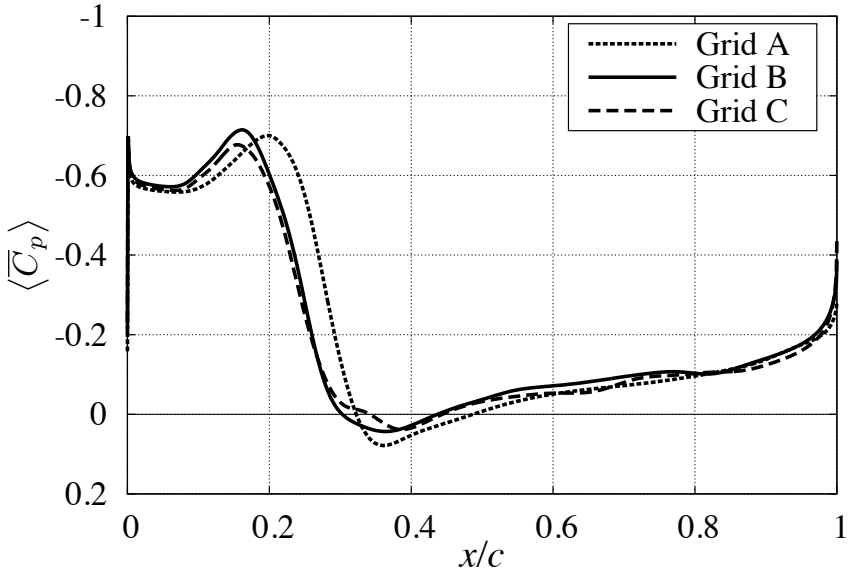

(a) Surface pressure distribution

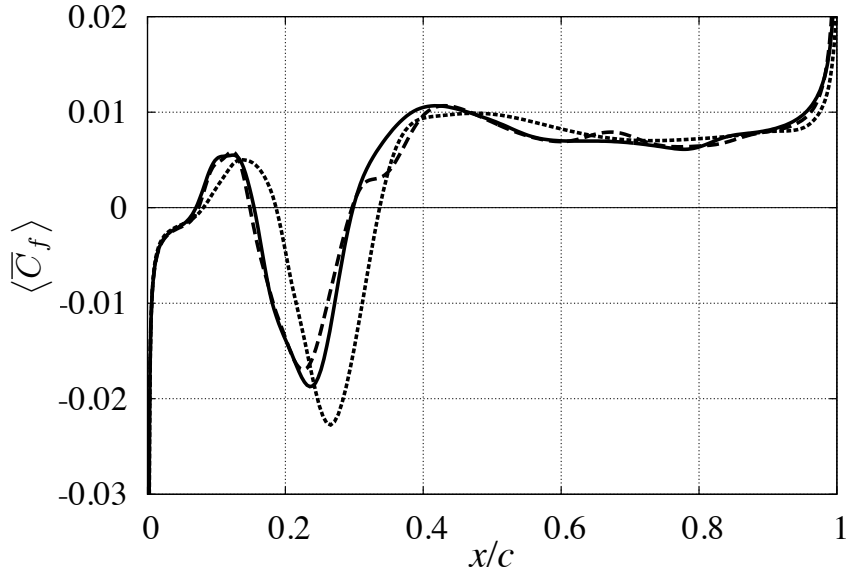

(b) Skin friction coefficient

Figure 5.2: Convergence study for the number of grid points.

Table 5.2: Cases of the time step size and maximum CFL number.

Time step	Δt	Maximum CFL
Time A	0.0001	0.60
Time B	0.0002	1.19
Time C	0.0005	2.98
Time D	0.0010	5.94

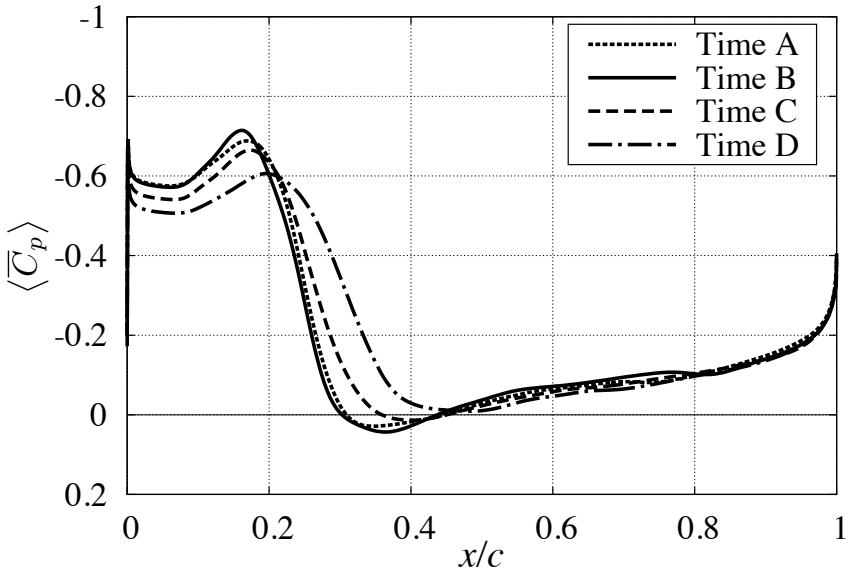

(a) Surface pressure distribution

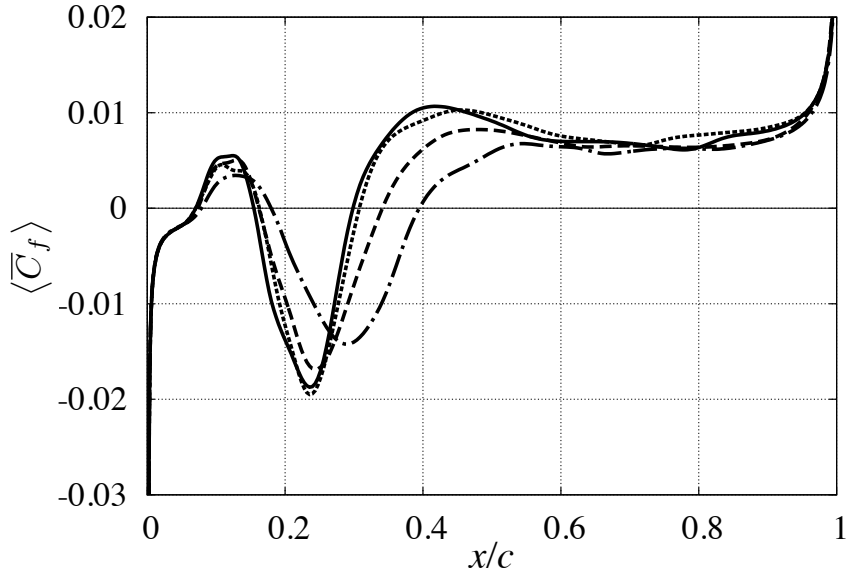

(b) Skin friction coefficient

Figure 5.3: Convergence study for the time step size.

Table 5.3: Cases of the minimum grid spacing in streamwise direction.

Minimum spacing	$\Delta x_{\min}$	$\Delta x_{\min}/\Delta y_{\min}$
Min A	0.00070	3.5
Min B	0.00035	1.75
Min C	0.00020	1.0
Min D	0.00010	0.5

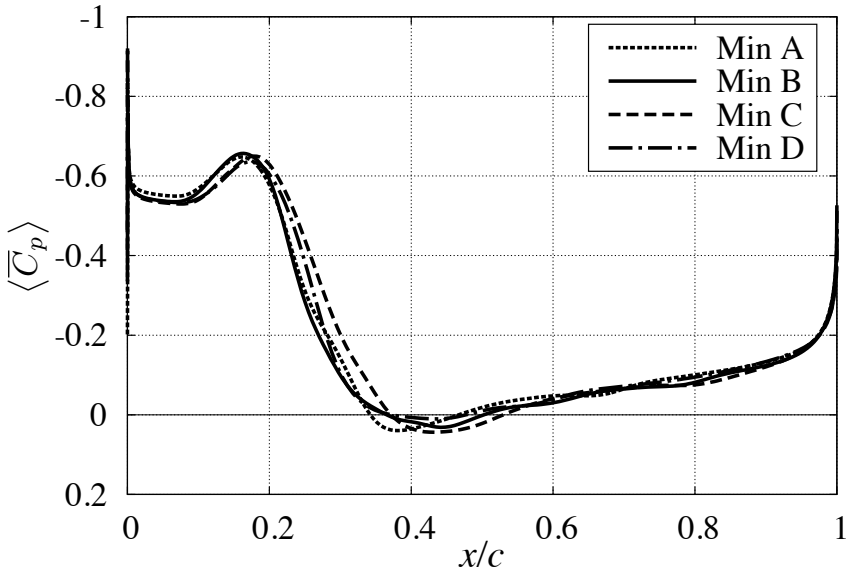

(a) Surface pressure distribution

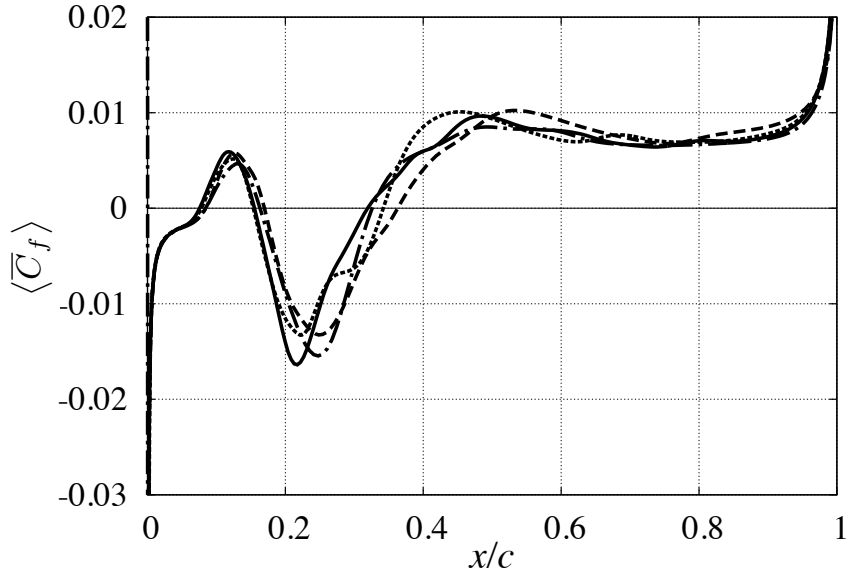

(b) Skin friction coefficient

Figure 5.4: Convergence study for the minimum grid spacing in the streamwise direction.

Figure 5.5 shows the comparison of reattachment points between several previous experimental (Kottke *et al.*, 1977; Lane & Loehrke, 1980; Ota *et al.*, 1981; Sasaki & Kiya, 1991; Hwang *et al.*, 1998) and numerical results (Tafti & Vanka, 1991*a*; Yanaoka & Ota, 1996; Yanaoka *et al.*, 2002; Thompson, 2012). Note that the Reynolds numbers and reattachment points are normalized by the plate thickness t. Therefore, for instance, $Re_c = 2.0 \times 10^4$ corresponds to $Re_t = 1,000$. Several previous studies reported that three-dimensional turbulent structures were observed from $Re_t \simeq 325$ (Lane & Loehrke, 1980), $Re_t \simeq 270$ (Ota *et al.*, 1981), and $Re_t \simeq 320$ (Sasaki & Kiya, 1991). Thus, if the critical Reynolds number for transition is considered as $Re_t = 270 \sim 320$, the present two-dimensional results show quantitatively good agreement with another previous studies before the critical Reynolds number. After the critical Reynol numbers, a tendency of decrease in the length of LSB is similarly observed although quantitative differences are seen.

Figure 5.6 shows the variation of reattachment points and drag coefficient on the upper surface of the flat plate in a wide range of Reynolds numbers ($1.0 \times 10^0 \leq Re_c \leq 1.0 \times 10^5$). As shown in Fig. 5.6 (a), the flow is fully attached on the plate surface at $Re_c < 2.0 \times 10^3$. In Fig. 5.6 (b), the theoretical curves proposed by Blasius (Schlichting & Gersten, 1979) expressed as follows:

$$\langle \overline{C}_D \rangle = \frac{1.328}{Re_c^{1/2}}, \tag{5.2}$$

and Kuo (Kuo, 1953) given as follows:

$$\langle \overline{C}_D \rangle = \frac{1.328}{Re_c^{1/2}} + \frac{4.12}{Re_c}, \tag{5.3}$$

are superimposed. A previous study (Sun & Boyd, 2004) reported that the flow in the ultra low Reynolds number region ($Re_c < 200$) should be carefully investigated because of the rarefied effects. Nevertheless, if I focus on the drag coefficient of the upper surface in the Reynolds number region where the flow is not separated, the present two-dimensional results shows good agreement with the Kuo's equation which expresses the drag of laminar viscous flow past a finite flat plate. On the other hand, in the Reynolds number region after separation, the drag coefficient sharply decreases and begins to apart from the theoretical curves. This may be attributed by the fact that the friction drag decreases due to the formation of separated area.

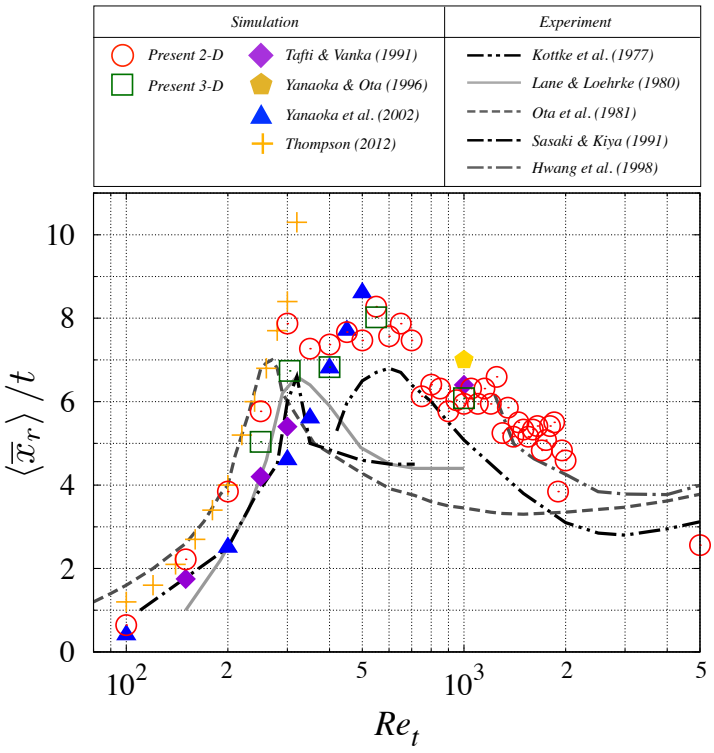

Figure 5.5: Variation of the reattachment points with the Reynolds numbers. The present two-dimensional (opened-circles, red) and three-dimensional (opened-squares, green) results are shown with several previous experimental and numerical results.

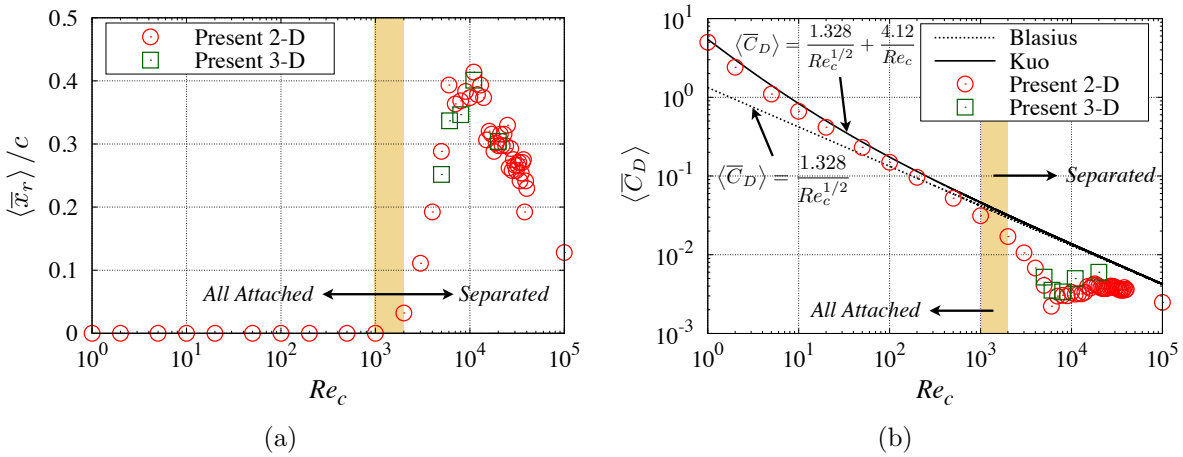

Figure 5.6: Variation of (a) reattachment point and (b) drag coefficient on the upper surface of the flat plate of the two-dimensional (opened-circles, red) and three-dimensional (opened-squares, green) with the Reynolds numbers from 1.0×10^0 to 1.0×10^5. The theoretical results of Blasius (dotted-line, Schlichting & Gersten, 1979) and Kuo (solid-line, Kuo, 1953) are shown in (b).

5.2 Predictability of instantaneous and averaged properties

5.2.1 Instantaneous and averaged flow fields

Figure 5.7 shows instantaneous spanwise vorticity fields of the two- and three-dimensional simulations at $Re_c = 5.0 \times 10^3$, 6.1×10^3, 8.0×10^3, 1.1×10^4, and 2.0×10^4. As already discussed in Sec. 3.2 and shown in the figures, the flow structures remains two-dimensional in the entire flow fields and those spanwise coherent vortices are convected to the downstream at $Re_c \leq 8.0 \times 10^3$ in the three-dimensional simulation. As expected, flow fields of the two-dimensional unsteady laminar simulation is similar to those of the three-dimensional simulations. On the other hand, at relatively higher Reynolds numbers ($Re_c = 1.1 \times 10^4$ and 2.0×10^4), three-dimensional turbulent structures appear in the three-dimensional simulations whereas the convection of the two-dimensional vortices without the vortex breakdown are observed in the two-dimensional simulations.

In spite of discrepancies of the instantaneous flow fields at higher Reynolds numbers, qualitatively similar features are obtained in the averaged flow fields of the two- and three-dimensional simulations. Figure 5.8 shows the averaged streamwise velocity flow fields of the two- and three-dimensional simulations. First of all, at $Re_c \leq 8.0 \times 10^3$, there is no difference in formation of LSBs, length of LSBs, and formation of the attached boundary layer in both simulations. Even at higher Reynolds numbers where three-dimensional turbulent structures are formed, the formation of LSBs and length of LSBs are qualitatively in agreement in both two- and three-dimensional simulations. In other words, with respect to flow fields where an LSB is formed, the formation of three-dimensional turbulent structures cannot be captured in the instantaneous two-dimensional simulations but the averaged flow field shows similar predictability to the three-dimensional simulation.

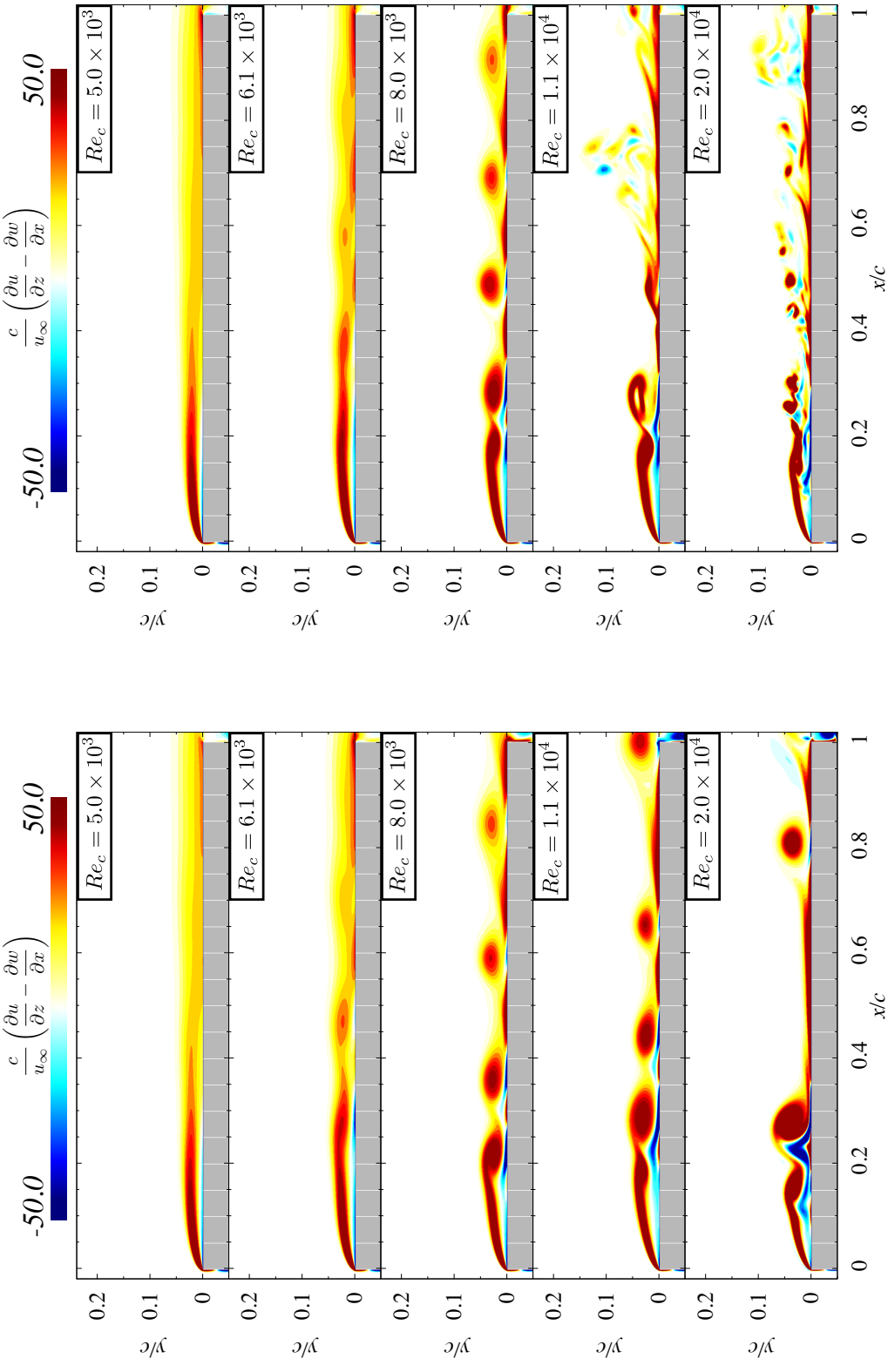

(a) Two-dimensional simulation

(b) Three-dimensional simulation

Figure 5.7: Instantaneous spanwise vorticity flow fields of (a) two-dimensional and (b) three-dimensional simulations at $Re_c = 5.0 \times 10^3$, 6.1×10^3, 8.0×10^3, 1.1×10^4, and 2.0×10^4.

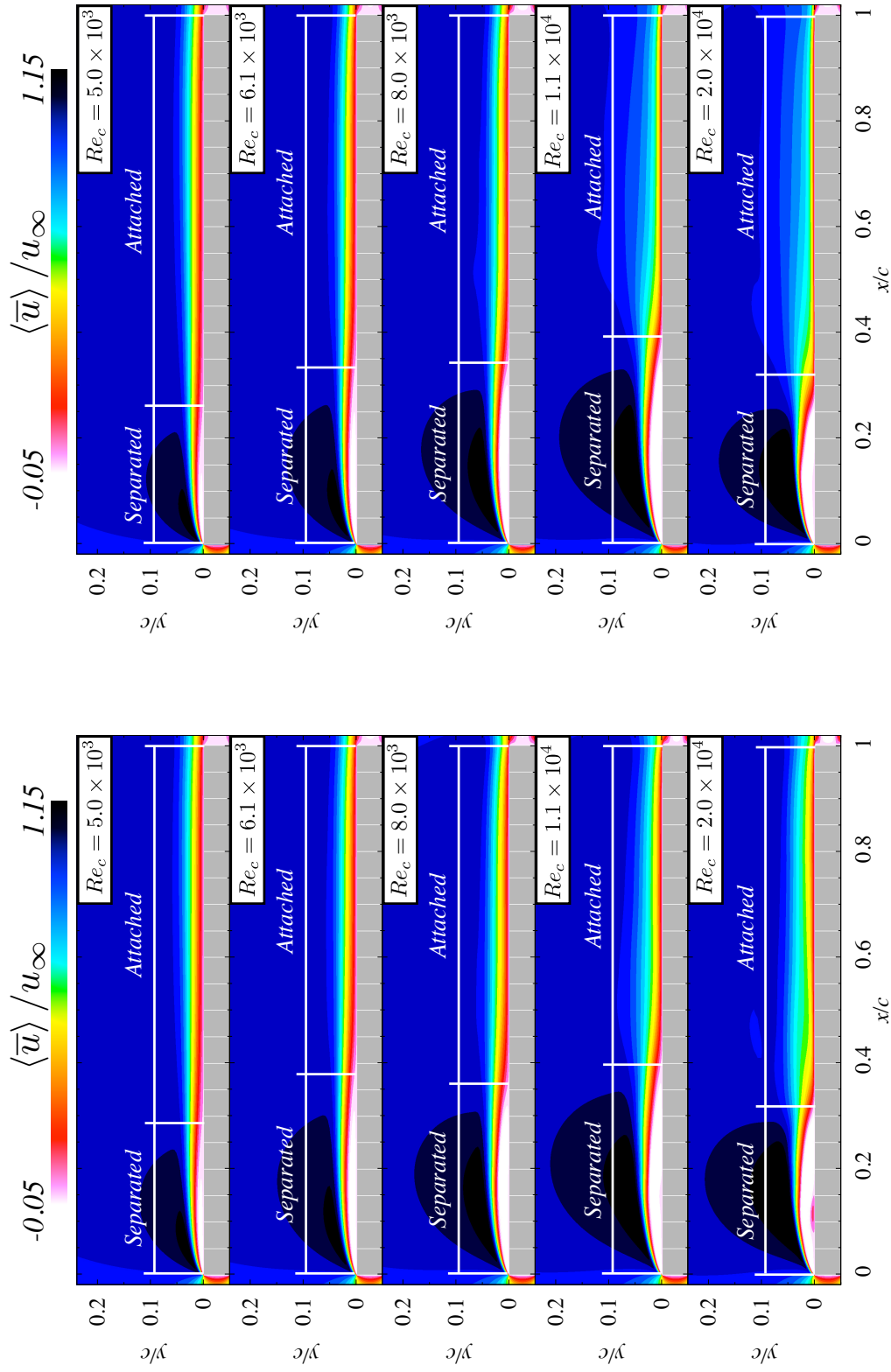

(a) Two-dimensional simulation

(b) Three-dimensional simulation

Figure 5.8: Averaged streamwise velocity flow fields of (a) two-dimensional and (b) three-dimensional simulations at $Re_c = 5.0 \times 10^3$, 6.1×10^3, 8.0×10^3, 1.1×10^4, and 2.0×10^4.

5.2.2 Predictability of averaged quantities

This section discusses the predictability of two-dimensional simulation on averaged physical quantities. First of all, the averaged surface pressure distribution and skin friction coefficient are shown in Fig. 5.9. Based on the flow field structures and the reattachment state shown in Sec. 3.3.3, the Reynolds number was divided into two regions such as the Reynolds numbers of the laminar reattachment ($Re_c \leq 8.0 \times 10^3$) and those of the turbulent reattachment ($Re_c \geq 1.1 \times 10^4$). Let us assume that the transition Reynolds number is $Re_c \simeq 1.0 \times 10^4$ from the following discussion for convenience. At lower Reynolds number where the laminar reattachment occurs, a good agreement between the two- and three-dimensional results is shown in both distributions. At higher Reynolds numbers where three-dimensional turbulent structures appear, a qualitatively good agreement between the two- and three-dimensional results is also observed in the reattachment point and shapes of each distribution. On the other hand, the overshoot distribution in the surface pressure distribution and skin friction coefficient is observed (e.g., $x/c \simeq 0.2$ at $Re_c = 1.1 \times 10^4$ or $x/c \simeq 0.15$ at $Re_c = 2.0 \times 10^4$). These areas correspond to the transition region in the three-dimensional simulation. The reason of appearing this overshoot phenomenon will be discussed in Sec. 5.3.

Figure 5.10 shows the tendency of time-averaged reattachment point variations to the Reynolds numbers in the two- and three-dimensional simulations. In case of the flat plate, the reattachment point corresponds to the length of LSB. In the three-dimensional simulations, the LSB shows the longest length around the transition Reynolds number, and thereafter it shrinks as increase in the Reynolds numbers. This trend is in good agreement with the experimental results reported by Anyoji *et al.* (2011) (see also Fig. 1.12). In particular, a quantitatively good agreement can be seen in both results even at the Reynolds numbers where three-dimensional turbulent structures appear. Figure 5.11 shows the time-averaged shape factor at the reattachment point and at a certain location within the attached boundary layer ($x/c = 0.7$). The definition of shape factor and determination of the reattachment state using the shape factor were discussed in Sec. 3.3.3. An interesting result is that the trend of varying laminar to turbulent reattachment can be predicted by using the shape factors of the two-dimensional simulations even which cannot capture the formation of three-dimensional turbulent structures. At the reattachment points shown in Fig. 5.11 (a), a decrease in shape factors clearly appears in both simulations around the transition Reynolds numbers. Furthermore, the shape factors of two-dimensional simulations show quantitatively good agreement with those of three-dimensional simulations ($\langle \overline{H} \rangle \simeq 3.9$ in the laminar reattachment case;

$\langle \overline{H} \rangle \simeq 2.6$ in the turbulent reattachment case). Although there is a quantitative difference in both simulations at the turbulent reattachment Reynolds numbers, the tendency of decrease of the shape factor is also observed within the attached boundary layer.

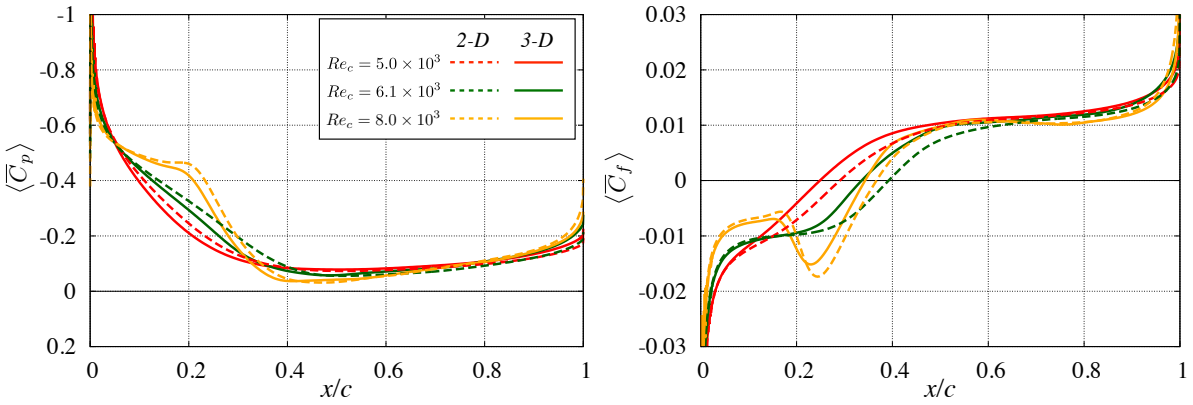

(a) Reynolds numbers of the laminar reattachment

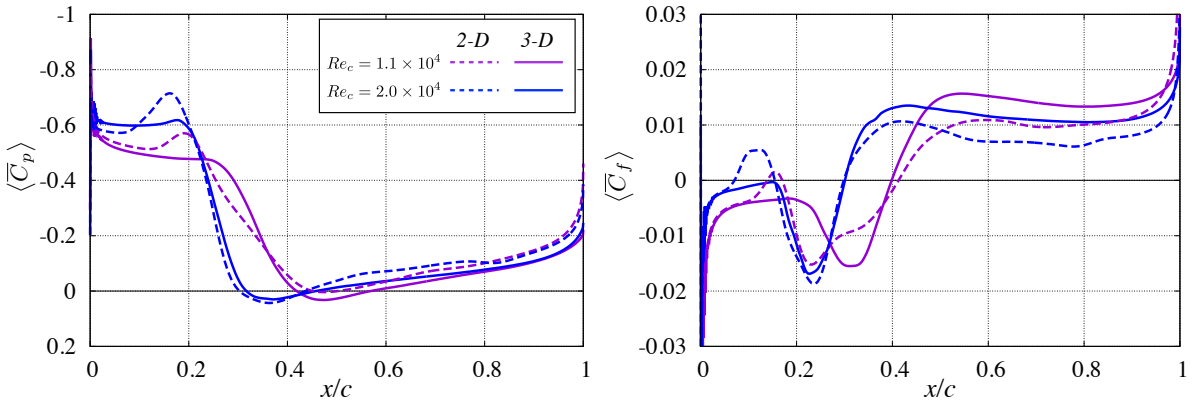

(b) Reynolds numbers of the turbulent reattachment

Figure 5.9: Averaged surface pressure distribution (left column) and skin friction coefficient (right column) of two-dimensional (dashed-line) and three-dimensional (solid-line) simulation results at (a) Reynolds numbers of the laminar reattachment ($Re_c = 5.0 \times 10^3$, red; 6.1×10^3, green; and 8.0×10^3, yellow) and (b) those of turbulent reattachment ($Re_c = 1.1 \times 10^4$, violet; and 2.0×10^4, blue) cases.

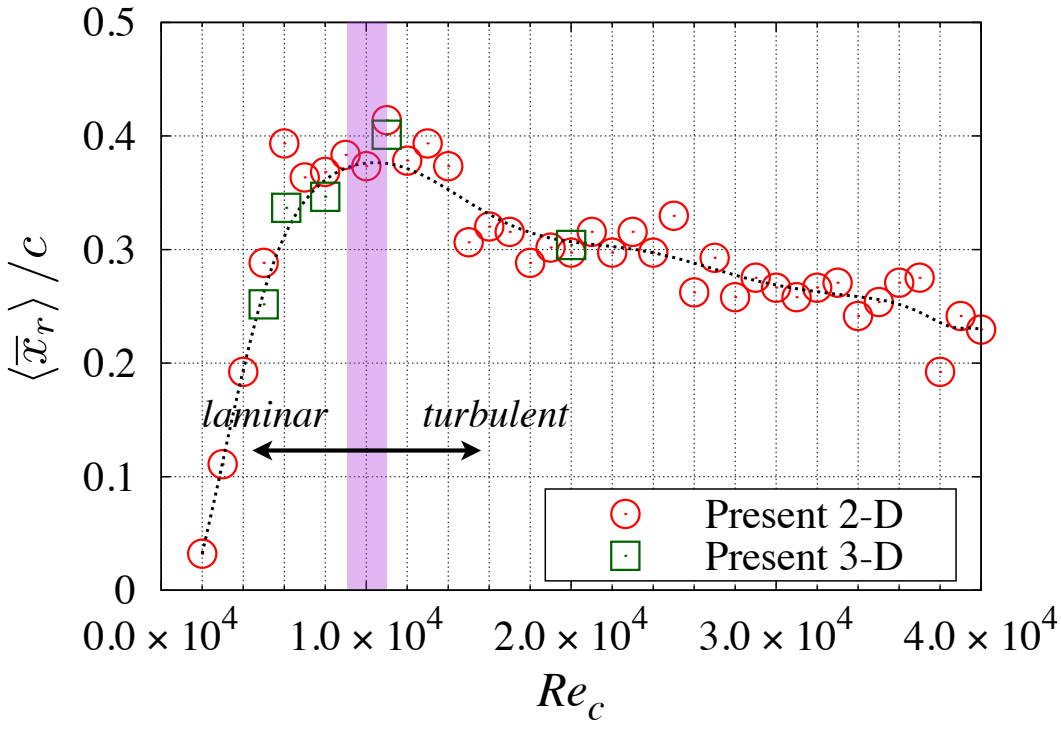

Figure 5.10: Averaged reattachment points of two-dimensional (opened-circles, red) and three-dimensional (opened-squares, green) simulations with an approximate curve of the two-dimensional results (dashed-line, black).

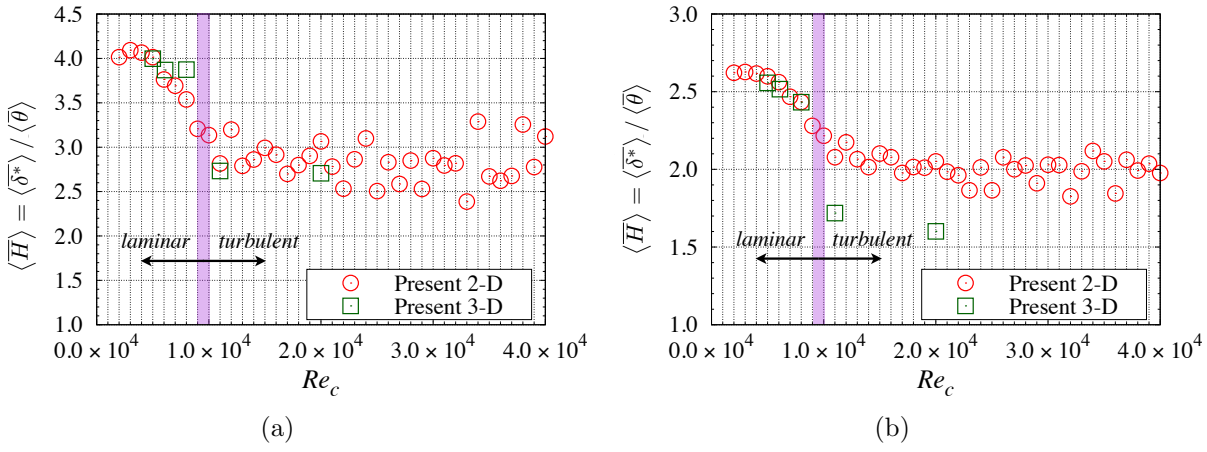

Figure 5.11: Averaged shape factors at (a) reattachment point and (b) attached boundary layer ($x/c = 0.7$) of two-dimensional (opened-circles, red) and three-dimensional (opened-squares, green) simulations.

On the ohter hand, it is observed some discrepancies between the two- and three-dimensional simulations. Figure 5.12 shows the averaged streamwise velocity profiles based on the wall unit. As expected, the profiles of two- and three-dimensional simulations show a good agreement at the laminar reattachment Reynolds numbers. On the other hand, at turbulent reattachment Reynolds numbers, the buffer ($5 < y^+ < 30$) and log-law region ($y^+ > 30$) which are characteristic distributions of a turbulent boundary layer can be seen in the three-dimensional simulations whereas those are not observed in the two-dimensional ones. Due to the differences in the velocity profiles, the drag coefficient also differs in both simulations. Figure 5.13 shows the variation of drag coefficients with the Reynolds numbers. Note that the drag coefficients shown in here indicate the results for the upper surface of the flat plate. From the figure, it is confirmed that the drag coefficient decreases as the Reynolds number increases under the transitional Reynolds number, and values of two- and three-dimensional simulations are quantitatively good agreement. This is caused that the separated region is elongated and the friction drag decreases as the length of LSB increases. On the other hand, quantitatively large differences are observed at the turbulent reattachment Reynolds numbers. After the transition Reynolds numbers, it can be seen that a sharp increase in the drag coefficients appears in the three-dimensional simulations whereas the increase width of the two-dimensional simulations is relatively small. It can be considered that this is attributed by the strong friction drag in the vicinity of the surface which is induced by the turbulent structures, and the three-dimensional simulation can capture those phenomena. Strictly speaking, however, this result suggests that it is difficult to predict the accurate friction drag by two-dimensional simulations because the contribution of the pressure drag due to the separation is negligible because the direction of pressure drag is perpendicular to the flow in the flat plate case. It is known, however, that contribution of the pressure drag to the total drag is larger than that of the friction drag when an LSB is formed around an airfoil (Kondo *et al.*, 2013; Lee *et al.*, 2015); and hence, it should be carefully concluded in terms of the predictability of drag coefficient. The predictability of the drag coefficient for flow fields around an airfoil will be shown in Sec. 6.2.3.

In summary, even in higher Reynolds numbers where three-dimensional turbulent structures appear, the two-dimensional unsteady laminar simulation can predict various averaged physical quantities except for the boundary layer profiles or drag of the surface.

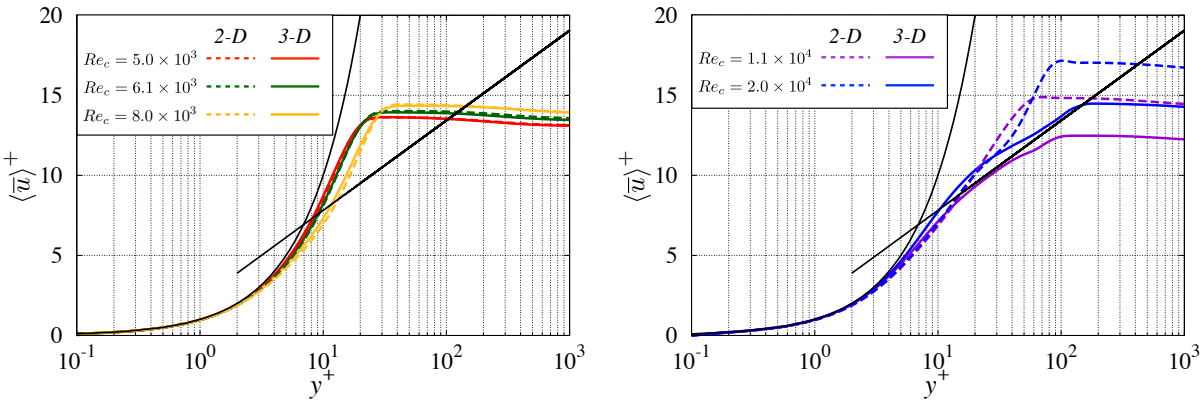

Figure 5.12: Averaged velocity profiles at attached boundary layer ($x/c = 0.7$) of the two-dimensional (dashed-line) and three-dimensional (solid-line) simulation results at (a) Reynolds numbers of the laminar reattachment ($Re_c = 5.0 \times 10^3$, red; 6.1×10^3, green; 8.0×10^3, yellow) and (b) those of turbulent reattachment ($Re_c = 1.1 \times 10^4$, violet; 2.0×10^4, blue) cases.

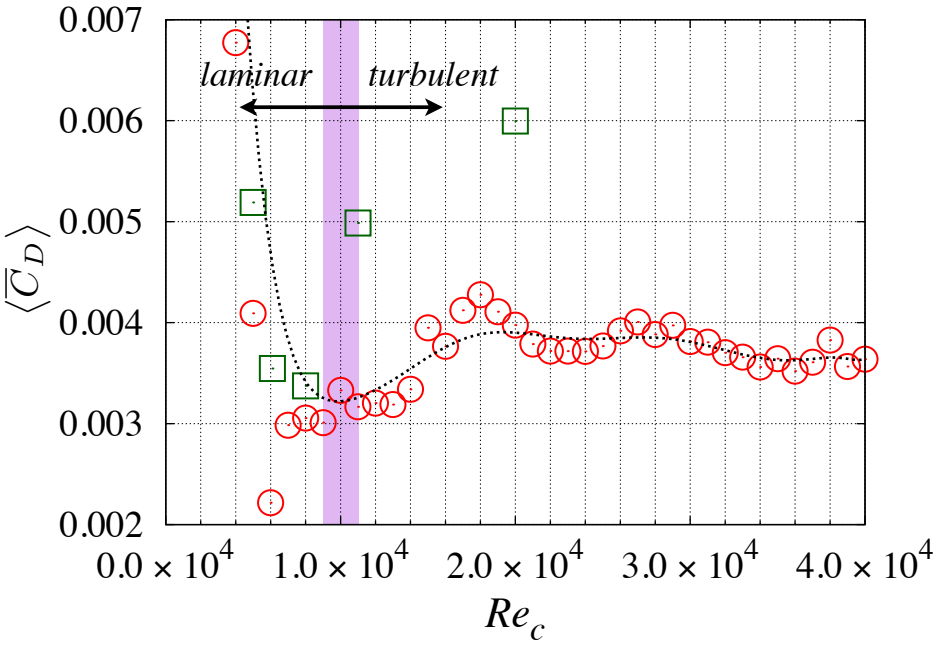

Figure 5.13: Variation of drag coefficient on the upper surface of the flat plate of the two-dimensional (opened-circles, red) and three-dimensional (opened-squares, green) with the Reynolds numbers from 1.0×10^3 to 4.0×10^4.

5.3 Predictability of surface pressure distribution

5.3.1 Classification of the separation bubble

In this section, detailed discussion will be conducted for the reason why the predictability of pressure distribution of two-dimensional simulation is similar to that of the three-dimensional one regardless of the Reynolds number and flow structure (see, Fig. 5.9). First of all, as shown in Sec. 3.3.1, the maximum TKE is investigated to classify characteristics of LSBs. Figure 5.14 shows the maximum TKE distributions of two- and three-dimensional simulations. Note that a location in the streamwise direction is normalized by the time-averaged reattachment points. First of all, the TKE is negligibly small at $Re_c = 5.0 \times 10^3$ and 6.1×10^3 through the entire LSB. At the higher Reynolds numbers ($Re_c = 8.0 \times 10^3$, 1.1×10^4 and 2.0×10^4), however, the distributions of two-dimensional simulation qualitatively differ to those of the three-dimensional one. First, the largest increase width is confirmed at 40% of the bubble length in the three-dimensional simulation, whereas it appears at 30% of the bubble length in the two-dimensional simulation. The next point is that the location of maximum TKE moves to upstream in the two-dimensional simulation, and its maximum value is obviously higher than that of the three-dimensional one. Nevertheless, if I adopt the same criteria as Sec. 3.3.1 (2% of u_∞^2) for dividing of the steady and fluctuating region, the LSB characteristics can be classified by LSB_S and LSB_SF. In other words, the flow inside the LSB is entirely steady state at $Re_c \leq 6.1 \times 10^3$, so the LSB_S is observed; on the other hand, the steady and fluctuating region coexist at $Re_c \geq 8.0 \times 10^3$, so the LSB_SF appears. From the following discussion, the distribution of two- and three-dimensional simulation within the steady and fluctuating region will be examined in detail.

5.3.2 Steady region of the separation bubble

In this section, a quantitative analysis within the steady region of LSB is discussed. Figure 5.15 shows budget of the time-averaged streamwise pressure gradient equation (Eq. (4.11)) in the steady region of the LSB_S and LSB_SF. It is seen that there is no significant differences in the distributions of each term in the two- and three-dimensional simulations. As similar to the three-dimensional simulations, it can be considered that the main contributor of appearing different pressure gradient in the same steady region is caused by the different distribution of the first viscous diffusion under the separated shear layer. The distributions of each term in both simulations, however, are obviously different at the location where the overshoot phenomenon is seen in the pressure distribution

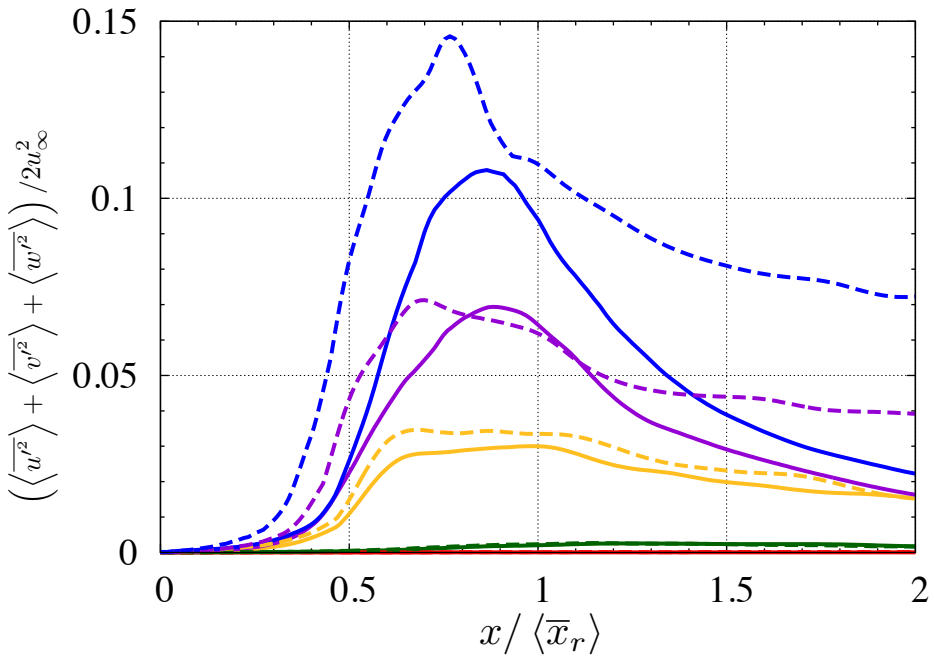

Figure 5.14: Maximum turbulent kinetic energy distribution of the two-dimensional (dashed-line) and three-dimensional (solid-line) simulation results at $Re_c = 5.0 \times 10^3$ (red), 6.1×10^3 (green), 8.0×10^3 (yellow), 1.1×10^4 (violet), and 2.0×10^4 (blue).

(e.g., $x/c \simeq 0.15$ at $Re_c = 2.0 \times 10^4$ in Fig. 5.9 (b)). For instance, as shown in Fig. 5.15 (e), all terms in the RHS of Eq. (4.11) are negligible at $x/c = 0.125$ in the three-dimensional simulation. In contrast, the negative gradient transport of the Reynolds stress are observed away from the surface. As a result, the negative viscous stress is induced near the surface, and it contributes to create $\partial\overline{p}/\partial x < 0$. This is caused by the fact that the Reynolds stress of two-dimensional simulation is overestimated by the two-dimensional vortex structure that is formed without showing the laminar-turbulent transition. Also, since this Reynolds stress works in the direction of ejecting from the surface to the freestream, the secondary separation occurs in the reverse flow region inside the LSB. Because of this strong secondary separation, the overshoot phenomenon is also observed in the skin friction coefficient. In short, since the flow basically has two-dimensional structures in the steady region of LSB, the pressure distribution can be accurately predicted even in the two-dimensional simulation. The mechanisms of appearing different pressure distribution depending on the Reynolds numbers are similar to those of the three-dimensional simulation. On the other hand, the reason of the overshoot of pressure distribution in the two-dimensional simulation is caused by the overestimation of Reynolds stress in the transition region.

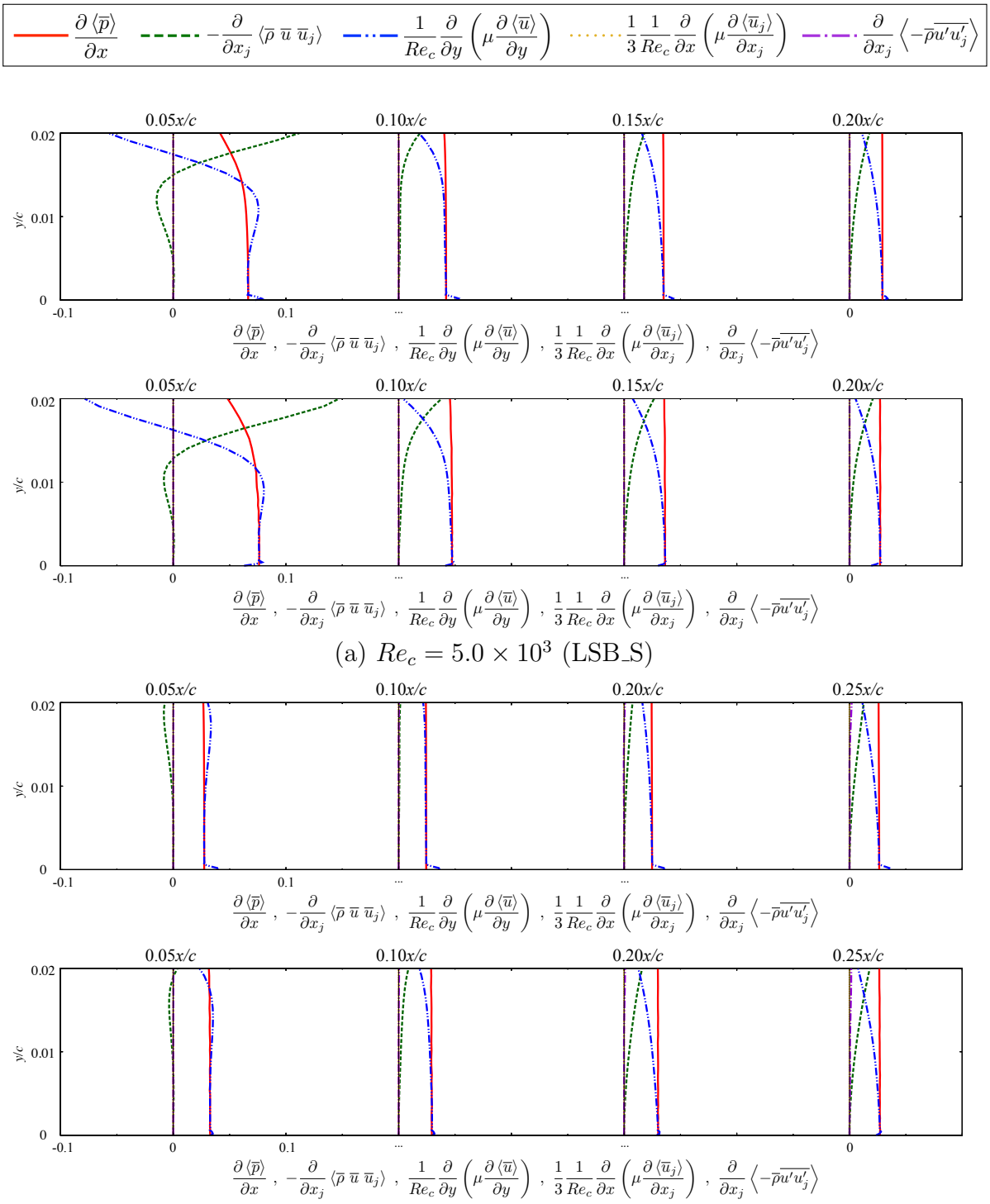

(a) $Re_c = 5.0 \times 10^3$ (LSB_S)

(b) $Re_c = 6.1 \times 10^3$ (LSB_S)

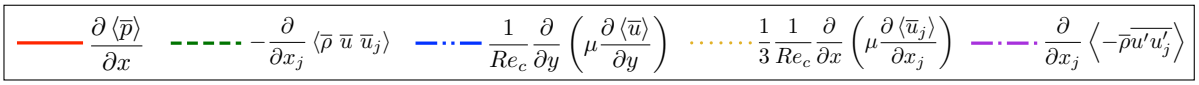

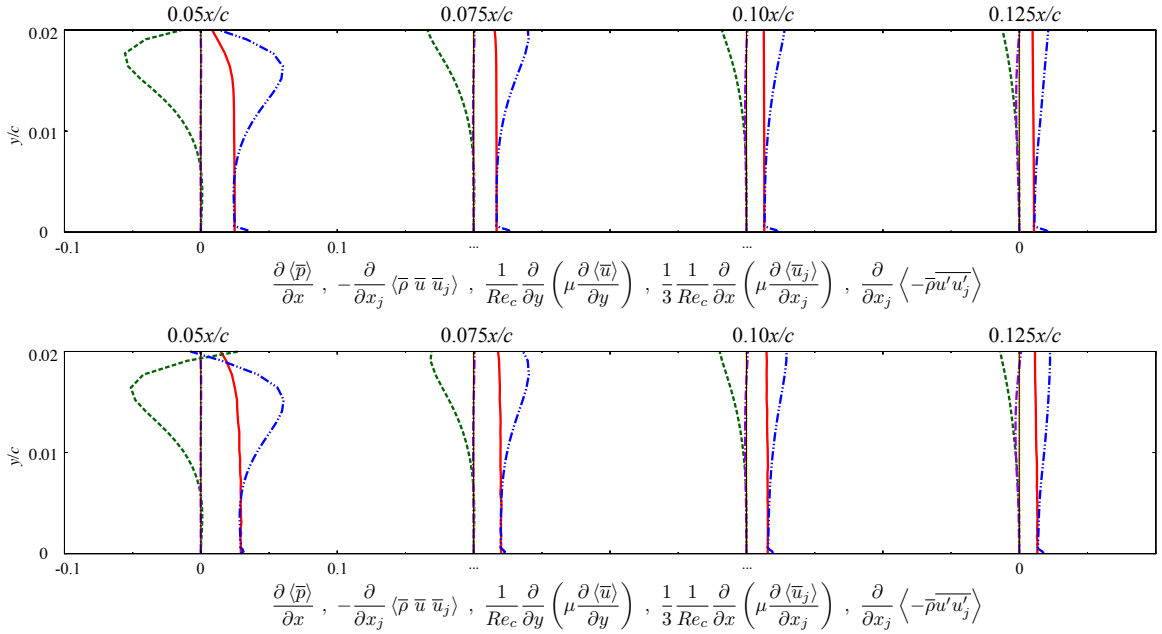

(c) $Re_c = 8.0 \times 10^3$ (LSB_SF)

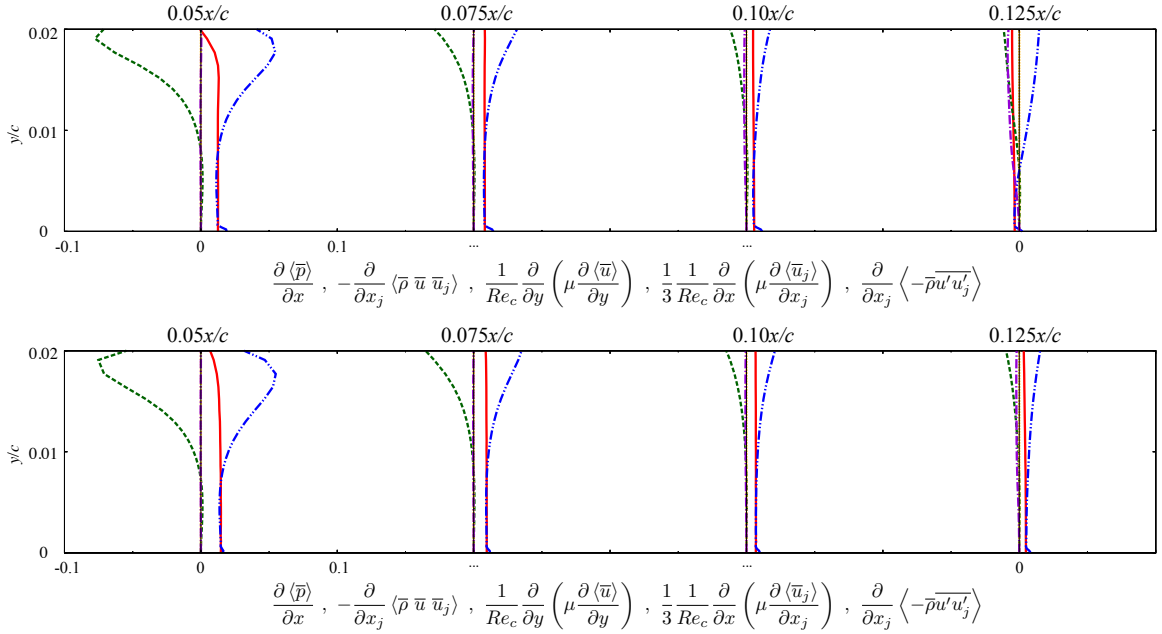

(d) $Re_c = 1.1 \times 10^4$ (LSB_SF)

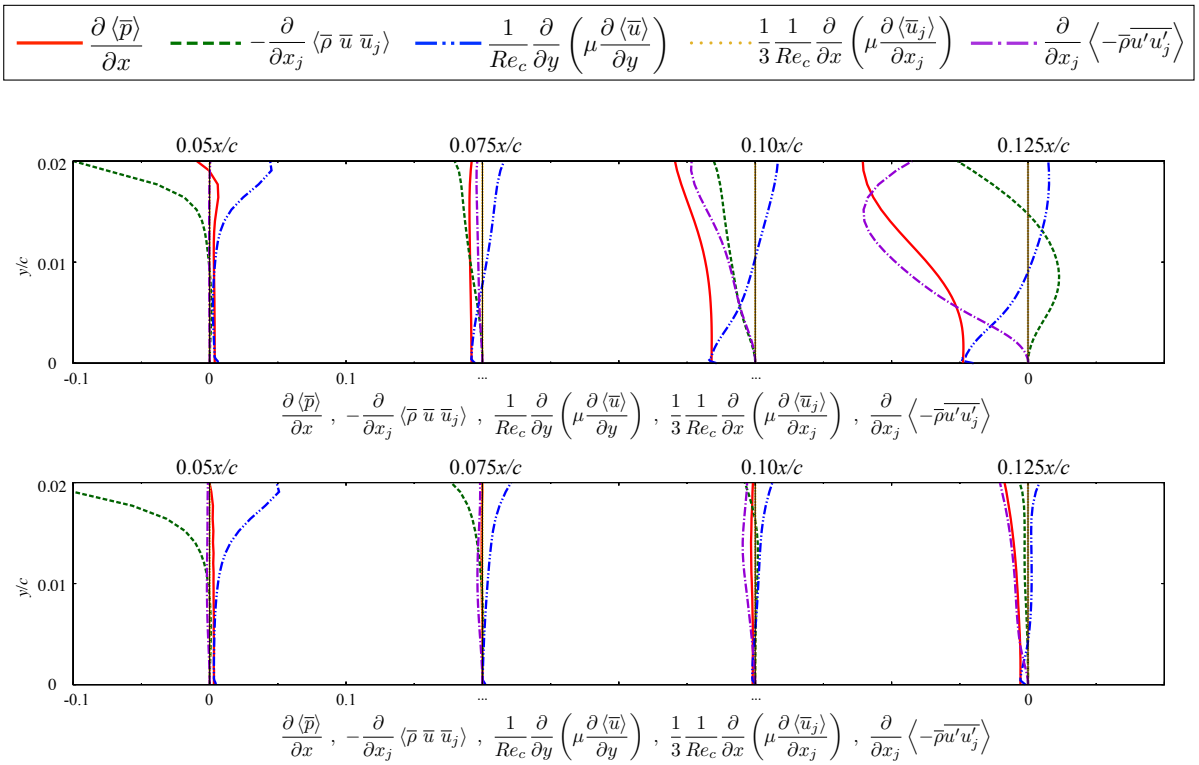

(e) $Re_c = 2.0 \times 10^4$ (LSB_SF)

Figure 5.15: Momentum budget in Eq. (4.11) in the wall-normal direction at several positions within the steady region at (a) $Re_c = 5.0 \times 10^3$ (LSB_S), (b) $Re_c = 6.1 \times 10^3$ (LSB_S), (c) $Re_c = 8.0 \times 10^3$ (LSB_SF), (d) $Re_c = 1.1 \times 10^4$ (LSB_SF), and (e) $Re_c = 2.0 \times 10^4$ (LSB_SF); Pressure gradient (solid-lines, red), convective (dashed-lines, green), the first viscous diffusion (dashed-double-dotted-lines, blue), the second viscous diffusion (dotted-lines, black), and gradient transport of Reynolds stress (dashed-dotted-lines, violet) terms. Top and bottom of each figure correspond to the two- and three-dimensional simulation results, respectively.

5.3.3 Fluctuating region of the separation bubble

In this section, a quantitative analysis within the fluctuating region of LSB will be explained. Thus, the results of $Re_c \geq 8.0 \times 10^3$ are only shown from the following discussion. Figure 5.16 shows budget of the time-averaged streamwise pressure gradient equation (Eq. (4.11)) in the fluctuating region of the LSB_SF. As similar to the three-dimensional simulation, it can be considered that the presence of Reynolds stress plays an important role in the formation of rapid pressure recovery. First of all, the second viscous diffusion is negligible irrespective of the Reynolds numbers. Although the influence of the convective term is observed together with the formation of the gradient transport of Reynolds stress, the effect of the gradient transport of the Reynolds stress is stronger than that of the convective term. It is similar to the three-dimensional results. As a result, it induces the strong first viscous diffusion near the surface and it contributes to make the rapid pressure recovery. It was mentioned in Sec. 4.4.1 that the characteristics of distribution described above do not depend on the instantaneous flow structure. Another noteworthy point is that the qualitative distributions of both simulations are similar in spite of the fact that three-dimensional turbulent structures are not captured in the two-dimensional simulation. This fact indirectly suggests that the rapid pressure recovery distribution does not largely depend on the flow structures.

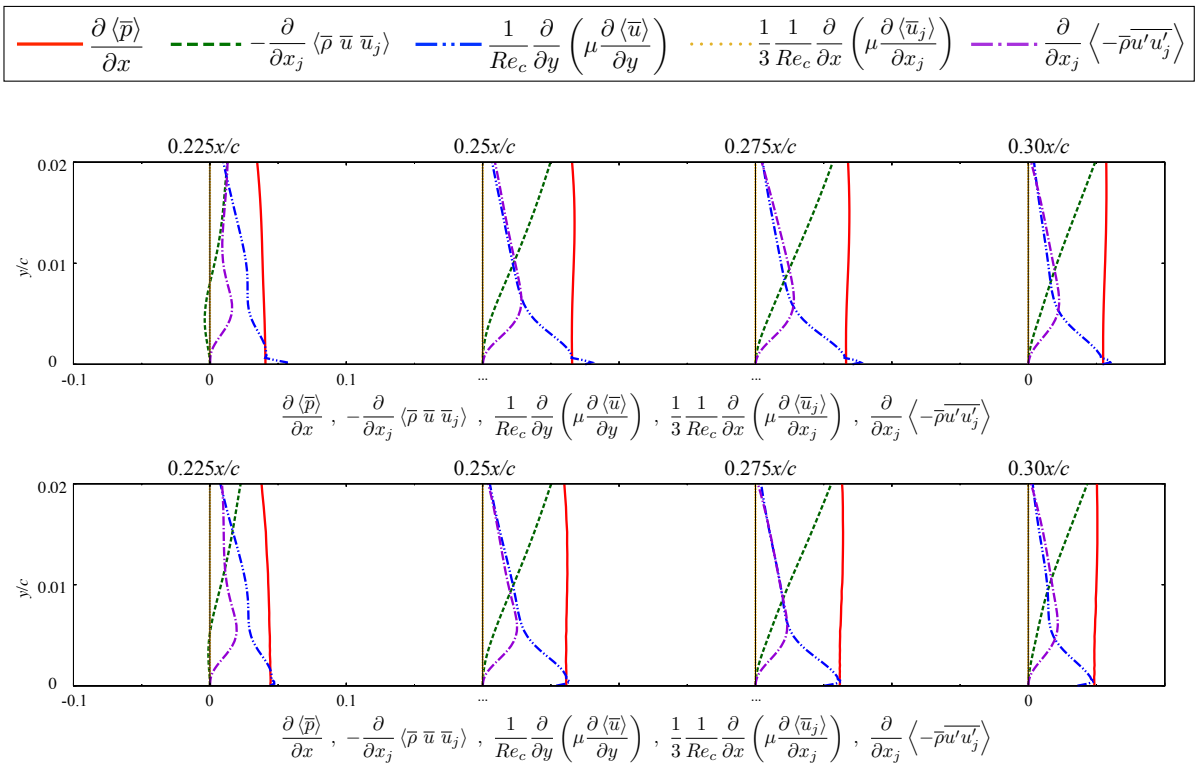

(a) $Re_c = 8.0 \times 10^3$

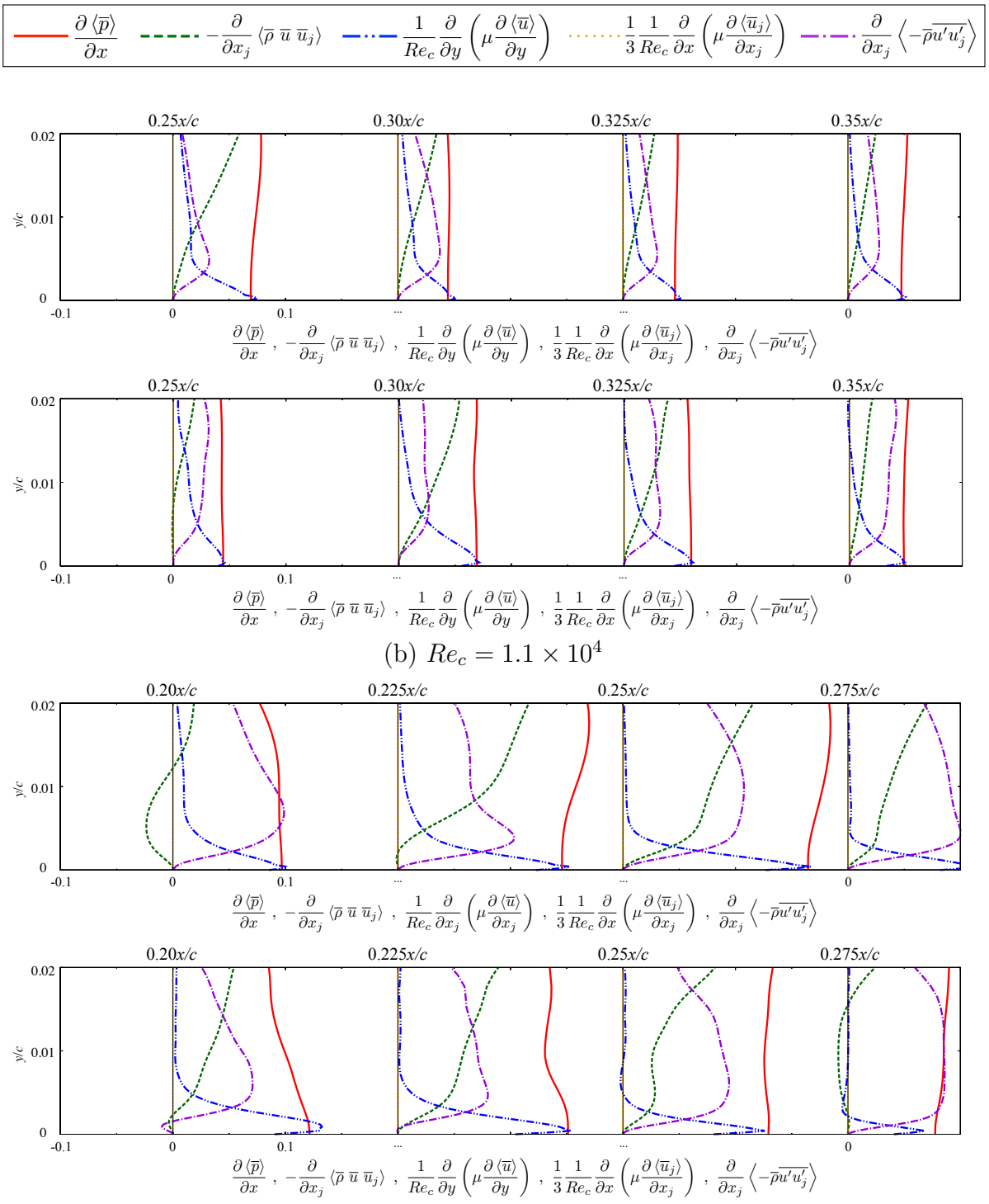

(b) $Re_c = 1.1 \times 10^4$

(c) $Re_c = 2.0 \times 10^4$

Figure 5.16: Momentum budget in Eq. (4.11) in the wall-normal direction at several positions within the fluctuating region at (a) $Re_c = 8.0 \times 10^3$, (b) $Re_c = 1.1 \times 10^4$, and (c) $Re_c = 2.0 \times 10^4$; Pressure gradient (solid-lines, red), convective (dashed-lines, green), the first viscous diffusion (dashed-double-dotted-lines, blue), the second viscous diffusion (dotted-lines, black), and gradient transport of Reynolds stress (dashed-dotted-lines, violet) terms. Top and bottom of each subfigure correspond to the two-dimensional and three-dimensional simulation results, respectively.

Secondly, the decomposition of fluctuating component discussed in Sec. 4.4.3 is applied to the two-dimensional simulation results. It is anticipated that the three-dimensional Reynolds stress component is always negligible in the two-dimensional simulation, because the three-dimensional turbulent structures do not appear. Analytically, the three-dimensional fluctuating component is calculated by

$$f'' = f - \langle f \rangle \,, \tag{5.4}$$

where f is an instantaneous variable. Since it is always satisfied that $f = \langle f \rangle$ in the two-dimensional simulation, the equation above provides

$$f'' = 0 \,. \tag{5.5}$$

It means that the only two-dimensional component contributes to the formation of the overall fluctuation ($f' = \tilde{f}$) or Reynolds stress ($\langle \overline{u_i' u_j'} \rangle = \langle \overline{\tilde{u}_i \tilde{u}_j} \rangle$). Figure 5.17 shows the flow fields of overall, two-dimensional, and three-dimensional Reynolds shear stress components in both simulations. As expected, it is confirmed that the three-dimensional component of the two-dimensional simulation is negligible regardless of the Reynolds numbers. Therefore, the overall component is only displayed from the following discussion. In the attached boundary layer region of the the overall component, the spatial distribution of Reynolds shear stress in the two-dimensional simulation is close to zero whereas those in the three-dimensional one have an effect to downstream of the reattachment point. Such a difference comes from the predictability of the three-dimensional fluctuating components. The magnitude of overall Reynolds shear stress around the transition region increases as the Reynolds number increases in both simulations. However, flow fields of the two-dimensional component clearly differ. In case of the three-dimensional simulation, its magnitude decreases as the Reynolds number increases, whereas it increases in the two-dimensional simulation. The variation trend of the two-dimensional Reynolds shear stress component in the two-dimensional simulation is similar to those of the three-dimensional Reynolds shear stress component in the three-dimensional simulation.

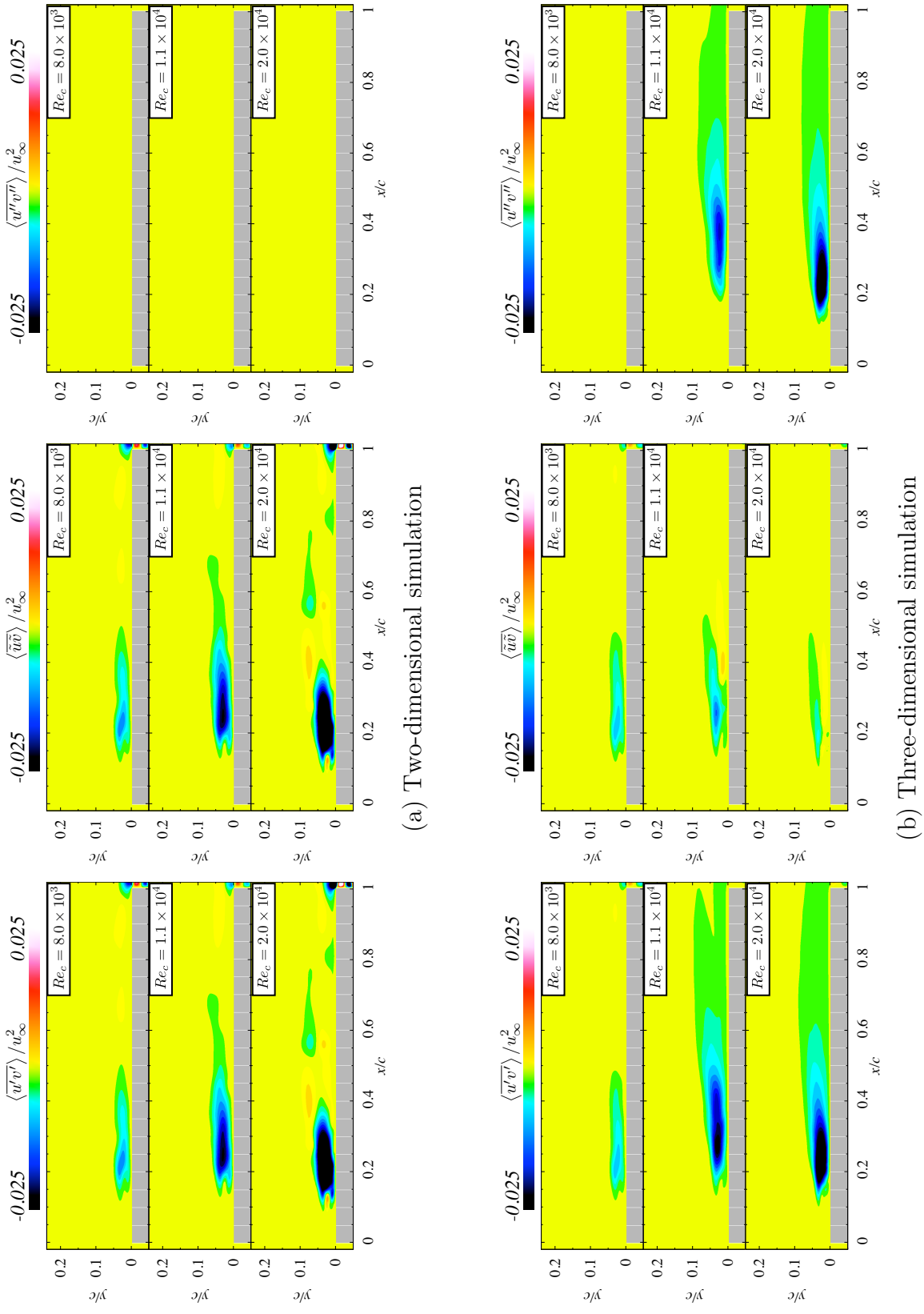

(a) Two-dimensional simulation

(b) Three-dimensional simulation

Figure 5.17: Reynolds shear stress flow fields of overall $\langle \overline{u'v'} \rangle$ (left column), two-dimensional $\langle \overline{\tilde{u}\tilde{v}} \rangle$ (middle column), and three-dimensional $\langle \overline{u''v''} \rangle$ (right column) components at $Re_c = 8.0 \times 10^3$, 1.1×10^4, and 2.0×10^4.

These characteristics are also confirmed by Fig. 5.18. The qualitative distributions of overall Reynolds stress are approximately same in both two- and three-dimensional simulations. The important fact is that the origin of creating the overall component is different. In case of the three-dimensional simulations, the three-dimensional component has a major influence on the formation of overall component at the Reynolds numbers where three-dimensional turbulent structures are observed ($Re_c \geq 1.1 \times 10^4$). On the other hand, as already mentioned in Eq. (5.5), only the two-dimensional component constitues the overall component in the two-dimensional simulation. It can be considered that the three-dimensional Reynolds shear stress component in the actual flow field is pushed into the two-dimensional one in the two-dimensional simulation.

Figure 5.19 shows the distributions of gradient transport of Reynolds shear stress that directly affects the pressure gradient. First, at $Re_c = 8.0 \times 10^3$, a good agreement is found between the two- and three-dimensional simulations. Although the distance from the surface where the maximum value appears is different in both simulations at $Re_c \geq 1.1 \times 10^4$, a common point is the generation of the positive distribution of overall component away from the surface. Thus, even if the three-dimensional turbulent structure cannot be captured in the two-dimensional simulation, the qualitative distribution of gradient transport of overall Reynolds stress is similar in both simulations; and hence the rapid pressure recovery also appears in the two-dimensional simulation.

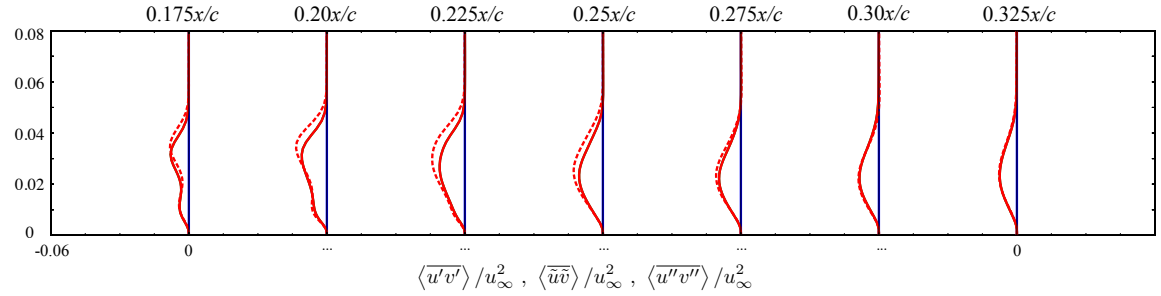

(a) $Re_c = 8.0 \times 10^3$

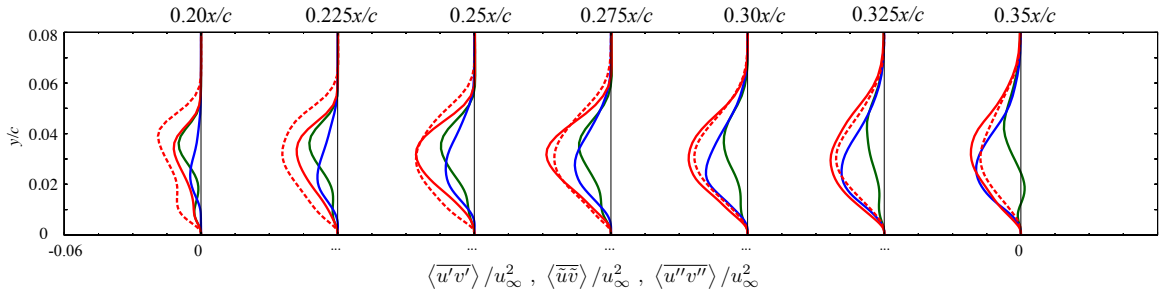

(b) $Re_c = 1.1 \times 10^4$

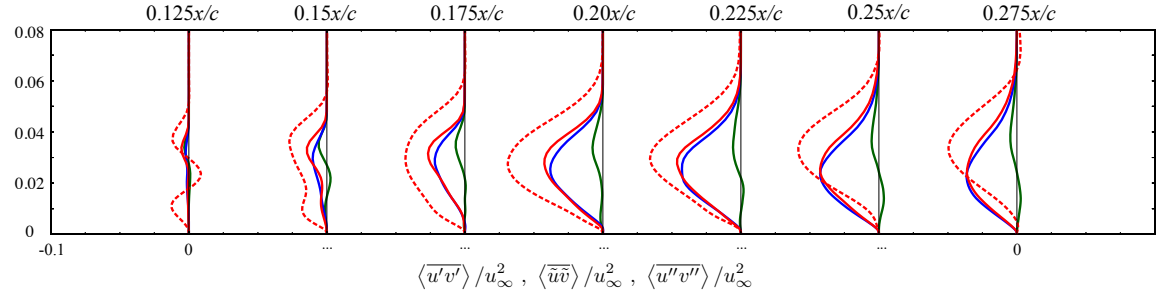

(c) $Re_c = 2.0 \times 10^4$

Figure 5.18: Budget of Reynolds shear stress of two-dimensional (dashed-line) and three-dimensional (solid-line) simulation results in the wall normal direction at several positions within the fluctuating region at (a) $Re_c = 8.0 \times 10^3$, (b) $Re_c = 1.1 \times 10^4$, and (c) $Re_c = 2.0 \times 10^4$; The overall Reynolds stress (red), two-dimensional (green), and three-dimensional (blue) components.

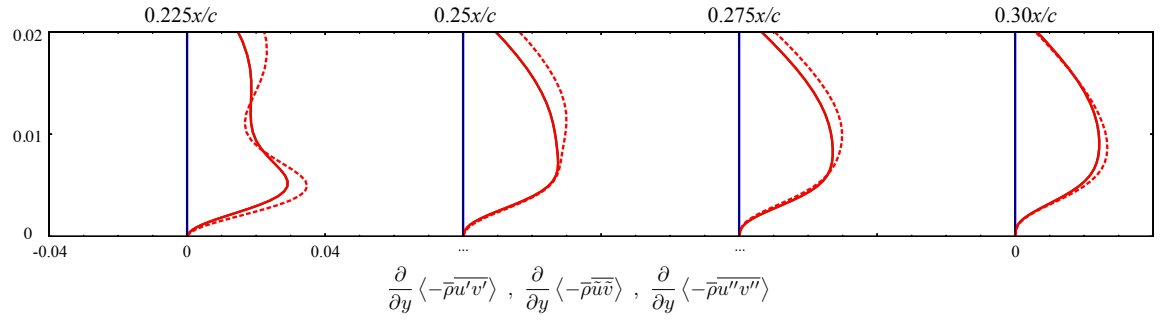

(a) $Re_c = 8.0 \times 10^3$

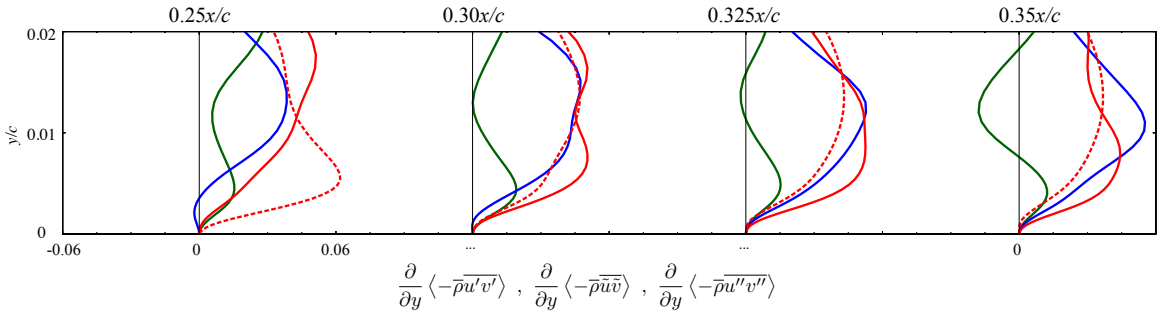

(b) $Re_c = 1.1 \times 10^4$

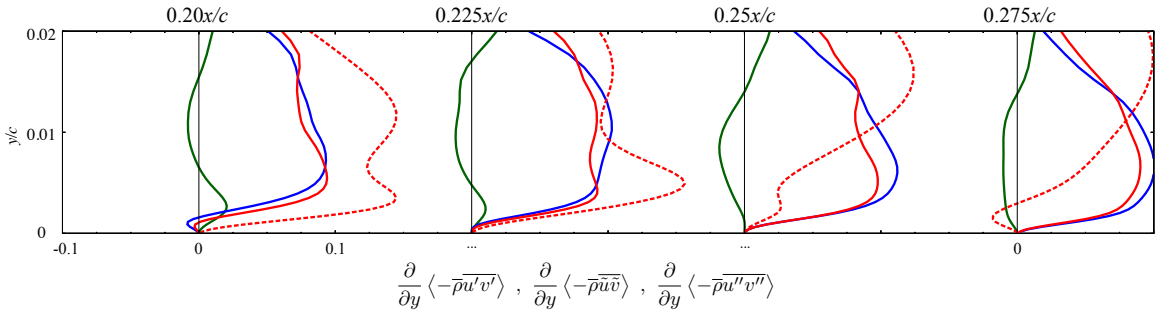

(c) $Re_c = 2.0 \times 10^4$

Figure 5.19: Budget of gradient transport of Reynolds shear stress of two-dimensional (dashed-line) and three-dimensional (solid-line) simulation results in the wall normal direction at several positions within the fluctuating region at (a) $Re_c = 8.0 \times 10^3$, (b) $Re_c = 1.1 \times 10^4$, and (c) $Re_c = 2.0 \times 10^4$; The overall (red), two-dimensional (green), and three-dimensional (blue) components.

5.4 Summary

In this chapter, two-dimensional unsteady laminar simulations are conducted for a 5% thickness right-angled blunt leading edge flat plate. First, instantaneous flow fields of the two-dimensional simulation show good agreement with those of the three-dimensional one at lower Reynolds numbers where the flow structures are maintained as two-dimensional ($Re_c \leq 8.0 \times 10^3$). At relatively higher Reynolds numbers ($Re_c \geq 1.1 \times 10^4$), on the other hand, three-dimensional turbulent structures are observed in the three-dimensional simulations whereas the convection of the two-dimensional vortices without breaking up appear in the two-dimensional simulation. In spite of these discrepancies in the instantaneous fields, the following characteristics are able to be predicted by the two-dimensional laminar simulation: the formation of an LSB, the tendency of varying reattachment points depending on the Reynolds numbers, and reattachment state. Moreover, the two-dimensional laminar simulation also reproduces the qualitative distribution of averaged surface pressure distribution and skin friction coefficient except for the overshoot phenomenon observed around the transient region. On the other hand, the present results indicate that an accurate prediction of the velocity profile in the wall-normal direction and friction drag on the surface is difficult in the two-dimensional simulation. Regarding the formation of the surface pressure distribution, the overshoot phenomenon is observed near the transition region at the Reynolds numbers where three-dimensional turbulent structures appear. The reason for the overshoot distributions in the two-dimensional simulation is explained by deriving the averaged pressure gradient equation; it is caused by a stronger estimation of the Reynolds stress than the three-dimensional simulation. The reason why the rapid pressure recovery in the fluctuating region can be predicted is because the three-dimensional Reynolds shear stress component in the actual flow field is pushed into the two-dimensional one in the two-dimensional simulation. Consequently, the magnitude of overall gradient transport of Reynolds shear stress of two-dimensional simulation becomes similar to that of the three-dimensional one. In conclusion, a critical point for the rapid pressure recovery is the generation of the positive distribution of overall component away from the surface in both simulations. Thus, even if the three-dimensional turbulent structure cannot be captured, the qualitative distribution becomes similar in both simulations; and hence the rapid pressure recovery also appears in the two-dimensional simulation.

Chapter 6

Application to flow around airfoils

In this chapter, numerical simulations are carried out for the flow field around an airfoil in order to show the usefulness of analysis discussed in the previous chapters. First, in Sec. 6.1, a three-dimensional LES is conducted and the formation mechanisms of surface pressure distribution around an LSB are discussed using the averaged streamwise pressure gradient equation. Section 6.2 discusses the predictability of aerodynamic characteristics of the two-dimensional unsteady laminar simulation. A previous study (Lee *et al.*, 2015) showed that qualitative estimation of airfoil aerodynamic characteristics using the two-dimensional unsteady laminar simulation are possible in a wide range of low Reynolds number region ($1.0 \times 10^4 \leq Re_c \leq 5.0 \times 10^4$). This thesis focuses on a relationship between the airfoil aerodynamic characteristics predictability and dependency on airfoil geometric shapes, so three different airfoil shapes are applied as analysis objects.

6.1 Formation mechanisms of surface pressure distribution

6.1.1 Computational setup

Analysis object The analysis object is the NACA0012 airfoil. A shape of NACA-series airfoil is described as follows (Jacobs *et al.*, 1933):

$$y = \pm\frac{t/c}{0.2}\left[0.2969\sqrt{\frac{x}{c}} - 0.1260\left(\frac{x}{c}\right) - 0.3516\left(\frac{x}{c}\right)^2 + 0.2843\left(\frac{x}{c}\right)^3 - 0.1015\left(\frac{x}{c}\right)^4\right] \quad (6.1)$$

where t is the maximum thickness of airfoil. Thus, the maximum thickness of the NACA0012 airfoil is 12% for the chord length and it is located at $x/c = 0.3$.

Computational grid and flow conditions Figure 6.1 shows a computational grid around the NACA0012 airfoil. Three levels of grid are adopted to evaluate the grid convergence. The number of grid points in the chordwise (N_ξ), spanwise (N_η), and wall-normal (N_ζ) directions are listed in Tab. 6.1. The results of grid convergence will be discussed in the following paragraph. A structured C-type grid is employed and the outer boundary is extended to 25 times of the chord length. The minimum grid spacing in the wall-normal direction is $\Delta\zeta_{\min} = 1.34 \times 10^{-4}$. Non-slip, adiabatic conditions are adopted on the surface (Sec. 2.6.1). The spanwise domain size is employed 20% of the chord length with the periodic boundary condition (Sec. 2.6.3). The reliability of adopting this spanwise domain size was already mentioned in Sec. 3.1.2. The free-stream Mach number (M_∞) with zero freestream turbulence, the specific heat ratio (γ), and the Prandtl number (Pr) are set to 0.2, 1.4, and 0.72, respectively. The Reynolds number based on the freestream velocity and airfoil chord length is set to $Re_c = 3.0 \times 10^4$, and the angle of attack (α) is set to $\alpha = 6.0°$.

Table 6.1: The number of grid points for three levels of systematic mesh refinement.

Grid	N_ξ	N_η	N_ζ	Total points
Grid A	555	107	145	8,610,825
Grid B	693	134	178	16,622,298
Grid C	873	169	225	33,195,825

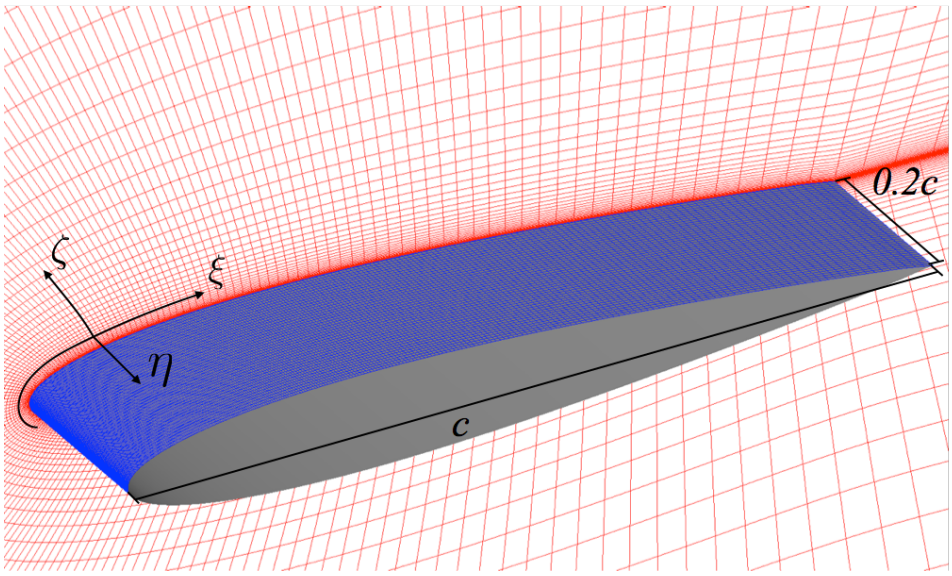

Figure 6.1: Computational grid (Grid B) for the NACA0012 airfoil. Every third grid point in each direction is shown.

Numerical schemes The spatial derivatives of the convective and viscous terms are evaluated by the sixth order compact difference scheme (Sec. 2.2.1) with the tenth order low-pass filtering (Sec. 2.2.2). The filtering coefficient α_f is set to be 0.495. The metrics and Jacobian are also calculated by the sixth order compact difference scheme (Sec. 2.2.3). The second order backward differencing which is converged by the ADI-SGS method (Sec. 2.4.1) and five subiterations (Sec. 2.4.2) are adopted for the time integration. The computational time step Δt is 2.0×10^{-4}[s] and the maximum local CFL number is approximately 1.6. Although there are many ways of representing subgrid-scale (SGS) effects, an implicit approach is applied because of the reasons mentioned in Sec. 2.5.2.

Accuracy assessments The three levels of systematic mesh refinement are conducted to investigate the grid convergence. Note that the grid convergence study is performed at $Re_c = 5.0 \times 10^4$ and $\alpha = 4.5°$. In general, a higher Reynolds number condition requires a finer grid resolution. Thus, it can be considered that the grid can be adopted at lower Reynolds number conditions if the quality of the grid satisfies the criteria of grid resolution at higher Reynolds number. Table 6.2 shows the maximum grid spacing of each grid normalized by the wall unit. The streamwise, spanwise, and wall-normal direction grid spacing are denoted as $\Delta\xi^+, \Delta\eta^+$, and $\Delta\zeta^+$, respectively. The maximum grid spacing and time step size of Grid B sufficiently satisfy the criteria mentioned in Sec. 3.1.4. The time- and spanwise-averaged surface pressure distribution and skin friction coefficient for the three grids are shown in Fig. 6.2. From the results, there is not significant differences between Grid B and Grid C; thus, Grid B is chosen for the analyses in the present study. Figure 6.3 shows a comparison between the present simulation ($Re_c = 3.0\times10^4$) and previous experimental ($Re_c = 3.3\times10^4$, Kim *et al.*, 2011) results of the averaged surface pressure distribution at $\alpha = 6.0°$. The flow characteristics within the Reynolds number of $O(10^4) \sim O(10^5)$ range are very sensitive to little change of the Reynolds number. As mentioned in Sec. 1.2, the freestream turbulent intensity which may exist in the experimental study also largely affects the flow characteristics. Thus, a quantitative comparison is difficult but the present results are qualitatively in good agreement with the experimental results.

Table 6.2: The maximum grid spacing of three levels of systematic mesh refinement ($Re_c = 5.0 \times 10^4$).

Grid	$\Delta\xi^+$	$\Delta\eta^+$	$\Delta\zeta^+$	Δt^+
Grid A	29.3	5.77	0.478	0.007
Grid B	26.2	4.54	0.458	0.007
Grid C	24.2	3.73	0.467	0.007

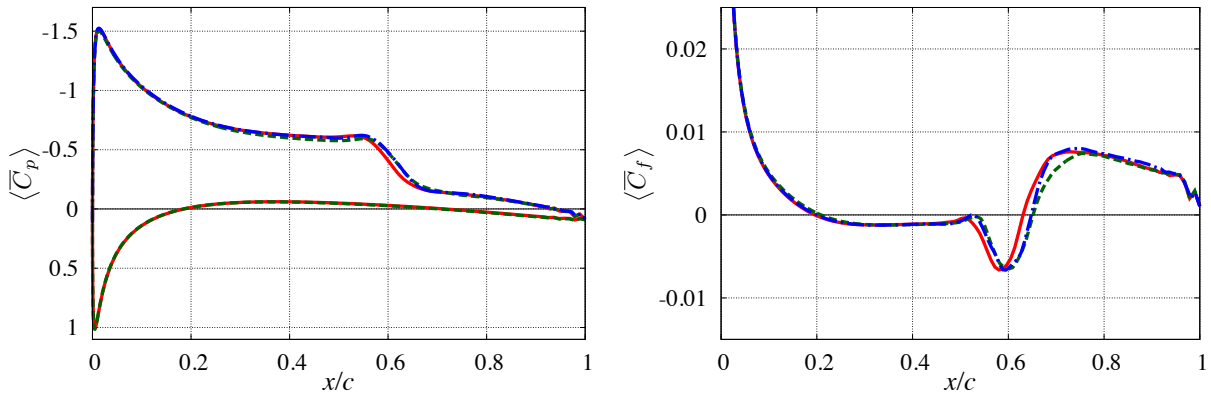

(a) Surface pressure distribution

(b) Skin friction coefficient

Figure 6.2: Time- and spanwise-averaged (a) surface pressure distribution and (b) skin friction coefficient results at $Re_c = 5.0 \times 10^4$ and $\alpha = 4.5°$ obtained by Grid A (solid-line, red), Grid B (dashed-line, green), and Grid C (dashed-dotted-line, blue).

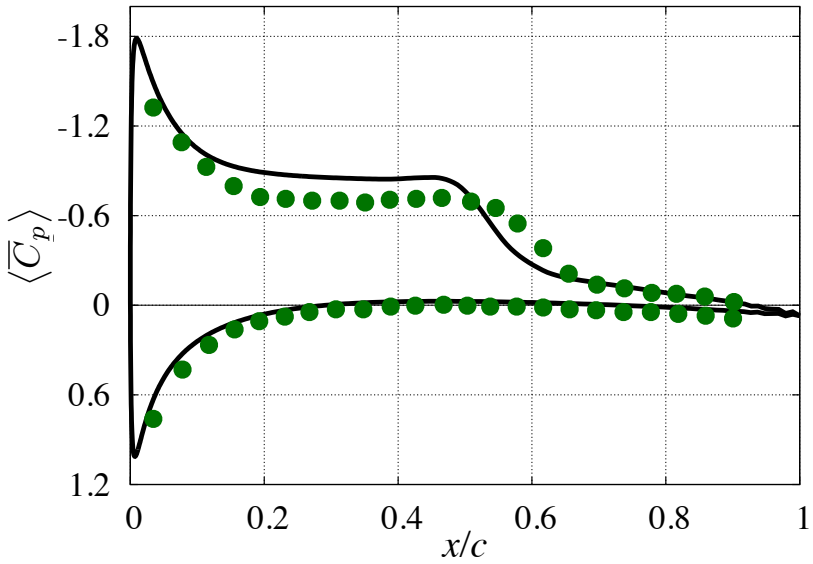

Figure 6.3: Time- and spanwise-averaged surface pressure distribution of the present simulation ($Re_c = 3.0 \times 10^4$; solid-line, black) and experimental results ($Re_c = 3.3 \times 10^4$; filled-circles, green; Kim *et al.*, 2011) at $\alpha = 6.0°$.

6.1.2 Classification of the separation bubble

Figure 6.4 (a) shows the time- and spanwise-averaged streamwise velocity field and surface pressure distribution. It is seen that an LSB is formed in the region of $0.08 \leq x/c \leq 0.59$. The TKE and distributions of its maximum value are shown in Fig. 6.4 (b). If the same criterion discussed in Sec. 3.3.1 (i.e., 2% of u_∞^2) is applied to divide the steady and fluctuating region, two different characteristic regions coexist within the LSB; the steady region at $0.08 \leq x/c \lesssim 0.42$ and the fluctuating region at $0.42 \lesssim x/c \leq 0.59$, respectively. The rapid pressure recovery observed in the latter region is similar to the LSB_SF case of the flat plate. Furthermore, the former region is roughly decomposed into two regions; a gradual pressure recovery at $0.08 \leq x/c \lesssim 0.20$ and a plateau pressure distribution at $0.20 \lesssim x/c \lesssim 0.42$. The first region is denoted by "LSB_S-Steady" for convenience, because the shape of pressure distribution is similar to that of the steady region of LSB_S in the flat plate case ($Re_c \leq 6.1 \times 10^3$). On the other hand, the plateau pressure distribution shown in the second region is similar to the steady region of LSB_SF in the flat plate case ($Re_c \geq 8.0 \times 10^3$), so this region is denoted by "LSB_SF-Steady". In summary, it can be considered that all three pressure distribution characteristics observed in the flat plate cases coexist within the current LSB.

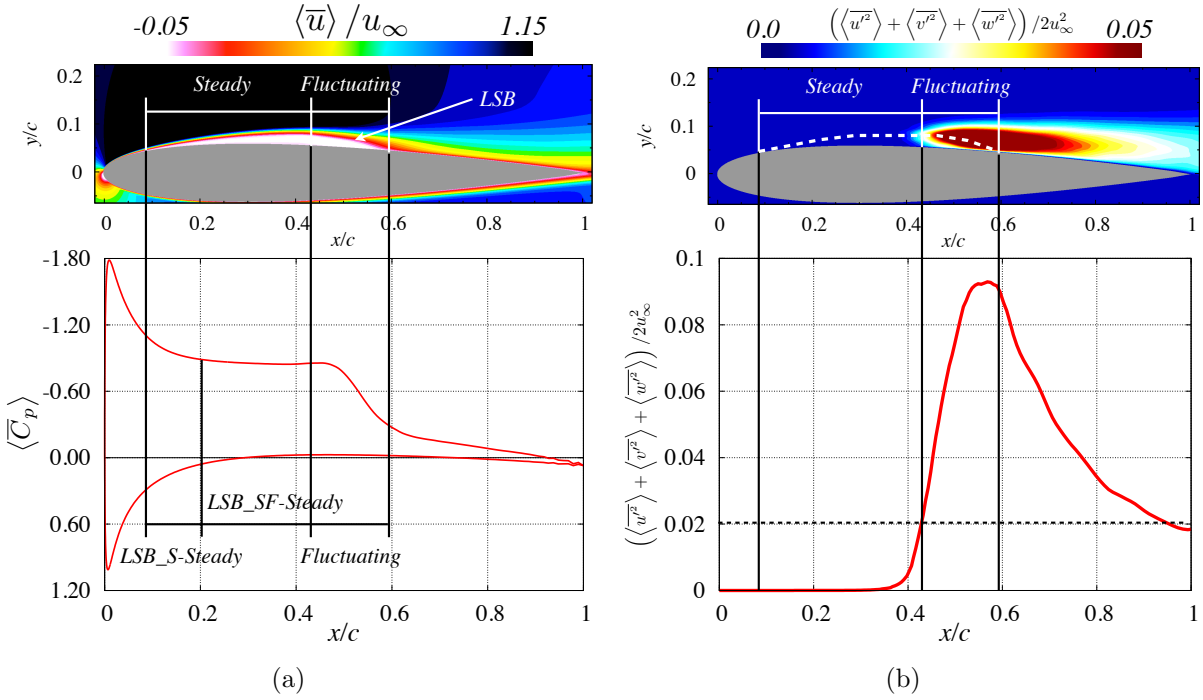

Figure 6.4: (a) Time- and spanwise-averaged streamwise velocity flow field and surface pressure distribution and (b) TKE flow field and maximum TKE distribution. The white dashed-line in (b) indicates the outer layer of LSB.

6.1.3 Spatial distribution of each term in pressure gradient equation

The spatial distributions of each term in Eq. (4.11) are shown in Fig. 6.5. First, in both the steady region, the convective effect is negligible inside of the LSB as shown in Fig. 6.5 (a). On the other hand, as similar to the flat plate cases, the influence of convective term becomes strong in the fluctuating region because of the nonlinear phenomena due to the laminar-turbulent transition. In terms of the second viscous diffusion (Fig. 6.5 (c)), its effect can be ignored throughout the flow fields because the flow field can be assumed as incompressible. Next, the gradient transport of Reynolds stress is approximately zero in both the steady region. On the other hand, in the fluctuating region, it can be confirmed that it has a positive distribution near the surface. The most significant difference among the region is observed in the first viscous diffusion term. As shown in Fig. 6.5 (b), it is activated near the surface in the LSB_S-Steady region, where the separated laminar shear layer exists close to the wall. As going to the downstream, the first viscous diffusion term near the surface becomes negligible in the LSB_SF-Steady region, and then the strong viscous effect appears again near the surface in the fluctuating region.

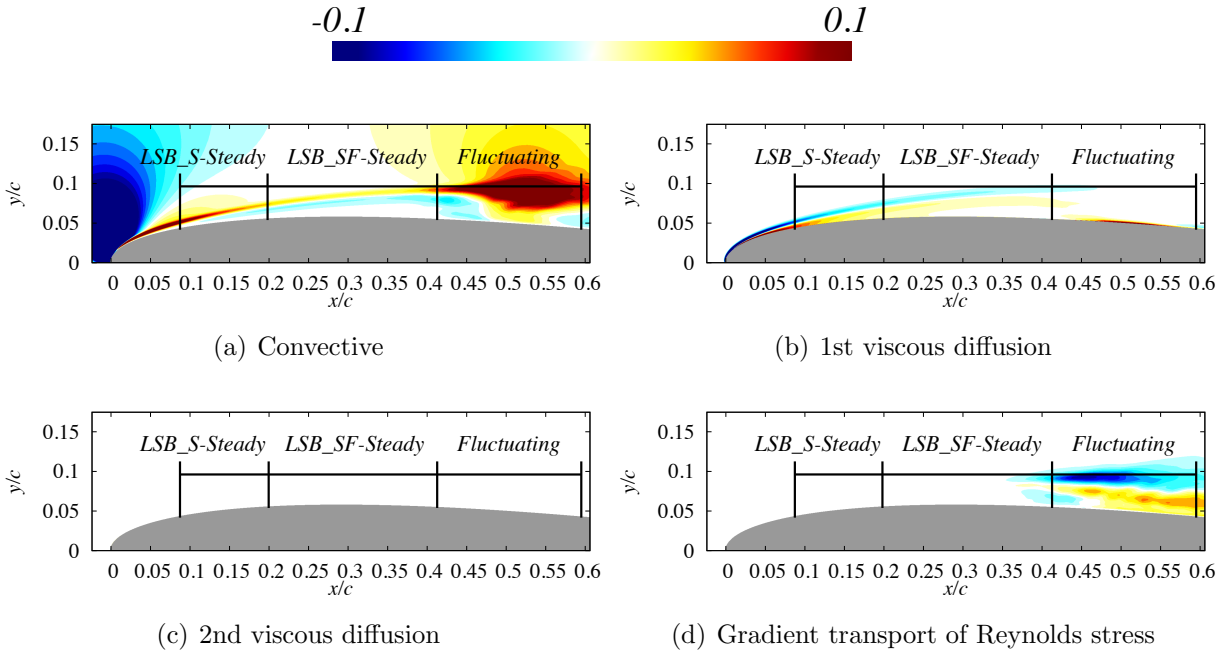

(a) Convective

(b) 1st viscous diffusion

(c) 2nd viscous diffusion

(d) Gradient transport of Reynolds stress

Figure 6.5: Spatial distributions of (a) convective, (b) the first viscous diffusion, (c) the second viscous diffusion, and (d) gradient transport of Reynolds stress terms in Eq. (4.11).

6.1.4 Momentum budget of each region

Figures 6.6 and 6.7 more clearly illustrate the effects of each term. In the LSB_S-Steady region, the first viscous diffusion mainly affects the generation of the favorable pressure gradient ($\partial\overline{p}/\partial x > 0$) near the surface. This is because the separated shear layer is located close to the surface and it results in the viscous shear stress near the wall. In case of the flat plate, thickness of the separated shear layer which creates the viscous shear stress near the surface was dominated by the Reynolds numbers. Added to that, these results suggest that the distance between the separated shear layer and the surface may also affect the formation of surface pressure distribution. In the LSB_SF-Steady region, effects of the viscous shear stress near the surface become negligible, and the plateau pressure region ($\partial\overline{p}/\partial x \simeq 0$) appears as similar to the steady region of the LSB_SF of the flat plate. It can be considered that the separated shear layer is sufficiently separated from the surface in this region, and it can be ignored the viscous shear stress near the wall caused by the separated shear layer. In the fluctuating region, the effect of Reynolds stress term is observed and the strong viscous diffusion is generated near the surface. In conclusion, it is also verified by the analysis of the NACA0012 that the distribution of viscous shear stress due to the separated laminar shear layer within the LSB and the generation of fluctuating component have a major role to the formation of the pressure gradient. Note that the laminar separation over an airfoil is induced by a continuously existed adverse pressure gradient due to the geometry of the airfoil surface. This is obviously different from the flat plate case. The mechanisms related to the formation of surface pressure distribution proposed in this thesis, however, are also available to the LSB which is formed around an airfoil.

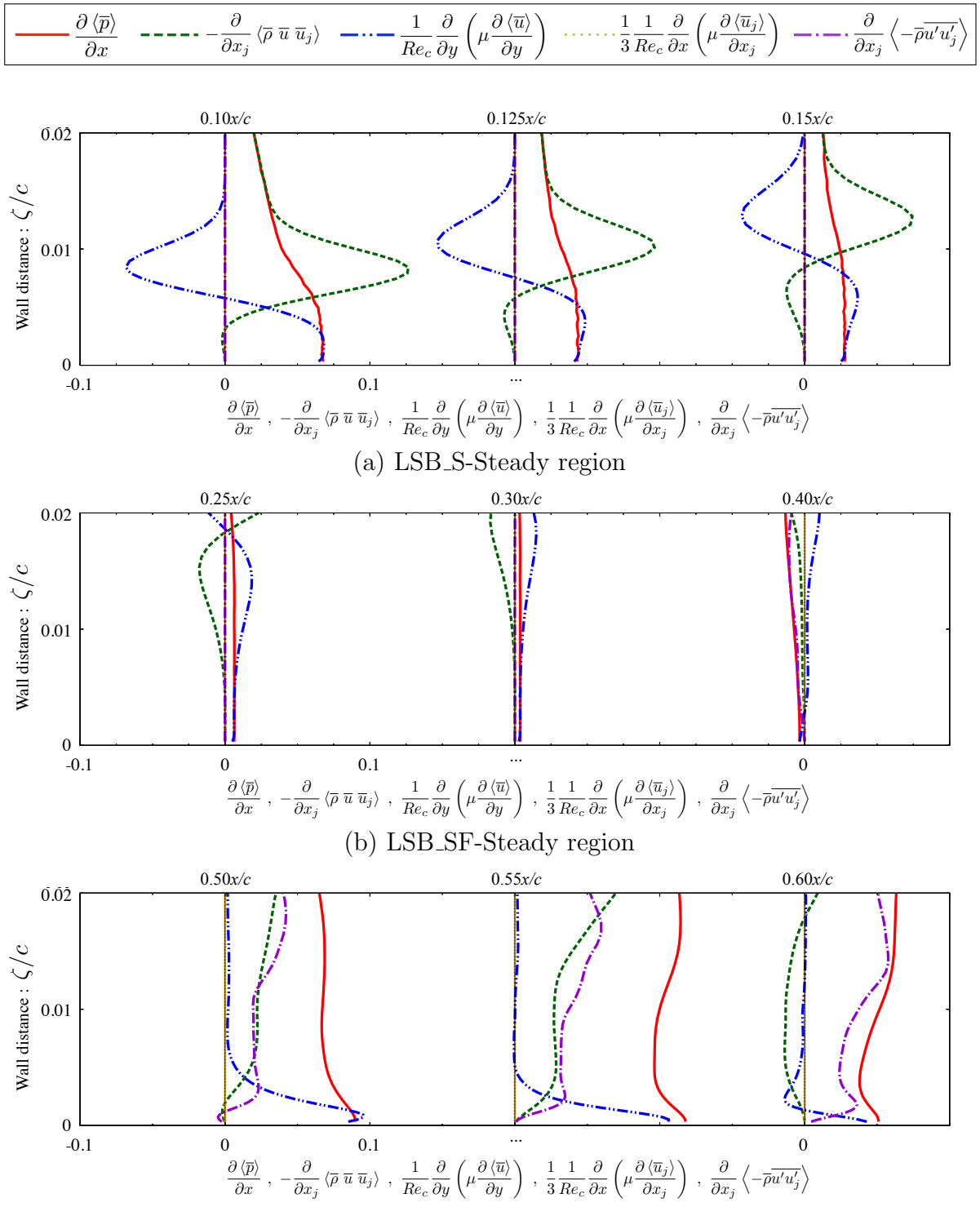

(a) LSB_S-Steady region

(b) LSB_SF-Steady region

(c) Fluctuating region

Figure 6.6: Momentum budget in Eq. (4.11) in the wall-normal direction at several positions within (a) LSB_S-Steady, (b) LSB_SF-Steady, and (c) fluctuating region; Pressure gradient (solid-lines, red), convective (dashed-lines, green), the first viscous diffusion (dashed-double-dotted-lines, blue), the second viscous diffusion (dotted-lines, black), and gradient transport of Reynolds stress (dashed-dotted-lines, violet) terms.

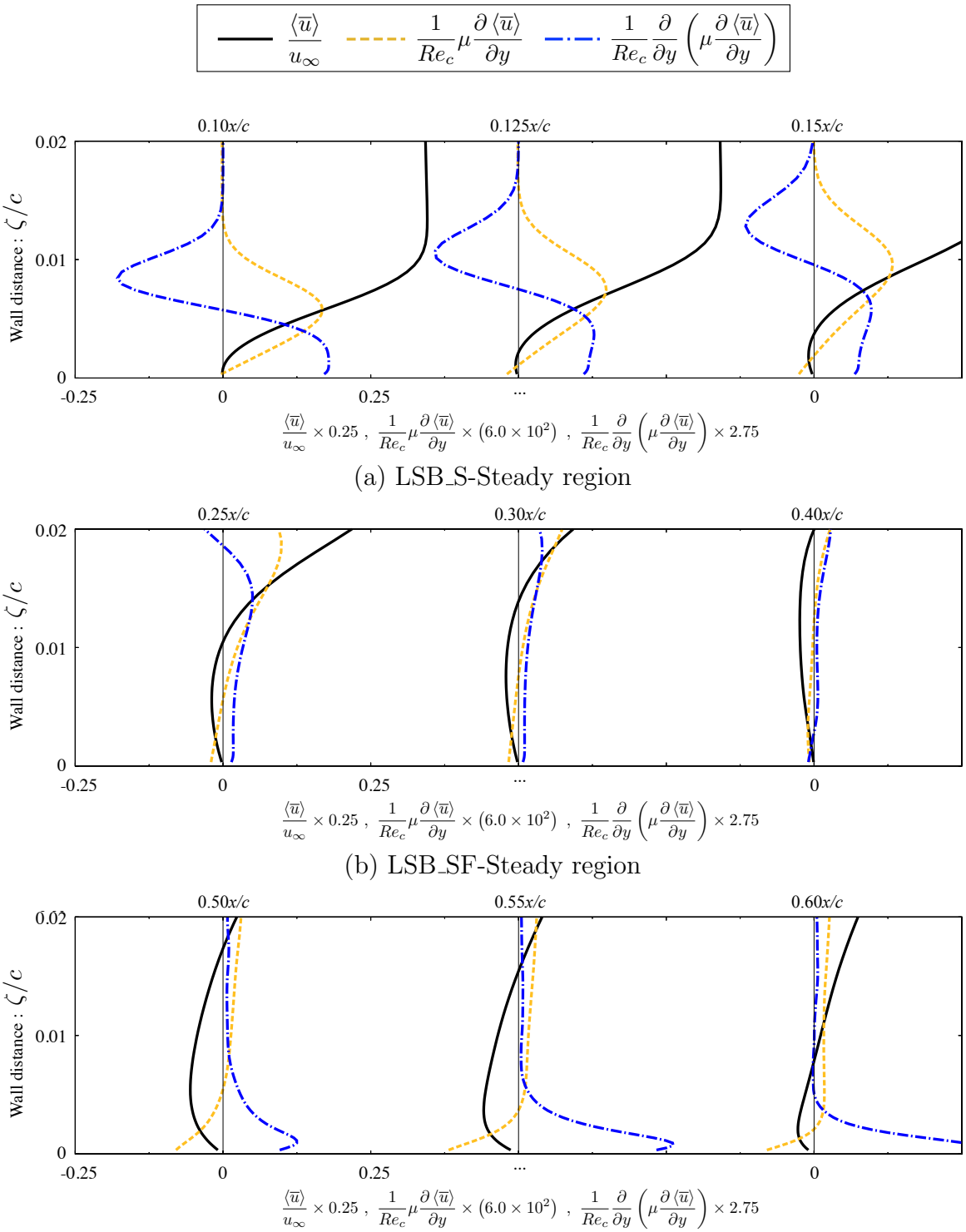

(a) LSB_S-Steady region

(b) LSB_SF-Steady region

(c) Fluctuating region

Figure 6.7: Time- and spanwise-averaged streamwise velocity (dashed-lines, black), viscous shear stress (solid-lines, yellow), and first viscous diffusion (dashed-dotted-lines, blue) at several positions within (a) LSB_S-Steady, (b) LSB_SF-Steady, and (c) fluctuating region.

6.2 Reliability of two-dimensional laminar simulation

6.2.1 Computational setup

Analysis object As analysis objects, I apply the NACA0012, NACA0006, and Ishii airfoils which are representative of thick-symmetric, thin-symmetric, and thin-cambered airfoils, respectively (see, Fig. 6.8). Anyoji *et al.* (2014) reported that the Ishii airfoil shows good aerodynamic performances at low Reynolds numbers.

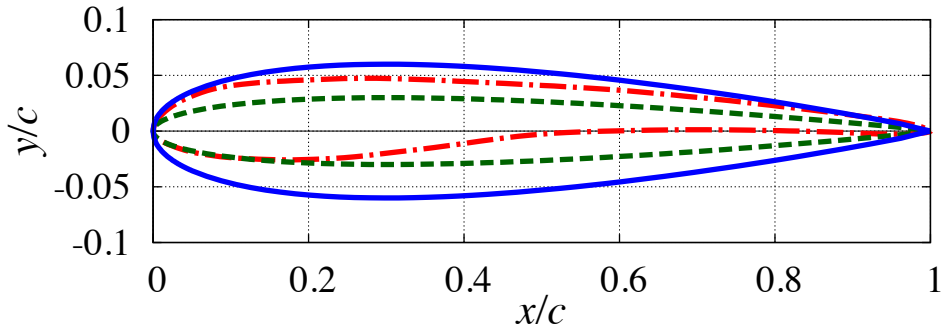

Figure 6.8: The geometric shape of the NACA0012 (solid line, blue), NACA0006 (dashed line, green), and Ishii (dashed-dotted line, red) airfoils.

Computational grid and flow conditions The computational grids around each airfoil are shown in Fig. 6.9. The grid topology, outer and wall boundary condition, and spanwise domain size of three-dimensional simulations are exactly same to the previous NACA0012 airfoil case (see, Sec. 6.1.1). The number of grid points of NACA0006 and Ishii airfoil are also same as those of Grid B of the NACA0012 airfoil, summarized in Tab. 6.1. One of the spanwise cross sections of the three-dimensional grid is used for two-dimensional simulations. The free-stream Mach number (M_∞) with zero freestream turbulence, the specific heat ratio (γ), and the Prandtl number (Pr) are set to 0.2, 1.4, and 0.72, respectively. The Reynolds number based on the free stream velocity and airfoil chord length (Re_c) is set to 3.0×10^4. In the three-dimensional simulation, the angles of attack (α) are set to 3.0°, 6.0°, and 9.0°. Simulations at α =1.5° and 4.5° are additionally conducted for the NACA0012 airfoil because nonlinearity of the lift coefficient has been reported (Ohtake *et al.*, 2007; Kim *et al.*, 2011). In the two-dimensional simulations, angles of attack are set to $\alpha = 0.0°$, 1.5°, 3.0°, 4.5°, 6.0°, 7.5°, and 9.0°.

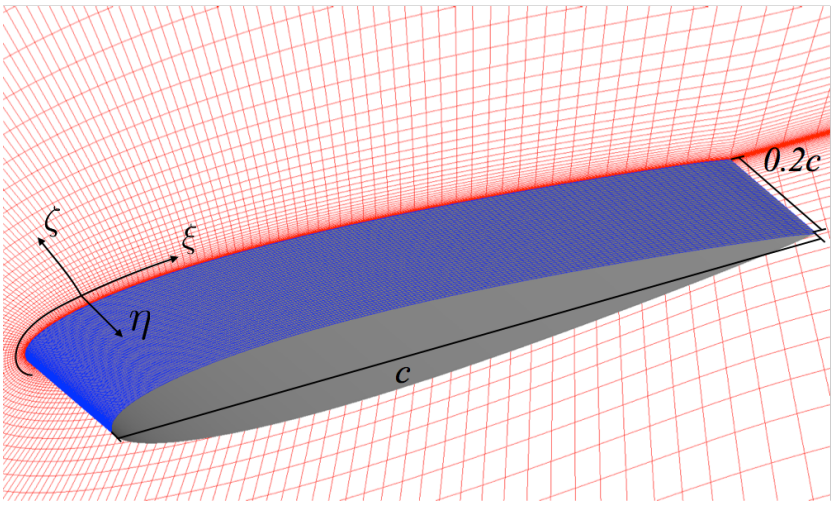

(a) NACA0012 (thick-symmetric)

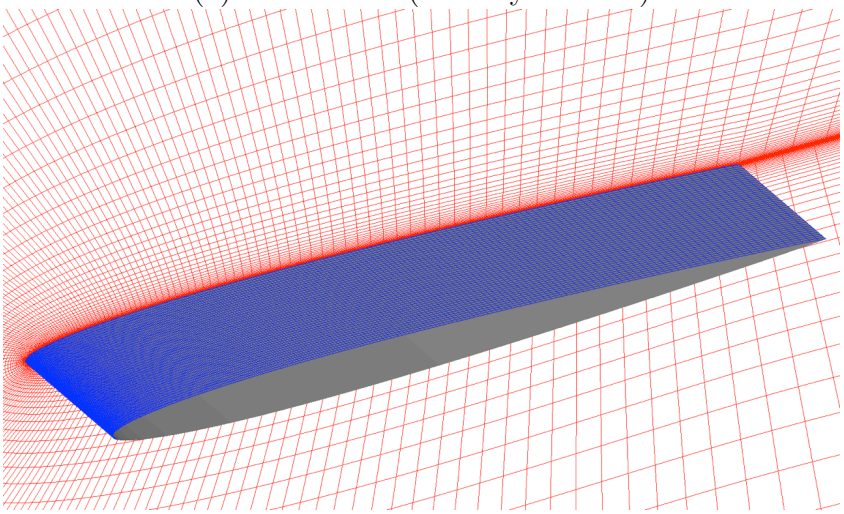

(b) NACA0006 (thin-symmetric)

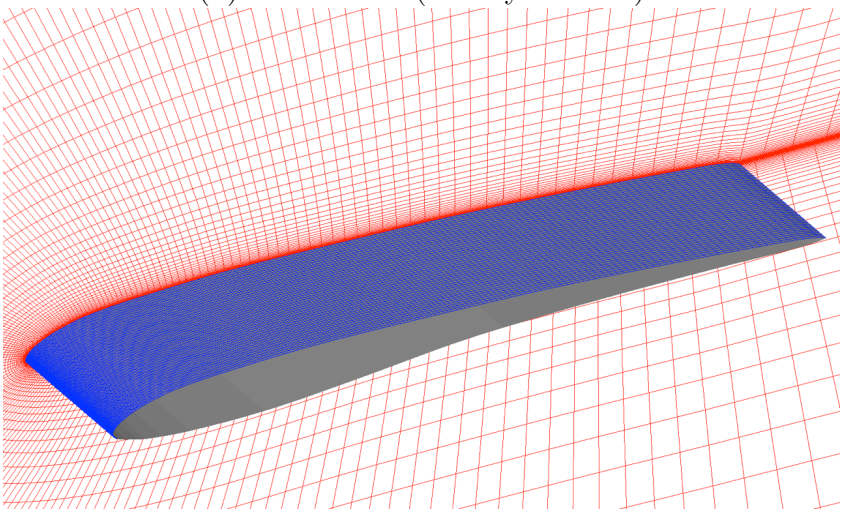

(a) Ishii (thin-cambered)

Figure 6.9: Computational grids for (a) NACA0012 (thick-symmetric), (b) NACA0006 (thin-symmetric), and (c) Ishii (thin-cambered) airfoils. Every third grid point in each direction is shown.

Numerical schemes In this section, three different numerical simulations are performed in addition to the two-dimensional unsteady laminar simulation. First of all, the numerical method of the three-dimensional large eddy simulation are mentioned in Sec. 6.1.1 and it is called as "3-D LES" in this section. The 3-D LES results will be used as a reference data. In the two-dimensional unsteady laminar simulation, the convective terms are calculated by the third order MUSCL without a limiter (Sec. 2.3.1) and the SHUS (Sec. 2.3.2) methods. The viscous terms are evaluated by the second order central difference scheme. The second order backward differencing with the ADI-SGS scheme (Sec. 2.4.1) is adopted for the time integration. The flow fields are assumed to be laminar over the entire region, so no turbulence models are employed. The two-dimensional unsteady laminar simulation is called as "2-D Lam" in the present section. In the RANS simulation, the methods for evaluating the convective, viscous terms, and time-integration are exactly the same as those of the 2-D Lam simulation. Baldwin-Lomax and Spalart-Allmaras turbulence models (Sec. 2.5.3) are adopted for turbulence analysis. The 2-D RANS simulations of each turbulence model are called as "2-D RANS(BL)" and "2-D RANS(SA)" in this section. The entire field is assumed to be a fully turbulent flow in both simulations.

Accuracy assessments Table. 6.3 summarizes the maximum grid spacing and time step size of each airfoil. The grid spacing in the streamwise, spanwise, and wall-normal direction are denoted as $\Delta\xi^+, \Delta\eta^+$, and $\Delta\zeta^+$, respectively. Note that the grid convergence study is conducted by using 3-D LES results at $Re_c = 3.0 \times 10^4$ and $\alpha = 6.0°$. It is confirmed that the maximum grid spacing and time step size of all airfoil grids sufficiently satisfy the criteria mentioned in Sec. 3.1.4.

Table 6.3: The maximum grid spacing and time step size of each airfoil grid ($Re_c = 3.0 \times 10^4$, $\alpha = 6.0°$).

Airfoil	$\Delta\xi^+$	$\Delta\eta^+$	$\Delta\zeta^+$	Δt^+
NACA0012	15.2	3.45	0.349	0.007
NACA0006	13.6	4.11	0.415	0.011
Ishii	16.3	3.55	0.358	0.007

6.2.2 Flow structures of instantaneous flow fields

Figure 6.10 shows instantaneous flow fields of the 3-D LES for each airfoil at $\alpha = 3.0°$, 6.0°, and 9.0°. From the figure, the flow structures are clearly different depending on the angle of attack. First of all, at $\alpha = 3.0°$ (see, Fig 6.10 (a)), the flow separates from the middle of the airfoil regardless of the airfoil shapes. Thereafter, the flow structures near the trailing edge are different depending on the airfoil shapes. In the NACA0012 airfoil, two-dimensional spanwise vortices are periodically created by the KH instability, and they are deformed to three-dimensional hairpin-like vortices near the trailing edge due to the secondary instability. Correspondingly, irregular variations are observed in the time histories of lift coefficient as shown in Fig. 6.11. On the other hand, the separated shear layer is extended to the trailing edge without showing the laminar-turbulent transition in the NACA0006 airfoil. After that, Karman vortex-like structures are formed from the trailing edge. It is also confirmed by the time histories of lift coefficients that this flow is not a completely steady state. In case of the Ishii airfoil, it is clearly seen two-dimensional coherent vortex structures caused by the KH instability, which is similar to those of the NACA0012 airfoil. However, the vortices are not collapsed to three-dimensional turbulent but maintain two-dimensional structures until the trailing edge. From the time histories of lift coefficients (Fig. 6.11), it is seen periodic variations due to convection of these two-dimensional vortices. As increasing in angle of attack ($\alpha = 6.0°$, Fig. 6.10 (b)), the flow structures are similar regardless of the airfoil shape. In other words, although separation point, location of the secondary instability, and length of the two-dimensional separated shear layer are different depending on the airfoil shape, the two-dimensional coherent vortices shedding from the separated shear layer turn into three-dimensional structures and reattaches to the airfoil surface. At the highest angle of attack in this study ($\alpha = 9.0°$, Fig. 6.10 (c)), the flow is massively separated from the leading edge and not reattached on the surface irrespective to the airfoil surface.

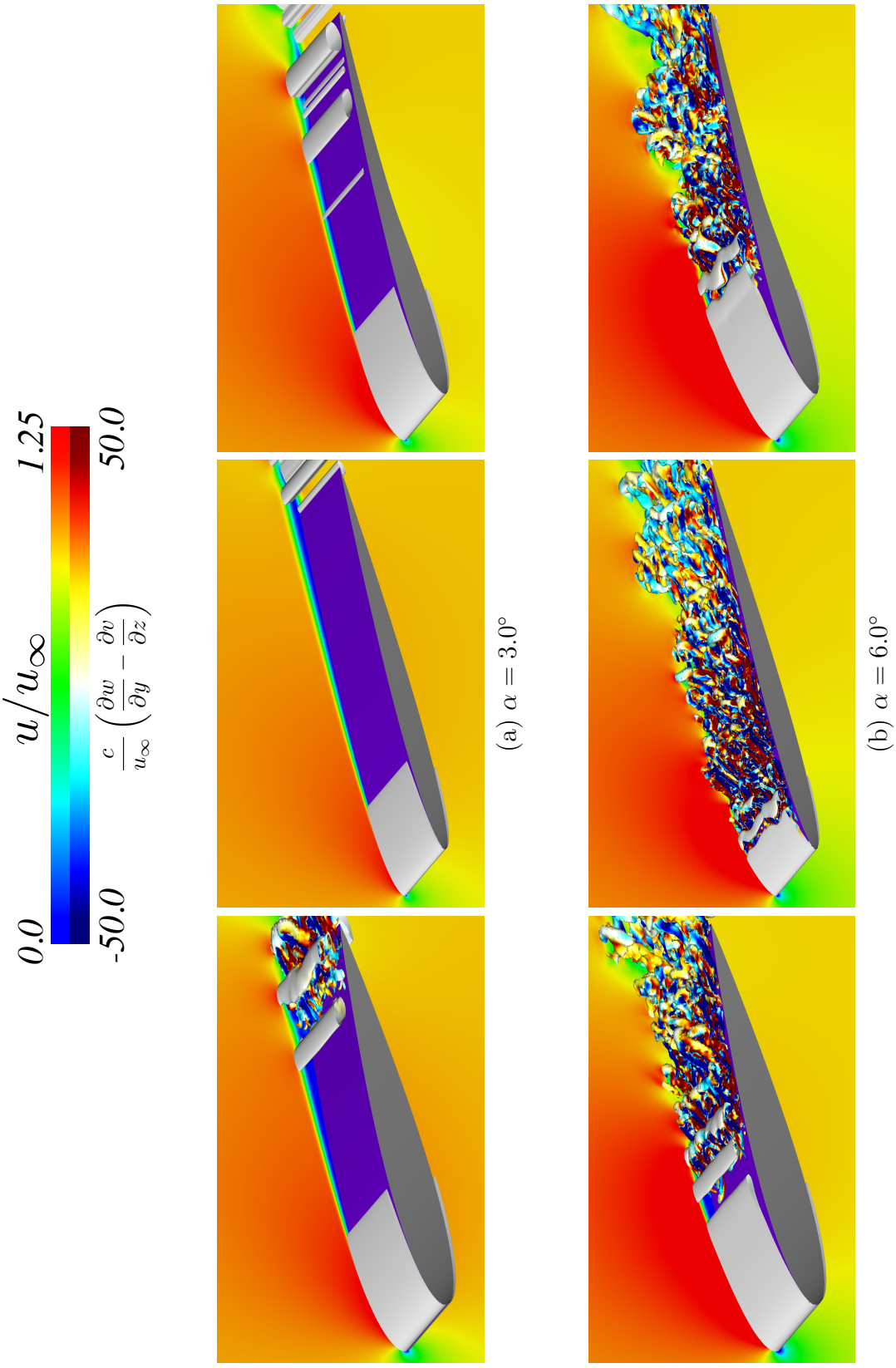

(a) $\alpha = 3.0°$ (b) $\alpha = 6.0°$

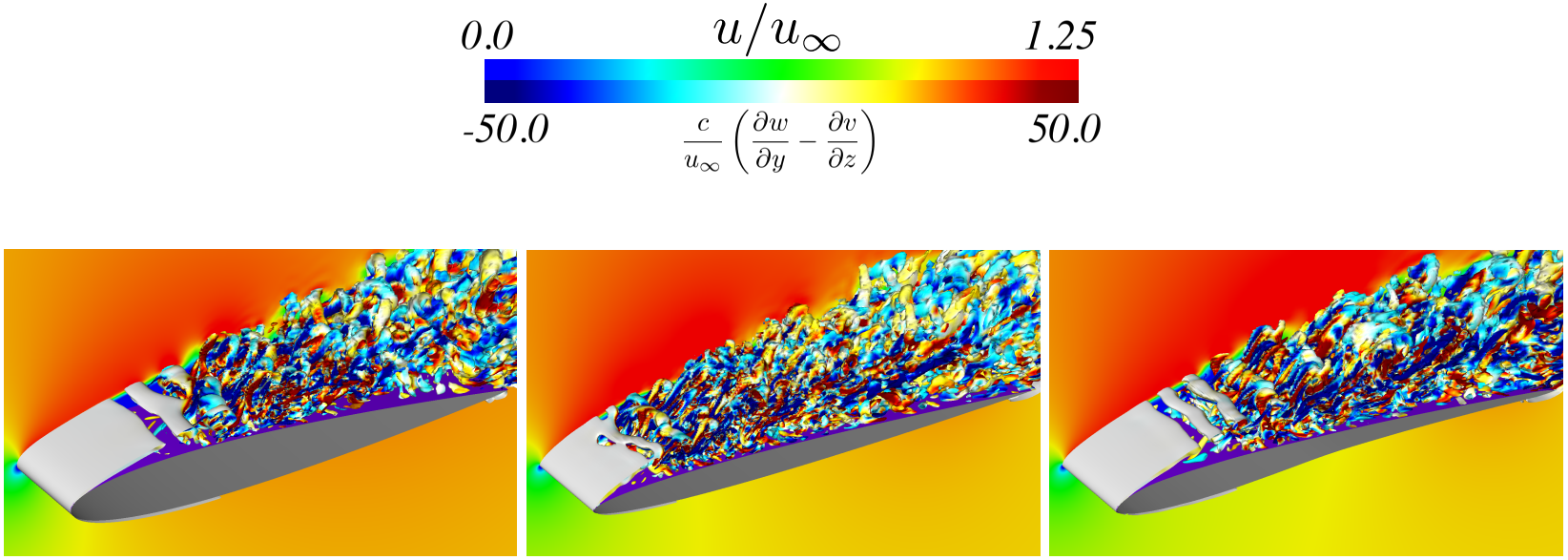

(c) $\alpha = 9.0°$

Figure 6.10: Instantaneous flow fields of the three-dimensional large eddy simulation for the NACA0012 (left), NACA0006 (middle), and Ishii (right) airfoils at (a) $\alpha = 3.0°$, (b) $\alpha = 6.0°$, and (c) $\alpha = 9.0°$. Streamwise velocity flow fields are shown on the side plane and the isosurfaces of the second invariant of a velocity gradient tensor ($Q_{cr} = 1.0$) colored by the streamwise vorticity are visualized.

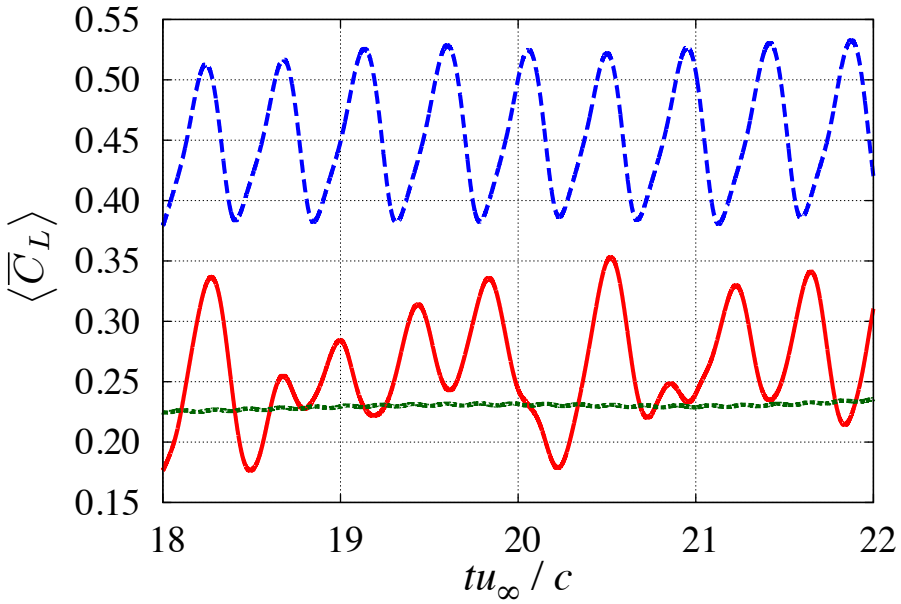

Figure 6.11: Time histories of the lift coefficient for the NACA0012 (solid-line, red), NACA0006 (dotted-line, green), and Ishii (dashed-line, blue) airfoils at $\alpha = 3.0°$.

6.2.3 Predictability of aerodynamic performance

From the following discussion, averaged characteristics will be discussed. Note that the statistical data is obtained by temporal averaging (two-dimensional simulations) and temporal and spanwise averaging (three-dimensional simulations) in the quasi-steady state. First of all, Fig. 6.12 shows the lift coefficient to angle of attack ($\langle \overline{C}_L \rangle - \alpha$) and the drag coefficient to angle of attack ($\langle \overline{C}_D \rangle - \alpha$) curves of all numerical methods for each airfoil. As concluded in Sec. 5.2.2, the 2-D Lam cannot estimate the accurate friction drag. From the figures, however, it is confirmed that there are no significant differences in terms of the drag coefficient predictability. This is caused by the fact that the magnitude of pressure drag due to the separation is significantly larger than that of the friction drag, and the contribution of friction drag to total drag coefficient becomes relatively small. Similar features were already reported by Kondo *et al.* (2013) and Lee *et al.* (2015). On the other hand, the predictability of lift characteristics is different depending on the numerical methods. The results show that $\langle \overline{C}_L \rangle - \alpha$ curves are basically linear for the NACA0006 and Ishii airfoils, and results of the two-dimensional simulation results are in good agreement with those of the 3-D LES in lower angles of attack region ($\alpha \leq 6.0°$) except for the 2-D RANS(BL). On the other hand, a strong nonlinearity is observed in the NACA0012 airfoil case, which was reported in previous experimental studies (Ohtake *et al.*, 2007; Kim *et al.*, 2011). In the 2-D Lam simulations, a negative lift coefficient is captured at $\alpha = 1.5°$ and it suddenly increases around $\alpha = 3.0° \sim 4.5°$. At $\alpha = 9.0°$, however, a stall phenomenon does not appear in the 2-D Lam simulation whereas it is observed in the 3-D LES results. In the 2-D RANS(SA) simulation, although the stall phenomenon at $\alpha = 9.0°$ is captured, the estimated lift coefficients show approximately linear at lower angles of attack region. On the other hand, the 2-D RANS(BL) simulation cannot estimate the qualitative characteristics of the lift coefficient to angle of attack curves, unlike the other two-dimensional simulations and the 3-D LES. In summary, if the qualitative predictability of aerodynamic performances are only focused, the present 2-D Lam simulation can evaluate variation of the lift coefficients. However, detailed flow field characteristics such as separation points, reattachment points, and formation of laminar separation bubbles should be investigated.

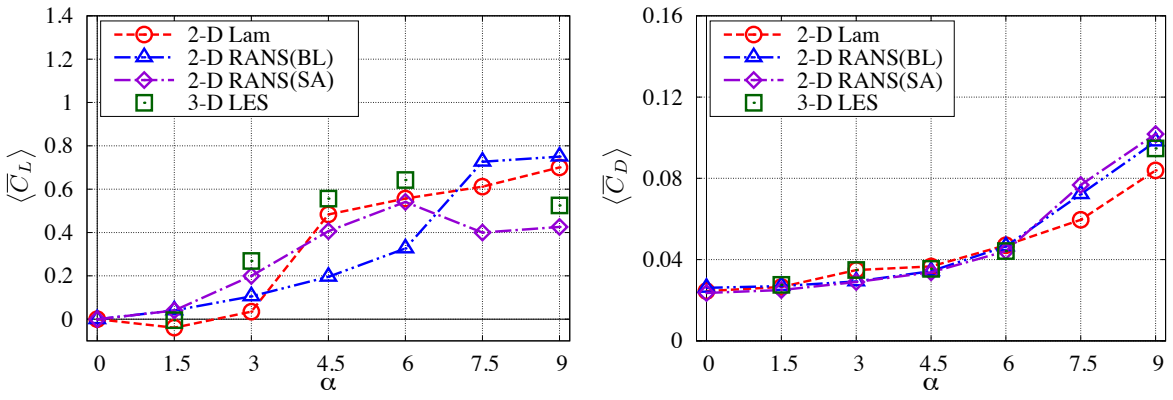

(a) NACA0012 (Thick-symmetric)

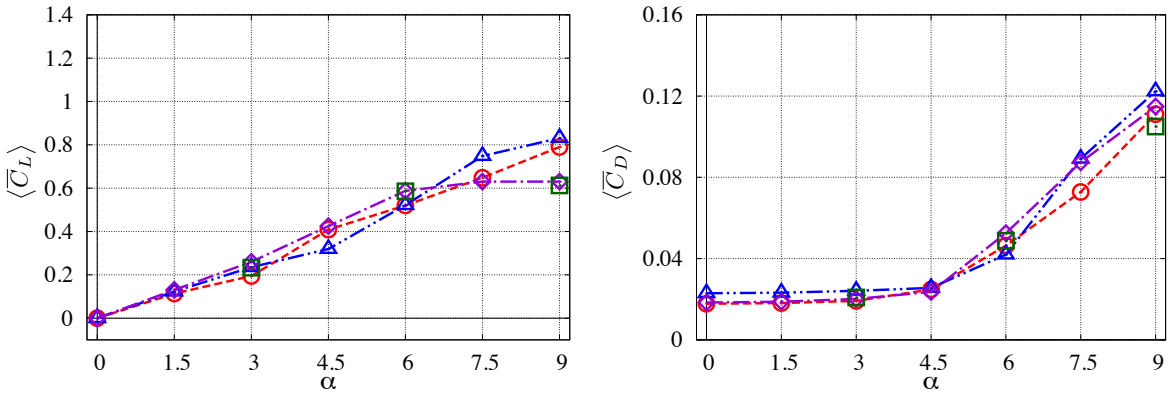

(b) NACA0006 (Thin-symmetric)

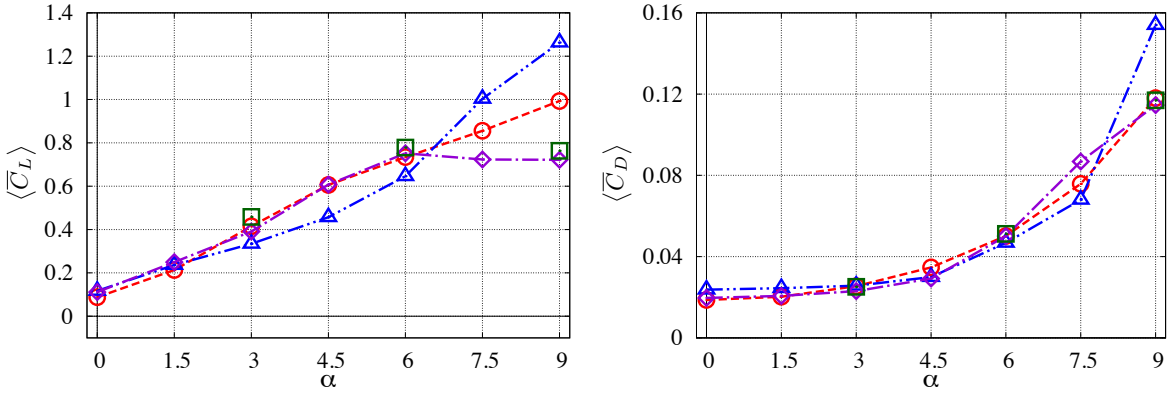

(c) Ishii (Thin-cambered)

Figure 6.12: The lift to angles of attack (left column) and drag to angles of attack (right column) curves of the 2-D Lam (opened-circles with dashed-lines, red), 2-D RANS(BL) (opened-triangles with dashed-double-dotted-lines, blue), 2-D RANS(SA) (opened-diamonds with dashed-dotted-line, violet), and 3-D LES (opened-squares, green) for (a) NACA0012, (b) NACA0006, and (c) Ishii airfoil.

6.2.4 Separation and reattachment points of averaged flow fields

The predictability of separation, reattachment points, and averaged streamwise velocity flow fields of each airfoil are shown in Figs. 6.13 and 6.14. The separation/reattachment points are determined by the locations where the skin friction coefficient turns from positive to negative/negative to positive. Figure 6.15 shows the averaged surface pressure distributions of the NACA0012 airfoil at $\alpha = 3.0°$, 6.0°, and 9.0°. First of all, let us focus on the separation and reattachment points of the NACA0012 airfoil at $\alpha = 3.0°$, 6.0°, and 9.0° (see, Fig. 6.13 (a)). In the 3-D LES results, the flow separates around $x/c \simeq 0.4$, but the separated shear layer does not reattach at $\alpha = 3.0°$. The separation point moves toward the leading edge with increasing the angle of attack, and the separated shear layer reattaches to the surface at $\alpha = 6.0°$; and hence, an LSB is observed. After that, a massively separated flow is formed without the reattachment at $\alpha = 9.0°$. The features at each angle of attack in the 3-D LES are observed irrespective of the airfoil shape, although the separation point at $\alpha = 3.0°$ in the NACA0006 airfoil is located near the trailing edge ($x/c \simeq 0.7$, Fig. 6.13 (b)). In the 2-D Lam simulation, the separation points are in good agreement with the 3-D LES results regardless of angles of attack and airfoil shapes. In terms of the reattachment points, a good consistency between the 2-D Lam and 3-D LES results is also obtained at low angles of attack ($\alpha \leq 6.0°$), and the length of the LSBs is relatively well estimated. On the other hand, the massive separation is not predicted at $\alpha = 9.0°$. As shown in Fig. 6.15, the surface pressure distributions of the 2-D Lam simulation are similar to those of the 3-D LES results at $\alpha = 3.0°$ and 6.0°. At $\alpha = 9.0°$, however, the 2-D Lam simulation predicts the constant pressure distribution followed by the rapid pressure recovery, which is often observed around an LSB. Due to the formation of an LSB, the 2-D Lam simulation fails to estimate the stall phenomenon. In the 2-D RANS(BL) simulation, the separation points exist in the downstream compared with for the 3-D LES. Moreover, an LSB is not formed because the reattachment points do not appear at all angles of attack. The fact that LSBs are not formed can be confirmed by the surface pressure distributions. As shown in Fig. 6.15, the typical shape of pressure distribution around the LSB which is mentioned above is not observed in the 2-D RANS(BL) simulations at $\alpha = 6.0°$. In the 2-D RANS(SA) simulation, the separation points are close to those of the 2-D Lam and 3-D LES results. As shown in the results of the NACA0012 airfoil (Fig. 6.13 (a)), however, the reattachment points are not observed at all of the angles of attack. Additionally, from the results in the NACA0006 airfoil case as shown in Fig. 6.13 (b), the reattachment points move to the upstream in the 2-D Lam simulation whereas they shift

to the downstream in the 2-D RANS(SA) simulations, as the angle of attack increases. These results indicate that the reattachment points may not be correctly estimated in the low angles of attack region ($\alpha \leq 6.0°$) by the 2-D RANS(SA) simulations. In summary, the 2-D Lam simulation shows a good predictability in terms of the qualitative aerodynamic performance as well as the flow characteristics except for high angles of attack, which accompanies the massive separation flow.

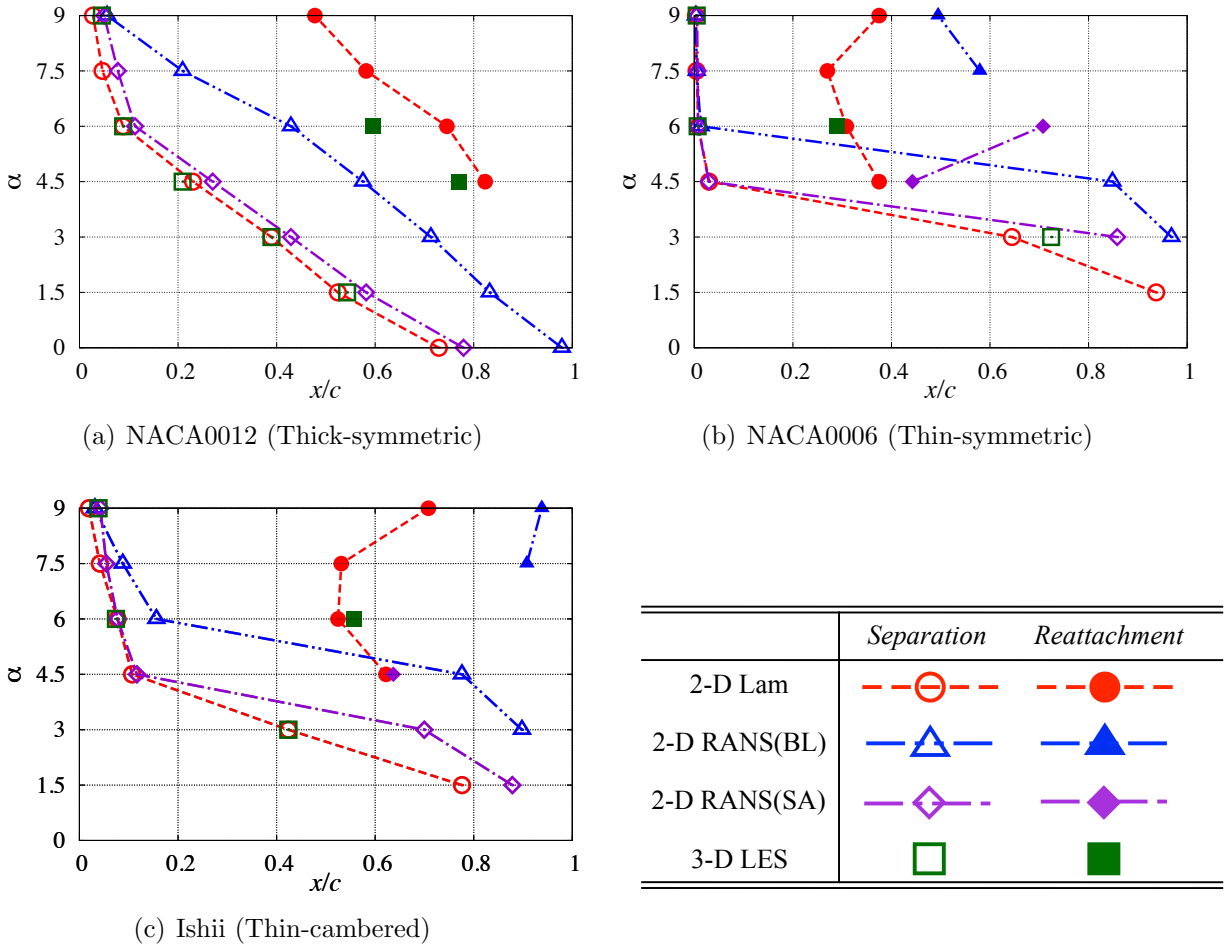

(a) NACA0012 (Thick-symmetric)

(b) NACA0006 (Thin-symmetric)

(c) Ishii (Thin-cambered)

Figure 6.13: Separation (opened-markers) and reattachment points (filled-markers) of the 2-D Lam (circles with dashed-lines, red), 2-D RANS(BL) (triangles with dashed-double-dotted-lines, blue), 2-D RANS(SA) (diamonds with dashed-dotted-line, violet), and 3-D LES (squares, green) for (a) NACA0012, (b) NACA0006, and (c) Ishii airfoil.

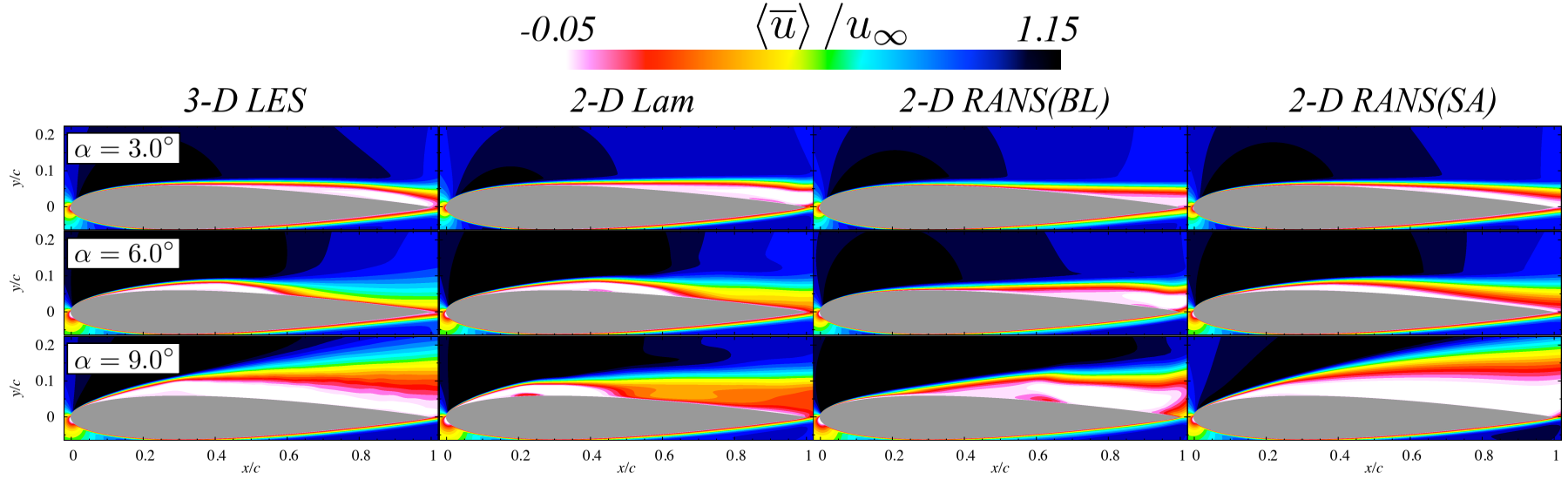

(a) NACA0012 (thick-symmetric)

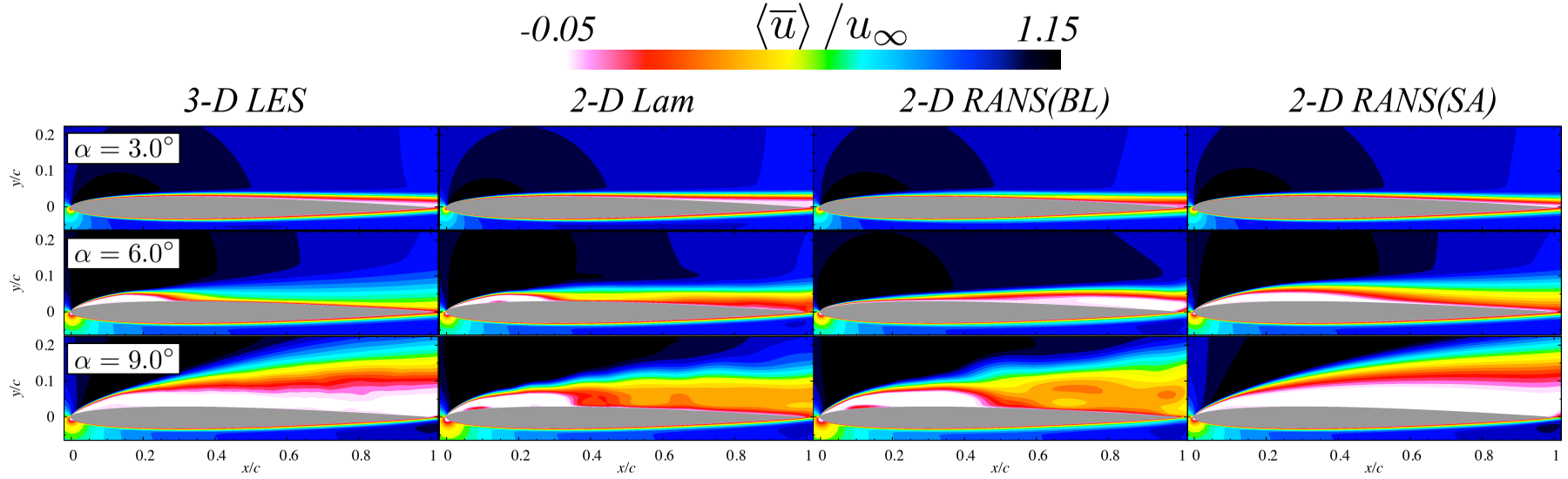

(b) NACA0006 (thin-symmetric)

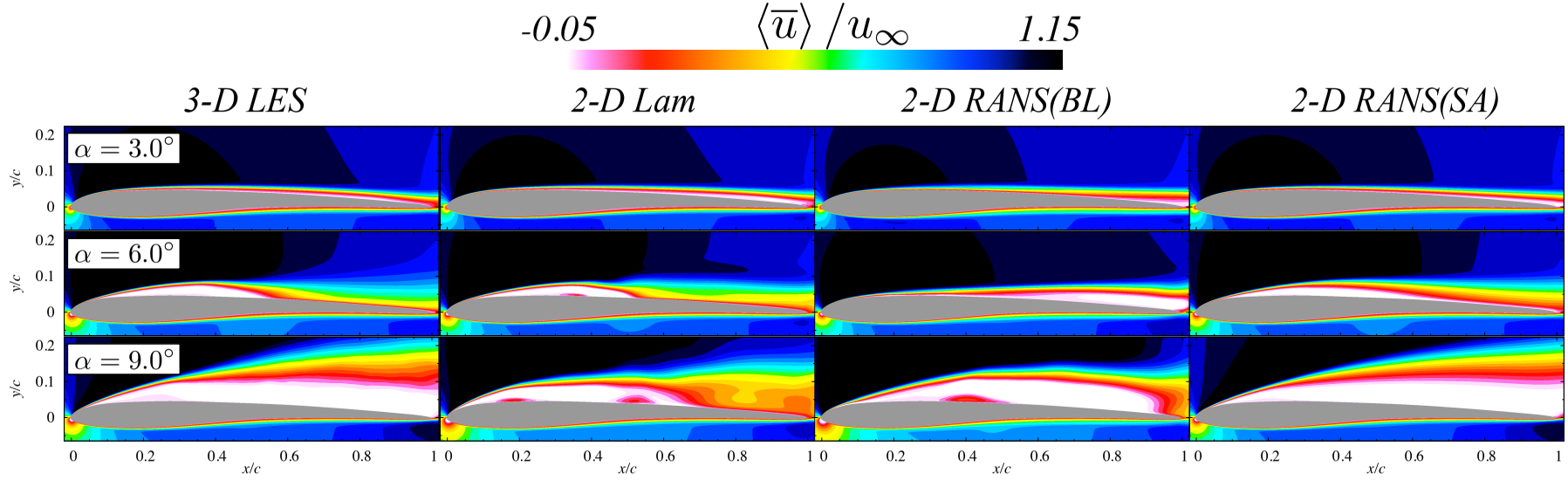

(c) Ishii (thin-cambered)

Figure 6.14: Averaged streamwise velocity fields of the 3-D LES (first column), 2-D Lam (second column), 2-D RANS(BL) (third column), and 2-D RANS(SA) (fourth column) for (a) NACA0012, (b) NACA0006, and (c) Ishii airfoil.

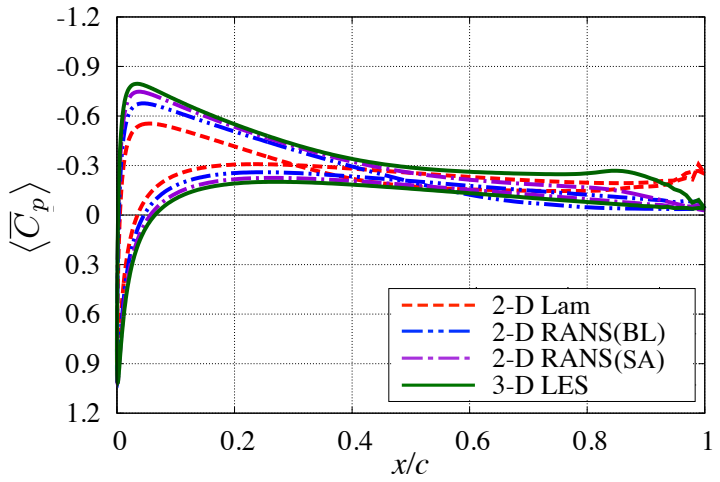

(a) $\alpha = 3.0°$

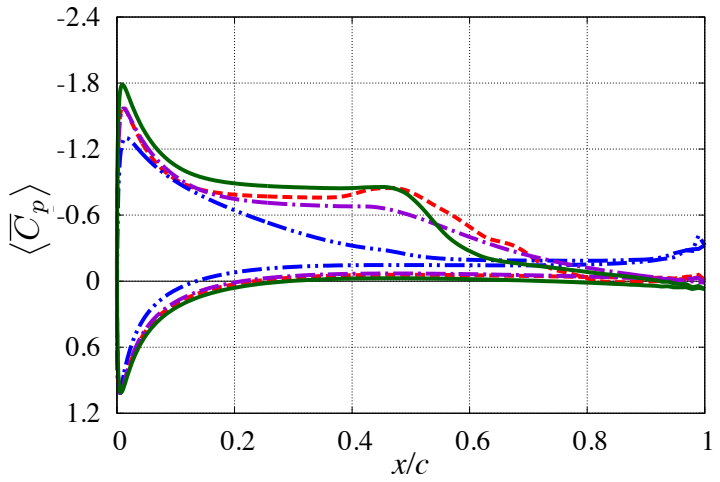

(b) $\alpha = 6.0°$

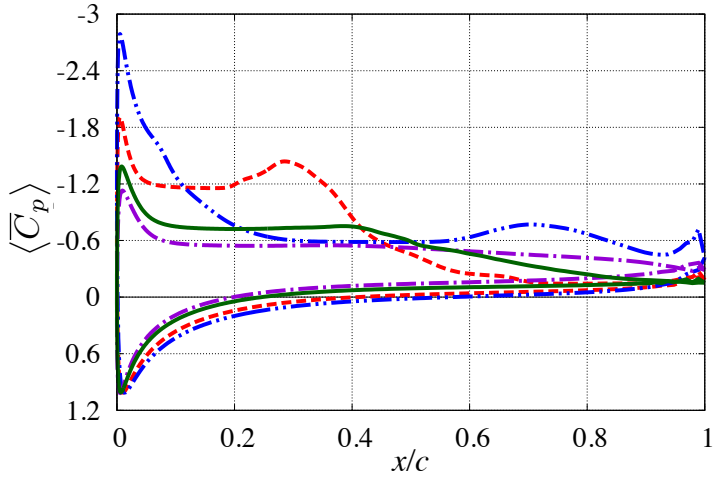

(c) $\alpha = 9.0°$

Figure 6.15: Time- and spanwise-averaged surface pressure distribution around the NACA0012 airfoil of the 2-D Lam (dashed-lines, red), 2-D RANS(BL) (dashed-double-dotted-lines, blue), 2-D RANS(SA) (dashed-dotted-line, violet), and 3-D LES (solid-lines, green) at (a) $\alpha = 3.0°$, (b) $\alpha = 6.0°$, and (c) $\alpha = 9.0°$.

6.3 Summary

This chapter investigates the formation mechanisms of surface pressure distribution and the reliability of two-dimensional unsteady laminar simulations for the flow fields around airfoils. Through the analysis of the this chapter, the following features are confirmed.

Formation mechanisms of surface pressure distribution First of all, the maximum turbulent kinetic energy distribution yields that the states inside LSB are decomposed into three parts: the LSB_S-Steady, LSB_SF-Steady, and fluctuating region. The pressure distributions corresponding to each region are the gradual pressure recovery, plateau pressure distributions, and rapid pressure recovery region, respectively. Therefore, it can be considered that all three pressure distribution characteristics shown in the flat plate cases coexist within the LSB. Next, it is examined the spatial distributions and momentum budget of each term of the averaged streamwise pressure gradient. From the results, it is also verified that the distribution of viscous shear stress due to the separated shear layer within the LSB and the generation of fluctuating component have a major role to the formation of the pressure gradient in each region. Therefore, the formation mechanisms of surface pressure distribution are similar to those of the flat plate, although the separation is induced by an adverse pressure gradient due to the geometry of the airfoil surface. It is also shown that the distance between the separated shear layer and the surface affects the surface pressure distribution in the steady region.

Reliability of two-dimensional laminar simulation The predictability of airfoil aerodynamic performances and formation of the LSB of the two-dimensional unsteady laminar simulations (2-D Lam) are assessed by comparing those of the three-dimensional large eddy simulation. It was shown that the 2-D Lam simulation which has a relatively low computational cost can be used for low Reynolds numbers to evaluate the qualitative aerodynamic characteristics except for high angles of attack which accompanies the massive separation flow. The predictability noted above appears regardless of the airfoil shape. Note that there are many analogous studies to calculate low Reynolds number flows, and development of improved turbulence or transition models would be needed. Without considering these points, however, it is shown that the low-cost 2-D Lam simulation without turbulence models can be adopted to estimate qualitative aerodynamic characteristics at low angles of attack ($\alpha \leq 6.0^\circ$). Also, by taking into account that angles of attack in cruise condition usually correspond to the lower angle of attack region, the 2-D Lam simulation can be a useful tool at the first step of designing airfoil shapes.

Chapter 7

Concluding remarks

This thesis focused on a laminar separation bubble (LSB) among factors that affect flow field characteristics of low Reynolds number ($Re_c = O(10^3) \sim O(10^5)$, where Re_c is a chord length based Reynolds number). First, from a physical point of view, high-accuracy three-dimensional large eddy simulations were carried out in order to elucidate physical mechanisms related to the formation of surface pressure distribution around an LSB. Next, from an engineering point of view, it was confirmed that the reliability of two-dimensional unsteady laminar simulation for an LSB flow which involves complicated nonstationary three-dimensional physical phenomena. In addition, it was shown that the two-dimensional unsteady laminar simulation may become a useful tool for evaluating airfoil aerodynamic performances in an engineering viewpoint.

In Chap. 3, three-dimensional large eddy simulations using the high-order compact finite difference scheme were performed for a 5% thickness right-angled blunt leading edge flat plate at zero angle of attack. The Reynolds numbers based on the plate length were set to $Re_c = 5.0\times10^3$, 6.1×10^3, 8.0×10^3, 1.1×10^4, and 2.0×10^4. The instantaneous flows considered in this thesis showed a fixed separation point at the leading edge and reattachment of the separated shear layer. Furthermore, depending on the Reynolds numbers, the laminar-turbulent transition was observed in the separated shear layer and the reattachment state also changed. More concretely, the laminar reattachment occurred at $Re_c \leq 8.0\times10^3$ while the turbulent reattachment appeared at $Re_c \geq 1.1\times10^4$. From the analysis based on the spatial distribution of turbulent kinetic energy (TKE) inside the LSBs, the characteristics of LSBs were classified as follows in this thesis: the steady laminar separation bubble (LSB_S) at $Re_c \leq 6.1 \times 10^3$ and the steady-fluctuating laminar separation bubble (LSB_SF) at $Re_c \geq 8.0 \times 10^3$. According to the classification above, the following three phenomena were newly observed;

- The shape of pressure distribution such as the constant pressure region followed by the rapid pressure recovery has been observed in many cases of an LSB. From the present simulation results, however, different shapes of pressure distribution were observed depending on the classification of LSB. First of all, in the LSB_S cases ($Re_c \leq 6.1 \times 10^3$), the gradual pressure recovery was observed without showing the plateau distribution in the entire separated region. On the other hand, in the LSB_SF cases ($Re_c \geq 8.0 \times 10^3$), the pressure distributions gradually began to show the typical plateau distribution in the steady region as increase in the Reynolds numbers, and the rapid pressure recovery appeared in the fluctuating region. Therefore, the results of LSB_S indicate that the formation of LSB is not always accompanying the typical shape of pressure distribution mentioned above.

- The reason of appearing the plateau pressure distribution region has been thought that because the velocity of the flow under the separated shear layer is slowly circulated. It can be considered as a practically steady state, so the streamwise pressure gradient is nearly zero and the pressure remains constant in this region. On the other hand, the present simulation results showed that the pressure distribution was different despite of the fact that a two-dimensional similar steady state appeared under the separated shear layer. The pressure was recovered gradually in the steady region of LSB_S whereas the constant pressure distribution was observed in that of LSB_SF. These results suggest that the different shapes of pressure distribution are affected by other factors rather than the steady flow condition under the separated shear layer.

- It has been thought that the rapid pressure recovery is caused by the momentum transfer from the freestream to the surface due to the three-dimensional turbulent structures. The result of $Re_c = 8.0 \times 10^3$, however, showed that the laminar reattachment may occur in spite of appearing the typical shape of pressure distribution around the LSB. It indicated that the pressure gradient can be suddenly varied even if there is no transition. Thus, the occurrence of rapid pressure recovery observed in the fluctuating region may not be always substantially affected by the three-dimensional structures.

In Chap. 4, the mechanisms behind the different shapes of pressure distribution within the LSB were newly proposed by using the averaged streamwise pressure gradient equation (Eq. (4.11)). Through the analysis of this chapter, following mechanisms were found in each of the steady (laminar part) and fluctuating (turbulent part) region of an LSB, respectively.

Steady region The reason of appearing different pressure gradient in the same steady region of LSB_S and LSB_SF was explained by the different distribution of the first viscous diffusion term (i.e., viscous shear stress). In the LSB_S case, the distribution of the positive first viscous diffusion term was observed near the surface, and it affected the formation of positive pressure gradient (i.e., gradual pressure recovery). As increasing the Reynolds numbers, the value of first viscous diffusion gradually decreased, and the first viscous diffusion effects near the surface became negligibly small. As a result, it led to the zero pressure gradient which corresponds to the constant pressure distributions. Next, from the streamwise velocity and viscous shear stress distributions, it was confirmed that the different viscous shear stress near the surface was affected by the different development of the separated shear layer depending on the Reynolds numbers. In the LSB_S, the separated shear layer was relatively thick by the low Reynolds numbers effects, and hence it caused the continuous viscous shear stress near the surface. This non-negligible viscous shear stress near the surface was responsible for the formation of positive first viscous diffusion. In the LSB_SF, the viscous shear stress near the surface became considerably smaller than that of the LSB_S due to the formation of a relatively thin shear layer. As a result, the negligibly small first viscous diffusion appeared near the surface.

Fluctuating region First of all, it was revealed that the presence of fluctuating component (i.e., Reynolds stress) and its gradient transport were main contributors for a rapid pressure recovery phenomenon. The presence of the gradient of Reynolds stress (so-called the gradient transport of overall Reynolds stress, GTOR, in the present study) induced the strong viscous shear stress near the surface, and it resulted in the rapid pressure recovery. One of the interesting result was that these characteristics did not depend on the instantaneous flow structure. In other words, even if the three-dimensional turbulent structures were not formed, the rapid pressure recovery was observed if two-dimensional spanwise-extended vortex structures produced sufficiently large fluctuating components. In order to investigate the relationship between the distributions of gradient transport of Reynolds stress and the flow structures, the GTOR was decomposed into a gradient transport of Reynolds normal stress in the streamwise direction and a gradient transport of Reynolds shear stress (GTRS) in the wall-normal direction. The decomposition results showed that the momentum transfer in the wall-normal direction induced by the GTRS component was an important factor for the rapid pressure recovery. Next, the GTRS was further decomposed into two- and three-dimensional components. It was shown that the two-dimensional spanwise vortex was totally responsible for the GTRS

at $Re_c = 8.0 \times 10^3$, whereas the three-dimensional turbulent structures was the main contributor to the GTRS at $Re_c \geq 1.1 \times 10^4$. Thus, it is elucidated that the gradient transport of Reynolds shear stress plays a main role in the rapid pressure recovery, but the formation of three-dimensional turbulent structures is not a necessary condition for it. In other words, the magnitude of gradient transport of Reynolds shear stress itself is more important rather than the physical phenomenon which creates the Reynolds shear stress.

According to the simulation results and physical mechanisms related to the formation of surface pressure distribution around LSBs as mentioned above, it becomes clear that the flow structures are basically two-dimensional, and to capture the behavior of the separated shear layer accurately is important in the steady region. In the fluctuating region, the magnitude of gradient of the Reynolds shear stress is more important rather than the physical phenomenon which creates it. Considering these physical mechanisms, it is expected that some characteristics of an LSB which includes complicated nonstationary three-dimensional flows can be captured even in a two-dimensional simulation. Thus, in Chap. 5, two-dimensional unsteady laminar simulations were carried out using a 5% thickness blunt leading edge flat plate to verify the reliability for flow fields around an LSB. The results showed that the following characteristics can be predicted by the two-dimensional laminar simulation; the formation of LSBs, the tendency of varying reattachment points depending on the Reynolds numbers, and reattachment state. Moreover, the two-dimensional laminar simulation also reproduced the qualitative distribution of averaged surface pressure distribution and skin friction coefficient except for the overshoot phenomena observed around the transition region. On the other hand, the accurate prediction of instantaneous flow structures and velocity profiles in the wall-normal direction were difficult in the two-dimensional laminar simulation. Regarding the formation of the surface pressure distribution, it was revealed that the overshoot phenomenon was caused by a stronger estimation of the Reynolds stress than the three-dimensional simulation. The reason why the rapid pressure recovery in the fluctuating region was able to be predicted was because the three-dimensional Reynolds shear stress component in the actual flow field was pushed into the two-dimensional one in the two-dimensional simulation. Consequently, the magnitude of overall gradient transport of Reynolds shear stress of two-dimensional simulation became similar to that of the three-dimensional one. In conclusion, a critical point for the rapid pressure recovery is the generation of the positive distribution of overall component away from the surface in both simulations. Thus, even if the three-dimensional turbulent structure cannot be captured, the qualitative distribution of the gradient transport of Reynolds shear

stress which is an important factor for the pressure gradient becomes similar in both simulations; and hence the rapid pressure recovery also appears in the two-dimensional simulation.

In Chap. 6, the analyses in the previous chapters were applied to a flow field around airfoils in order to show the engineering usefulness of the discussion in the present thesis. For this purpose, the three-dimensional large eddy simulation were conducted for the NACA0012, NACA0006, and Ishii airfoils. Two-dimensional Reynolds-averaged Navier-Stokes simulations with the Baldwin-Lomax and Spalart-Allmaras turbulence models were additionally performed as comparison objects. From the results, the following features were confirmed.

Formation mechanisms of surface pressure distribution First of all, the maximum turbulent kinetic energy distribution provided the fact that the flow states inside an LSB were decomposed into three parts; the LSB_S-Steady, LSB_SF-Steady, and fluctuating region. The pressure distributions corresponding to each region stated above were the gradual pressure recovery, plateau pressure distributions, and rapid pressure recovery region, respectively. Therefore, it can be considered that all three pressure distribution characteristics shown in the flat plate cases coexist within the LSB. Next, it was also verified that the formation mechanisms of surface pressure distribution were similar to those of the flat plate, although the separation was induced by a continuously changed adverse pressure gradient due to the geometry of the airfoil surface. It was shown that the distance between the separated shear layer and the surface affected the viscous shear stress near the surface and the surface pressure distribution of the steady region. It is anticipated that the mechanism revealed by the present thesis is able to apply to flow fields around an LSB irrespective of the Reynolds numbers. Further note that the methodology of momentum budget from the averaged pressure gradient equation can be also used to any time- and spanwise-averaged flow fields regardless of flow conditions (e.g., Reynolds numbers, angles of attack, geometric shapes of airfoils, etc.), because the equation is derived from the governing equation of the fluid dynamics.

Reliability of two-dimensional laminar simulation The predictability of aerodynamic performances (lift and drag coefficients) and formation of the LSB of the two-dimensional unsteady laminar simulations were assessed by comparing those of the three-dimensional large eddy simulation results. From the results, the two-dimensional unsteady laminar simulation which has a relatively low computational cost can be used for low Reynolds numbers to evaluate the qualitative aerodynamic characteristics except

for high angles of attack which accompanies massive separation flows. The predictability mentioned above appears regardless of the airfoil shape. From an engineering point of view, by taking into account that angles of attack in a cruise condition usually correspond to the lower angle of attack region, the two-dimensional unsteady laminar simulation can be a useful tool at the first step of designing airfoil shapes. Considering together with the results of previous studies (Kojima *et al.*, 2013; Lee *et al.*, 2015) and those of this thesis, it has been confirmed that an applicable range of the two-dimensional unsteady laminar simulation is at least for flow fields of which the Reynolds number is below 5.0×10^4.

Appendix A

Effect of cross-sectional aspect ratio of flat plate on flow characteristics

A.1 Introduction

Characteristics of the low Reynolds number flows drastically change with a little variation of Reynolds numbers. Thus, it is important to understand the flow field characteristics in a wide range of Reynolds numbers. Especially, one of the important features of the low Reynolds number flows is a formation of LSB, because an LSB affects not only the flow field characteristics but also the mechanical efficiency (e.g., see Sec. 1.3). Here, let us focus on the variation of the reattachment points to the Reynolds number. As already shown in Fig. 5.5, it moves to downstream as the Reynolds number increases in the range of $Re_t < 320 \sim 400$ and a good consistency is obtained between several previous studies. On the other hand, at $Re_t > 320 \sim 400$, all the results show that the reattachment points move to the leading edge but their values are not quantitatively consistent. One more point should be noted is that many experimental studies have set the Reynolds numbers based on the plate thickness, because the plate length based Reynolds number cannot be specified by assuming as an infinite length in experiments. It has not been sufficiently discussed, however, that comparisons of the reattachment point based on the plate thickness are reasonable or not. The discussion is also insufficient that quantitative discrepancies shown in the higher Reynolds numbers region are resulted by the physical phenomena depending on the plate thickness or errors of each measurement method. Therefore, numerical experiments are conducted to investigate the effects of aspect ratio of flat plate on flow field characteristics at the constant Reynolds number based on the plate thickness.

A.2 Computational setup

The third order MUSCL (Sec. 2.3.1) with SHUS (Sec. 2.3.2) are employed for evaluating the convective terms. The viscous terms are computed by the second order central differencing without any turbulence model. The second order backward differencing converged by the ADI-SGS method (Sec. 2.4.1) is adopted for time integration. Therefore, the numerical methods used in this chapter are the two-dimensional unsteady laminar simulations which are exactly same as those in Chap. 5. The freestream Mach number is set to 0.2 with zero turbulence intensity. Two cases of plate length based Reynolds numbers (Re_t) are conducted: $Re_t = 250$ for the laminar reattachment and $Re_t = 1,000$ for the turbulent reattachment. The flat plate aspect ratios (t/c, where t : plate thickness and c : plate chord length) are set to 0.01, 0.025, 0.05, and 0.1. In particular, since the simulation code used in this study adopts the plate length based Reynolds number as a variable, it is necessary to set the plate length based Reynolds numbers differently according to the aspect ratio in order to make the thickness based Reynolds number equal. Tables A.1 and A.2 summarize the plate length based Reynolds number for each aspect ratio.

Before conducting the numerical experiments, some factors which may lead the numerical errors are already investigated $t/c = 0.05$ case in Sec. 5.1.4. It was shown that Grid B, Time A, and Min A are required. These criteria, however, are only effective for the discussion of the plate length based Reynolds number. In other words, the criteria above are not satisfied in the thickness based discussion if the same criteria are applied to all the aspect ratio. Thus, the number of grid points, time step size, and minimum grid spacing should be changed in an appropriate way for each aspect ratio. In consideration of these issues, computational grids as shown in Fig. A.1 are prepared so as to satisfy the criteria. That is, the blue region in each figure has the same grid quality (spacing) irrespective of the aspect ratio when considering the thickness based Reynolds number. The information of grid for each aspect ratio is listed in Tab. A.3. It is confirmed that the grids of four aspect ratio cases satisfy the criteria above.

A.3 Results and discussion

Figure A.2 shows the reattachment points of the present simulation results. The results indicate that the effects of aspect ratio of the plate can be ignored at $Re_t = 250$ where the laminar reattachment appears. At the turbulent reattachment Reynolds number ($Re_t = 1,000$), however, the reattachment points move downstream as the aspect ratio

Table A.1: Plate length based Reynolds numbers for each aspect ratio in the laminar reattachment case.

t/c	Re_c	Re_t
0.01	25,000	250
0.025	10,000	250
0.05	5,000	250
0.1	2,500	250

Table A.2: Plate length based Reynolds numbers for each aspect ratio in the turbulent reattachment case.

t/c	Re_c	Re_t
0.01	100,000	1,000
0.025	40,000	1,000
0.05	20,000	1,000
0.1	10,000	1,000

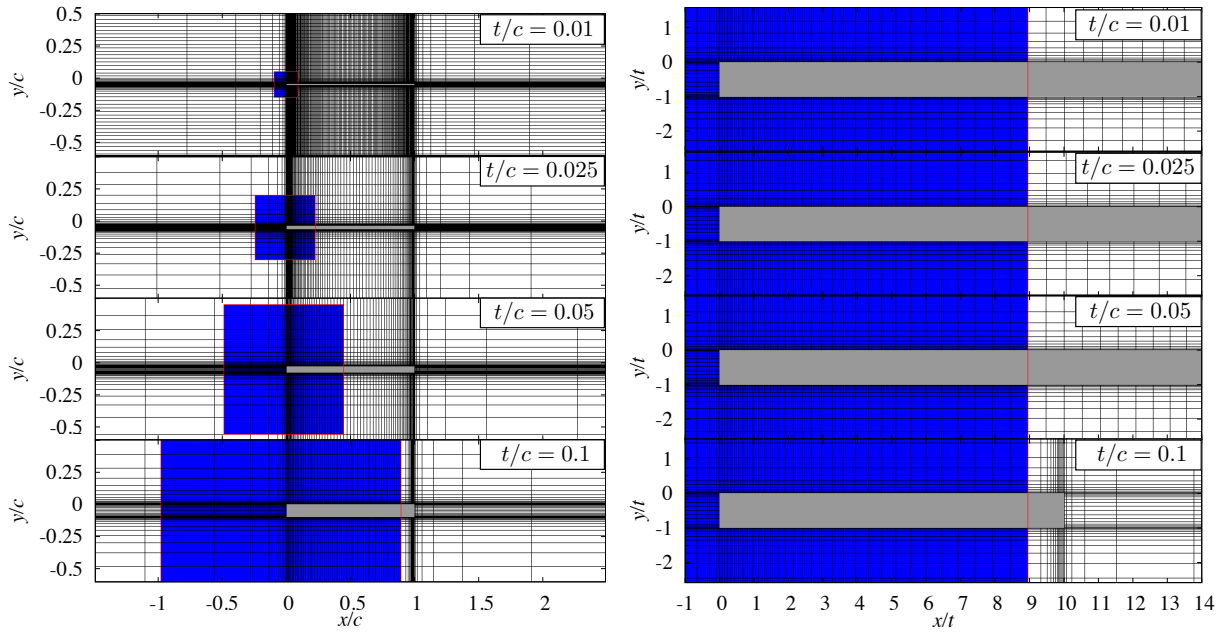

(a) Viewpoint of the plate chord length.

(b) Viewpoint of the plate thickness.

Figure A.1: Computational grids visualized on the basis of (a) plate chord length and (b) plate thickness. The square region colored by blue indicate the same grid quality region regardless of the aspect ratio.

Table A.3: The number of grid points, minimum grid spacing, time step size, and maximum CFL number for each aspect ratio.

t/c	N_x	N_y	N_z	Total points	Δx	Δy	Δt	Max. CFL
0.01	890	667	1	593,630	0.00014	0.00004	0.00004	1.18
0.025	530	250	1	213,590	0.00035	0.0001	0.0001	1.19
0.05	471	250	1	169,089	0.0007	0.0002	0.0002	1.19
0.1	350	250	1	94,850	0.0014	0.0002	0.0002	0.60

decreases. Figure A.3 shows the time-averaged surface pressure distribution and skin friction coefficients of each Reynolds number case. From the figure, it is confirmed that the influence of the aspect ratio in both of the distributions is negligible in the laminar reattachment case. A slightly different distribution is seen at $t/c = 0.1$, but it is considered that the difference is caused by the direct influence of the wake flow due to the relatively short length of the plate. In the turbulent reattachment case, the suction peak of pressure distribution changes according to the aspect ratio. Furthermore, the length of the plateau pressure distribution region and the location of rapid pressure recovery are different depending on the aspect ratio. In terms of the skin friction coefficient, the position where the negative peak value appears varies depending on the aspect ratio. On the other hand, there is no significant difference regardless of the variation of the aspect ratio in terms of the magnitude of the negative peak value as well as that in the attached boundary layer region. Figures A.4 and A.5 are time-averaged streamwise velocity and instantaneous spanwise vorticity flow fields at $Re_t = 250$ and $1,000$, respectively. As shown in Fig. A.4, there is no difference between the time-averaged and instantaneous flow fields due to the effects of the aspect ratio at $Re_t = 250$. On the other hand, the location of the spanwise vortex shedding from the separated shear layer moves downstream as decrease in the aspect ratio at $Re_t = 1,000$. It can be considered that some flow fields characteristics in the downstream are different depending on the aspect ratio at this Reynolds number, and flow of the downstream affects those of the leading edge. These features are qualitatively confirmed by the turbulent kinetic energy flow fields shown in Fig. A.6. From the figure, it is seen that the location where the turbulent kinetic energy begins to form moves toward the leading edge as increase in the aspect ratio. From Fig. A.7, the location where the maximum turbulent kinetic energy appears is shifted to the trailing edge as the aspect ratio decreases.

In conclusion, the effects of aspect ratio can be negligible at the laminar reattachment Reynolds number ($Re_t = 250$). In the turbulent reattachment case ($Re_t = 1,000$), however, the reattachment points move to downstream as the aspect ratio decreases. At

this Reynolds number, there is a possibility that the flow fields characteristics such as instantaneous flows, time-averaged flows, the turbulent kinetic energy near the leading edge and the reattachment points are varied depending on the aspect ratio, and the aspect ratio may be one factor that causes discrepancies of the reattachment points shown in Fig. 5.5. Therefore, the discussion using the thickness based Reynolds number should be carefully considered. It is also worth to note that upstream flow characteristics are varied by a feedback loop of acoustic wave generated from the trailing edge (Desquesnes *et al.*, 2007; Plogmann *et al.*, 2013). The present results also suggest that the transition and LSB characteristics may be differed by the downstream or the trailing edge flow, and characteristics of feedback loop of acoustic wave may be affected by the aspect ratio of the flat plate.

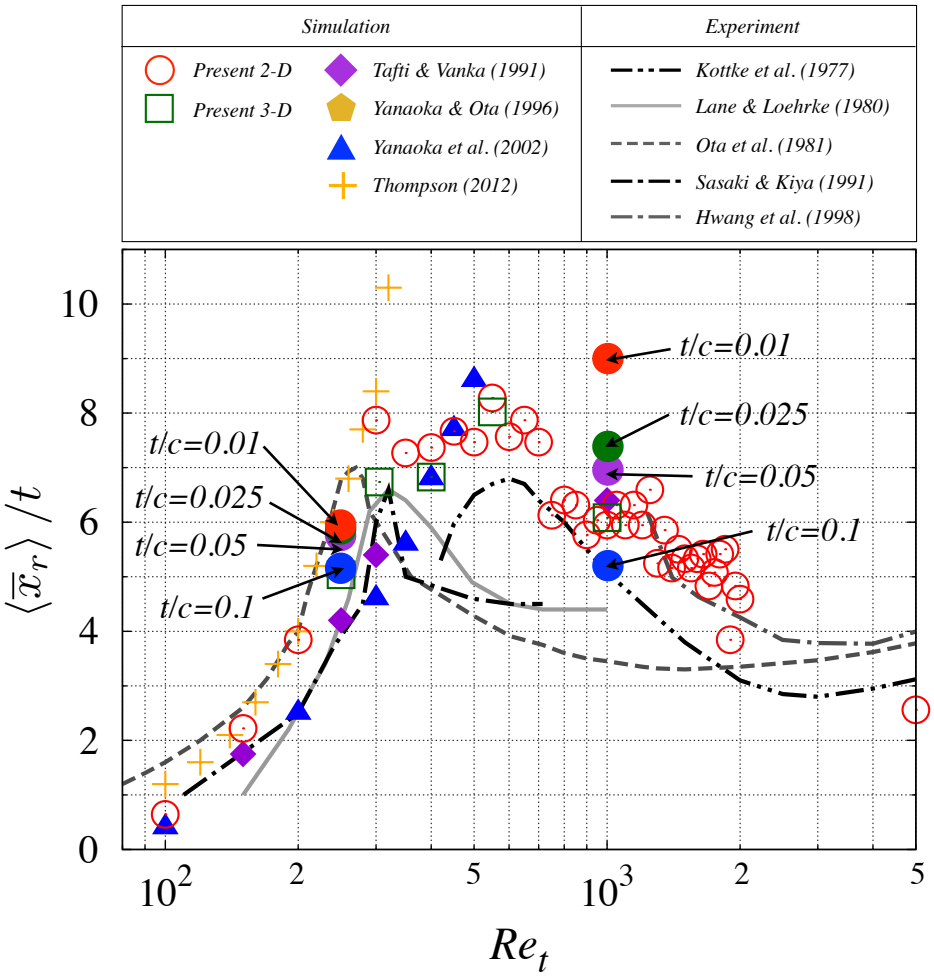

Figure A.2: Variation of the reattachment points with the aspect ratio $t/c = 0.01$ (filled-circles, red); $t/c = 0.025$ (filled-circles, green); $t/c = 0.05$ (filled-circles, violet); and $t/c = 0.1$ (filled-circles, blue). The present two-dimensional (opened-circles, red) and three-dimensional (opened-squares, green) results are shown with several previous experimental and numerical results.

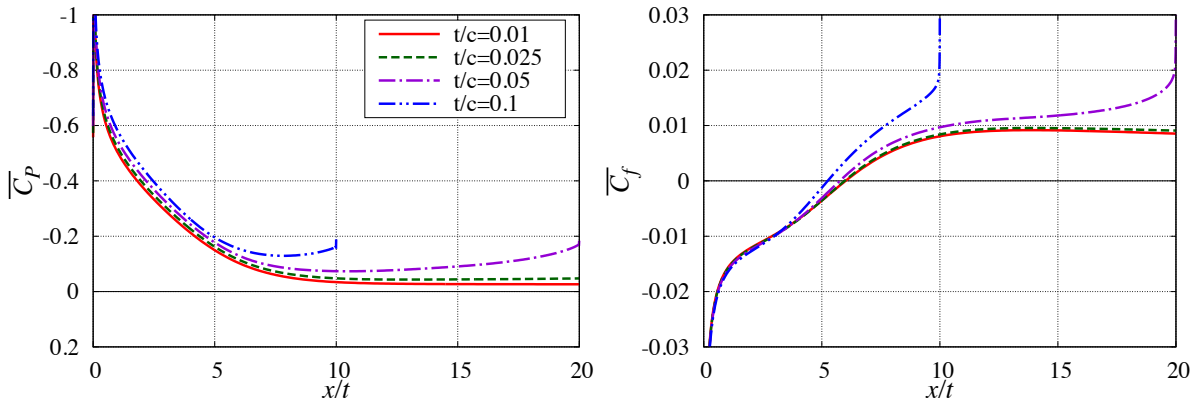

(a) $Re_t = 250$

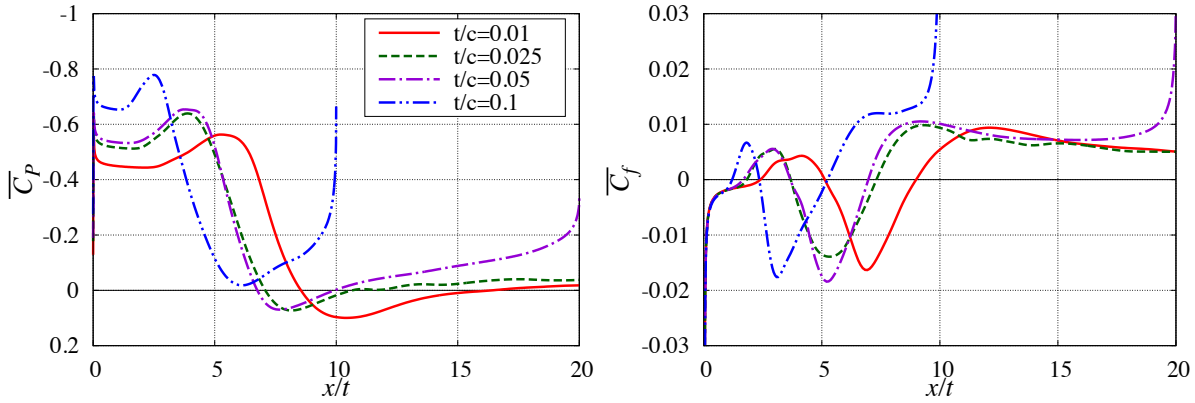

(b) $Re_t = 1,000$

Figure A.3: Time-averaged surface pressure distribution (left column) and skin friction distribution (right column) of $t/c = 0.01$ (solid line, red), $t/c = 0.025$ (dashed-line, green), $t/c = 0.05$ (dashed-dotted-line, violet), and $t/c = 0.1$ (dashed-double-dotted-line, blue) at (a) $Re_t = 250$ and (b) $Re_t = 1,000$.

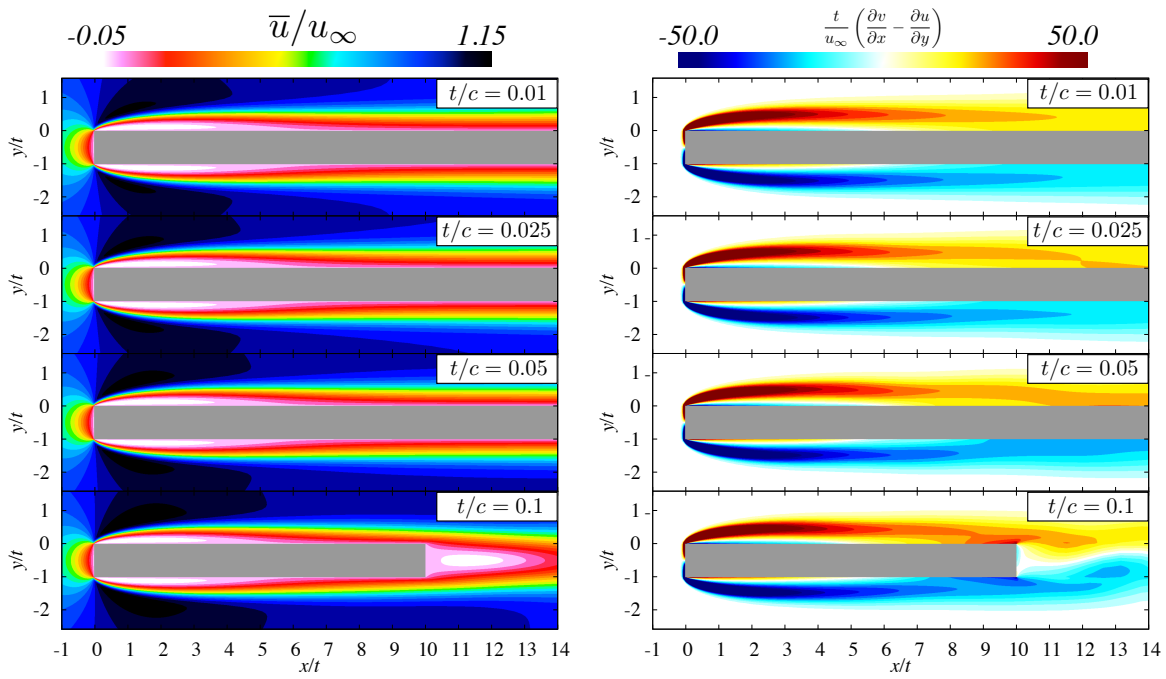

(a) Averaged streamwise velocity (b) Instantaneous spanwise vorticity

Figure A.4: (a) Averaged streamwise velocity and (b) instantaneous spanwise vorticity flow fields of $t/c = 0.01$, 0.025, 0.05, and 0.1 at $Re_t = 250$.

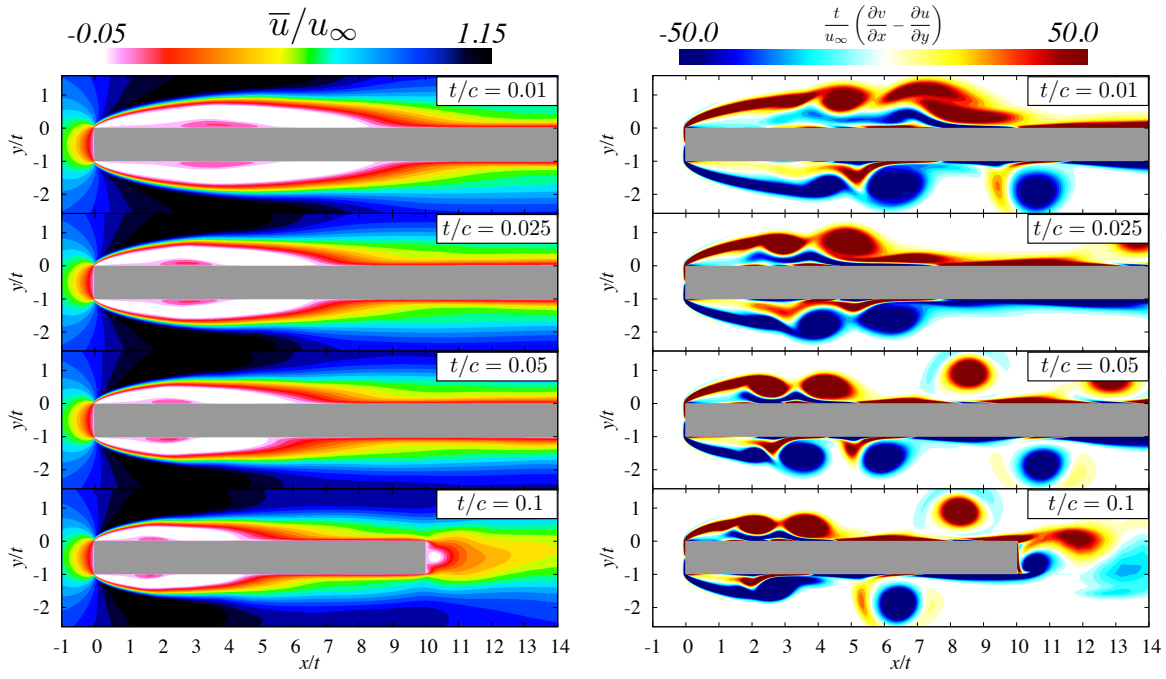

(a) Averaged streamwise velocity (b) Instantaneous spanwise vorticity

Figure A.5: (a) Averaged streamwise velocity and (b) instantaneous spanwise vorticity flow fields of $t/c = 0.01$, 0.025, 0.05, and 0.1 at $Re_t = 1,000$.

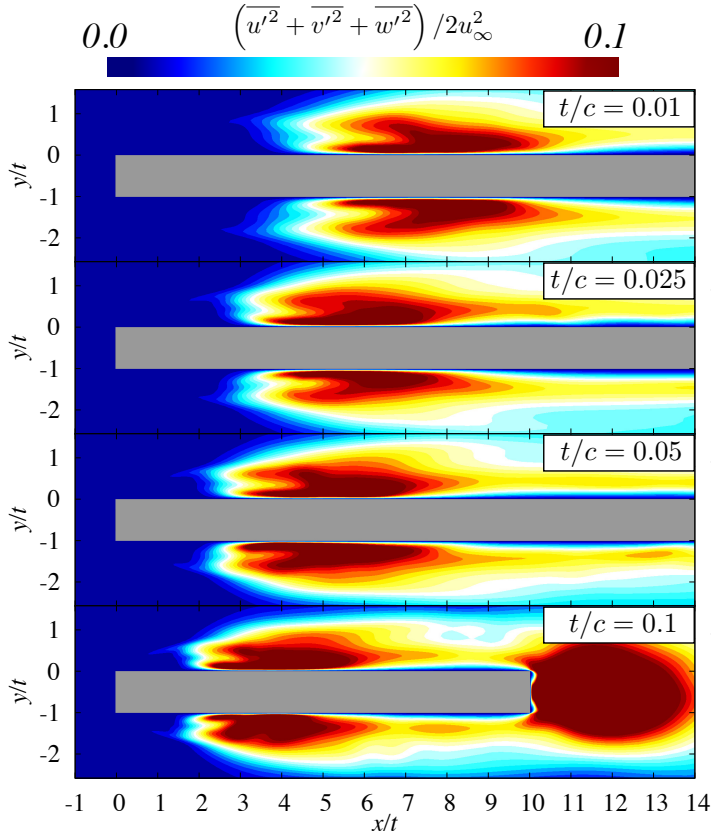

Figure A.6: Turbulent kinetic energy flow fields of $t/c = 0.01$, 0.025, 0.05, and 0.1 at $Re_t = 1,000$.

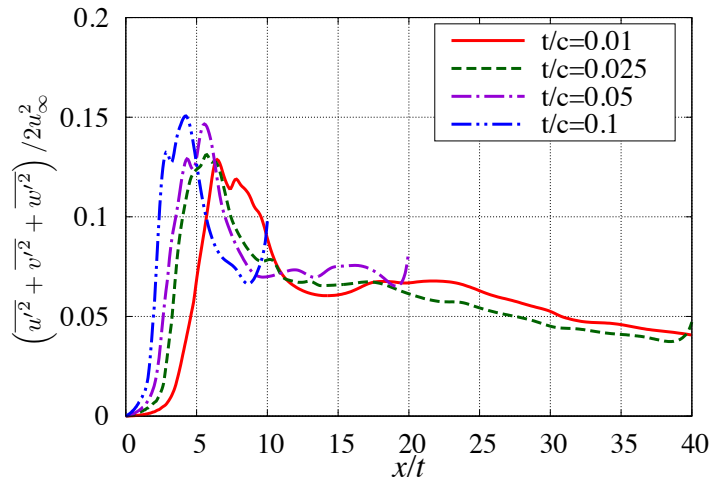

Figure A.7: Maximum turbulent kinetic energy distributions of $t/c = 0.01$ (solid line, red), $t/c = 0.025$ (dashed-line, green), $t/c = 0.05$ (dashed-dotted-line, violet), and $t/c = 0.1$ (dashed-double-dotted-line, blue) at $Re_t = 1,000$.

References

Abdo, M. & Mateescu, D., (2005). "Low-Reynolds number aerodynamics of airfoils at incidence". In 43rd AIAA Aerospace Sciences Meeting and Exhibit, *AIAA 2005-1038*.

Abe, Y., Iizuka, N., Nonomura, T. & Fujii, K., (2013). "Conservative metric evaluation for high-order finite difference schemes with the GCL identities on moving and deforming grids". *Journal of Computational Physics* **232** (1): 14–21.

Abe, Y., Nonomura, T., Iizuka, N. & Fujii, K., (2014). "Geometric interpretations and spatial symmetry property of metrics in the conservative form for high-order finite-difference schemes on moving and deforming grids". *Journal of Computational Physics* **260** (1): 163–203.

Alam, M. & Sandham, N. D., (2000). "Direct numerical simulation of 'short' laminar separation bubbles with turbulent reattachment". *Journal of Fluid Mechanics* **410**: 223–250.

Alam, Md M., Zhou, Y., Yang, H. X., Guo, H. & Mi, J., (2010). "The ultra-low Reynolds number airfoil wake". *Experiments in Fluids* **48** (1): 81–103.

Almutairi, J. H., Jones, L. E. & Sandham, N. D., (2010). "Intermittent bursting of a laminar separation bubble on an airfoil". *AIAA Journal* **48** (2): 414–426.

Alpert, P., (1981). "Implicit filtering in conjunction with explicit filtering". *Journal of Computational Physics* **44** (1): 212–219.

Alving, A. E. & Fernholz, H. H., (1995). "Mean-velocity scaling in and around a mild, turbulent separation bubble". *Physics of Fluids* **7** (8): 1956–1969.

Andersson, B., Andersson, R., Hakansson, L., Mortensen, M., Sudiyo, R. & van Wachem, B., (2012). "Computational fluid dynamics for engineers". *Cambridge University Press*.

Anyoji, M., Nonomura, T., Aono, H., Oyama, A., Fujii, K., Nagai, H. & Asai, K., (2014). "Computational and experimental analysis of a high-performance airfoil under low-Reynolds-number flow condition". *Journal of Aircraft* **51** (6): 1864–1872.

Anyoji, M., Nose, K., Ida, S., Numata, D., Nagai, H. & Asai, K., (2011). "Aerodynamic measurements in the Mars wind tunnel at Tohoku university". In 49th AIAA Aerospace Sciences Meeting including the New Horizons Forum and Aerospace Exposition, *AIAA 2011-0852*.

Aono, H., Nonomura, T., Anyoji, M., Oyama, A. & Fujii, K., (2012). "A numerical study of the effects of airfoil shape on low Reynolds number aerodynamics". In the Eighth International Conference on Engineering Computational Technology, *Paper 131*.

Aono, H., Sekimoto, S., Sato, M., Yakeno, A., Nonomura, T. & Fujii, K., (2015). "Computational and experimental analysis of flow structures induced by a plasma actuator with burst modulations in quiescent air". *Mechanical Engineering Journal* **2** (4): 15–00233.

Arena, A. V. & Mueller, T. J., (1980). "Laminar separation, transition, and turbulent reattachment near the leading edge of airfoils". *AIAA Journal* **18** (7): 747–753.

Argyropoulos, C. D. & Markatos, N. C., (2015). "Recent advances on the numerical modelling of turbulent flows". *Applied Mathematical Modelling* **39** (2): 693–732.

Baldwin, B. S. & Barth, T. J., (1991). "A one-equation turbulence transport model for high Reynolds number wall-bounded flows". In 29th Aerospace Sciences Meeting, *AIAA 1991-0610*.

Baldwin, B. S. & Lomax, H., (1978). "Thin layer approximation and algebraic model for separated turbulent flow". In 16th AIAA Aerospace Sciences Meetings, *AIAA 1978-0257*.

Beam, R. M. & Warming, R. F., (1978). "An implicit factored scheme for the compressible Navier-Stokes equations". *AIAA Journal* **16** (4): 393–402.

Bodony, D. J. & Lele, S. K., (2005). "On using large-eddy simulation for the prediction of noise from cold and heated turbulent jets". *Physics of Fluids* **17** (8): 085103.

Bogey, C. & Bailly, C., (2006). "Large eddy simulations of round free jets using explicit filtering with/without dynamic Smagorinsky model". *International Journal of Heat and Fluid Flow* **27** (4): 603–610.

Boris, J. P., Grinstein, F. F., Oran, E. S. & Kolbe, R. L., (1992). "New insights into large eddy simulation". *Fluid Dynamics Research* **10** (4-6): 199–228.

Boutilier, M. S. H. & Yarusevych, S., (2012). "Parametric study of separation and transition characteristics over an airfoil at low Reynolds numbers". *Experiments in Fluids* **52** (6): 1491–1506.

Bredberg, J., (2001). "On two-equation eddy-viscosity models". Chalmers University of Technology, *Internal Report 01/8*.

Brinkerhoff, J. R. & Yaras, M. I., (2011). "Interaction of viscous and inviscid instability modes in separation-bubble transition". *Physics of Fluids* **23** (12): 124102.

Buresti, G., (2015). "A note on Stokes' hypothesis". *Acta Mechanica* **226** (10): 3555–3559.

Burgmann, S. & Schröder, W., (2008). "Investigation of the vortex induced unsteadiness of a separation bubble via time-resolved and scanning PIV measurements". *Experiments in Fluids* **45** (4): 675–691.

Cadieux, F. & Domaradzki, J. A., (2015). "Performance of subgrid-scale models in coarse large eddy simulations of a laminar separation bubble". *Physics of Fluids* **27** (4): 045112.

Cadieux, F., Domaradzki, J. A., Sayadi, T. & Bose, S., (2014). "Direct numerical simulation and large eddy simulation of laminar separation bubbles at moderate Reynolds numbers". *Journal of Fluids Engineering* **136** (6): 060902.

Carmichael, B. H., (1982). "Low Reynolds number airfoil survey, volume 1". National Aeronautics and Space Administration, *NASA-CR-165803-VOL-1*.

Castiglioni, G., Domaradzki, J. A., Pasquariello, V., Hickel, S. & Grilli, M., (2014). "Numerical simulations of separated flows at moderate reynolds numbers appropriate for turbine blades and unmanned aero vehicles". *International Journal of Heat and Fluid Flow* **49**: 91–99.

Catalano, P. & Tognaccini, R., (2010). "Turbulence modeling for low-Reynolds-number flows". *AIAA Journal* **48** (8): 1673–1685.

Chakravarthy, S. R., (1984). "Relaxation methods for unfactored implicit upwind schemes". In 22nd AIAA Aerospace Sciences Meeting, *AIAA 1984-0165*.

Chang, P. K., (1970). "Separation of flow". *Pergamon Press*.

Chapman, D. R., (1979). "Computational aerodynamics development and outlook". *AIAA Journal* **17** (12): 1293–1313.

Cherry, N. J., Hillier, R. & Latour, M. E. M. P., (1984). "Unsteady measurements in a separated and reattaching flow". *Journal of Fluid Mechanics* **144**: 13–46.

Choi, H. & Moin, P., (1994). "Effects of the computational time step on numerical solutions of turbulent flow". *Journal of Computational Physics* **113** (1): 1–4.

Choi, H. & Moin, P., (2012). "Grid-point requirements for large eddy simulation: Chapman's estimates revisited". *Physics of Fluids* **24** (1): 011702.

Choudhry, A., Arjomandi, M. & Kelso, R., (2015). "A study of long separation bubble on thick airfoils and its consequent effects". *International Journal of Heat and Fluid Flow* **52**: 84–96.

Counsil, J. N. N. & Goni Boulama, K., (2012). "Validating the URANS shear stress transport $\gamma - Re_\theta$ model for low-Reynolds-number external aerodynamics". *International Journal for Numerical Methods in Fluids* **69** (8): 1411–1432.

Courant, R., Friedrichs, K. & Lewy, H., (1967). "On the partial difference equations of mathematical physics". *IBM Journal of Reserach and Development* **11** (2): 215–234.

Craft, T. J., Launder, B. E. & Suga, K., (1996). "Development and application of a cubic eddy-viscosity model of turbulence". *International Journal of Heat and Fluid Flow* **17** (2): 108–115.

Crivellini, A. & D'Alessandro, V., (2014). "Spalart-Allmaras model apparent transition and RANS simulations of laminar separation bubbles on airfoils". *International Journal of Heat and Fluid Flow* **47**: 70–83.

Dandois, J., Garnier, E. & Sagaut, P., (2007). "Numerical simulation of active separation control by a synthetic jet". *Journal of Fluid Mechanics* **574**: 25–58.

Davidson, P. A., (2015). "Turbulence: An introduction for scientists and engineers". *Oxford University Press*.

Deardorff, J. W., (1970). "A numerical study of three-dimensional turbulent channel flow at large Reynolds numbers". *Journal of Fluid Mechanics* **41** (2): 453–480.

Debesse, Ph., Pastur, L., Lusseyran, F., Fraigneau, Y., Tenaud, C., Bonamy, C., Cavalieri, A. V. G. & Jordan, P., (2016). "A comparison of data reduction techniques for the aeroacoustic analysis of flow over a blunt flat plate". *Theoretical and Computational Fluid Dynamics* **30** (3): 253–274.

Deck, S., Gand, F., Brunet, V. & Ben Khelil, S., (2014). "High-fidelity simulations of unsteady civil aircraft aerodynamics: stakes and perspectives. Application of zonal detached eddy simulation". *Philosophical Transactions of the Royal Society of London A: Mathematical, Physical and Engineering Sciences* **372** (2022): 20130325.

Del Alamo, J. C., Jiménez, J., Zandonade, P. & Moser, R. D., (2004). "Scaling of the energy spectra of turbulent channels". *Journal of Fluid Mechanics* **500**: 135–144.

Deng, X., Mao, M., Tu, G., Liu, H. & Zhang, H., (2011). "Geometric conservation law and applications to high-order finite difference schemes with stationary grids". *Journal of Computational Physics* **230** (4): 1100–1115.

Deng, X. & Zhang, H., (2000). "Developing high-order weighted compact nonlinear schemes". *Journal of Computational Physics* **165** (1): 22–44.

Dengel, P. & Fernholz, H. H., (1990). "An experimental investigation of an incompressible turbulent boundary layer in the vicinity of separation". *Journal of Fluid Mechanics* **212**: 615–636.

Desquesnes, G., Terracol, M. & Sagaut, P., (2007). "Numerical investigation of the tone noise mechanism over laminar airfoils". *Journal of Fluid Mechanics* **591**: 155–182.

Diwan, S. S. & Ramesh, O. N., (2009). "On the origin of the inflectional instability of a laminar separation bubble". *Journal of Fluid Mechanics* **629**: 263–298.

Diwan, S. S. & Ramesh, O. N., (2012). "Relevance of local parallel theory to the linear stability of laminar separation bubbles". *Journal of Fluid Mechanics* **698**: 468–478.

Dovgal, A. V., Kozlov, V. V. & Michalke, A., (1994). "Laminar boundary layer separation: Instability and associated phenomena". *Progress in Aerospace Sciences* **30** (1): 61–94.

Ehrhard, J. & Moussiopoulos, N., (2000). "On a new nonlinear turbulence model for simulating flows around building-shaped structures". *Journal of Wind Engineering and Industrial Aerodynamics* **88** (1): 91–99.

Ekaterinaris, J. A, (2005). "High-order accurate, low numerical diffusion methods for aerodynamics". *Progress in Aerospace Sciences* **41** (3-4): 192–300.

Farve, A., (1983). "Turbulence: Space-time statistical properties and behavior in supersonic flows". *Physics of Fluids* **26** (10): 2581–2863.

Freund, J. B. & Colonius, T., (2009). "Turbulence and sound-field POD analysis of a turbulent jet". *International Journal of Aeroacoustics* **8** (4): 337–354.

Frohlich, J. & von Terzi, D., (2008). "Hybrid LES/RANS methods for the simulation of turbulent flows". *Progress in Aerospace Sciences* **44** (5): 349–377.

Fujii, K., (1994). "Numerical methods for computational fluid dynamics". *University of Tokyo Press*.

Fujii, K., (1998). "Simple ideas for the accuracy and efficiency improvement of the compressible flow simulation methods". In Proceedings of the international CFD Workshop on Supersonic Transport Design, p. 20–23.

Fujii, K., (1999). "Efficiency improvement of unified implicit relaxation/time integration algorithms". *AIAA Journal* **37** (1): 125–128.

Fujii, K. & Obayashi, S., (1986). "Practical applications of new LU-ADI scheme for the three-dimensional Navier-Stokes computation of transonic viscous flows". In 24th Aerospace Sciences Meeting, *AIAA 1986-0513*.

Fujii, K. & Obayashi, S., (1987). "Navier-Stokes simulations of transonic flows over a wing-fuselage combination". *AIAA Journal* **25** (12): 1587–1596.

Fyfe, D. J., (1966). "Economical evaluation of Runge-Kutta formulae". *Mathematics of Computation* **20** (1966): 392–392.

Gaitonde, D. V. & Visbal, M. R., (2000). "Pade-type higher-order boundary filters for the Navier-Stokes equations". *AIAA Journal* **38** (11): 2103–2112.

Galbraith, M. & Visbal, M. R., (2010). "Implicit large eddy simulation of low-Reynolds-number transitional flow past the SD7003 airfoil marshall". In 40th Fluid Dynamics Conference and Exhibit, *AIAA 2010-4737*.

Garmann, D.J. & Visbal, M.R., (2015). "Interactions of a streamwise-oriented vortex with a finite wing". *Journal of Fluid Mechanics* **767**: 782–810.

Garmann, D. J., Visbal, M. R. & Orkwis, P. D., (2013). "Comparative study of implicit and subgrid-scale model large-eddy simulation techniques for low-Reynolds number airfoil applications". *International Journal for Numerical Methods in Fluids* **71** (12): 1546–1565.

Gaster, M., (1967). "The structure and behaviour of laminar separation bubble". Aeronautical Research Council, *ARC R&M 3595*.

Georgiadis, N. J., Rizzetta, D. P. & Fureby, C., (2010). "Large-eddy simulation: current capabilities, recommended practices, and future research". *AIAA Journal* **48** (8): 1772–1784.

Germano, M., Piomelli, U., Moin, P. & Cabot, W. H., (1991). "A dynamic subgrid-scale eddy viscosity model". *Physics of Fluids A: Fluid Dynamics* **3** (7): 1760–1765.

Ghosal, S., Lund, T. S., Moin, P. & Akselvoll, K., (1995). "A dynamic localization model for large-eddy simulation of turbulent flows". *Journal of Fluid Mechanics* **297**: 402.

Gourdain, N., Sicot, F., Duchaine, F. & Gicquel, L., (2014). "Large eddy simulation of flows in industrial compressors: a path from 2015 to 2035." *Philosophical Transactions of the Royal Society of London A: Mathematical, Physical and Engineering Sciences* **372** (2022): 20130323.

Grinstein, F. F. & Fureby, C., (2002). "Recent progress on MILES for high Reynolds number flows". *Journal of Fluids Engineering* **124** (4): 848–861.

Gross, A. & Fasel, H. F., (2010). "Active flow control for NACA 6-series airfoil at Re=64,200". *AIAA Journal* **48** (9): 1889–1902.

Guynn, M. D., Croom, M. A., Smith, S. C., Parks, R. W. & Gelhausen, P. A., (2003). "Evolution of a Mars airplane concept for the ARES Mars scout mission". In

2nd AIAA Unmanned Unlimitied Conference and Workshop & Exhibit, *AIAA 2003-6578*.

Hain, R., Kähler, C. J. & Radespiel, R., (2009). "Dynamics of laminar separation bubbles at low-Reynolds-number aerofoils". *Journal of Fluid Mechanics* **630**: 129–153.

Harten, A., Engquist, B., Osher, S. & Chakravarthy, S. R., (1987). "Uniformly high order accurate essentially non-oscillatory Schemes, III". *Journal of Computational Physics* **71** (2): 231–303.

Hirsch, C., (2007). "Numerical computation of internal & external flows". *Springer*.

Ho, C.-M. & Huerre, P., (1984). "Perturbed free shear layers". *Annual Review of Fluid Mechanics* **16**: 365–424.

Hodson, H. P. & Howell, R. J., (2005). "The role of transition in high-lift low-pressure turbines for aeroengines". *Progress in Aerospace Sciences* **41** (6): 419–454.

Horton, H. P., (1968). "Laminar separation bubbles in two- and three-dimensional incompressible flow". Ph.d. thesis, *Queen Mary University of London*.

Hosseinverdi, S. & Fasel, H. F., (2015). "Laminar-turbulent transition in a laminar separation bubble in the presence of free-stream turbulence". *Procedia IUTAM* **14**: 570–579.

Howard, R. J. A., Alam, M. & Sandham, N. D., (2000). "Two-equation turbulence modelling of a transitional separation bubble". *Flow, Turbulence and Combustion* **63** (1): 175–191.

Hoyas, S. & Jimenez, J., (2006). "Scaling of the velocity fluctuations in turbulent channels up to $Re_\tau = 2003$". *Physics of Fluids* **18** (1): 011702.

Hu, H. & Yang, Z., (2008). "An experimental study of the laminar flow separation on a low-Reynolds-number airfoil". *Journal of Fluids Engineering* **130** (5): 051101.

Huang, R. F. & Lee, H. W., (1999). "Effects of freestream turbulence on wing-surface flow and aerodynamic performance". *Journal of Aircraft* **36** (6): 965–972.

Hunt, J. C. R., Wray, A. A. & Moin, P., (1988). "Eddies, streams, and convergence zones in turbulent flows". Center for Turbulence Research, Stanford University, *CTR-S88*.

Hussain, A. K. M. F. & Reynolds, W. C., (1970). "The mechanics of an organized wave in turbulent shear flow". *Journal of Fluid Mechanics* **41** (2): 241–258.

Hwang, K. S., Sung, H. J. & Hyun, J. M., (1998). "Flow and mass transfer measurements for a flat plate of finite thickness in pulsating flow". *International Journal of Heat and Mass Transfer* **41** (18): 2827–2836.

Iizuka, N., (2006). "Study of Mach number effect on the dynamic stability of a blunt re-entry capsule". Ph.d. thesis, *University of Tokyo*.

Ishihara, T., Gotoh, T. & Kaneda, Y., (2009). "Study of highReynolds number isotropic turbulence by direct numerical simulation". *Annual Review of Fluid Mechanics* **41**: 165–180.

Jacobs, E. N., Ward, K. E. & Pinkerton, R. M., (1933). "The characteristics of 78 related airfoil sections from tests in the variable-density wind tunnel". National Advisory Committee for Aeronautics, *NACA Report No. 460*.

Jahanmiri, M., (2011). "Laminar separation bubble: Its structure, dynamics and control". Chalmers University of Technology, *Research Report 2011:06*.

Jameson, A., (1995*a*). "Analysis and design of numerical schemes for gas dynamics, 1: Artificial diffusion, upwind biasing, limiters and their effect on accuracy and multigrid convergence". *International Journal of Computational Fluid Dynamics* **4** (3-4): 171–218.

Jameson, A, (1995*b*). "Analysis and design of numerical schemes for gas dynamics, 2: Artificial diffusion and discrete shock structure". *International Journal of Computational Fluid Dynamics* **5** (1-2): 1–38.

Jameson, A., Schmidt, W. & Turkel, E., (1981). "Numerical solutions of the Euler equations by finite volume methods using Runge-Kutta time-stepping schemes". In 14th AIAA Fluid and Plasma Dynamics Conference, *AIAA 1981-1259*.

Jiang, G. S. & Shu, C. W., (1996). "Efficient implementation of weighted ENO schemes". *Journal of Computational Physics* **126** (1): 202–228.

Johnson, D. A. & King, L. S., (1985). "A mathematically simple turbulence closure model for attached and separated turbulent boundary layers". *AIAA Journal* **23** (11): 1684–1692.

Jones, L. E., Sandberg, R. D. & Sandham, N. D., (2008). "Direct numerical simulations of forced and unforced separation bubbles on an airfoil at incidence". *Journal of Fluid Mechanics* **602**: 175–207.

Jones, L. E., Sandberg, R. D. & Sandham, N. D., (2010). "Stability and receptivity characteristics of a laminar separation bubble on an aerofoil". *Journal of Fluid Mechanics* **648**: 257–296.

Jones, W. P. & Launder, B. E., (1972). "The prediction of laminarization with a two-equation model of turbulence". *International Journal of Heat and Mass Transfer* **15** (2): 301–314.

Karasu, I., Genç, M. S. & Açikel, H. H., (2013). "Numerical study on low Reynolds number flows over an aerofoil". *Journal of Applied Mechanical Engineering* **2** (5): 1–7.

Kawai, S. & Fujii, K., (2005). "Analysis and prediction of thin-airfoil stall phenomena with hybrid turbulence methodology". *AIAA Journal* **43** (5): 953–961.

Kawai, S. & Fujii, K., (2008). "Compact scheme with filtering for large-eddy simulation of transitional boundary layer". *AIAA Journal* **46** (3): 690–700.

Kawai, S. & Larsson, J., (2012). "Wall-modeling in large eddy simulation: Length scales, grid resolution, and accuracy". *Physics of Fluids* **24** (1): 015105.

Kawai, S. & Larsson, J., (2013). "Dynamic non-equilibrium wall-modeling for large eddy simulation at high Reynolds numbers". *Physics of Fluids* **25** (1): 015105.

Kawai, S., Shankar, S. K. & Lele, S. K., (2010). "Assessment of localized artificial diffusivity scheme for large-eddy simulation of compressible turbulent flows". *Journal of Computational Physics* **229** (5): 1739–1762.

Kim, D. H., Chang, J. W. & Chung, J., (2011). "Low-Reynolds-number effect on aerodynamic characteristics of a NACA 0012 airfoil". *Journal of Aircraft* **48** (4): 1212–1215.

Kim, J., Moin, Pa. & Moser, R., (1987). "Turbulence statistics in fully developed channel flow at low Reynolds number". *Journal of Fluid Mechanics* **177**: 133–166.

Kim, K. H., Kim, C. & Rho, O.-H., (2001). "Methods for the accurate computations of hypersonic flows I. AUSMPW$^+$ scheme". *Journal of Computational Physics* **174** (1): 38–80.

Kim, K. H., Lee, J. H. & Rho, O. H., (1998). "An improvement of AUSM schemes by introducing the pressure-based weight functions". *Computers & Fluids* **27** (3): 311–346.

Kitamura, K. & Hashimoto, A., (2016). "Reduced dissipation AUSM-family fluxes: HR-SLAU2 and HR-AUSM$^+$-up for high resolution unsteady flow simulations". *Computers & Fluids* **126** (1): 41–57.

Kitamura, K. & Shima, E., (2013). "Towards shock-stable and accurate hypersonic heating computations: A new pressure flux for AUSM-family schemes". *Journal of Computational Physics* **245** (15): 62–83.

Kiya, M. & Sasaki, K., (1985). "Structure of large-scale vortices and unsteady reverse flow in the reattaching zone of a turbulent separation bubble". *Journal of Fluid Mechanics* **154**: 463–491.

Kobayashi, H., (2005). "The subgrid-scale models based on coherent structures for rotating homogeneous turbulence and turbulent channel flow". *Physics of Fluids* **17** (4): 045104.

Kobayashi, H., Ham, F. & Wu, X., (2008). "Application of a local SGS model based on coherent structures to complex geometries". *International Journal of Heat and Fluid Flow* **29** (3): 640–653.

Kojima, R., Nonomura, T., Oyama, A. & Fujii, K., (2013). "Large-eddy simulation of low-Reynolds-number flow over thick and thin NACA airfoils". *Journal of Aircraft* **50** (1): 187–196.

Kondo, K., Aono, H., Nonomura, T., Anyoji, M., Oyama, A., Liu, T., Fujii, K. & Yamamoto, M., (2014). "Analysis of Owl-like airfoil aerodynamics at low Reynolds number flow". *Transactions of the Japan Society for Aeronautical and Space Sciences, Aerospace Technology Japan* **12** (ists29): TK_35–TK_40.

Kondo, K., Aono, H., Nonomura, T., Oyama, A., Fujii, K. & Yamamoto, M., (2013). "Large-eddy simulations of Owl-like wing under low Reynolds number condition". In Proceedings of the ASME 2013 Fluids Engineering Division Summer Meeting, *FEDSM2013-16377*.

Kottke, V., Blenke, H. & Schmidt, K. G., (1977). "Einfluss von anstromprofil und trubulenzientensitat auf die unstromung langsangestromter paltten endlicher dicke". *Warme-und Stoffubertraung* **10**: 159–174.

Koutsavdis, E. K., Blaisdell, G. A. & Lyrintzis, A. S., (1999). "A numerical investigation of two-dimensional jets using spatial filtering". In 5th AIAA/CEAS Aeroacoustics Conference, *AIAA 1999-1875*.

Kuhl, C. A., (2009). "Design of a Mars airplane propulsion system for the aerial regional-scale environmental survey (ARES) mission concept". National Aeronautics and Space Administration, *NASA/TM-2009-215700*.

Kunz, P. J., (2003). "Aerodynamic and desing for ultra-low Reynolds number flight". Ph.d. thesis, *Stranford University*.

Kuo, Y. H., (1953). "On the flow of an incompressible viscous fluid past at moderate Reynolds numbers". *Journal of Mathematics and Physics* **32** (1-4): 83–101.

Laitone, E. V., (1996). "Aerodynamic lift at Reynolds numbers below 7×10^4". *AIAA Journal* **34** (9): 1941–1942.

Laitone, E. V., (1997). "Wind tunnel tests of wings at Reynolds numbers below 70,000". *Experiments in Fluids* **23** (5): 405–409.

Lane, J. C. & Loehrke, R. I., (1980). "Leading edge separation from a blunt plate at low Reynolds number". *Journal of Fluids Engineering* **102** (4): 494–496.

Larsson, J., Kawai, S., Bodart, J. & Bermejo-moreno, I., (2015). "Large eddy simulation with modeled wall-stress: recent progress and future directions". *Mechanical Engineering Reviews* **3** (1): 15–00418.

Larsson, J. & Wang, Q., (2014). "The prospect of using large eddy and detached eddy simulations in engineering design, and the research required to get there". *Philosophical Transactions of the Royal Society of London A: Mathematical, Physical and Engineering Sciences* **372** (2022): 20130329.

Launder, B. E., Reece, G. J. & Rodi, W., (1975). "Progress in the development of a Reynolds-stress turbulence closure". *Journal of Fluid Mechanics* **68** (3): 537–566.

Launder, B. E. & Sharma, B. I., (1974). "Application of the energy-dissipation model of turbulence to the calculation of flow near a spinning disc". *Letters in heat and mass transfer* **1** (2): 131–138.

Lee, D., Nonomura, T., Oyama, A. & Fujii, K., (2015). "Comparison of numerical methods evaluating airfoil aerodynamic characteristics at low Reynolds number". *Journal of Aircraft* **52** (1): 296–306.

Lekoudis, S. G. & Sengupta, Y. K., (1986). "Two-dimensional turbulent boundary layers over rigid and moving swept wavy surfaces". *Physics of Fluids* **29** (4): 964–970.

Lele, S. K., (1992). "Compact finite difference schemes with spectral-like resolution". *Journal of Computational Physics* **103** (1): 16–42.

Lengani, D., Simoni, D., Ubaldi, M. & Zunino, P., (2014). "POD analysis of the unsteady behavior of a laminar separation bubble". *Experimental Thermal and Fluid Science* **58**: 70–79.

Leschziner, M., Li, N. & Tessicini, F., (2009). "Simulating flow separation from continuous surfaces: routes to overcoming the Reynolds number barrier." *Philosophical Transactions of the Royal Society of London A: Mathematical, Physical and Engineering Sciences* **367** (1899): 2885–2903.

Liou, M. S., (1996). "A sequel to AUSM: AUSM$^+$". *Journal of Computational Physics* **129** (2): 364–382.

Liou, M.-S., (2006). "A sequel to AUSM, Part II: AUSM$^+$-up for all speeds". *Journal of Computational Physics* **214** (1): 137–170.

Liou, M.-S. & Steffen, C. J., (1993). "A new flux splitting scheme". *Journal of Computational Physics* **107** (1): 23–39.

Lissaman, P. B. S., (1983). "Low-Reynolds-number airfoils". *Annual Review of Fluid Mechanics* **15**: 223–239.

Liu, X. D., Osher, S. & Chan, T., (1994). "Weighted essentially non-oscillatory schemes". *Journal of Computational Physics* **115** (1): 200–212.

Loginov, M. S., Adams, N. A. & Zheltovodov, A. A., (2006). "Large-eddy simulation of shock-wave/turbulent-boundary-layer interaction". *Journal of Fluid Mechanics* **565**: 135–169.

Lombard, C. K., Bardina, J., E., Venkatapathy. & Oliger, J., (1983). "Multi-dimensional formulation of CSCM - An upwind flux difference eigenvector split method for the compressible Navier-Stokes equations." In 6th Computational Fluid Dynamics Conference, *AIAA 1983-1895*.

Maccormack, R. W., (1982). "A numerical method for solving the equations of compressible viscous flow". *AIAA Journal* **20** (9): 1275–1281.

Marsden, O., Bogey, C. & Bailly, C., (2008). "Direct noise computation of the turbulent flow around a zero-incidence airfoil". *AIAA Journal* **46** (4): 874–883.

Martinez-Aranda, S., Garcia-Gonzalez, A. L., Parras, L., Velazquez-Navaro, J. F. & del Pino, C., (2016). "Comparison of the aerodynamic characteristics of the NACA0012 airfoil at low-to-moderate Reynolds numbers for any aspect ratio". *International Journal of Aerospace Science* **4** (1): 1–8.

Marty, Ph., Michel, F. & Tochon, P., (2008). "Experimental and numerical study of the heat transfer along a blunt flat plate". *International Journal of Heat and Mass Transfer* **51** (1-2): 13–23.

Marxen, O. & Henningson, D. S., (2011). "The effect of small-amplitude convective disturbances on the size and bursting of a laminar separation bubble". *Journal of Fluid Mechanics* **671**: 1–33.

Marxen, O., Lang, M. & Rist, U., (2012). "Discrete linear local eigenmodes in a separating laminar boundary layer". *Journal of Fluid Mechanics* **711**: 1–26.

Marxen, O., Lang, M. & Rist, U., (2013). "Vortex formation and vortex breakup in a laminar separation bubble". *Journal of Fluid Mechanics* **728**: 58–90.

Marxen, O., Lang, M., Rist, U., Levin, O. & Henningson, D. S., (2009). "Mechanisms for spatial steady three-dimensional disturbance growth in a non-parallel and separating boundary layer". *Journal of Fluid Mechanics* **634**: 165–189.

Marxen, O., Rist, U. & Wagner, S., (2004). "Effect of spanwise-modulated disturbances on transition in a separated boundary layer". *AIAA Journal* **42** (5): 937–944.

Matsuura, K. & Kato, C., (2007). "Large eddy simulation of compressible transitional cascade flows". *Journal of Fluid Science and Technology* **2** (3): 558–569.

Mayle, R. E., (1991). "The role of laminar-turbulent transition in gas turbine engines". *Journal of Turbomachinery* **113** (4): 509–536.

McDonough, J. M., (2004). "Introductory lectures on turbulence, Physics, mathematics and modeling". University of Kentucky, *Lecture notes*.

Meneveau, C., Lund, T. S. & Cabot, W. H., (1996). "A Lagrangian dynamic subgrid-scale model of turbulence". *Journal of Fluid Mechanics* **319**: 353–385.

Menter, F. R., (1994). "Two-equation eddy-viscosity turbulence models for engineering applications". *AIAA Journal* **32** (8): 1598–1605.

Moin, P. & Mahesh, K., (1998). "Direct numerical simulation: A tool in turbulence research". *Annual Review of Fluid Mechanics* **30**: 539–578.

Moin, P., Squires, K., Cabot, W. & Lee, S., (1991). "A dynamic subgrid-scale model for compressible turbulence and scalar transport". *Physics of Fluids A: Fluid Dynamics* **3** (11): 2746–2757.

Monkewitz, P. A. & Huerre, P., (1982). "Influence of the velocity ratio on the spatial instability of mixing layers". *Physics of Fluids* **25** (7): 1137–1143.

Morgan, B., Duraisamy, K., Nguyen, N., Kawai, S. & Lele, S. K., (2013). "Flow physics and RANS modelling of oblique shock/turbulent boundary layer interaction". *Journal of Fluid Mechanics* **729**: 231–284.

Morinishi, Y. & Koga, K., (2014). "Skew-symmetric convection form and secondary conservative finite difference methods for moving grids". *Journal of Computational Physics* **257** (15): 1081–1112.

Mueller, T. J. & DeLaurier, J. D., (2003). "Aerodynamics of small vehicles". *Annual Review of Fluid Mechanics* **35**: 89–111.

Murray, J. E. & Tartabini, P. V., (2001). "Development of a Mars airplane entry, descent, and flight trajectory". National Aeronautics and Space Administration, *NASA/TM-2001-209035*.

Muti Lin, J. C. & Pauley, L. L., (1996). "Low-Reynolds-number separation on an airfoil". *AIAA Journal* **34** (8): 1570–1577.

Nakano, T., Fujisawa, N., Oguma, Y., Takagi, Y. & Lee, S., (2007). "Experimental study on flow and noise characteristics of NACA0018 airfoil". *Journal of Wind Engineering and Industrial Aerodynamics* **95** (7): 511–531.

Nishida, H. & Nonomura, T., (2009). "ADI-SGS scheme on ideal magnetohydrodynamics". *Journal of Computational Physics* **228** (9): 3182–3188.

Nisizima, S. & Yoshizawa, A., (1987). "Turbulent channel and Couette flows using an anisotropic $k - \epsilon$ model". *AIAA Journal* **25** (3): 414–420.

Nonomura, T. & Fujii, K., (2009). "Effects of difference scheme type in high-order weighted compact nonlinear schemes". *Journal of Computational Physics* **228** (10): 3533–3539.

Nonomura, T., Iizuka, N. & Fujii, K., (2010). "Freestream and vortex preservation properties of high-order WENO and WCNS on curvilinear grids". *Computers & Fluids* **39** (2): 197–214.

Obayashi, S. & Kuwahara, K., (1986). "An approximate LU factorization method for the compressible Navier-Stokes equations". *Journal of Computational Physics* **63** (1): 157–167.

Obayashi, S., Matsushima, K., Fujii, K. & Kuwahara, K., (1986). "Improvements in efficiency and reliability for Navier-Stokes computations using the LU-ADI factorization algorithm". In 24th Aerospace Sciences Meeting, *AIAA 1986-0338*.

Ohtake, T., Nakae, Y. & Motohashi, T., (2007). "Nonlinearity of the aerodynamic characteristics of NACA 0012 aerofoil at low Reynolds number". *Journal of the Japan Society for Aeronautical and Space Sciences* **55** (644): 439–445 (In Japanese).

Olson, D. A., Katz, A. W., Naguib, A. M., Koochesfahani, M. M., Rizzetta, D. P. & Visbal, M. R., (2013). "On the challenges in experimental characterization of flow separation over airfoils at low Reynolds number". *Experiments in Fluids* **54** (2): 1470.

Osher, S. & Solomon, F., (1982). "Upwind difference schemes for hyperbolic systems of conservation laws". *Mathematics of Computation* **38** (158): 339–374.

Ota, T., Asano, Y. & Okawa, J., (1981). "Reattachment length and transition of the separated flow over blunt flat plates". *Bulletin of the Japan Society of Mechanical Engineers* **24** (192): 941–947.

Oyama, A., Fujii, K., Shimoyama, K. & Liou, M.-S., (2005). "Pareto-optimality-based constraint-handling technique and its application to compressor design". In 17th AIAA Computational Fluid Dynamics Conference, *AIAA 2005-4983*.

Pauley, L. L., Moin, P. & Reynolds, W. C., (1990). "The structure of two-dimensional separation". *Journal of Fluid Mechanics* **220**: 397–411.

Piomelli, U., (1999). "Large-eddy simulation: achievements and challenges". *Progress in Aerospace Sciences* **35** (4): 335–362.

Piomelli, U. & Balaras, E., (2002). "Wall-layer models for large-eddy simulations". *Annual Review of Fluid Mechanics* **34**: 349–374.

Plogmann, B., Herrig, A. & Würz, W., (2013). "Experimental investigations of a trailing edge noise feedback mechanism on a NACA 0012 airfoil". *Experiments in Fluids* **54** (5): 1480.

Pope, S. B., (2000). "Turbulent flows". *Cambridge University Press*.

Pulliam, T. H., (1986). "Solution methods in computational fluid dynamics". *Notes for the von Kármán Institute For Fluid Dynamics Lecture Series* **2** (6): 441–474.

Pulliam, T. H. & Chaussee, D. S., (1981). "A diagonal form of an implicit approximate-factorization algorithm". *Journal of Computational Physics* **39** (2): 347–363.

Pulliam, T. H. & Steger, J. L., (1980). "Implicit finite-difference simulations of three-dimensional compressible flow". *AIAA Journal* **18** (2): 159–167.

Reynolds, O., (1895). "On the dynamical theory of incompressible viscous fluids and the determination of the criterion". *Philosophical Transactions of the Royal Society of London A: Mathematical, Physical and Engineering Sciences* **186**: 123–161.

Reynolds, W. C. & Hussain, A. K. M. F., (1972). "The mechanics of an organized wave in turbulent shear flow. Part 3. Theoretical models and comparisons with experiments". *Journal of Fluid Mechanics* **54** (2): 263–288.

Rinoie, K. & Hata, K., (2004). "Turbulent energy balances inside short bubble formed on NACA 0012 airfoil". *AIAA Journal* **42** (6): 1261–1264.

Rinoie, K., Okuno, M. & Sunada, Y., (2009). "Airfoil stall suppression by use of a bubble burst control plate". *AIAA Journal* **47** (2): 322–330.

Rinoie, K., Shingo, M. & Sato, J., (1990). "Measurements of short bubble and long bubble formed on NACA 63-009 airfoil". *Journal of the Japan Society for Aeronautical and Space Sciences* **38** (436): 249–257 (In Japanese).

Rinoie, K. & Takemura, N., (2004). "Oscillating behaviour of laminar separation bubble formed on an aerofoil near stall". *The Aeronautical Journal* **108** (1081): 153–163.

Ripley, M. D. & Pauley, L. L., (1993). "The unsteady structure of two-dimensional steady laminar separation". *Physics of Fluids A: Fluid Dynamics* **5** (12): 3099–3106.

Rizzetta, D. P., Visbal, M. R. & Morgan, P. E., (2008). "A high-order compact finite-difference scheme for large-eddy simulation of active flow control". *Progress in Aerospace Sciences* **44** (6): 397–426.

Roberts, S. K. & Yaras, M. I., (2006). "Large-eddy simulation of transition in a separation bubble". *Journal of Fluids Engineering* **128** (2): 232–238.

Roberts, W. B., (1980). "Calculation of laminar separation bubbles and their effect on airfoil performance". *AIAA Journal* **18** (1): 25–31.

Robinet, J.-C., (2013). "Instabilities in laminar separation bubbles". *Journal of Fluid Mechanics* **732**: 1–4.

Rodríguez, D., Gennaro, E. M. & Juniper, M. P., (2013*a*). "The two classes of primary modal instability in laminar separation bubbles". *Journal of Fluid Mechanics* **734**: R4.

Rodríguez, D. & Theofilis, V., (2010). "Structural changes of laminar separation bubbles induced by global linear instability". *Journal of Fluid Mechanics* **655**: 280–305.

Rodríguez, I., Lehmkuhl, O., Borrell, R. & Oliva, A., (2013*b*). "Direct numerical simulation of a NACA0012 in full stall". *International Journal of Heat and Fluid Flow* **43**: 194–203.

Roe, P. L., (1981). "Approximate Riemann solvers, parameter vectors and difference schemes". *Journal of Computational Physics* **43** (2): 357–372.

Rubinstein, R. & Barton, J. M., (1990). "Nonlinear Reynolds stress models and the renormalization group". *Physics of Fluids A: Fluid Dynamics* **2** (8): 1472–1476.

Rumsey, C. L., Allison, D. O., Biedron, R. T., Buning, P. G., Gainer, T. G., Morrison, J. H., Rivesr, S. M., Mysko, S. J. & Witkowski, D. P., (2001). "CFD sensitivity transport near analysis of a modern civil buffet-onset conditions". National Aeronautics and Space Administration, *NASA/TM-2001-211263*.

Rumsey, C. L. & Spalart, P. R., (2009). "Turbulence model behavior in low Reynolds number regions of aerodynamic flowfields". *AIAA Journal* **47** (4): 982–993.

Sasaki, K. & Kiya, M., (1991). "Three-dimensional vortex structure in a leading-edge separation bubble at moderate Reynolds numbers". *Journal of Fluids Engineering* **113** (3): 405–410.

Sato, M., Nonomura, T., Okada, K., Asada, K., Aono, H., Yakeno, A., Abe, Y. & Fujii, K., (2015). "Mechanisms for laminar separated-flow control using dielectric-barrier-discharge plasma actuator at low Reynolds number". *Physics of Fluids* **27** (11): 117101.

Sayadi, T., Hamman, C. W. & Moin, P., (2013). "Direct numerical simulation of complete H-type and K-type transitions with implications for the dynamics of turbulent boundary layers". *Journal of Fluid Mechanics* **724**: 480–509.

Sayadi, T. & Moin, P., (2012). "Large eddy simulation of controlled transition to turbulence". *Physics of Fluids* **24** (11): 114103.

Schlatter, P. & Orlu, R., (2010). "Assessment of direct numerical simulation data of turbulent boundary layers". *Journal of Fluid Mechanics* **659**: 116–126.

Schlichting, H. & Gersten, K., (1979). "Boundary layer theory". *Springer-Verlag Berlin Heidelberg*.

Schmidt, S. & Thiele, F., (2003). "Detached eddy simulation of flow around A-airfoil". *Flow, Turbulence and Combustion* **71** (1): 261–278.

Schmitz, F. W., (1967). "Aerodynamics of the model airplane Part I. Airfoil measurements". National Aeronautics and Space Administration, *NASA-TM-X-60976*.

Schubauer, G. B. & Spangengerg, W. G., (1960). "Forced mixing in boundary layers". *Journal of Fluid Mechanics* **8** (1): 10–32.

Sengupta, T. K. & Lekoudis, S. G., (1985). "Calculation of two-dimensional turbulent boundary layers over rigid and moving wavy surfaces". *AIAA Journal* **23** (4): 530–536.

Shan, H., Jiang, L. & Liu, C., (2005). "Direct numerical simulation of flow separation around a NACA 0012 airfoil". *Computers & Fluids* **34** (9): 1096–1114.

Shih, T.-H., Liou, W. W., Shabbir, A., Yang, Z. & Zhu, J., (1995). "A new $k-\epsilon$ eddy viscosity model for high reynolds number turbulent flows". *Computers & Fluids* **24** (3): 227–238.

Shima, E. & Jounouchi, T., (1997). "Role of CFD in aeronautical engineering(No.14) -AUSM type upwind schemes-". In Proceedings of the 14th NAL Symposium on Aircraft Computational Aerodynamics, p. 7–12.

Shima, E. & Kitamura, K., (2011). "Parameter-free simple low-dissipation AUSM-family scheme for all speeds". *AIAA Journal* **49** (8): 1693–1709.

Shu, C. W. & Osher, S., (1988). "Efficient implementation of essentially non-oscillatory shock-capturing schemes". *Journal of Computational Physics* **77** (2): 439–471.

Shu, C. W. & Osher, S., (1989). "Efficient implementation of essentially non-oscillatory schemes, II". *Journal of Computational Physics* **83** (1): 32–78.

Sillero, J. A., Jimenez, J. & Moser, R. D., (2013). "One-point statistics for turbulent wall-bounded flows at Reynolds numbers up to $\delta^+ \approx 2000$". *Physics of Fluids* **25** (10): 105102.

Simoni, D., Ubaldi, M. & Zunino, P., (2012). "Loss production mechanisms in a laminar separation bubble". *Flow, Turbulence and Combustion* **89** (4): 547–562.

Smagorinsky, J., (1963). "General circulation experiments with the primitive equations I. The basic experiment". *Monthly Weather Review* **91** (3): 99–164.

Smith, S. C., Guynn, M. D., Streett, C. L. & Beeler, G. B., (2003). "Mars airplain airfoil desing with application to ARES". In 2nd AIAA Unmanned Unlimitied Conference and Workshop & Exhibit, *AIAA 2003-6607*.

Spalart, P. R., (2009). "Detached-eddy simulation". *Annual Review of Fluid Mechanics* **41**: 181–202.

Spalart, P. R. & Allmaras, S. R., (1992). "A one-equation turbulence model for aerodynamic flows". In 30th AIAA Aerospace Sciences Meeting & Exhibit, *AIAA 1992-0439*.

Spalart, P. R. & Strelets, M. Kh., (2000). "Mechanisms of transition and heat transfer in a separation bubble". *Journal of Fluid Mechanics* **403**: 329–349.

Speziale, C. G., Abid, R. & Anderson, E. C., (1992). "Critical evaluation of two-equation models for near-wall turbulence". *AIAA Journal* **30** (2): 324–331.

Speziale, C. G., Sarkar, S. & Gatski, T. B., (1991). "Modelling the pressure-strain correlation of turbulence: An invariant dynamical systems approach". *Journal of Fluid Mechanics* **227**: 245–272.

Steger, J. L., (1978). "Implicit finite-difference simulation of flow about arbitrary two-dimensional geometries". *AIAA Journal* **16** (7): 679–686.

Steger, J. L. & Warming, R. F., (1981). "Flux vector splitting of the inviscid gasdynamic equation with application to finite-difference method". *Journal of Computational Physics* **40** (2): 263–293.

Stevenson, J. P. J., Walsh, E. J., Nolan, K. P. & Davies, M. R. D., (2014). "Separation & free-stream turbulence: implications for surface aerodynamics & heat transfer". *Journal of Physics: Conference Series* **525** (012018).

Stokes, G. G., (1845). "On the theories of the internal friction of fluids in motion, and of the equilibrium and motion of elastic solids". *Transaction of the Cambridge Philosophical Society* **8**: 287–319.

Suluksan, K. & Juntasaro, E., (2008). "Assessment of intermittency transport equations for modeling transition in boundary layers subjected to freestream turbulence". *International Journal of Heat and Fluid Flow* **29** (1): 48–61.

Sun, Q. & Boyd, I. D., (2004). "Flat-plate aerodynamics at very low Reynolds number". *Journal of Fluid Mechanics* **502**: 199–206.

Sunada, S., Yasuda, T., Yasuda, K. & Kawachi, K., (2002). "Comparison of wing characteristics at an ultralow Reynolds number". *Journal of Aircraft* **39** (2): 331–338.

Sutherland, W., (1893). "The viscosity of gases and molecular force". *Philosophical Magazine Series 5* **36** (223): 507–531.

Tafti, D. K. & Vanka, S. P., (1991*a*). "A numerical study of flow separation and reattachment on a blunt plate". *Physics of Fluids A: Fluid Dynamics* **3** (7): 1749–1759.

Tafti, D. K. & Vanka, S. P., (1991*b*). "A three-dimensional numerical study of flow separation and reattachment on a blunt plate". *Physics of Fluids A: Fluid Dynamics* **3** (12): 2887–2909.

Tang, L., (2008). "Reynolds-Averaged Navier-Stokes simulation of low-Reynolds-number airfoil aerodynamics". *Journal of Aircraft* **45** (3): 848–856.

Tani, I., (1964). "Low speed flows involving bubble separations". *Progress in Aerospace Sciences* **5**: 70–103.

Tani, I., Iuchi, M. & Komoda, H., (1961). "Experimental investigation of flow separation associated with a step or a groove". *Report/Aeronautical Research Institute, University of Tokyo* **27** (4): 119–137.

Tannehill, J. C., Anderson, D. A. & Pletcher, R. H., (1997). "Computational fluid mechanics and heat transfer". *Taylor & Francis*.

Tennekes, H. & Lumley, J. L., (1972). "A first course in turbulence". *MIT Press*.

Thomas, P. D. & Lombard, C. K., (1979). "Geometric conservation law and its application to flow computations on moving grids". *AIAA Journal* **17** (10): 1030–1037.

Thompson, M. C., (2012). "Effective transition of steady flow over a square leading-edge plate". *Journal of Fluid Mechanics* **698**: 335–357.

Tucker, P. G., (2011). "Computation of unsteady turbomachinery flows: Part 2-LES and hybrids". *Progress in Aerospace Sciences* **47** (7): 546–569.

Uzun, A., Blaisdell, G. A. & Lyrintzis, A. S., (2004). "Application of compact schemes to large eddy simulation of turbulent jets". *Journal of Scientific Computing* **21** (3): 283–319.

Van Albada, G. D., Van Leer, B. & Roberts, W. W., (1982). "A comparative study of computational methods in cosmic gas dynamics". *Astronomy and Astrophysics* **108** (1): 76–84.

Van Driest, E. R., (1956). "On turbulent flow near a wall". *Journal of the Aeronautical Sciences* **23** (11): 1007–1011.

Van Leer, B., (1982). "Flux vector splitting for the Euler equations". In Eighth International Conference on Numerical Methods in Fluid Dynamics, p. 507–512. *Springer Berlin Heidelberg*.

Vinokur, M., (1974). "Conservation equations of gasdynamics in curvilinear coordinate systems". *Journal of Computational Physics* **14** (2): 105–125.

Vinokur, M. & Yee, H. C., (2002). "Extension of efficient low dissipation high order schemes for 3-D curvilinear moving grids". In Frontiers of Computational Fluid Dynamics 2002, p. 129–164. *World Scientific Publishing Company*.

Visbal, M. R., (2009). "High-fidelity simulation of transitional flows past a plunging airfoil". *AIAA Journal* **47** (11): 2685–2697.

Visbal, M. R. & Gaitonde, D. V., (1999). "High-order-accurate methods for complex unsteady subsonic flows". *AIAA Journal* **37** (10): 1231–1239.

Visbal, M. R. & Gaitonde, D. V., (2002). "On the use of higher-order finite-difference schemes on curvilinear and deforming meshes". *Journal of Computational Physics* **181** (1): 155–185.

Visbal, M. R. & Rizzetta, D. P., (2002). "Large-eddy simulation on curvilinear grids using compact differencing and filtering schemes". *Journal of Fluids Engineering* **124** (4): 836–847.

Wada, Y. & Liou, M.-S., (1997). "An accurate and robust flux splitting scheme for shock and contact discontinuities". *SIAM Journal on Scientific Computing* **18** (3): 633–657.

Wang, S., Zhou, Y., Mahbub Alam, Md. & Yang, H., (2014). "Turbulent intensity and Reynolds number effects on an airfoil at low Reynolds numbers". *Physics of Fluids* **26** (11): 115107.

Watmuff, J. H., (1999). "Evolution of a wave packet into vortex loops in a laminar separation bubble". *Journal of Fluid Mechanics* **397**: 119–169.

Wendt, J. F., (2008). "Computational fluid dynamics: An introduction". *Springer-Verlag Berlin Heidelberg*.

White, F. M., (2006). "Viscous fluid flow". *McGraw-Hill International Edition*.

Wilcox, D. C., (1988). "Reassessment of the scale-determining equation for advanced turbulence models". *AIAA Journal* **26** (11): 1299–1310.

Wilcox, D. C, (2001). "Turbulence modeling: An overview". In 39th Aerospace Sciences Meeting & Exhibit, *AIAA 2001-0724*.

Wilcox, D. C., (2006). "Turbulence modeling for CFD". *DCW industries Inc. La Canada*.

Windte, J., Scholz, U. & Radespiel, R., (2006). "Validation of the RANS-simulation of laminar separation bubbles on airfoils". *Aerospace Science and Technology* **10** (6): 484–494.

Wissink, J. G. & Rodi, W., (2006). "Direct numerical simulation of flow and heat transfer in a turbine cascade with incoming wakes". *Journal of Fluid Mechanics* **569**: 209–247.

Yakeno, A., Kawai, S., Nonomura, T. & Fujii, K., (2015). "Separation control based on turbulence transition around a two-dimensional hump at different Reynolds numbers". *International Journal of Heat and Fluid Flow* **55**: 52–64.

Yakhot, V., Orszag, S. A., Thangam, S., Gatski, T. B. & Speziale, C. G., (1992). "Development of turbulence models for shear flows by a double expansion technique". *Physics of Fluids A: Fluid Dynamics* **4** (7): 1510–1520.

Yanaoka, H. & Ota, T., (1996). "Three-dimensional numerical simulation of separated and reattached flow and heat transfer over blunt flat plate at high Reynolds number". *Transactions of the Japan Society of Mechanical Engineers, Series B* **62** (601): 3439–3445 (In Japanese).

Yanaoka, H., Yoshikawa, H. & Ota, T., (2002). "Numerical simulation of laminar flow and heat transfer over a blunt flat plate in square channel". *Journal of Heat Transfer* **124** (1): 8–16.

Yanaoka, H., Yoshikawa, H. & Ota, T., (2003). "Direct numerical simulation of turbulent separated flow and heat transfer over a blunt flat plate". *Journal of Heat Transfer* **125** (5): 779–787.

Yang, Z., (2015). "Large-eddy simulation: Past, present and the future". *Chinese Journal of Aeronautics* **28** (1): 11–24.

Yarusevych, S., Sullivan, P. E. & Kawall, J. G., (2006). "Coherent structures in an airfoil boundary layer and wake at low Reynolds numbers". *Physics of Fluids* **18** (4): 044101.

Yarusevych, S., Sullivan, P. E. & Kawall, J. G., (2009). "On vortex shedding from an airfoil in low-Reynolds-number flows". *Journal of Fluid Mechanics* **632**: 245–271.

Yee, H. C., (1987). "Construction of explicit and implicit symmetric TVD schemes and their applications". *Journal of Computational Physics* **68** (1): 151–179.

Yoon, S. & Jameson, A., (1988). "Lower-upper symmetric-Gauss-Seidel method for the Euler and Navier-Stokes equations". *AIAA Journal* **26** (9): 1025–1026.

You, D., Ham, F. & Moin, P., (2008). "Discrete conservation principles in large-eddy simulation with application to separation control over an airfoil". *Physics of Fluids* **20** (10): 101515.

Zaki, T. A., Wissink, J. G., Rodi, W. & Durbin, P. A., (2010). "Direct numerical simulations of transition in a compressor cascade: the influence of free-stream turbulence". *Journal of Fluid Mechanics* **665**: 57–98.

Zhang, H., Reggio, M., Trepanier, J. Y. & Camarero, R., (1993). "Discrete form of the GCL for moving meshes and its implementation in CFD scheme". *Computers & Fluids* **22** (1): 9–23.

Zhang, W., Hain, R. & Kahler, C. J., (2008). "Scanning PIV investigation of the laminar separation bubble on a SD7003 airfoil". *Experiments in Fluids* **45** (4): 725–743.

Zhang, W. & Samtaney, R., (2016). "Assessment of spanwise domain size effect on the transitional flow past an airfoil". *Computers & Fluids* **124** (2): 39–53.